

TEMPORAL CHANGES IN SEISMIC ANISOTROPY AS A NEW ERUPTION FORECASTING TOOL?

by

Alexander Gerst

*A thesis submitted to Victoria University of Wellington
for the degree of*

*Master of Science
in Geophysics*

Institute of Geophysics, School of Earth Sciences
Victoria University of Wellington
Te Whare Wānanga o te Upoko o te Ika a Māui
Wellington, New Zealand

March 2003

FRONTISPIECE



NOTHING IN LIFE IS TO BE FEARED.
IT IS ONLY TO BE UNDERSTOOD.

Marie Curie

ABSTRACT

The orientation of crustal anisotropy changed by ~ 80 degrees in association with the 1995/96 eruption of Mt. Ruapehu volcano, New Zealand. This change occurred with a confidence level of more than 99.9%, and affects an area with a radius of at least 5 km around the summit. It provides the basis for a new monitoring technique and possibly for future mid-term eruption forecasting at volcanoes.

Three deployments of seismometers were conducted on Mt. Ruapehu in 1994, 1998 and 2002. The fast anisotropic direction was measured by a semi-automatic algorithm, using the method of shear wave splitting. Prior to the eruption, a strong trend for the fast anisotropic direction was found to be around NW-SE, which is approximately perpendicular to the regional main stress direction. This deployment was followed by a moderate phreatomagmatic eruption in 1995/96, which ejected material with an overall volume of around 0.02–0.05 km³. Splitting results from a deployment after the eruption (1998) suggested that the fast anisotropic direction for deep earthquakes (>55 km) has changed by around 80 degrees, becoming parallel to the regional stress field. Shallow earthquakes (<35 km) also show this behaviour, but with more scatter of the fast directions. Another deployment (2002) covered the exact station locations of both the 1994 and the 1998 deployments and indicates further changes. Fast directions of deep events remain rotated by 80 degrees compared to the pre-eruption direction, whereas a realignment of the shallow events towards the pre-eruption direction is observed.

The interpretation is that prior to the eruption, a pressurised magma dike system overprinted the regional stress field, generating a local stress field and therefore altering the fast anisotropic direction via preferred crack alignment. Numerical modelling suggests that the stress drop during the eruption was sufficient to change the local stress direction back to the regional trend, which was then observed in the 1998 experiment. A refilling and pressurising magma dike system is responsible for the newly observed realignment of the fast directions for the shallow events, but is not yet strong enough to rotate the deeper events with their longer delay times and lower frequencies. These effects provide a new method for volcano monitoring at Mt. Ruapehu and possibly at other volcanoes on Earth. They might, after further work, serve as a tool for eruption forecasting at Mt. Ruapehu or elsewhere. It is therefore proposed that changes in anisotropy around other volcanoes be investigated.

ACKNOWLEDGEMENTS

This thesis is not only the result of a year of field work, data processing, reading and writing, but it is also the result of the knowledge and the help of others. It is entirely impossible to name all the people that contributed to the success of this study, yet I will attempt to mention the most important ones.

First of all I thank my parents, Hans-Dieter and Brigitte Gerst, for the support I have always got from them, without any form of doubt or question.

I thank my advisors Martha Savage and Friedemann Wenzel for all their support, useful advice and ideas. Thanks also to Martha for always having an open door for me and for the help with the field work. Thanks to John Gamble for teaching me everything about volcanoes and about never forgetting the fun side of things. Thanks to Ralph Wahrlich, for helping me with uncountable computer problems and for always staying nice and friendly in the heat of things. Thanks to Tim Stern for all the scientific advice and the awesome snowboard ride from the top of Mt. Ruapehu.

My field work was made possible by the invaluable help of Sonja Hofmann, Mike Hagerty, Martha Savage, Dennis Gerst, Frederik Gerst, Mathieu Duclos, Frederique Jeandron, Tony Hurst and Geoff Kilgour. I can not thank you enough for voluntarily helping me to carry truck batteries up and down Mt. Ruapehu, and to still keep smiling. The field work was logistically supported by Harry Keys and the Department of Conservation (DOC) with friendly support and permissions to access the national park.

Thanks to Ken Gledhill, Mike Hagerty, Euan Smith, Kevin Furlong, Tony Hurst, John Townend and John Gamble for the help and many useful discussions. Thanks also to Matthew D. Hall, Andrew Orme, John Townend, Stephanie Simmonds, Kevin Furlong, Michelle Salmon and Tim Stern for reviewing my manuscripts.

Thanks to Matthew D. Hall and Andrew Orme for being very good friends and flatmates, and for the introduction into the Kiwi lifestyle. Thanks also to John & Sue Hall for an incredibly warm welcome and an unforgettable Kiwi Christmas.

Thanks to Iain & Glenna Matcham for bringing me to New Zealand, for a Scottish wedding, and for making me wear a kilt. Thanks to Andy, Anna, Audrey, Brett, Etienne, Katie, Kevin, Kitty, Kunal, Marda, Mark, Martin, Mathieu, Matt, Michelle, Ralph, Sandra, Sonja,

Stefan, Susanne, Vicky and Wanda for great BBQs, climbing evenings, snowboarding trips, drinks, pavlovas, pool games and parties.

Thanks to Jürgen Neuberg, Graham Stuart and David Frances from Leeds University for collecting and providing the 1994 and 1998 data, together with Tony Hurst (IGNS), Peter McGinty, and Bernice Hicks (VUW). Thanks to Vicky Miller for important help with her data. Thanks to the Heads of School, Euan Smith and Phil Morisson for administrative help, to the librarian Jill Ruthven, to the owners of Lahar Farm for the permission to access their land, and to IGNS for letting their volcano observatory become my second home. Thanks to Dee, Marie, Marita and Morna for being helpful and always friendly school administrators.

Thanks to all my friends at home in Germany for keeping in touch over one and a half years. A special thanks to Gabi for never giving up calling me.

Thanks to Brett, Stefan and Mark for numerous jumps out of perfectly good aeroplanes, and to my parachute for keeping me alive in every respect. Thanks to Andy Nyblade and Doug Wiens for taking me down to Antarctica, and to Kevin Furlong for setting my trip in motion.

Thanks to Karen Williams, W.H. Freeman publishers, Etienne Audoine, Vicky Miller and John Gamble for the friendly permissions to print some of their figures or photos. Thanks to Shinji Toda for the useful help with his Coulomb software

Thank you all very much, I couldn't have done it without you!

A special thanks goes to Sonja Hofmann for an infinite amount of smiles and patience. And yet there is no way of thanking enough for not even hesitating a second to climb Mt. Ruapehu with me in a winter blizzard at -10°C , only to dig out a data disk under one metre of solid ice.

This study was funded by the New Zealand Earthquake Commission (EQC) and by a scholarship of the German Academic Exchange Service (DAAD). The majority of maps in this thesis were produced using the free Generic Mapping Tools (GMT; Wessel and Smith, 2001). The seismic processing was done using the Seismic Analysis Code (SAC 2000; Tapley et al., 1990). Figures describing the data dependencies were mainly generated with the MATLAB software, and numeric models were calculated with the Coulomb program. The typesetting of this thesis was done with \LaTeX , which proved to be an outstandingly helpful software for this purpose, and is freely available.

The photograph in the Frontispiece was printed with the friendly permission of John Gamble, and shows the initial explosion of the 1996 eruption.

CONTENTS

Frontispiece	iii
Abstract	v
Acknowledgements	vii
Table Of Contents	ix
List Of Figures	xiii
List Of Tables	xvi

Chapters

1 Introduction	1
1.1 Motivation of this work	1
1.1.1 Why the 2002 deployment is critically important for this study	2
1.1.2 The need for eruption forecasting tools	4
1.2 Regional tectonic settings	5
1.2.1 The Central Volcanic Region and the Taupo Volcanic Zone	7
1.3 The local tectonic setting of Mt. Ruapehu volcano	10
1.3.1 Eruption style and volcanic hazards at Mt. Ruapehu	12
1.3.2 The 1995 / 1996 eruption sequence	13
1.3.3 Velocity model	14
2 Seismic anisotropy	17
2.1 Theoretical background	17
2.1.1 Hexagonal anisotropy	20
2.1.2 Systems of anisotropy with a lower order of symmetry	23
2.1.3 The cause of mantle anisotropy	24
2.1.4 Effect on the waveforms	26
2.1.5 Delay times and percent anisotropy	26

2.1.6	Multiple layers of anisotropy	27
2.1.7	The shear wave window	28
2.2	Observations	29
2.2.1	Seismic anisotropy in the vicinity of volcanoes	29
2.2.2	Discoveries of temporal changes in seismic anisotropy	32
3	Method	35
3.1	Data processing	35
3.2	How to measure shear wave splitting	36
3.2.1	Reprocessing of 1994 and 1998 data	37
3.2.2	The Silver & Chan algorithm	38
3.2.3	NULL measurements	42
3.2.4	Cycle Skipping	44
3.3	The slope corrected shear wave angle	49
3.4	Mean value and error analysis	52
3.4.1	Obtaining the mean value of splitting measurements	52
3.4.2	Why angles have to be doubled	53
3.4.3	Calculating standard deviation and errors : The Von Mises Statistics .	53
3.4.4	The difference between standard deviation and standard error	57
4	Data acquisition	59
4.1	The CHARM experiment	59
4.1.1	Setup	60
4.1.2	Relation to previous deployments	61
4.1.3	Equipment	63
4.1.4	Logistics	63
4.2	Information about previous deployments at Mt. Ruapehu	64
4.2.1	The 1994 deployment	64
4.2.2	The 1998 deployment	65
5	Results	69
5.1	General results of the deployments	69
5.2	Raypaths and source locations	84
5.3	Examination for dependencies on different parameters	92

6	Discussion	101
6.1	Authenticity of the changes in anisotropy	101
6.2	The source region of the anisotropy	103
6.3	The model	105
6.3.1	How can a dike change the fast direction?	108
6.3.2	Further observations that agree with this model.	112
6.3.3	Observations that require further refinement of the model.	115
6.3.4	Numerical modelling	117
6.3.5	Could the fast direction have changed by exactly 90° ?	122
6.4	Alternative models	123
6.5	Seismicity associated with the changes in anisotropy	125
7	Summary & conclusions	129
7.1	Implications	132
7.2	Answered questions	132
7.3	Testable predictions	133
7.4	The suitability of FWVZ as a long term monitoring station	134
7.5	Unanswered questions and future recommendations	135
 Appendices		
A	Mathematical appendix	137
A.1	Calculating the Christoffel matrix for the isotropic case	137
B	Data properties	139
B.1	Splitting results without multiple frequency filters	139
B.2	Instrument recording times	142
B.3	Data quality control	143
B.3.1	Check for rotated components	143
B.3.2	Sun compass test for correct orientation	144
C	List of all measurements	145
D	Data processing software	165
D.1	Description of routines used	165
D.2	List of newly developed programs for future users	168
D.2.1	UNIX shell, NAWK and C++ programs	168
D.2.2	SAC macros	169

References and indices**References** **170****Index** **183**

FIGURES

1.1	The Ring Of Fire: An overview over continental plate margins	5
1.2	Bathymetric image of New Zealand	6
1.3	Sketch of a cross cut through the CVR	7
1.4	Map of the CVR and the TVZ	8
1.5	Photograph of Mt. Ruapehu	10
1.6	Map of New Zealand volcanoes	10
1.7	Lava formations and vents in the Tongariro Volcanic Centre	11
1.8	A cross cut through the North Island of New Zealand	12
1.9	The 1996 eruption from the town of Ohakune	13
1.10	Map of five year seismicity around New Zealand	15
2.1	Illustration of possible wave polarisations	20
2.2	Illustration of shear wave splitting	22
2.3	Shear wave splitting in the presence of two layers of anisotropy	28
3.1	Data processing flow chart	35
3.2	How to un-split an S-wave	39
3.3	The NULL phenomenon	43
3.4	Example for an A-quality measurement	45
3.5	Example for an A-quality measurement	46
3.6	Example for an AB-quality measurement	46
3.7	Example for a B-quality measurement	47
3.8	Example for a C-quality measurement	47
3.9	Example for a NULL measurement	48
3.10	Example for cycle skipping	48
3.11	The slope corrected shear wave window	49
3.12	Incidence angle on a slope	49
3.13	Geometry of incoming rays at a slope	50
3.14	Effect of doubling the angles	53
3.15	Validity of the Von Mises Distribution	54

4.1	Digital elevation model of Mt. Ruapehu with the CHARM stations	59
4.2	Field picture of LTUR2 station	62
4.3	Map with station locations	66
4.4	3D perspective view of all available earthquake sources	67
5.1	Overview of the splitting results: Combined results as histograms	74
5.2	Map of individual splitting results, 1994	75
5.3	Map of individual splitting results, 1998	77
5.4	Map of individual splitting results, CHARM 2002	79
5.5	Overview of the splitting results: Individual station histograms	80
5.6	Shallow events from 1998 and 2002 with special data selection criteria	81
5.7	Map of NULL measurements, 1998	82
5.8	Map of NULL measurements, CHARM 2002	83
5.9	Raypaths of the 1994 and 1998 measurements	85
5.10	Raypaths of the 2002 measurements	86
5.11	Vertical cross section of the 1994 results	87
5.12	3D perspective view of the 2002 measurements	88
5.13	Vertical cross section of the 1998 results	89
5.14	3D perspective view of the used earthquakes	90
5.15	Vertical cross section of the 2002 results	91
5.16	Fast directions vs. depth	93
5.17	Frequency vs. depth	94
5.18	Delay time vs. frequency	95
5.19	Delay time vs. period	96
5.20	Delay time vs. depth	97
5.21	Fast direction vs. frequency	98
5.22	Delay time vs. hypocentral distance	99
5.23	Fast direction vs. back azimuth	100
5.24	Delay time vs. time (2002)	100
5.25	Delay time vs. time (1994)	100
6.1	Illustration of dikes and sills in a volcanic system	106
6.2	Anisotropy model for 1994, 1998 and 2002	107
6.3	Model of crustal crack orientation before and after the 1995/96 eruption . . .	108
6.4	Initial polarisations of 2002 events	114
6.5	Stress changes caused by an opening dike	118
6.6	Grid displacement of the numeric dike model	119
6.7	Shallow seismicity rate ($M_L \leq 0$) at Mt. Ruapehu between 1988 and 2002 . .	127

6.8	Seismicity rate ($M_L \geq 2$) at Mt. Ruapehu between 1988 and 2002	127
B.1	Splitting measurements with only one measurement per event	140
B.2	Individual station histograms with only one measurement per event	141
B.3	Recording times of the CHARM instruments	142
B.4	Estimating back azimuth from first motion	143
D.1	Data processing flow chart	165

TABLES

3.1	Earthquake selection criteria	36
3.2	Numbers of available and selected events	37
3.3	Quality mark definitions	38
3.4	Slope angles for recording stations	51
4.1	Station locations and equipment of the CHARM project	60
4.2	Station locations and equipment of the 1994 deployment	65
4.3	Station locations and equipment of the 1998 deployment	65
5.1	Results of individual stations and deployments	71
5.2	Special results of the 1998 and 2002 shallow data	73
B.1	Sun compass test for rotated components	144
C.1	List of individual measurements, 1994 deployment	146
C.2	List of individual measurements, 1998 deployment	149
C.3	List of individual measurements, 2002 deployment	153
D.1	Earthquake selection criteria	166

CHAPTER 1

INTRODUCTION

This chapter will give an overview of the motivation for this project and its objectives. It will illustrate previous work in this field and show the relation of this work to volcanic hazard assessment on Mt. Ruapehu and other volcanoes in the world. An introduction to the regional tectonic setting of New Zealand and the local setting of Mt. Ruapehu volcano will also be given.

1.1 Motivation of this work

The aim of this study is to investigate possible changes in seismic velocities and stress in the earth's crust, which might be associated with an eruption sequence at Mt. Ruapehu volcano, New Zealand. Such changes – if they are recurring – might serve as an indicator for imminent eruptions at the mountain and therefore as an eruption forecasting tool.

It is known that volcanic eruptions are almost always preceded by magma movements in the feeder system of the volcano. Such movements involve high pressures and great masses, and are therefore likely to influence the stress state of the crust in the immediate vicinity of the volcano. This stress state is the main subject of this investigation. Geophysical methods are used for this task, of which the most important one is the method of shear wave splitting.

Shear wave splitting occurs in the earth, and is the acoustical analogue to the optical phenomenon of birefringence. This means that a shear wave travelling in an anisotropic medium (like the crust) will split into a fast and a slow S-wave, with these waves polarised perpendicular to each other. The *polarisation direction of the first shear wave*^{*} is measured at the surface, and can be used as a tool to obtain information about the in-situ state of stress in the earth's crust by measuring its *velocity anisotropy*.

The first indications for a temporal change in *seismic velocity anisotropy*[†] were observed by Miller and Savage (2001), when analysing shear wave splitting data from two seismometer

^{*}from this point on called the *fast direction*

[†]from this point on referred to as *anisotropy*

deployments at Mt. Ruapehu, the first carried out in 1994 and the second in 1998. Temporal changes were suggested as the most likely, but not the unique explanation for observed phenomena, and concerns about effects from heterogeneities, frequency, and back azimuth dependencies could not be rejected (See Section 1.1.1). The lack of compelling evidence directly lead to this project, which was designed to clarify the matter and to critically assess the results from the two deployments. In order to do so, a third seismometer deployment was carried out in 2002, covering station locations from both previous deployments. The results of the project and a comprehensive interpretation of all three deployments will be presented in this thesis, together with an overview of the theories and techniques that were applied.

The main objectives of this study can be expressed in the form of the following six questions:

1. Did the direction of seismic anisotropy change between 1994 and 1998?
2. Where did this change in anisotropy occur?
3. Can it be associated with a volcanic eruption at Mt. Ruapehu?
4. Will such a change happen again?
5. What are the processes that lead to such a change?
6. Will this behaviour lead to a usable method for forecasting volcanic eruptions?
7. What should be done in the future – both at Mt Ruapehu and on other volcanoes on Earth?

This thesis will attempt to provide a satisfying answer to each one of these questions.

1.1.1 Why the 2002 deployment is critically important for this study

When comparing the data from the 1994 and the 1998 deployments, the most striking feature is a systematic difference in the average polarisation of the fast S-waves (Miller and Savage, 2001), indicating differences in the anisotropic medium. Since the two deployments covered approximately the same regions (within 10 km of Mt. Ruapehu), and since a major volcanic eruption occurred between the two deployments, a temporal change of anisotropy seems to be a valid explanation for the differences. However, there are several scenarios that could account for a systematic difference in the observed fast directions without the necessity for assuming a temporal change.

- Station locations from the two deployments in 1994 and 1998 were different by a minimum of 1 km, and a maximum of >10 km. Furthermore, the 1998 deployment consisted

of only three stations. With the given frequencies of around 1–3 Hz, and surface S-wave speeds of around 1.3 km/s, it must be assumed that the stations all sample different regions of the shallow crust (i.e. the raypaths, and the affected zones around the raypaths do not overlap). Therefore, lateral heterogeneities in the anisotropic medium (as can be expected in the vicinity of complex structures such as volcanoes) can lead to systematic differences in the measured fast directions between the stations and thus also to apparent differences between the two deployments. This effect is observed in a number of studies, where stations as close together as 200 m yielded average fast directions as different as 45° without a temporal change (e.g. Munson and Thurber, 1993; Munson et al., 1995; Savage et al., 1989; Gledhill, 1991b; Booth et al., 1985; Chen, 1987). This is a major concern that has to be proven wrong before a temporal change in anisotropy can be assumed.

- The frequency filters that were used for filtering the seismic traces before the measurement was obtained showed systematic differences between the two deployments. This was the result of different noise properties of the two datasets, which caused different filters to yield different signal to noise ratios (i.e. the 1994 events were mainly filtered with 1–7 Hz, whereas the 1998 events were mainly filtered with 1–3 Hz). Since there are reported cases of frequency dependent anisotropy (e.g. Marson-Pidgeon and Savage, 1997; Audoine, 2002), choosing systematically different frequency filters can lead to systematically different fast directions. To address this problem, Miller (2000) attempted to re-filter the 1994 events with the same filter as the 1998 events, but scattering of the now very noisy measurements, and an insufficient number of measurements led to an ambiguous result. Therefore the question about the effects of frequency filtering has to be investigated.
- Effects of back azimuth dependence, and dependence on the initial polarisation of the S-wave have not been investigated. Babuška and Cara (1991), Silver and Savage (1994), and Saltzer et al. (2000) show that in the case of an inclined system of anisotropy, or in the presence of more than one layers of anisotropy, a complex dependency of the fast direction on the back azimuth or the initial polarisation emerges. These systematic variations of the fast direction can lead to an apparent change in anisotropy if systematic differences in the back azimuth or in the initial polarisations existed during the two deployments.

These examples show that from the data obtained in 1994 and 1998, the question of whether the anisotropy has changed can not be answered conclusively. Yet the answer to this question is critical for assessing the value of the method in regard to forecasting future eruptions at Mt. Ruapehu. In order to do so, a third deployment was planned to investigate all mentioned effects in combination with the data from 1994 and 1998. This thesis will describe

the implementation and the results of a third deployment, and will attempt to provide a comprehensive interpretation of all data that were obtained in 1994, 1998, and 2002.

1.1.2 The need for eruption forecasting tools

Mt. Ruapehu is a potentially dangerous volcano on the North Island of New Zealand. Eruptions at Mt. Ruapehu have led to the loss of life in the past, and every year thousands of skiers and snowboarders are at risk while performing winter sports on the volcano. Furthermore, important parts of New Zealand's infrastructure and industry are vulnerable to eruptions at Mt. Ruapehu (an overview over volcanic hazards at Mt. Ruapehu will be given in Section 1.3.1).

Eight years after the 1945 eruption at Mt. Ruapehu, on Christmas Eve 1953, the wall of a refilling Crater Lake suddenly collapsed and generated a large lahar (i.e. a volcanic mudflow), which surged down the Whangaehu valley in the southwest of the mountain. This lahar destroyed the Tangiwai railway bridge 38 km downstream, shortly before the Auckland–Wellington express train arrived at the bridge. The train was derailed and partially dragged into the lahar, causing the loss of 151 lives. This lahar was not immediately preceded by an eruption, but is nevertheless a consequence of the 1945 eruption at Mt. Ruapehu (Healy, 1954).

Several eruptions at Mt. Ruapehu have occurred with little or no warning in the past (e.g. such as increased seismicity or gas emissions), with more than 50 small eruptions occurring during the last 50 years (Latter, 1986), all of which were possibly life threatening to persons within a certain radius of the Crater Lake. Even though there are many sophisticated methods that help to forecast volcanic eruptions, the ability to reliably predict them is not yet sufficient.

This problem applies to most volcanoes on Earth. It is estimated that about 10% of the world's population lives in the close proximity of an active volcano (Peterson, 1986) and is therefore threatened by volcanic eruptions. Several hundred thousand people have been killed by volcanic eruptions in the last few centuries, one of the most recent being the eruption of Nevado del Ruiz (Colombia) in 1985, which killed more than 22,000 people in a debris flow (e.g. Fisher et al., 1997). Eighteen hundred years ago, an eruption at Lake Taupo, New Zealand ejected around 100 km^3 of hot volcanic ash and rocks within hours and annihilated every form of life within several hundred kilometres from the volcano in a matter of minutes. Ash and gas discharge rates of up to 40 km^3 per second have been suggested for this eruption (Dade and Huppert, 1996). Fortunately, this last scenario took place at a time when New Zealand was not inhabited by humans, but similar eruptions are likely to occur again within geologic timescales (e.g. several thousand years), in an area that is now densely populated by humans.

It is obvious from the reasons above that a thorough understanding of the mechanisms in the interior of volcanoes is necessary, which might eventually lead to a more reliable way of predicting volcanic eruptions and therefore to saving lives.

1.2 Regional tectonic settings



Figure 1.1 New Zealand and The Ring Of Fire: An overview of continental plate margins. Red dots mark the places where active volcanoes exits. The New Zealand volcanoes are part of a band of active volcanoes, which encircles the pacific plate and is called the Ring Of Fire. (Source: USGS)

New Zealand lies at the boundary between the Pacific and the Australian plate (See Figure 1.1). On the North Island, this plate boundary zone is dominated by the subduction of the oceanic crust of the Pacific plate beneath the continental crust of the Australian plate (See Figure 1.2). Subduction is oblique under the North Island of New Zealand, and obliqueness increases towards the south, eventually turning into a transpressional boundary with a major strike slip component within the South Island of New Zealand. Movement in this region occurs as reverse-dextral movement on the Alpine Fault system (Figure 1.2). Subduction rates vary from about 50 mm per year (Walcott, 1978; Anderson and Webb, 1994) in the north, to around 37 mm strike slip component in the centre of the South Island (DeMets et al., 1990). Further south, the subduction zone switches polarity, and the oceanic crust of the Australian plate is being subducted beneath the Pacific plate (Cole, 1990).

An arc-trench system (called the Taupo-Hikurangi arc-trench system) extends from the Hikurangi trough on the east side of the system to the Taupo Volcanic Zone in the centre of the North Island (Figure 1.2).

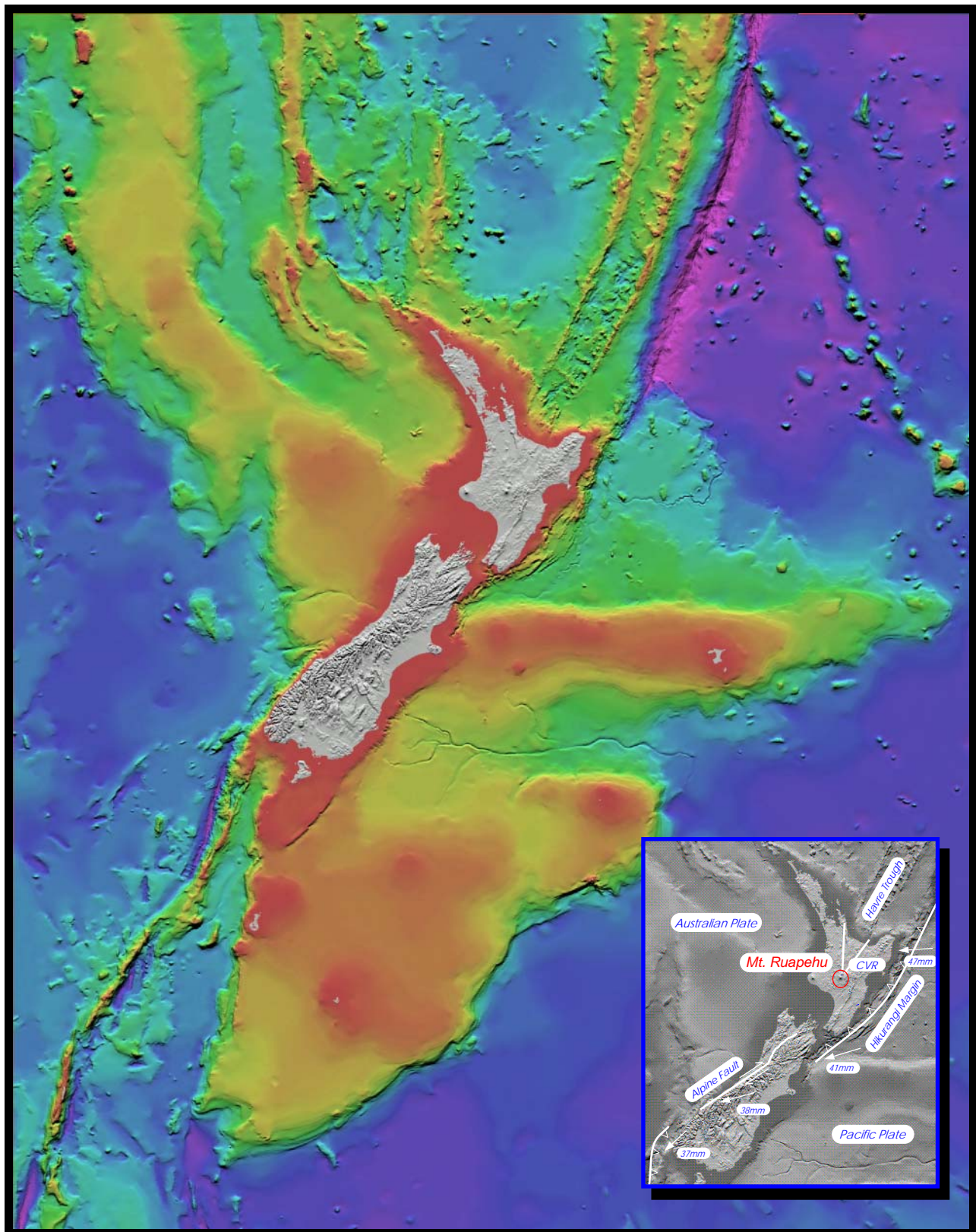


Figure 1.2 *Living on an active continental boundary: Bathymetric image of New Zealand.* Kindly supplied by the National Institute for Water and Atmospheric Research (NIWA). The map key shows a tectonic interpretation with data from DeMets et al. (1990).

1.2.1 The Central Volcanic Region and the Taupo Volcanic Zone

The Central Volcanic Region (CVR; Figure 1.4) is a wedge-shaped basin of predominantly Quaternary rhyolitic and andesitic volcanism (Cole, 1990), and represents the continental continuation of an otherwise oceanic back-arc spreading zone (Havre Trough). It is dominated by normal faulting and extensional structures, and is defined by a distinct low in gravity and seismic velocities (Stern, 1985). Due to the subduction of dense and old oceanic lithosphere under the North Island, the stress between the two plates is relatively low and the subducting plate is rolling back towards the east (Figure 1.3; Stern, 1987; Smith et al., 1989). This causes extension in the CVR and results in thinning of the continental lithosphere, accompanied by the intrusion of hot mantle material from below. Crustal thicknesses as little as 15 km (Stern and Davey, 1985) are observed, which are confirmed by a recent study (the NIGHT project; Stratford and Stern, 2002).

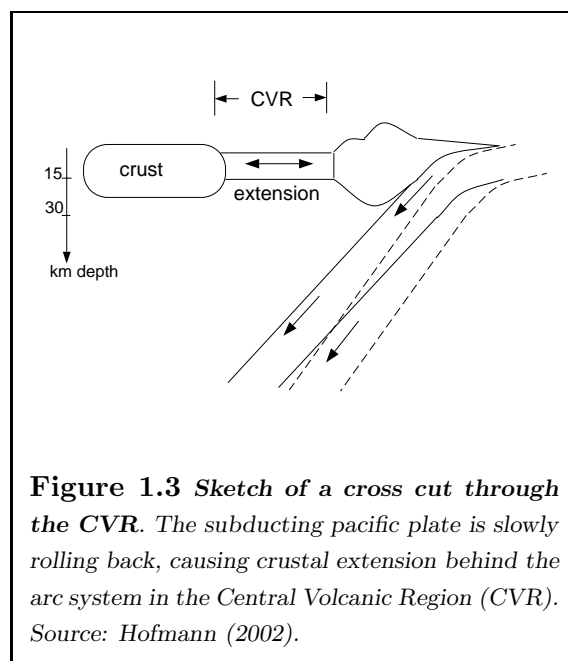


Figure 1.3 Sketch of a cross cut through the CVR. The subducting Pacific plate is slowly rolling back, causing crustal extension behind the arc system in the Central Volcanic Region (CVR). Source: Hofmann (2002).

The Taupo Volcanic Zone (TVZ) is the youngest and easternmost part of the CVR and describes the portion that is currently volcanically active (<2 Ma). It is approximately 300 km long (200 km on land), up to 60 km wide, and can be divided into a young (mostly < 200 ka), predominantly andesitic volcanic front (or arc) in the east and a predominantly rhyolitic basin in the western part (Figure 1.4). The common eastern boundary of the CVR and the TVZ is the present volcanic front, of which Mt. Ruapehu is the southernmost volcano. This volcanic front was constantly migrating south-eastwards in the past, and does so at the present day (e.g. Calhaem, 1973; Stern et al., 1987). At the same time, it is rotating clockwise due to the oblique subduction of the Pacific plate, which is consistent with the rotation of sediments in the eastern part of the North Island (Walcott, 1984; Wright and Walcott, 1986).

Different opinions exist about the correct name of the basin to the west of the arc (See Cole, 1990). The term “back-arc basin” seems most appropriate due to the fact that the TVZ is located behind the arc of an active trench system, and has a subduction related origin (Taylor and Karner, 1983). However, some argue that back-arc basins usually refer to oceanic crust instead of continental crust (as in the TVZ), and that the term “marginal basin” therefore seems more appropriate. Others suggest a “rifted arc” (i.e. an arc that is disrupted by rifting; Wilson et al., 1995). This study will use the term “back-arc basin”,

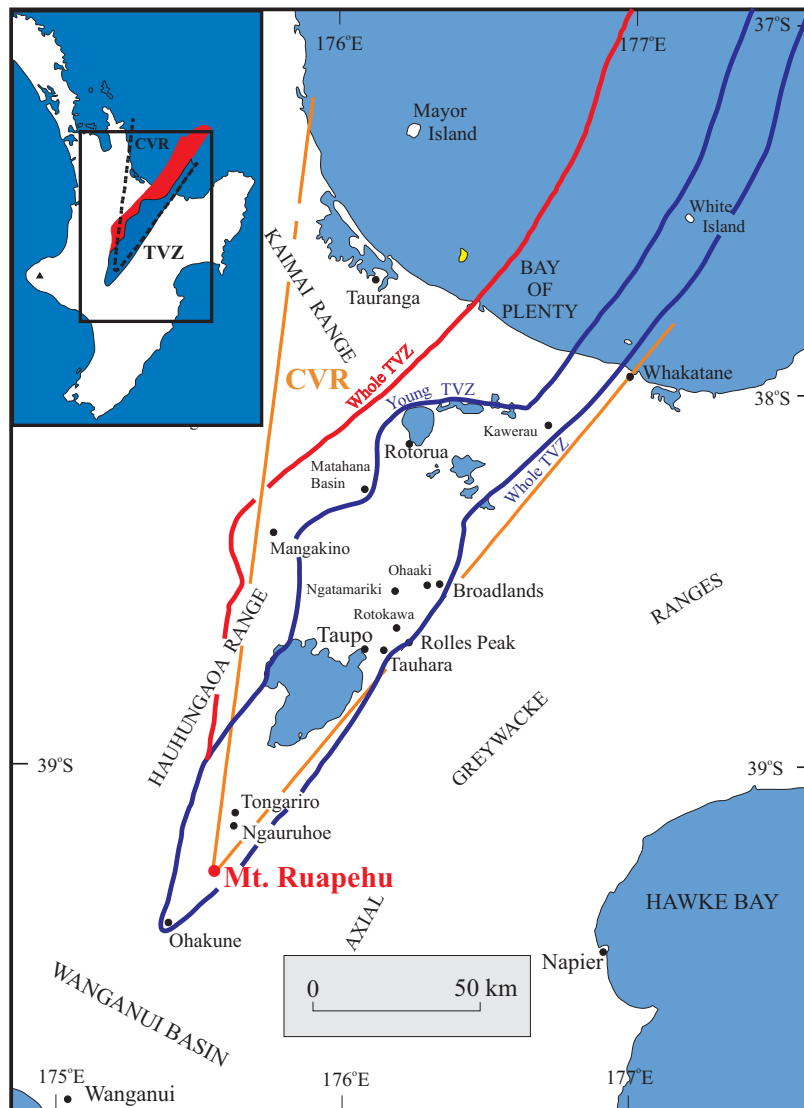


Figure 1.4 Map of the CVR and the TVZ. The orange region marks the Central Volcanic Region (CVR); the blue region marks the young part of the Taupo Volcanic Zone (TVZ), which is also the volcanic front (or arc). The red and the blue zone together represent the whole TVZ (adapted from Miller (2000) and Wilson et al. (1995)).

following the former definition.

There are different estimates of the extension rate in the TVZ, ranging from 3 to 18 mm per year, depending on the method of measurement and the location within the CVR (overview in Villamor and Berryman, 2001). From the average spreading rate and the width of the zone, an approximate start time of the spreading is 4 Ma before present. Magnetic anomaly data from the Havre Trough suggests a start around 3 Ma ago (Malhoff et al., 1982), and is therefore roughly consistent with the other results. Andesitic volcanic activity in the TVZ can be traced back to at least 2 Ma (e.g. Wilson et al., 1995). Present strain rates, derived by GPS measurements, are around $0.15 \times 10^6/\text{yr}$ to $0.2 \times 10^6/\text{yr}$, with an

extensional azimuth of 120° to 130° (e.g. Darby and Meertens, 1995; Cole et al., 1995). This extensional strain direction is oriented perpendicular to the dominant normal faults in the zone, and suggests a regional maximum horizontal principal stress direction of around 30° to 40° (NNE-SSW to NE-SW). Such a maximum horizontal stress direction is also consistent with regional anisotropy studies (Audoine, 2002).

The TVZ consists of mainly rhyolitic volcanic deposits, reaching to depths of at least 2 to 3 km (e.g. Stern, 1987; Cole, 1990), according to borehole and seismic data. Suggested bulk volumes of these deposits range around $20,000 \text{ km}^3$, of which more than $15,000 \text{ km}^3$ ($\approx 85\%$) are rhyolitic deposits (with typically 70-77% SiO_2). Andesites are an order of magnitude less abundant ($\approx 15\%$), and basalt and dacite only have suggested volumes of around 100 km^3 ($\approx 1\%$) each (e.g. Gamble et al., 1993; Wilson et al., 1995). These volumes can only be minimum values, since the thickness of the deposits is not exactly known. Eight rhyolitic caldera centres have so far been identified in the central segment of the TVZ, with ages up to 1.6 Ma (Wilson et al., 1995). This central TVZ is the most frequently active and productive silicic volcanic system on Earth, erupting rhyolite at an average rate of around $0.3 \text{ m}^3/\text{s}$ (Houghton et al., 1995). Several single eruptions ejected material with volumes well in excess of 1000 km^3 . Magmas are generated in the mantle wedge below the TVZ by the interaction of H_2O released from a dehydrating subducting slab, which leads to partial melting in the mantle (anatexis). The magmas are initially largely basaltic and undergo a complex process of partial melting, fractional recrystallisation, crustal assimilation, and magma mixing (e.g. Gamble et al., 1993; Wilson et al., 1995). This leads to a wide variety of compositions of the erupted material. It is remarkable that no rhyolitic volcanism occurs in the north and the south part of the central TVZ; these areas are dominated by andesitic volcanism (e.g. White Island, Tongariro, or Ruapehu). The most recent voluminous eruptions in the TVZ originated from Lake Taupo in 186 A.D. ($\approx 100 \text{ km}^3$ ejected material), and from Mt. Tarawera in 1886 ($\approx 2 \text{ km}^3$ ejected material).

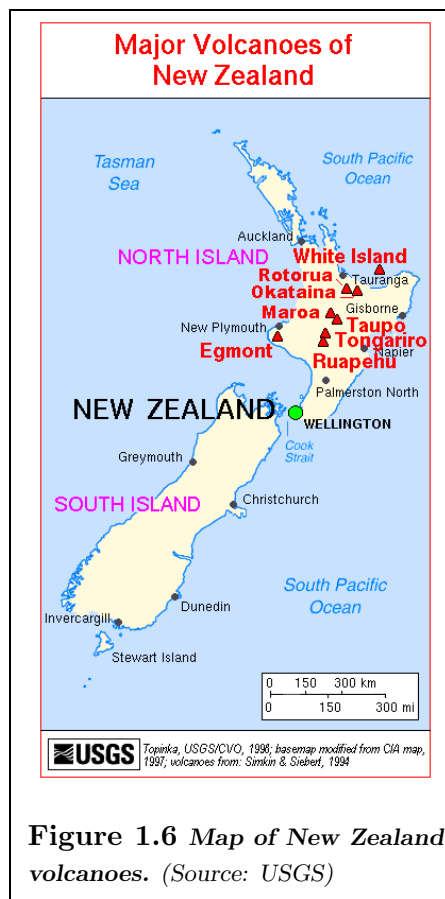
The total heat output of the TVZ is suggested to be at least 4200 MW, which can be expressed as an equivalent heat flow of $700\text{--}800 \text{ mW/m}^2$ if the area of convective transfer of heat is assumed to be $5000\text{--}6000 \text{ km}^2$ (Stern, 1987; Bibby et al., 1995). This heat flow is 13 times greater than the continental norm and is one of the highest reported in a back-arc basin (Cole et al., 1995).

To the west and east of the TVZ, the upper crust consists of pre-volcanic *greywacke* sediments. These might be continuous under the TVZ, but the heat flux requires that the entire sub-volcanic crust is replaced by intermediate to silicic intrusions if the heat flow is due to cooling crustal magmatic intrusions. (e.g. Stern, 1985, 1987). Explosion seismology studies in the TVZ report low surface velocities ($<2 \text{ km/s}$) and crustal wave speeds of $3.0\text{--}6.1 \text{ km/s}$, overlying a layer of $7.4\text{--}7.5 \text{ km/s}$ at a depth of around 15 km (Stern and Davey, 1985).



Figure 1.5 *Mt. Ruapehu in the setting sun (2002)*

1.3 The local tectonic setting of Mt. Ruapehu volcano



Mt. Ruapehu lies in the Tongariro Volcanic Centre at the southern boundary of the TVZ (Figures 1.4 and 1.6), and is the largest active andesite-dacite volcano on the onshore part of the TVZ with an estimated cone volume of around 110 km^3 (Hackett and Houghton, 1989). It is also the highest mountain on the North Island of New Zealand, with an elevation of 2797 m above sea level, forming an eroded active strato-volcano with an almost permanent snow cap.

The Tongariro Volcanic Centre consists of several active volcanoes, which are located on a NNE-SSW striking line: Mt. Ruapehu, Mt. Ngauruhoe and Mt. Tongariro (see Figure 1.7). This volcanic vent alignment is very likely caused by the regional stress pattern (e.g. Nakamura, 1977), with an inferred maximum horizontal stress direction of around NNE-SSW. This direction also coincides with the orientation of several exposed volcanic dike structures in the Tongariro Volcanic Centre (e.g. Pinnacle Ridge and Meads Wall

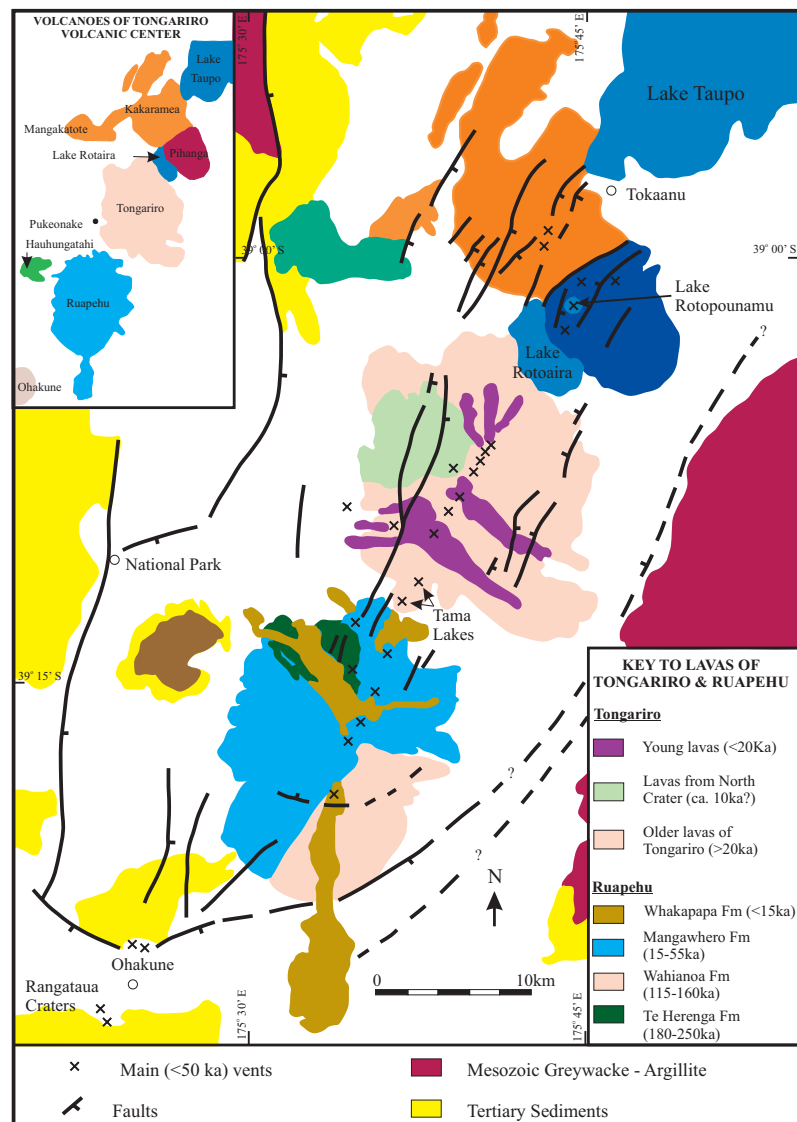


Figure 1.7 Lava formations and vents in the Tongariro Volcanic Centre. Note the strong NNE-SSW alignment of faults and vents (from Cole (1990) and Miller (2000), with corrected dates from Gamble et al. (2003)).

Dyke on Mt. Ruapehu; John Gamble, pers. comm.). The area is dominated by typically NNE-SSW trending faults, which are suggested to be caused by magmatic intrusion into shallow (<10 km) crustal reservoirs and overlying dike injection, again aligned with the stress field (Cole, 1990).

The depth of the subducted plate under Mt. Ruapehu is around 100 km (see Figure 1.8), and is marked by a narrow region of intensive seismicity, known as the *Wadati-Benioff zone* (see Figure 1.10 and Chapter 4, Figure 4.4; Anderson and Webb, 1994; Reyners and Stuart, 2002).

Stratigraphy on and around Mt. Ruapehu consists of four major formations. They are

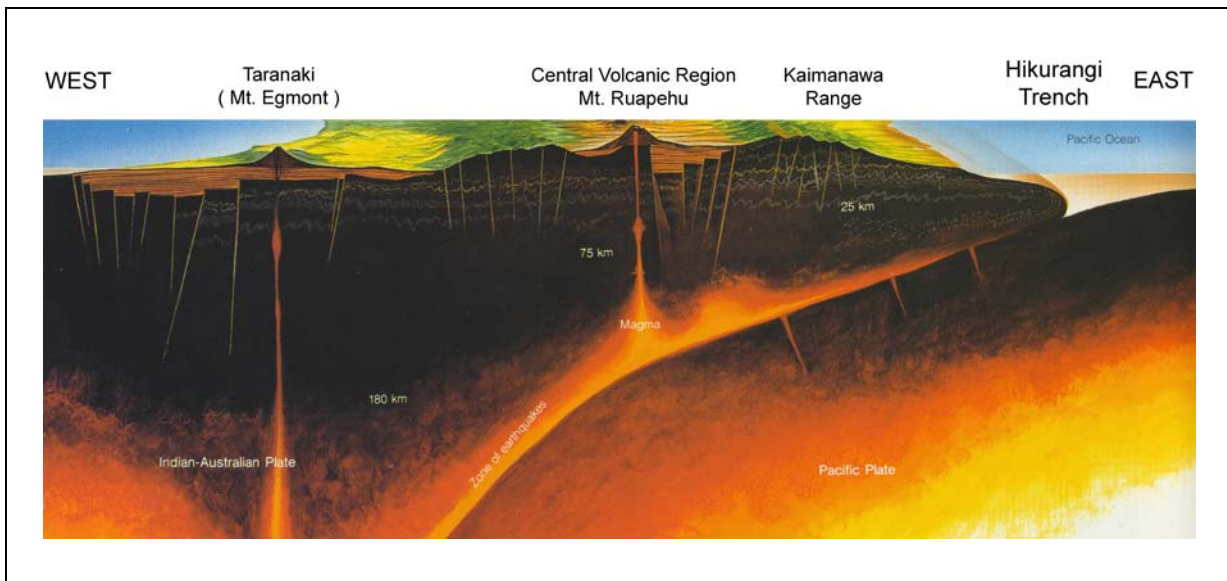


Figure 1.8 A cross cut through the North Island. Interpretation of the plate kinematics under the North Island of New Zealand. Kindly supplied by Karen Williams (Artist unknown; Williams, 2001).

(from oldest to youngest) Te Herenga (250–180 ka), Wahianoa (160–115 ka), Mangawhero (55–15 ka), and Whakapapa (<15 ka), which are dated by radiometric methods (Hackett and Houghton, 1989; Gamble et al., 2003). Even though the oldest of these formation reaches back only 250 ka, there is petrologic evidence for volcanic activity at Mt. Ruapehu as early as 340 ka (e.g. Gamble et al., 2003). The average flux of erupted material at Mt Ruapehu is $0.6 \text{ km}^3/\text{ka}$ ($\sim 0.02 \text{ m}^3/\text{s}$), but periods with more than $1 \text{ km}^3/\text{ka}$ existed.

Pyroclastic rocks and lavas from Mt. Ruapehu are porphyritic basaltic andesites. Phenocrysts are dominated by plagioclase, clinopyroxene, orthopyroxene and Fe-Ti oxides (Gamble et al., 2003). SiO_2 contents vary over a wide range between around 53% and 67%.

1.3.1 Eruption style and volcanic hazards at Mt. Ruapehu

Over the last several thousand years, volcanic activity at Mt. Ruapehu has mainly been concentrated in a vent system beneath the Crater Lake (Gamble et al., 2003). This Crater Lake is filled with around 10^7 m^3 of acid water, with varying pH values sometimes lower than pH 1 (e.g. Nairn and Scott, 1996). Therefore, the most recent activity at Mt. Ruapehu has mainly been phreatomagmatic, but several other eruption styles (or the evidence for them) were observed in the past (e.g. extrusion of lava flows, strombolian and sub-plinian eruptions, lava dome extrusion and disruption, sector collapse, collapse of the Crater Lake wall, flank vent eruptions; Houghton et al., 1987).

Hazards from Mt. Ruapehu exist mainly in the form of lahars, which have a consistency similar to wet concrete, and reach speeds of up to 100 km/h with flow rates exceeding 2000



Figure 1.9 *The 1996 eruption from the town of Ohakune in 15 km distance.* (Photo: John Gamble)

m^3/s (Manville et al., 1998). These lahars have destroyed ski field facilities, hydroelectric power canals, power lines, roads, and rail bridges during various eruptions of the last century. Deposits suggest that lahars reach distances of up to 160 km from Mt. Ruapehu (e.g. Houghton et al., 1987). Especially vulnerable to lahars are people in the crater area and on the ski fields. Lahars are estimated to take approximately 90 s to reach the upper Whakapapa ski field, therefore leaving only little time for evasive actions (Sherburn and Bryan, 1999). Every year, around 500,000 people visit the mountain to perform winter sports or other outdoor activities (Houghton et al., 1987), with peak times of far more than 10,000 people per day (Nairn and Scott, 1996).

A second hazard is the ashfall that is associated with an eruption cloud. In the recent history, ashfalls at Mt. Ruapehu resulted in drinking water contamination, crop damage, widespread fish loss, collapse of buildings, and the closure of roads and international airports (Houghton et al., 1987; Johnston et al., 2000). Further sources of hazards on Mt. Ruapehu are ballistic block fall, sector collapse and lava flows.

1.3.2 The 1995 / 1996 eruption sequence

The largest historical eruption of Mt. Ruapehu took place between September 1995 and August 1996 (Johnston et al., 2000), following a series of phreatomagmatic explosions in an

increasingly warming Crater Lake. The first eruptions took place in the Crater Lake, generating major lahars down the flanks of the volcano and through the ski fields (a photograph of the 1996 eruption is shown in the Frontispiece). After the lake water was ejected, the eruptions grew drier and more sustained. Acidic ash was deposited up to 250 km from the mountain (Johnston et al., 2000) by a 12 km high volcanic plume (e.g. Bryan and Sherburn, 1999).

Peak times of the eruption sequence were 18–25 September 1995, 7–14 October 1995, and 17–18 June 1996. The eruptions were largely accompanied by 1–2 Hz volcanic tremor and occasional volcanic earthquakes (Nairn and Scott, 1996). Since the initial lahar generating explosions took place with no warning, thousands of skiers had been on the Whakapapa ski field on the day of the eruption, and therefore partially in the pathways of the lahars. It has to be assumed that the main circumstance leading to the lack of casualties at this eruption was that it took place in the early evening, shortly after the ski fields closed for the day. A group of tourists had visited the crater lake one hour before the eruption, and fortunately was already far enough away when the eruption started (Ruapehu Alpine Lifts Ltd., pers. comm.). Buildings and facilities on the ski field were destroyed, as well as electricity transmission lines. The minimum estimate for the economic damage caused by the 1995/1996 eruption sequence lies around NZ\$130,000,000 (New Zealand dollars).

Estimates for the erupted volume lie between 0.02 km³ and 0.05 km³ (e.g. Bryan and Sherburn, 1999; Nairn and Scott, 1996), and the recurrence time for this type of eruption at Mt. Ruapehu is estimated to be 25 years (e.g. Gamble et al., 2003).

1.3.3 Velocity model

The data processing in this study is largely independent of the velocity model for the crust under Mt. Ruapehu. However, for the calculation of the shear wave window (for explanation see Section 2.1.7) a near-surface wave speed is necessary. Also, for the calculation of the *percent anisotropy* (see Section 2.1.5), an average shear wave speed between source and receiver is necessary. These calculations were based on the following velocity models.

A model determined from seismic refraction profiles and earthquake seismology (Latter, 1981) consists of the following layers (from top to bottom): a low-velocity, laharic or pyroclastic surface material with $V_P \approx 1.4$ km/s ($V_S \approx 1.0$ km/s), sometimes capped by andesite lava flows. This material is underlain by sub-horizontal Tertiary sediments at around sea level with $V_P \approx 2.35$ km/s ($V_S \approx 1.4$ km/s). Below the sediments, a horizontal layer of around 0.65 km thickness is inferred, interpreted as weathered greywacke with $V_P \approx 3.8$ km/s ($V_S \approx 2.2$ km/s). The lowest layer is interpreted as schistose greywacke, starting at a depth of around 1 km below sea level with $V_P \approx 5.1$ km/s ($V_S \approx 2.9$ km/s), and grading down into an average wave speed of $V_P \approx 5.4$ km/s ($V_S \approx 3.12$ km/s). A V_P/V_S -ratio of 1.73 has been assumed

throughout. This model is refined by Hurst (1998), who obtain best results for determining shallow earthquake hypocentres when assuming surface layer wave speeds of $V_P \approx 2.0 \pm 0.2$ km/s down to a depth of 2 km beneath Crater Lake (i.e. approximately 0.5 km above sea level).

In this study, a surface layer velocity of $V_S = 1.6$ km/s was assumed for the calculation of the shear wave window, which is higher than in all suggested models, and which therefore yields the most conservative shear wave window (i.e. selects the data with the highest quality).

For larger depths, Latter's model can be extended by the velocity model reported by Hayes (2002), who relocated earthquakes from the Waiouru earthquake swarm (some 20 km southeast of Mt. Ruapehu). However, in this study, Hayes' model was only used to obtain a rough estimate for the average S-wave speed of waves travelling through the uppermost 10 km of the crust (≈ 2.5 km/s).

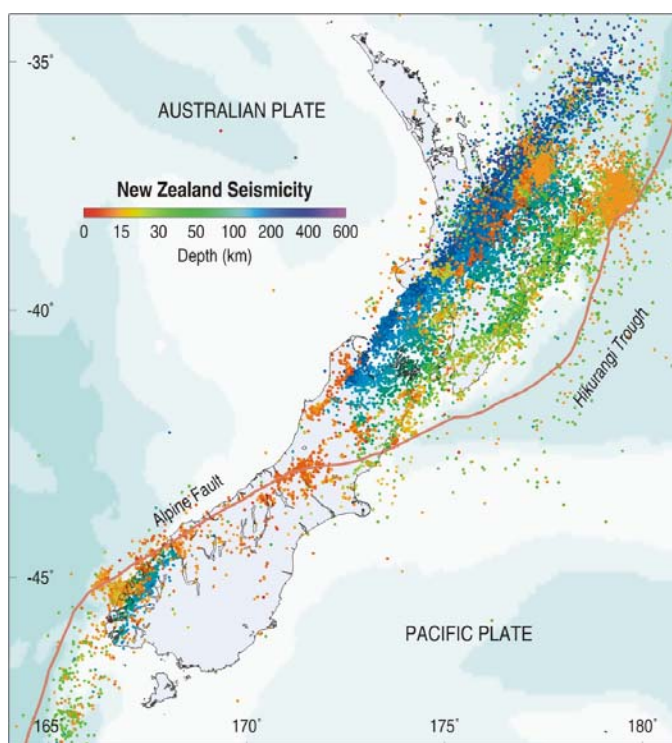


Figure 1.10 Five year seismicity around New Zealand. The strong correlation of earthquake locations with depth depicts the subducting Pacific plate under the North Island. Further south, the system transforms to lateral movement on the Alpine Fault, and eventually switches polarity south of New Zealand. (Source: IGNS)

CHAPTER 2

SEISMIC ANISOTROPY

This chapter will concentrate on the theory of anisotropy and its mathematical background. It will explain the basic derivations of formulae and their relation to observed phenomena.

2.1 Theoretical background

The aim of this section is to show the theory and the mathematical derivations that lead to understanding body wave behaviour in anisotropic media. Starting from the most general equation in seismology, it will explain why S-wave splitting occurs, and how to calculate the wave velocities in an anisotropic medium. The derivations in this chapter generally follow the approach from Crampin (1984) and Babuška and Cara (1991), with slight modifications.

The start of the derivation will be the three dimensional elastodynamic equation of motion for a continuous, homogeneous medium. For small displacements \vec{u} compared with the wavelength, it describes Newton's law of force balance and can be written as:

$$\rho \frac{\partial^2 u_i}{\partial t^2} = \frac{\partial \sigma_{ij}}{\partial x_j} \quad (2.1)$$

for $i, j = 1, 2, 3$, where u_i are the components of the displacement vector \vec{u} , and ρ is the density of the medium. Please note that the *Einstein summation convention* is used throughout this chapter. σ_{ij} are the components of the second-order stress tensor, which is related to the most general law for linear elasticity, *Hooke's law*:

$$\sigma_{ij} = c_{ijkl} \varepsilon_{kl} \quad (2.2)$$

for $i, j, k, l = 1, 2, 3$, where c_{ijkl} represents the fourth-order tensor of elastic moduli and defines the material properties of the medium. In the most general form, it has $3^4 = 81$ terms. ε_{kl}

are the components of the second-order strain tensor in the medium and are defined by

$$\varepsilon_{kl} = \frac{1}{2} \left(\frac{\partial u_l}{\partial x_k} + \frac{\partial u_k}{\partial x_l} \right) \quad (2.3)$$

Both stress and strain tensors are symmetric, i.e. $\sigma_{ij} = \sigma_{ji}$ and $\varepsilon_{kl} = \varepsilon_{lk}$. This leads to $c_{ijkl} = c_{jikl}$ and $c_{ijkl} = c_{ijlk}$, which reduces the number of independent coefficients in c_{ijkl} to 36. Thermodynamic assumptions further reduce the number to 21 coefficients ($c_{ijkl} = c_{klij}$). This means that the most general form of anisotropic elastic medium can be described by 21 independent parameters (Lay and Wallace, 1995; Aki and Richards, 1980).

Inserting Equations 2.3 and 2.2 in Equation 2.1 produces

$$\rho \frac{\partial^2 u_i}{\partial t^2} = c_{ijkl} \frac{\partial^2 u_l}{\partial x_j \partial x_k}, \quad (2.4)$$

which represents the wave equation in an anisotropic medium. The displacement vector \vec{u} of a plane wave travelling in this medium can be expressed as:

$$u_i = a_i f \left(t - \frac{n_m x_m}{c} \right) \quad (2.5)$$

for $i, m = 1, 2, 3$; where a_i is the vector amplitude of the wave in direction i (polarisation direction), c is the phase velocity and n_m are the components of the normal vector \vec{n} pointing into the propagation direction of the wave. $f \left(t - \frac{n_m x_m}{c} \right)$ is an arbitrary wavelet function at time t and position \vec{x} (with the components x_m). The derivatives of \vec{u} in time and space can be expressed as:

$$\frac{\partial^2 u_i}{\partial t^2} = a_i f'' \left(t - \frac{n_m x_m}{c} \right) \quad (2.6)$$

$$\frac{\partial^2 u_l}{\partial x_j \partial x_k} = \frac{n_j n_k}{c^2} a_l f'' \left(t - \frac{n_m x_m}{c} \right) \quad (2.7)$$

Inserting these derivatives into Equation 2.4 leads directly to:

$$\rho a_i = \frac{1}{c^2} c_{ijkl} n_j n_k a_l, \quad (2.8)$$

which can be written as:

$$\frac{c_{ijkl} n_j n_k}{\rho} a_l - c^2 a_i = 0 \quad (2.9)$$

a_i can also be written as $\delta_{il} a_l$, where δ_{il} is the Kronecker delta function. This allows Equation

2.9 to be simplified to:

$$\left(m_{il} - c^2\delta_{il}\right)a_l = 0 \quad (2.10)$$

with:

$$m_{il} = \frac{c_{ijkl}n_jn_k}{\rho}. \quad (2.11)$$

m_{il} are the components of the so called *Christoffel Tensor* \underline{M} , and are **dependent on a certain propagation direction** \vec{n} (Babuška and Cara, 1991). It describes the propagation velocities of waves with a common propagation direction but various polarisation directions \vec{a} , as will be explained below.

Equation 2.10 can be considered a classic eigenvalue problem:

$$\underline{M}\vec{a} = c^2\vec{a}. \quad (2.12)$$

Solutions exist for $\det(\underline{M} - c^2\underline{1}) = 0$, which represents a polynomial of degree 3. $\underline{1}$ is the identity matrix.

Every polarisation vector \vec{a} that satisfies Equation 2.12 is an eigenvector of \underline{M} . In general there are three vectors satisfying this equation, which are mutually orthogonal to each other due to the symmetry of the Christoffel matrix. c_i^2 is the eigenvalue for the i -th eigenvector ($i = 1, 2, 3$), and represents the squared phase velocity for a polarisation direction parallel to this vector. *

An implication of this is that a body wave that is polarised in the direction of one of the three eigenvectors does not experience a polarisation change while travelling. These three “stable” body waves are commonly called quasi-P, quasi-S₁ and quasi-S₂. They are travelling with different velocities and are not “real” P or S-waves because their polarisation directions are not strictly parallel or perpendicular to the propagation direction. The reason for this is that the propagation direction does not generally coincide with an eigenvector of \underline{M} . However, depending on the anisotropic parameters of the medium, they are often close to each other. For most rocks, the particle motion is less than 10° away from being parallel or perpendicular to the propagation direction (Savage, 1999; Babuška and Cara, 1991).

As a simplification, these quasi-waves are from now on referred to as P, S₁ and S₂, of which the two last are also often called *fast S-wave* and *slow S-wave*.

A wave entering the anisotropic medium with an arbitrary polarisation vector \vec{a} can be described as a superposition of the three eigenvectors and their respective body waves. Since

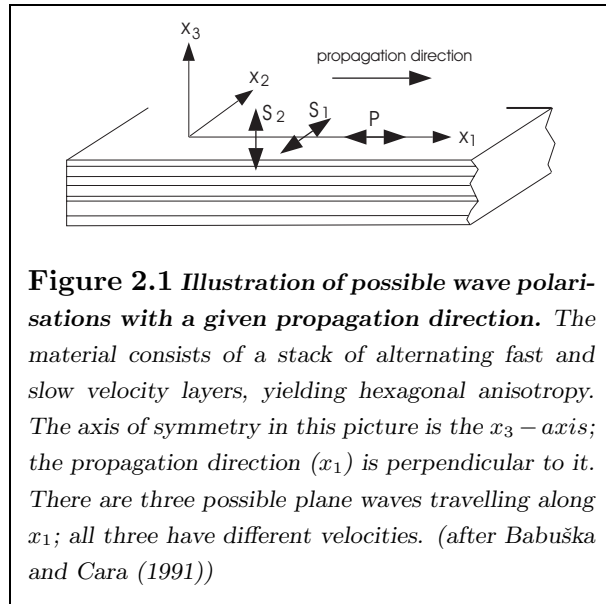
*Note that phase and group velocity are generally not strictly parallel to each other in an anisotropic medium, even though they are almost parallel for weak anisotropy (<15%). The energy of a seismic wave always travels with the group velocity.

they are travelling with different velocities, the wave will inevitably split up into the three waves (P, S_1 and S_2), each one travelling at its own speed. This is the acoustical analogue to the optical phenomenon of *birefringence*, and is sometimes also called *shear wave double refraction*.

2.1.1 Hexagonal anisotropy

The equations above describe the most general system of anisotropy possible, without any symmetries involved. However, in the case of anisotropy in the earth's crust, the system often has symmetries that reduce the number of independent coefficients in the elasticity tensor. One very common anisotropic system is the system of hexagonal anisotropy (radial anisotropy). It naturally occurs in ice, as well as in layered media, and is described by five independent coefficients, as well as by its orientation. An example of this would be a stack of alternating layers of fast and slow material. The system has a vertical axis of symmetry, therefore an S-wave travelling vertically (parallel to x_3 -axis) has a speed independent of its polarisation, i.e. it will not split.

However, a wave travelling perpendicular to the axis of symmetry will have an S-velocity dependent on its polarisation direction (See Figure 2.1). Intuitively, it seems logical that an



S-wave with a polarisation vector perpendicular to the plane of fast and slow layers (S_2) will be travelling with a velocity that lies somewhere in between the fast and slow velocities of the layers. Yet an S-wave with a polarisation vector *in* this plane (S_1) can travel mainly in fast layers without being severely influenced by the slow layers, therefore it is faster (S-wave anisotropy).

The behaviour of P-waves is similar: a P-wave that is polarised and therefore also travelling along the axis of symmetry has to cross both fast and slow layers. Thus

it has a slower velocity than a P-wave that is travelling exclusively in a fast layer (P-wave anisotropy).

Returning to the case of general anisotropy, the fourth-order tensor c_{ijkl} can be conveniently expressed as 6-by-6 matrix C_{ij} , where $C_{ij} = c_{klmn}$ with $i = k = l$ if $k = l$, and $i = 9 - k - l$ if $k \neq l$, and $j = m = n$ if $m = n$, and $j = 9 - m - n$ if $m \neq n$ (Babuška and

Cara, 1991):

$$(C_{ij}) = \begin{pmatrix} c_{1111} & c_{1122} & c_{1133} & c_{1123} & c_{1113} & c_{1112} \\ c_{2211} & c_{2222} & c_{2233} & c_{2223} & c_{2213} & c_{2212} \\ c_{3311} & c_{3322} & c_{3333} & c_{3323} & c_{3313} & c_{3312} \\ c_{2311} & c_{2322} & c_{2333} & c_{2323} & c_{2313} & c_{2312} \\ c_{1311} & c_{1322} & c_{1333} & c_{1323} & c_{1313} & c_{1312} \\ c_{1211} & c_{1222} & c_{1233} & c_{1223} & c_{1213} & c_{1212} \end{pmatrix} \quad (2.13)$$

In the case of hexagonal anisotropy, (C_{ij}) has five independent coefficients A, C, F, L, N which are called Love's coefficients (Love, 1927):

$$(C_{ij}) = \begin{pmatrix} A & A-2N & F & 0 & 0 & 0 \\ A-2N & A & F & 0 & 0 & 0 \\ F & F & C & 0 & 0 & 0 \\ 0 & 0 & 0 & L & 0 & 0 \\ 0 & 0 & 0 & 0 & L & 0 \\ 0 & 0 & 0 & 0 & 0 & N \end{pmatrix} \quad (2.14)$$

This means that there are at least five measurements necessary to determine the coefficients in a laboratory experiment. In this case, the axis of symmetry is the x_3 -axis.

If, for example, the direction of propagation is the x_1 -axis, the Christoffel tensor reduces to:

$$(m_{ij}) = \underline{M} = \frac{1}{\rho} \begin{pmatrix} A & 0 & 0 \\ 0 & N & 0 \\ 0 & 0 & L \end{pmatrix} \quad (2.15)$$

with a system of eigenvectors that are parallel to the coordinate axes x_1, x_2, x_3 . The respective eigenvalues can be read from the diagonal components: they are $c_1^2 = A/\rho$, $c_2^2 = N/\rho$ and $c_3^2 = L/\rho$. In the case of horizontal layering or crack induced anisotropy, $A > N > L$. A wave with a polarisation parallel to the x_1 -axis (and therefore also parallel to the propagation direction in this case) will travel with a velocity of $c_1 = \sqrt{A/\rho}$ (P-wave). The wave with a polarisation direction parallel to x_2 will be the fast S-wave with a velocity of $c_2 = \sqrt{N/\rho}$. Finally, the wave with a polarisation direction parallel to x_3 (and therefore parallel to the axis of symmetry in this case) will be the slow S-wave, and travels with a velocity of $c_3 = \sqrt{L/\rho}$ (see also Figure 2.1). Note that there are also hexagonal symmetry systems with $A > L >$

N , where the fast S-wave is polarised parallel to the axis of symmetry:

$$\begin{aligned} V_P &= c_1 = \sqrt{A/\rho} \\ V_{S1} &= c_2 = \sqrt{N/\rho} \\ V_{S2} &= c_3 = \sqrt{L/\rho} \end{aligned} \quad (2.16)$$

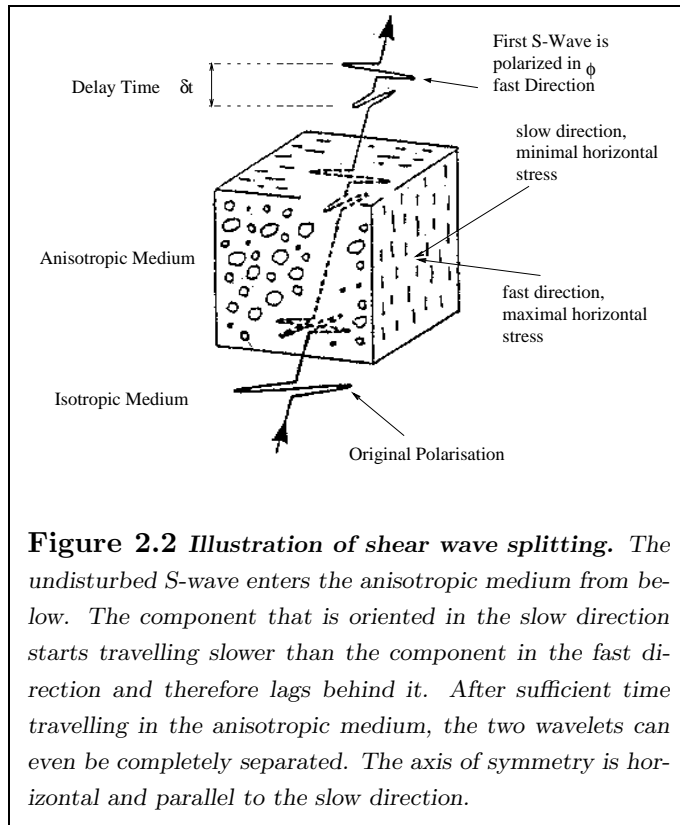
with $A > N > L$.

In the case of a propagation direction parallel to the axis of symmetry (x_3), two of the three eigenvalues are degenerate, i.e. $c_{1,2}^2 = L/\rho$. This means that all waves with a polarisation vector in the x_1, x_2 -plane travel at the same speed, and at the speed of the axis of symmetry – in this case, slow. As a result of this, $S_1 = S_2$ and no shear wave splitting occurs.

An example for using this theory to derive the parameters in the isotropic case is shown in Appendix A.1.

Another system with equivalent properties is a medium that is homogeneous and isotropic by itself, but with cracks aligned in a certain direction. Figure 2.2 shows such a system, the only difference from the case above (and to Figure 2.1) being that the axis of symmetry is now

horizontal (perpendicular to the crack planes). Since cracks are either fluid or air-filled, they slow down a wave that has to cross them. Thus the principle is the same as above: a (horizontal) P-wave that travels perpendicular to the crack planes, and therefore along the axis of symmetry, has to cross many cracks. A P-wave that is travelling along the cracks never has to cross one and is therefore faster. The same behaviour is valid for S-waves: an (in this case vertical) S-wave with a polarisation vector parallel to the crack planes can travel faster than an S-wave with a polarisation vector perpendicular to the crack planes. These polarisation directions are from now on called the *fast direction* and the *slow direction*. The slow direction is parallel to the axis of symmetry, and therefore perpendicular to the crack planes. The fast direction lies in the crack planes. Note that a medium with randomly oriented cracks does not yield this form of anisotropy. The effective anisotropy of a medium is also



The slow direction is parallel to the axis of symmetry, and therefore perpendicular to the crack planes. The fast direction lies in the crack planes. Note that a medium with randomly oriented cracks does not yield this form of anisotropy. The effective anisotropy of a medium is also

strongly dependent on the wavelength in relation to the size of the features that are causing the anisotropy. Therefore a medium which shows anisotropy at long wavelengths may merely behave heterogeneously at short wavelengths (Crampin et al., 1984a).

The model above is assumed to be representing the mechanism of anisotropy in the upper 10 to 15 km of the earth's crust. The preferred alignment of otherwise randomly oriented dry or fluid filled cracks, microcracks, or aligned pore space is caused by a predominant main stress direction in the crust (e.g. Crampin and Booth, 1985; Savage et al., 1989). Cracks with a plane that is perpendicular to the maximum principal stress direction can be forced to close, while cracks with a plane perpendicular to the minimum principal stress direction widen up[†] (see Figure 2.2). This behaviour is confirmed by experiments by Nur and Simmons (1969) on igneous rocks. The stresses required for this process are one or two orders of magnitude less than the stresses that are needed to actually generate and to enlarge cracks in a medium (Crampin et al., 1990). Therefore it is very sensitive to even minor stress changes in the anisotropic body and reflects these changes almost instantaneously. This phenomenon is called *extensive-dilatancy anisotropy* (EDA, Crampin et al., 1984b; Crampin, 1987; Babuška and Cara, 1991) and exists in the upper 10 to 15 km in the crust. At greater depths, corresponding to pressures of 200 – 300 MPa, the anisotropy largely disappears due to closure of all cracks (e.g. Kern, 1990). Note that below a few hundred metres in depth the minimum stress is typically horizontal and is therefore causing EDA cracks with vertical crack planes, aligned in the direction of the maximum horizontal stress (Crampin, 1994).

As a result of this phenomenon, the measured crustal fast direction becomes an indicator for the present maximum horizontal stress direction in the crust.

Yet it has to be noted that there are also other mechanisms that lead to a preferred crack alignment and therefore to anisotropy. These are (Crampin and Lovell, 1991): [a] alignment of stress-induced cracks in the close vicinity of active fault zones, [b] preferential mineral alignment, and [c] alignment of cracks by past tectonic regimes (lithologic anisotropy). However, none of these processes take place in the timescales that are the focus of this study (less than 10 years). They therefore only play a marginal role in the explanation of the observed changes in shear wave splitting.

2.1.2 Systems of anisotropy with a lower order of symmetry

The two hexagonal models above both describe possible scenarios in the crust. Thus there are cases where both systems exist at the same time, e.g. a horizontally layered medium that

[†]This process represents a systematic change in the aspect ratio of pre-existing cracks. An important part of the concept is that the orientations of the cracks themselves do not change during the process. However, the overall alignment of the cracks does change, since only the ones with a certain orientation remain open. Therefore this process will be referred to from now on as “crack alignment” for convenience

has a preferred crack orientation. This is basically a linear superposition of two hexagonal systems, one with a vertical axis of symmetry and the other one with a horizontal axis of symmetry. The resulting anisotropic system is called *orthorhombic* (e.g. Crampin and Lovell, 1991), and is described by nine independent elastic coefficients (Crampin, 1984). Due to this lower order of symmetry, the wave behaviour is generally more complicated than in a hexagonal system. However, when the wave is travelling vertically or near-vertically, the system behaves similarly to a hexagonal system with a horizontal axis of symmetry. Therefore they can not be distinguished from each other in this case. This is not very surprising if one considers the fact that a vertically travelling S-wave will not split in a hexagonal system with a vertical axis of symmetry (as mentioned above). Therefore only the system with the horizontal axis of symmetry influences the wave.

An example of a mineral that naturally has an orthorhombic anisotropic system is olivine, which occurs mainly in the earth's mantle.

2.1.3 The cause of mantle anisotropy

In contrast to highly fractured rocks in the earth's crust, the earth's mantle does not contain many cracks or fractures. Therefore the source of mantle anisotropy has to be different from the source of crustal anisotropy.

In the ductile environment of the mantle, *crystalline anisotropy* is the main mechanism for anisotropic behaviour (Crampin et al., 1984a; Silver and Chan, 1991). This phenomenon occurs when individual anisotropic crystals in a crystalline solid have preferred orientations over a large volume (*lattice-preferred orientation*, or LPO). In the mantle, these crystals are olivine and possibly orthopyroxene crystals, which have pronounced anisotropic properties (Crampin et al., 1984a). Today it is widely accepted that the crystals are oriented by at least two processes. One is a deformation process called *dislocation creep*, which is the motion of crystalline dislocations within grains, and causes a preferred mineral orientation if the stresses are high enough (e.g. Nicolas and Christensen, 1987). The other process is called *dynamic recrystallisation*, and represents the dissolving of unfavourably aligned crystals under pressure, and their subsequent recrystallisation in a more favourable alignment. This process enhances the effects of the dislocation creep.

At high temperatures ($>900^\circ$) and for large strain ($>150\%$) by progressive simple shear, olivine *s*-axes align within the foliation plane and nearly parallel to the lineation direction and the direction of ductile shear. These conditions often occur in the mantle (e.g. Vinnik et al., 1992) and are associated with plate movements and convection currents (Crampin et al., 1984a). Olivine has an intrinsic orthorhombic anisotropic symmetry system. However, since mostly only the *a*-axes are aligned, and the *b* and *c* axes are more or less random, the effective anisotropic system is often hexagonal. There are many variations of this behaviour

and complicated dependencies on parameters like strain, temperature and grain size exist. Recent studies report of further complications for H₂O saturated mantle materials (Jung and Karato, 2001). In summary however, it appears to be valid for most cases (Savage, 1999), that:

- the fast direction Φ is parallel to the a -axis orientations of olivine;
- the fast direction Φ is subparallel to the horizontal flow direction, or the extension direction;
- for simple shear and large strains, the maximum extension is approximately parallel to shear (Silver and Chan, 1991).

Since only crack induced anisotropy can be considered a direct indicator of present stress, mantle anisotropy can not only express present stress or strain, but also “frozen” anisotropy from the last important period of coherent internal deformation (Silver and Chan, 1991). Therefore the common conception is that in a non-active region, anisotropy indicates a paleo strain direction, while in active regions it reflects the present strain.

Anisotropic behaviour of the mantle was observed at depths down to 650 km (e.g. Mainprice and Silver, 1993; Wookey et al., 2002), and in the D” layer above the core-mantle boundary with up to 3% anisotropy (Kendall and Silver, 1996). The lower mantle seems to be largely isotropic (Kaneshima and Silver, 1992).

Anisotropy in subduction zones shows an even more complicated behaviour than in the rest of the mantle. Fast polarisations of ScS waves have been reported perpendicular to the trench in Japan, South America or Tonga (e.g. Bowman and Ando, 1987; Fischer and Wiens, 1996), while other subduction zones often yield trench-parallel polarisation directions (e.g. Silver and Chan, 1991; Audoiné, 2002). Observations range from Φ being parallel to the strike of the trench, to being subparallel to back-arc extension directions, to being parallel to convergence direction, to being parallel to strikes of major shear systems. See Savage (1999) for a comprehensive overview and discussion.

Currently, there are at least two accepted mechanisms that lead to the observed behaviour. One possibility is a two dimensional *corner flow* of material parallel to the relative plate motion (i.e. the mantle material is dragged along the subducting plate), which yields fast directions parallel to the convergence direction and therefore perpendicular to the trench. Another model suggests that the subducting plate, rather than entraining the asthenosphere, may act as a barrier to asthenospheric flow in some cases. Such a barrier would channel the flow parallel to the slab, especially at subduction zones where the slab is retreating, or rolling back (see Figure 1.3). Therefore fast directions are expected to be parallel to the trench in this case.

This behaviour is also seen in New Zealand, where trench-parallel fast directions are observed both above and below the slab (e.g. Marson, 1997; Audoin, 2002). Measurements from deep events under Mt. Ruapehu are therefore expected to show a similar, trench parallel fast direction. This, however, only applies if the waves are not further influenced by additional crustal anisotropy along their path.

Typical values for percent anisotropy (for definition see 2.1.5) in subduction zones are between 0.5% and 2% for the mantle above and below the slab, and up to 5% in the slab (e.g. Savage, 1999). Delay times as high as 4 s are observed (Russo and Silver, 1994).

2.1.4 Effect on the waveforms

A property of S-waves in an isotropic medium is their linearly polarised particle motion, i.e. a particle on the raypath vibrates only in one direction. When an S-wave with an arbitrary polarisation direction enters an anisotropic medium travelling in a direction other than the axis of symmetry, the wave splits into the two waves S_1 and S_2 , with perpendicular polarisations, one travelling faster than the other. This leads to a time shift δt between the two wavelets and causes the particle motion to change. When the lag is small in comparison with the period of the wave, then the particle motion changes from being linear to being elliptical. The only exceptions to this are S-waves that are entering the anisotropic medium with a polarisation direction parallel to either the fast or the slow direction. These waves will not split since they only have a component in one of the two directions.

Vinnik et al. (1989) show with a simple geometrical relation that when the S-wave is split by a fraction of the wavelength ($\delta t \ll T$), the component perpendicular to the initial polarisation represents the derivative of the component parallel to the initial polarisation.

When a wave travels for a sufficient time in the anisotropic medium, the two wavelets will eventually separate completely (as is the case in Figure 2.2). The two S-waves S_1 and S_2 have linear particle motions, which are pointing in the fast and slow direction, respectively. This causes the particle motion at a position along the raypath to assume a cruciform shape. An example of this will be shown in Chapter 3, Figure 3.5.

2.1.5 Delay times and percent anisotropy

The delay time δt between the split waves results from the two S-wave speeds and the length of the path in the anisotropic medium:

$$\delta t = L \left(\frac{1}{V_{S1}} - \frac{1}{V_{S2}} \right), \quad (2.17)$$

where V_{S1} and V_{S2} represent the two quasi-shear wave speeds for the given propagation direction; and L is the length of the anisotropic path traversed. From these two wave speeds, a percent anisotropy can be defined (e.g. Savage, 1999):

$$k_S = 200 \frac{V_{S1} - V_{S2}}{V_{S1} + V_{S2}}, \quad (2.18)$$

which, in the case of simple hexagonal anisotropy with a propagation perpendicular to the axis of symmetry, can also be derived from the two Love parameters N and L (Babuška and Cara, 1991; Savage, 1999):

$$k_S = \frac{200 \left(\sqrt{N/L} - 1 \right)}{\sqrt{N/L} + 1}. \quad (2.19)$$

For $V_{S1} - V_{S2} \ll V_S$, Equations 2.17 and 2.18 can be combined to:

$$k_S = \frac{\delta t}{L} V_S \cdot 100, \quad (2.20)$$

where V_S is the average S-wave speed for the given propagation direction.

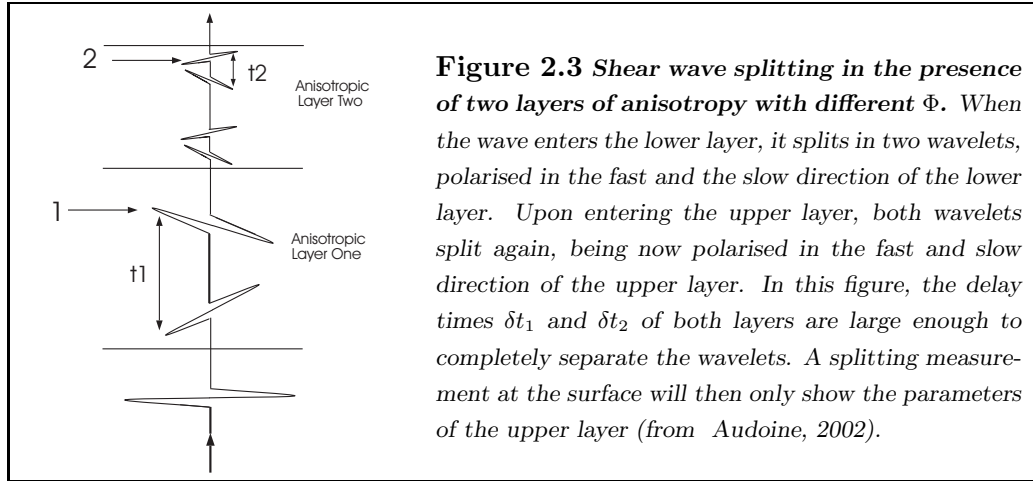
This anisotropy is not equal to the so called *intrinsic anisotropy*, which describes the percent difference between the fastest and the slowest wave speed in a medium. k_S depends on the propagation direction of the wave and has therefore often a lower value than the intrinsic anisotropy.

For typical crustal anisotropy, average delay times range from 0.05 to 0.2 s. However, some studies report delay times as high as 0.5 s recorded at stations above fault lines (Savage et al., 1990). Mantle delay times are much higher than crustal ones, and are reported to be as high as 4 s (Russo and Silver, 1994)

2.1.6 Multiple layers of anisotropy

When a shear wave passes through two anisotropic layers with arbitrary fast directions on its way to the receiver, the observed splitting parameters depend strongly on the thickness and percent anisotropy of the layers, and on the wavelength.

If the anisotropy is strong enough, a wave entering the lower layer will completely split while passing through it. The two split wavelets then enter the upper layer, which has a different fast direction than the lower one. Therefore, both wavelets split up again in the fast and slow direction of the upper layer. The first wavelet arriving at the receiver will thus be polarised in the fast direction of the upper layer, and the splitting measurement will show this as the fast direction. The splitting measurement is therefore not influenced by the lower layer (see Figure 2.3).



However, when the layers are sufficiently thin, or the anisotropy too weak, then the wavelets can not separate completely, and a complicated waveform results. This waveform could be misinterpreted if the presence of more than one layer is not known, but often a measurement can not even be obtained due to bad quality and non-matching waveforms. Silver and Savage (1994) show that if measurements are obtained, a characteristic $\pi/2$ -periodicity of the measured fast directions as a function of initial polarisation results. This pattern can help to identify two (or more) layers of anisotropy.

2.1.7 The shear wave window

When shear wave splitting is measured, in most cases the receivers are located at or close to the earth's surface. However, the particle motion on the earth's surface does not always represent the particle motion of an incoming S-wave along its path. Due to interaction of the incoming wave with the surface, the measured particle motion gets distorted and can adopt an elliptical wave form even if travelling in an isotropic medium. This leads to apparent shear wave splitting with an apparent fast direction pointing into the direction of the incoming wave, or the back azimuth. However, Nuttli (1961) showed that the distortion is only significantly strong if the incidence angle of the S-wave is larger than the critical S_V to P conversion angle at the free surface:

$$i_c = \arcsin\left(\frac{v_S}{v_P}\right) \quad v_S, v_P : \text{near surface S and P-wave velocities} \quad (2.21)$$

Assuming a normal $\frac{v_S}{v_P}$ -ratio of around $1/\sqrt{3}$ (i.e. a Poisson's ratio of 0.25), the critical shear wave angle is close to 35° , i.e. near-vertical incidence (Babuška and Cara, 1991).

Crampin and Lovell (1991) point out that there are also sub-surface shear wave windows at internal interfaces. These are defined by various critical angles of S_1 , S_2 , P_1 and P_2 conversions. The properties of the incident shear wave are preserved in the innermost window, and

complications get stronger beyond each window. However, in most cases these disturbances at sub-surface windows are likely to be negligible (Crampin and Lovell, 1991).

Due to this phenomenon, measurements of shear wave splitting with an incidence angle larger than 35° at the surface should not be included in the results. This can be especially difficult in an area with large differences in topography, since the slope angle around the station has to be included in this calculation (see Section 3.3).

A theoretical study from Neuberg and Pointer (2000) reinforces the notion that waveforms from very shallow incidence angles generate elliptical particle motion even without the presence of anisotropy, especially when recording extremely shallow (<1 km) local earthquakes in the vicinity of strong topography like volcanoes. This is also confirmed in a study by Hagerty and Benites (2003), who recorded long period seismic events beneath Mt. Tongariro volcano, New Zealand.

One characteristic of measurements that were obtained from rays with a large deviation from vertical is a π -periodicity of the fast directions in the back azimuth (e.g. Crampin and Booth, 1985). In case of a single, but dipping layer of anisotropy (i.e. an inclined axis of symmetry), fast directions will be obtained that show a characteristic 2π -periodicity, even if only near-vertical raypaths are selected (Silver and Savage, 1994).

2.2 Observations

At the present day, crustal anisotropy is observed in many locations around the world. There are far too many studies to be mentioned here. Savage (1999) gives a comprehensive overview on the topic of seismic anisotropy and the present state of observations. An even more detailed discussion of crustal anisotropy is given by Crampin (1994).

Since the purpose of this study is to investigate possible changes in anisotropy at Mt. Ruapehu volcano, it will focus on mainly two areas in the field of seismic anisotropy:

1. Anisotropy in the vicinity of volcanic systems; and
2. Investigations of temporal changes in anisotropy elsewhere in the world.

These two areas will be discussed in the following sections.

2.2.1 Seismic anisotropy in the vicinity of volcanoes

Several surveys have been conducted in recent years to determine anisotropy around volcanic systems. Savage et al. (1989) analysed shear wave data from a seismometer deployment on the South flank of Kilauea Volcano and the East Rift Zone, Hawaii, and from a deployment in

the Phlegraean Fields, Italy. Strong S-wave splitting was observed in Hawaii, and an average fast direction was found to be parallel to the regional maximum horizontal stress direction, with a minimum velocity anisotropy of about 5%. However, large variations ($\approx 50^\circ$) of fast directions were found at stations that had a separation of only 6 km. The conclusion was drawn that local, near-site stress conditions affect the measured fast directions. The dataset from the Phlegraean Fields caldera, Italy, shows similar behaviour. Average fast directions were found to be only 9° different from the maximum compressive stress direction, derived from fault-plane solutions. Here, a minimum of 7% velocity anisotropy in the upper 4 km of the crust was observed with only a small amount of pervasive anisotropy. The measured delay times were about 0.2 s.

Booth et al. (1992) examined data from 84 shear wave records obtained at the seismometer station AIN at Kaoiki, Hawaii. Shear wave splitting was found with delay times around 0.19 s, and a fast direction that is consistent with anisotropy being caused by cracks aligned approximately perpendicular to the direction of the least principal stress. The data was also examined for a temporal change in anisotropy associated with the magnitude $M=6.6$ mainshock in the Kaoiki Region, which occurred in November 1983. However, no evidence for such a change was found.

Munson and Thurber (1993) and later Munson et al. (1995) analysed data from five different seismometer arrays that were deployed in southern Hawaii. Velocity anisotropy exceeding 10% was found to be contained in the upper 3 to 8 km of the crust, which resulted in delay times between 0.1 and 0.2 s. A search for temporal changes in anisotropy associated with the 1983 Kaoiki main shock ($M_L=6.6$) was unsuccessful. The recording time lasted from eight months before to one year after the earthquake, and the observed fast directions were generally consistent with independent information on stress orientation. Remarkably, several closely spaced stations showed a 45° difference in the fast directions over a distance as small as 200 metres. This emphasises the importance of consistent station locations down to a scale of a few metres when searching for temporal variations.

Bianco et al. (1999) investigated the 1995/96 seismic crises at Mt. Vesuvius volcano, Italy and found fast directions parallel to the main fault system of the volcano. Crack alignment due to stress can not clearly be distinguished from structure related alignment, therefore the mechanism for the crack alignment remains unknown in this case. Comparison of the data with results from previous studies yielded no temporal change in anisotropy.

A study by Lees and Wu (1999) uses P-wave anisotropy to investigate stress and crack distribution in three dimensions at Coso geothermal field in California. Velocity anisotropy of up to 8% was found in very shallow parts of the crust (0.5 – 1 km depth) with a horizontal fast direction. The measured fast directions coincide with the principal stress direction, which was obtained in an independent study using earthquake focal mechanisms.

All of the above mentioned studies find a strong anisotropic behaviour of the crust and mostly a strong correlation between the fast directions and the maximum horizontal compressive stress direction (σ_H), which was always derived by independent methods. Thus, the presence of extensive dilatancy anisotropy (EDA, Crampin et al., 1984b), was suggested for these cases. As mentioned above, this theory predicts a fast direction parallel to the maximum horizontal stress direction due to preferred closure of cracks that are perpendicular to this direction, causing hexagonal anisotropy. Not only volcano related studies, but also the majority of general crustal shear wave studies report similar behaviour. However, it should be pointed out that there are also studies that report polarisation directions not being aligned with σ_H . Savage et al. (1990) investigated shear wave splitting in the Long Valley Caldera, California, and found a fast direction that is parallel to both the strike of the fault and σ_H . Therefore the two cases can not be distinguished. However, at a station above the Hilton creek fault, a pattern of fast directions varying with the azimuth suggests an inclined axis of symmetry and matches the dip of the fault zone. Therefore fault controlled anisotropy seems more likely than EDA in this case. Gledhill (1991a) postulates that both EDA and near-surface structural anisotropy in the form of oriented fractures in the direct vicinity of an active fault system in New Zealand contribute to the measured fast directions. Zhang and Schwartz (1994) report similar behaviour at the Loma Prieta segment of the San Andreas Fault system.

Newer studies also confirm EDA as being the general source of crustal anisotropy, while structure controlled anisotropy seems to be present in the close vicinity of fault zones, where stresses often exceed the strength of the rock (e.g. Zinke and Zoback, 2000; Evans et al., 1995).

Several studies (e.g. Booth et al., 1992; Munson et al., 1995; Savage et al., 1990; Bianco et al., 1999) searched for temporal changes in anisotropy around volcanoes, associated with earthquakes or volcanic eruptions. However, to the knowledge of the author, apart from the changes reported from Mt. Ruapehu, no evidence for such a temporal change at a volcano has been found to the present day. The paper by Miller and Savage (2001), which motivated this study, includes data from the 1994 and 1998 deployments, and reports indications for a temporal change in anisotropy between 1994 and 1998. However, the station locations of these two deployments were several kilometres apart, which in many other studies produced major changes in the measured fast directions without a temporal change (as shown above, e.g. Savage et al., 1989; Gledhill, 1991a; Munson et al., 1995; Booth et al., 1985; Chen, 1987). Therefore no proof for a temporal change in anisotropy has yet been reported.

2.2.2 Discoveries of temporal changes in seismic anisotropy

Shortly after the theory of extensive dilatancy anisotropy (EDA) emerged, there were suggestions that measuring this anisotropy could be used to detect and forecast temporal stress changes that are associated with earthquakes (e.g. Crampin et al., 1984a). Many studies investigated possible changes, until in 1988 the first discovery of temporal changes in anisotropy was claimed [‡].

Peacock et al. (1988) observed normalised delay times [§] of 186 local earthquakes in the Anza Seismic Gap, Southern California, increasing by 0.003 s per km path length over a period of three years after 1986. Delay times were manually determined, i.e. the time between the onset of the fast S-wave and the onset of elliptical particle motion was measured. The interpretation was that extensive dilatancy anisotropy (EDA) is responsible for the changes in delay time by reacting to a changing stress field associated with the San Jacinto fault. The observed fast directions were stable, and oriented parallel to the maximum stress direction, which was determined via source mechanisms. Crampin et al. (1990) later claimed to observe a change in delay times at the same stations near the time of the North Palm Springs earthquake ($M_L = 5.6$) of July 8, 1986.

However, Aster et al. (1990) processed the same dataset as Peacock et al. (1988) and Crampin et al. (1990) with an automatic algorithm, and could not confirm any temporal changes. Considerable scatter of delay times between 0 s and 0.2 s was reported. The conclusion was drawn that the results from the earlier studies are invalid. Crampin et al. (1991) later defended their studies and showed that the automatic algorithm, used by Aster et al. (1990), is not appropriate to automatically pick S-wave arrivals. It was shown that the algorithm often picks wrong windows with no identifiable S-wave features and therefore leads to large scatter in the measured delay times. This was replied to by Aster et al. (1991), who showed that manual picks from Crampin et al. (1990) were also wrong in several cases. It was further claimed that analysis of waves from nearly identical earthquake sources limits possible temporal changes to a fraction of those reported by Crampin et al. (1990).

The above discussion showed that measuring anisotropy solely by determining the time of linear particle motion after the first S-wave arrival is a disputable technique, even though temporal changes were observed. It has to be noted that there is a more advanced, semi-automatic method of determining delay times and polarisation directions available now, which was used in this study (see Section 3.2.2).

Earlier, Booth et al. (1985) investigated shear wave splitting of the Turkish Dilatancy Projects (TDP) near the North Anatolian Fault, and found mostly consistent fast directions

[‡]first claims actually came from Gupta (1973), who analysed moderate-sized earthquakes in Nevada, but these claims were later shown to be unsupported by the presented evidence (e.g. Ryall and Savage, 1974)

[§]Normalised delay times are the measured delay times, divided by the length of the traversed path

which were attributed to EDA. However, fast directions from one station were different by 60° from fast directions of a station that was deployed one year later in a distance of only 1.2 km. The possibility of a temporal change was suggested, but Chen (1987) later proved by reoccupying both sites that there were no temporal changes, but there was a spatially rapid change in fast direction. This example further emphasises the need for consistent station locations when investigating temporal changes in anisotropy.

Temporal changes have also been reported by Booth et al. (1990), occurring during an earthquake swarm in Arkansas. The polarisations of the fast shear waves correlated with the regional stress field, and the delay times between split shear waves appeared to increase before, and to decrease at or after each earthquake. This behaviour was attributed to stress changes before and after each main shock, changing the aspect ratios of EDA cracks in the medium.

Liu et al. (1997) investigated shear wave splitting in Parkfield, Central California, and found evidence for temporal changes in delay times, associated with a $M_L = 4$ earthquake. Fast directions were observed being parallel to σ_H , with the exception of one station that was situated directly on the San Andreas Fault. At this station, fast directions were observed parallel to the strike of the fault zone. At two stations, the normalised time delays seem to increase before, and abruptly decrease near the time of the earthquake by about 2 ms/km. However, the statistical significance of this temporal change is only 68%, which means that there is a one in three chance of being wrong. The largest total delay time in this dataset was 80 ms, corresponding to about 2% to 3% anisotropy in the uppermost 8 to 14 km of the crust.

An example of the possibilities arising from temporal changes in anisotropy is reported by Crampin et al. (1999). At 10 November 1998, rising normalised delay times over a period of three months at two stations in Iceland, approaching a level of 10 ms/km (which was considered a critical level from previous observations), led to an earthquake forecast with a specific time-magnitude window. This forecast predicted an earthquake between the time of the forecast and three months later, with a magnitude varying from $M_L \geq 5$ (if it happened soon) to $M_L \geq 6$ (if it happened three months later). Three days later, a $M_L = 5$ earthquake occurred close to one of the two stations. This example of a successfully “stress-forecast” earthquake emphasises the possibilities of anisotropy as a new tool in seismology. However, expectations should not be raised too high, since at the present time, almost ideal conditions have to be given for such a forecast (see Crampin et al., 1999).

Evidence for man-made temporal changes in anisotropy is reported by Bokelmann and Harjes (2000). Shear wave splitting at the German Continental Deep Drilling Program (KTB) borehole was observed under particularly well-controlled conditions during a hydraulic fracturing experiment. Within 12 hours of the start of the injection of fluid at 9 km depth, the

difference between the fast and the slow wave speed decreased by 2%, and then assumed a steady state. This behaviour was explained by the presence of EDA cracks that respond to stress release due to induced seismicity during the injection experiment.

A very recent study by Tadokoro and Ando (2002) is one of the rare cases where temporal changes in the fast directions were observed. A station network on the Nojima fault zone, Japan, deployed after the 1995 Hyogo-ken Nanbu earthquake, was used to measure anisotropic parameters. Fast directions during a period of 9-12 months after the main shock were observed being parallel to σ_H , with the exception of one station directly on the fault, which yielded fault strike-parallel fast directions. Measurements of this station during a second period (33 to 45 months after the main shock) showed that fast directions had changed by 68° , being now parallel to σ_H and to the fast directions of the other stations. Rapid fault healing within 33 months after the earthquake was suggested as mechanism for the change, closing fault controlled (i.e. fault parallel) cracks and allowing stress controlled EDA cracks (parallel to σ_H) to open. It has to be noted that the crucial station was moved by 130 metres between the two deployment periods, but it was argued that this spatial distance of less than a wavelength can not be responsible for an apparent temporal change.

All studies mentioned above report a change in anisotropic parameters, either in delay time, or in polarisation directions. Several further ones are listed in Crampin and Zatsepin (1997). The presence of EDA is widely accepted and explains most of the observations.

CHAPTER 3

METHOD

This chapter will describe the method that is used to process the data and to obtain information about physical parameters beneath the ground. Detailed information will be given about the algorithm that is used to determine the fast direction and delay time for each measurement. Also, theories and methods for the error evaluation of the results will be explained.

3.1 Data processing

A detailed overview of the data collection will be given in Chapter 4. This section will concentrate on the data processing methods.

Data preparation

Once the data disk had been retrieved from the field, the data was loaded onto the computer system and processed with several different programs. Detailed information about the software routines can be found in Appendix D. The aim of this first processing step was to generate files in SEED format, of which each one contains all recordings of only one

earthquake. For extracting these events from the raw data, earthquake catalogue data were used, provided by the Institute of Geological and Nuclear Sciences, New Zealand (IGNS). The earthquake locations were determined using CUSP (Caltech-USGS Seismic Processor).

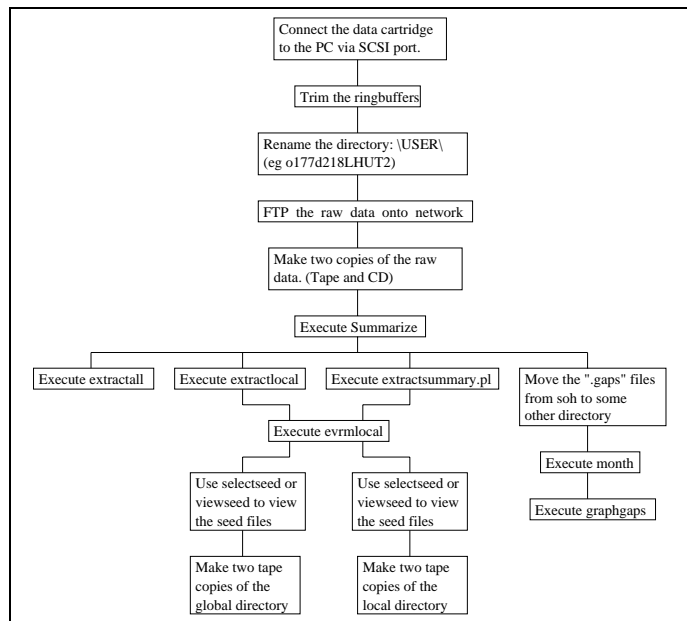


Figure 3.1 Data processing flow chart For a detailed description see Appendix D

Data selection

After extracting every event into a separate file, the events were divided into different “blocks”, depending on their distance from the receivers, and their magnitude (see Table 3.1). Of the numerous event-files, the ones had to be selected that were suitable for S-wave splitting measurements. The events were manually divided into mainly three categories: *very_nice*, *usable* and *not_usable*. The following aspects were considered for the categorisation:

Block	Distance	Magnitudes
Block1	$\leq 1.5^\circ$	2.0 - 2.9
Block2	$\leq 3^\circ$	3.0 - 3.4
Block3+	$\leq 5^\circ$	≥ 3.5

Table 3.1
Earthquake selection criteria
Distance is measured radially from
Mt. Ruapehu

1. Signal to Noise ratio of traces (usually larger than ~ 3).
2. Clarity of S-wave onset.
3. No “leakage” of S-wave energy from the horizontal components onto the vertical component (sign for converted phases or shallow incidence angle).
4. No sinusoidal wavelets, since they are vulnerable to cycle skipping (see Section 3.2.4).

These criteria had to be satisfied for at least one station per event. Since the priority in this project was a very high data quality, only events in the category “very_nice” were included in further processing.

Out of a total number of 830 events in blocks 1, 2 and 3+, 142 were selected in this category and therefore used for S-wave splitting measurements (see Table 3.2). Every one of these events is recorded by a maximum of seven stations and therefore yield the possibility of seven measurements. However, sometimes only one or two stations per event had a usable waveform, which further reduced the number of measurements. In the 2002 experiment (see Chapter 4), a total of 424 measurements were obtained, including A, AB, B and C marks, as well as NULL measurements of all qualities.

3.2 How to measure shear wave splitting

The last section described how the raw data were prepared and selected for the shear wave splitting measurements. How these measurements were obtained will be described in this section. It will concentrate on software and methods, so that all processes can be reproduced.

After selecting the data, the SEED files were converted into the SAC file format. The data were not corrected for instrument response, since Gralp CMG-40T seismometers were used, which have a sufficiently flat response curve between 0.033 Hz and 50 Hz (i.e. 0.02 s

Block	# available events	# selected events (“very_nice”)
Block1	206	47
Block2	202	32
Block3+	422	63
Total	830	142

Table 3.2

Numbers of available and selected events in the CHARM 2002 experiment. Note that defining the blocks is only a very basic method to counter the energy loss of increasingly distant earthquakes by selecting increasing magnitudes. Thus it is not surprising that the ratio of available vs. selected events fluctuates for different blocks.

to 30 s period). Phase corrections are also not necessary, since only the relative times are important for this study.

Before the splitting measurements were obtained, every recording of an event was filtered with different frequency filters in the range of 0.1 to 10 Hz, and the effect on the wavelet was observed. Usually, the filter generating the clearest wavelet and the highest Signal to Noise ratio was chosen for the splitting measurement. If two filters resulted in significantly different wavelet shapes, then both were chosen for a splitting measurement. Typical frequency filters were butterworth bandpass filters from 0.1 to 1 Hz, 0.5 to 3 Hz, or 1 to 7 Hz. These filter values also proved to be suitable in other crustal anisotropy studies (Audoin, 2002). See Appendix D for more details on the programs.

Following the selection of appropriate frequency filters, the shear wave splitting measurement was carried out by a SAC macro. After the right window for the measurement is manually picked (i.e. encompassing both S-waves) and the splitting values are obtained, the program offers the possibility to view the corrected waveforms and to give a quality mark for the measurement. Further, the user picks the start and end time of the main wavelet, which leads to a calculation of the main frequency of this measurement. All output of the program was written to a so called *measurement file*, which exists for every station and contains information about every measurement that was obtained at this station. A list of all measurement files is given in Appendix C. For a detailed description of the algorithm which is used for the shear wave splitting, see Section 3.2.2.

The quality marks that are given to every measurement range from A to C and NULLA to NULLC. A definition of the marks is given in Table 3.3.

3.2.1 Reprocessing of 1994 and 1998 data

The datasets from 1994 and 1998 have been processed for shear wave splitting before (Miller and Savage, 2001). However, no record was kept of the frequency filters and main frequencies

Mark	Definition	Example
A	Excellent	Figure 3.4 (p. 45)
AB	Very Good, with small flaw	Figure 3.6 (p. 46)
B	Good, but flaws present	Figure 3.7 (p. 47)
C	Acceptable, but ambiguous	Figure 3.8 (p. 47)
NULL<A/AB/B/C>	NULL measurement with mark	Figure 3.9 (p. 48)

Table 3.3
Quality mark definitions

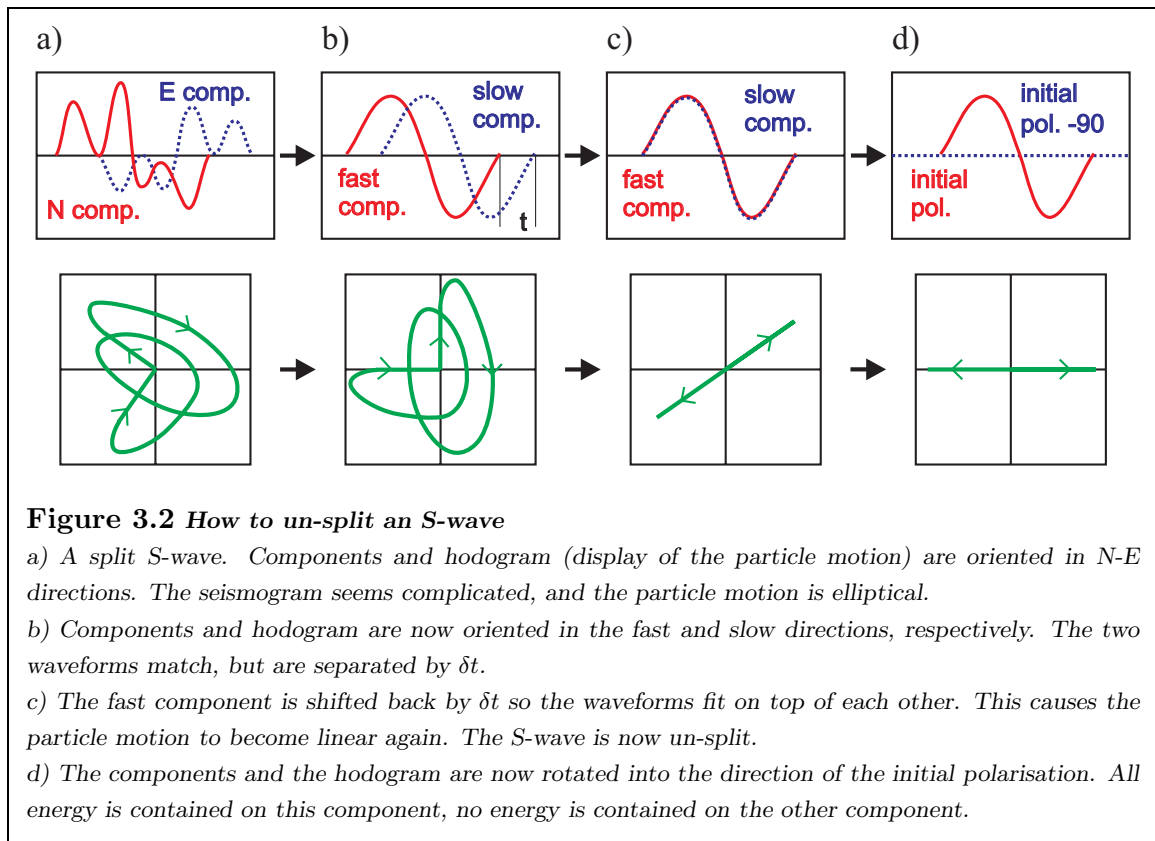
of the events. Also, only a small range of filters was used and not all available data was processed. In order to obtain a comparable database for all three deployments, the crucial parts of the datasets were reprocessed with the newly developed software. These were the 1994 deep measurements (>55 km) and the 1998 shallow measurements (<35 km).

For the 1994 deep dataset, all events from the old processing were reprocessed. These were events with a magnitude $M_L > 3$ within a distance of 1° from Mt. Ruapehu. For the 1998 shallow dataset, all events from the old processing were reprocessed plus all events with a magnitude $M_L > 3$ within a distance of 1.5° . Events with an unknown depth (e.g. depth stated as zero) were excluded.

For the rest of the old data, the measurement files were converted into the new format so all results could be processed and interpreted. These data have been filtered with bandpass filters from 1 to 3 Hz or 1 to 7 Hz, which is in the range of the filters used in the new processing. Thus the possibility of a systematic difference in filtering can be excluded. A list of all measurement files from the 1994, 1998 and 2002 datasets is given in Appendix C.

3.2.2 The Silver & Chan algorithm

The kernel of the splitting measurement macro is an algorithm developed by Silver and Chan (1991). It is implemented in a program that was originally written by Paul Silver and then extended several times. The general idea is to un-split the S-wave with its elliptical particle motion to produce a linearly polarised S-wave. The algorithm calculates an eigenvalue of a waveform based matrix and tries to minimise it. The parameters $(\bar{\Phi}, \delta t)$ that lead to the smallest eigenvalue are considered the true parameters of the splitting measurement. This algorithm will now be described in detail.



Un-splitting the S-wave

The approach for estimating the parameters Φ and δt is based on trying to un-split the S-wave so that the original isotropic waveform will be restored. The assumption is made that the S-wave has a small angle of incidence (i.e. a vertical raypath). Therefore the polarisation plane is known to be horizontal (the polarisation vector \vec{a} is contained in that plane and has an azimuth of α towards North).

i) It is helpful to look at the following case first: Assume that the parameters Φ , δt and the original polarisation are known. In which case the un-splitting of the wave is trivial. The way to do this is to rotate the North and East components of the wave into the direction of Φ and perpendicular to Φ . The wave is now in the coordinate system of the fast and slow direction (see Figure 3.2 b). In this coordinate system, the waveforms of the fast and the slow direction should be the same, the only difference being that the waveform of the slow direction lags behind the fast one by δt . Now the wave can simply be un-split by shifting the fast component backwards by δt (or alternatively shifting the slow component forward by δt – this is equivalent since only relative times are important). Then the wave is no longer split, but still rotated in the direction of the fast and slow components (3.2 c). A simple rotation into the direction of the initial polarisation will finally produce the familiar shape of a linear S-wave seismogram: All energy will be on the component of the initial polarisation, the other component will contain no energy (3.2 d).

ii) Now assume that the parameters Φ and δt of a wave are known, but the initial polarisation is unknown. The procedure is similar to i), up to the point where the un-split wave is rotated into its initial polarisation. Since it is not known, a method has to be found to determine its direction. A well known property of an S-wave in an isotropic medium is its linearity, i.e. the particles only vibrate in one direction. If the particle motion was drawn in a plot, an observer could easily pick the initial polarisation by just looking at the plot and judging the direction of the particle motion (3.2 c). However, this might not be so easy if noise is present.

This is where the *Eigenvalues* λ_i of the *covariance matrix* of the horizontal components provide valuable information. The components of the horizontal covariance matrix (Silver and Chan, 1991) are:

$$c_{ij}(\Phi, \delta t) = \int_{-\infty}^{\infty} u_i(t) u_j(t - \delta t) dt \quad i, j = 1, 2 \quad (3.1)$$

where $u_i(t)$ is the particle motion vector at the time t . $\delta t = 0$ in this case, since the delay time is corrected already while un-splitting the wave. c_{ij} is therefore the cross-correlation of component i with component j .

This 2x2 matrix is a mathematical property of the waveform, yet it also has a simple meaning: Equation 3.1 shows that the diagonal components of this matrix represent an autocorrelation, i.e. a kind of integral over one component of the particle motion. Thus they can be imagined as a measure of the relative surface spanned by one component of the particle motion. As a result of this, the matrix assumes a singular shape when rotated into the polarisation-direction of the wave: The component c_{11} is maximal, since it represents the particle movement into this direction. The other components are zero since there is no movement in the direction perpendicular to the polarisation direction (Fig. 3.2 d). This rotation represents a rotation of the matrix into the system of its eigenvectors, which then automatically assumes a diagonal shape (in this case even singular), with its eigenvalues as diagonal components. Therefore it is easier to just calculate the eigenvalues of the matrix, instead of trying every possible rotation. The larger eigenvalue (λ_1) has an eigenvector that points into the direction of the initial polarisation, the other eigenvalue (λ_2) is zero.

This effect is used by the algorithm: It simply calculates the eigenvalues and their respective eigenvectors and therefore determines the polarisation of a wave. Note that in the presence of noise or elliptical particle motion, the smaller eigenvalue can never become equal to zero. Thus the size of the small eigenvalue is a measure for the linearity of the waveform, and the larger eigenvalue has an eigenvector that points in the direction of the polarisation, even if noise is present.

iii) Now assume that none of the parameters Φ , δt or the original polarisation are known. This means that the wave can not be un-split as in i) and ii). Yet it is possible to assume an arbitrary, (and probably wrong) pair of Φ - δt , and to un-split the S-wave with them. Then the algorithm described in ii) will calculate the eigenvalues, but none of them will be close to zero, since the alleged un-splitting of the S-wave did not produce a linear particle motion.

However, it is possible to try every potential pair of Φ and δt in a grid search, and map the resulting smaller eigenvalue λ_2 in a 2D plot. It can then be assumed that the Φ - δt pair that produces the smallest eigenvalue is the best one, since it produced the most singular covariance matrix and therefore the most linear waveform. Silver and Chan (1991) show that minimising λ_2 is equivalent to maximising λ_1 or λ_1/λ_2 , due to invariance of the trace ($\lambda_1 + \lambda_2$) of the matrix with respect to changes in δt and Φ .

For Φ , a range -90° to 90° is searched in steps of 1° . For δt , a range of 0 s to 2.0 s with an increment of 0.01 s is searched. This leads to a total of 36,000 eigenvalue calculations, which can be computed in a fraction of a second. The pair Φ - δt with the smallest λ_2 eigenvalue is automatically chosen as the solution, and the resulting waveforms are displayed for judgement by the experimenter. An example of this plot is shown in Figure 3.4 (page 45).

Criteria for the quality of a measurement are:

- Contour plot: Existence of one clear maximum (Figure 3.4 (12)).
- Contour plot: Small size of the 95% confidence area (closest contour in plot).
- Linearity of corrected particle motion (11).
- Matching waveforms of corrected wavelet (9).
- Stability of the solution with regard to changes of the manually picked window.
- Removal of energy on the component perpendicular to the initial polarisation (7).
- No “correction” (=removal) of noise on this component (7).
- Width of window: Is the whole wavelet included (1 - 9)?
- No sinusoidal waveform (to avoid cycle skipping; see Section 3.2.4).
- High Signal to Noise ratio (1), (2).
- Clarity of S-wave onset and wavelet.
- No S-wave signature on the vertical component (3).

The referenced numbers are shown in Figure 3.4 on page 45 . Several measurement examples with different qualities are shown in Figures 3.4 to 3.9.

Note that the fast and the slow wavelet do not always match each other perfectly, i.e. they display slightly different waveforms. The reason for this is that they have different polarisations and thus respond differently to the structure between source and receiver (e.g. Liu et al., 1997). This is also one of the reasons why attempts to fully automate the splitting measurement algorithm were only partially successful in the past (e.g. Crampin et al., 1991, see Section 2.2.2).

3.2.3 NULL measurements

NULL measurements are obtained if one of the following conditions is true:

1. The medium is isotropic ($\delta t = 0$)
2. The initial polarisation of the wave is parallel to the fast anisotropic direction ($\alpha = \Phi \pm 180^\circ$)
3. The initial polarisation of the wave is parallel to the slow anisotropic direction ($\alpha = \Phi \pm 90^\circ$)

In this case the S-wave will not split and it therefore retains its near linear particle motion. This has two effects on the behaviour of the algorithm, and is expressed as a prominent U-shaped pattern in the contour plot (Figure 3.9):

1. All Φ values in the grid search that belong to a pair with $\delta t = 0$ will lead to a minimal eigenvalue λ_2 since the particle motion is already linear without shifting the wavelet.
2. For δt values in the grid search that correspond to $\Phi = \alpha \pm 90^\circ$, the eigenvalue will also be minimal. This happens because the component that is shifted during the un-splitting contains no energy (perpendicular to α). Thus it has no effect on the waveform and the particle motion will stay linear even for an arbitrary δt .

As a result of this, the meaning of a NULL measurement is ambiguous in the three above mentioned cases ($\delta t = 0$, $\alpha = \Phi \pm 180^\circ$ or $\alpha = \Phi \pm 90^\circ$). However, when a large number of NULL measurements are obtained with similar directions, the first case can be excluded (See Chapter 5, Figure 5.8). Yet a 90° ambiguity in the fast direction always remains. Another consequence for the behaviour of the algorithm is that the position of the minimum is determined by noise and can not be trusted. Under the assumption that anisotropy is present, the solution for Φ has to be manually picked as being one of the two “bars” of the U. In this project, the positive value was chosen for consistency reasons. The value for δt is insignificant and should not be used for any interpretation.

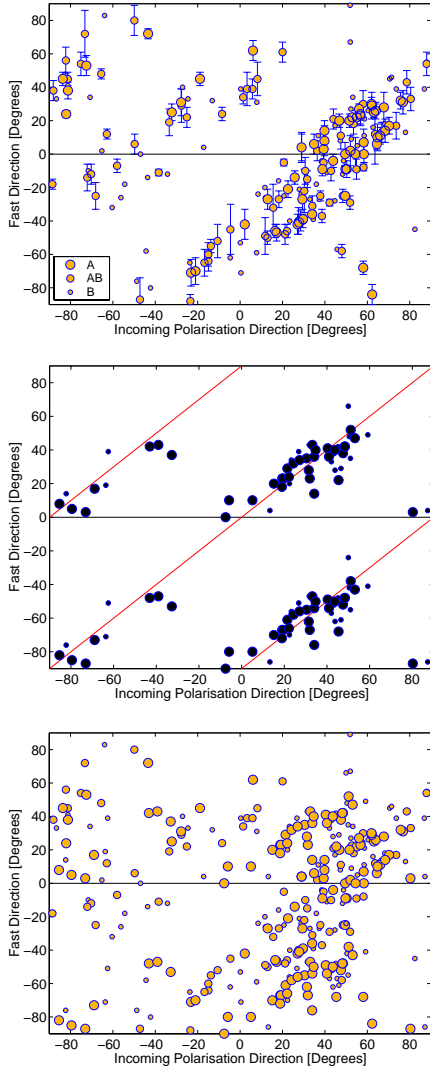


Figure 3.3 The NULL phenomenon

top: 2002, all valid splitting measurements

The plot shows the fast direction Φ vs. initial polarisation α . If interpreted by itself, the plot seems to reveal a prominent dependency of Φ on the initial polarisation. However, the reason for this is that NULL measurements are not included in the plot. This is common practise since NULLs are ambiguous in Φ and are therefore being separated from valid measurements for argumentation reasons. The size of the dots represent the quality of the measurement.

centre: 2002, all NULL measurements

In this plot, only NULL measurements are shown. Since their fast direction is ambiguous by 90° , both directions are plotted for each NULL. It is clear that the NULLs gather on straight lines where $\Phi = \alpha \pm 90^\circ$, which is only a visualisation of the definition of a NULL measurement. Potentially valid measurements from the area close to the lines are interpreted as NULLs if the noise level is higher than the signal on the transverse component (i.e. the component 90° to α). They are therefore also missing in the plot above. The width of this area is thus directly linked to the S/N level of the data.

bottom: 2002, NULLs and valid measurements.

This plot shows NULLs as well as splitting measurements. They are plotted in the same colour to emphasise that there is no existing dependency of the parameters in this plot. The clustering of events on the right merely shows a predominant polarisation of earthquakes in this direction.

NULL measurements can be a source for data misinterpretation in shear wave studies. They will therefore be examined closer: For the reasons explained above it is obvious that a situation, where the initial polarisation α of a wave is close to (or perpendicular to) the fast direction Φ , will lead to a NULL measurement. One property of NULL measurements is that they are ambiguous in Φ and therefore experimenters tend to separate them from valid measurements. This means that NULLs are often left out of plots that serve to investigate a relationship between different parameters. If a plot is made for Φ vs. initial polarisation α , the missing NULLs lead to a characteristic pattern of blank spots, even though the relationship between Φ and α might be random. This plot is illustrated in Figure 3.3. Two zones of blank spots stretch over the plot, each with a gradient of 1, encompassing the line where $\Phi = \alpha$. All measurements in that zone are interpreted as NULLs because their particle motion is already very linear and can not be further linearised. In other words, they do not seem to have any energy on the component perpendicular to the initial polarisation. In theory, this zone of

blank spots should be infinitely thin. However, in practise it also includes measurements that have energy on the perpendicular component, but smaller than the noise level. An implication of this is that the width of the zone is determined by the noise level. It could even be used to calculate an average S/N ratio for the dataset.

3.2.4 Cycle Skipping

Cycle skipping is a phenomenon that occurs when the split wavelet contains only a very narrow range of frequencies. This can have a natural cause, or it can be induced by applying a narrow bandpass filter to the data (e.g. 1 to 2 Hz). In this case the wavelet looks sinusoidal, i.e. there is no clear onset and the waveform match is ambiguous. For example, one wavelet could match the other one both in one position, and also when it is shifted by a half or full cycle or their multiples. Then two or more minima appear in the contour plot, of which both are possible solutions for un-splitting the wave. Only one of them is the real one, however. With no noise present, the real minimum should still be deeper than the cycle-skipped one and correctly be picked by the algorithm. Yet sometimes the two minima have such similar values that the wrong one is picked due to noise interference. Then the determined delay time is wrong by multiples of half a wavelength:

$$\tilde{\delta t} = \delta t \pm n \cdot T/2 \quad n = 1, 2, \dots \quad (3.2)$$

where $\tilde{\delta t}$ is the measured delay time, δt is the real delay time, n is the number of skipped half-cycles and T is the wavelength. There are two possible consequences for the measured fast direction:

1. One or more cycles are skipped so that the slow component lags behind even more. In this case the obtained fast direction is not affected by the cycle skipping. Only the delay time is wrong as shown above.
2. One or more cycles are skipped so that the slow component jumps in front of the fast component. In this case the algorithm interprets the actual slow component as fast because it has to shift it back in time to match it with the other component. This leads to the obtained fast direction being wrong by 90° , in addition to a false delay time.

In general, cycle skipping should be avoided. Suspicious signs are the above mentioned sinusoidal wavelets and a prominent pattern of minima that is aligned along a line of constant Φ , with a spacing of $T/2$. Also, an alternating pattern of minima along two constant lines of Φ , separated by 90° is possible. See Figure 3.10 for an example. In this study, all measurements were examined for signs of cycle skipping, and eliminated if in doubt.

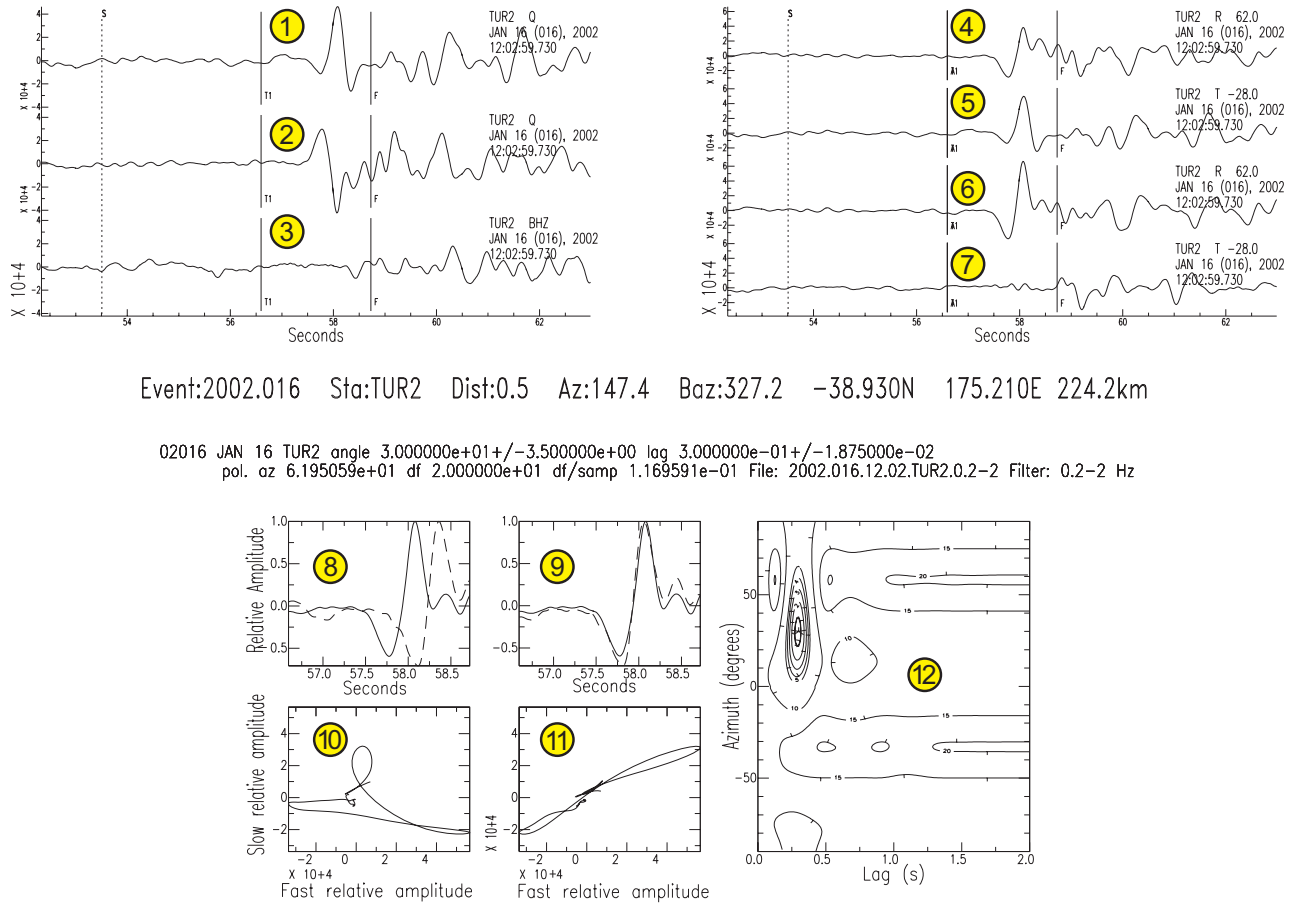
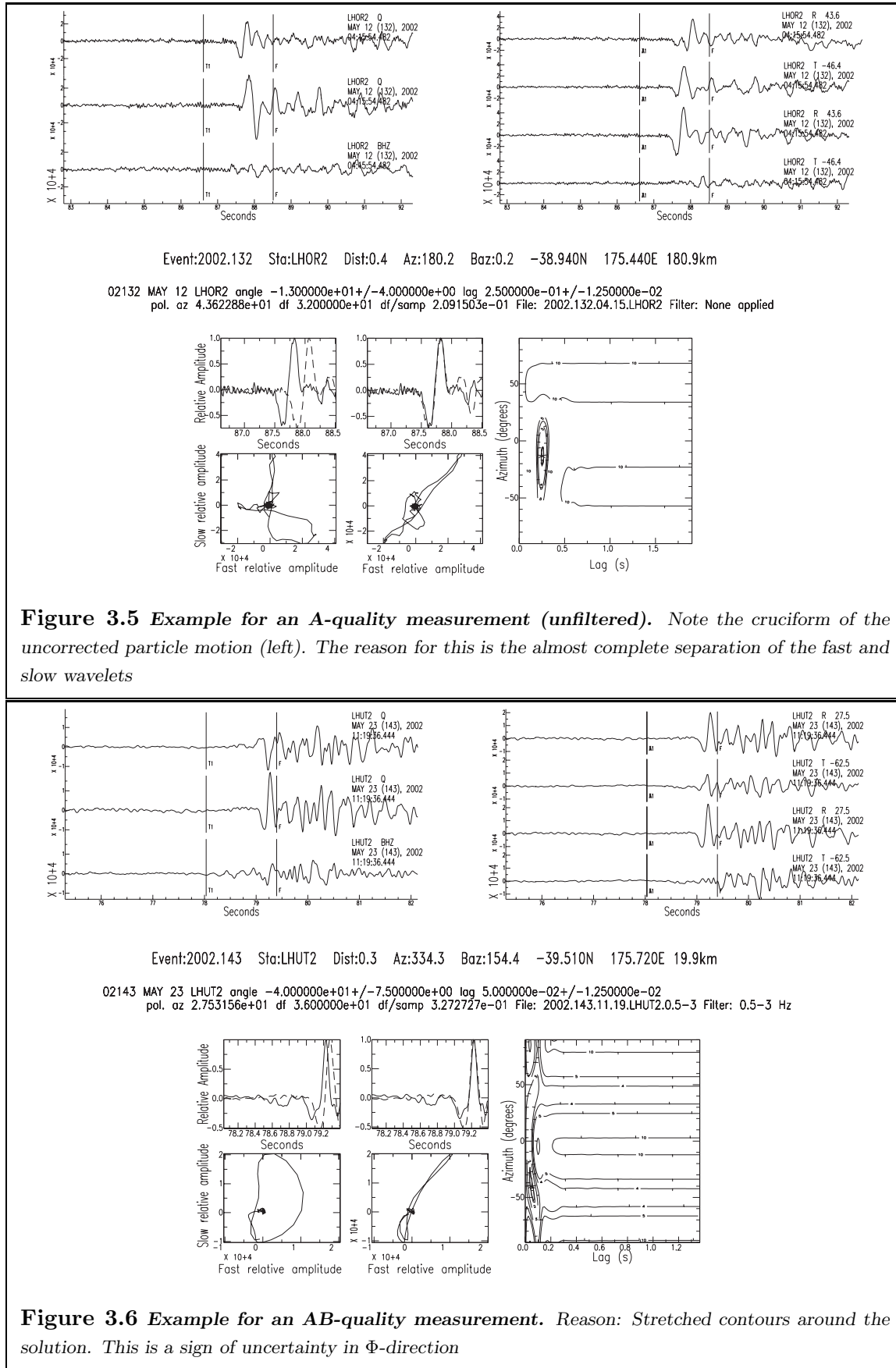
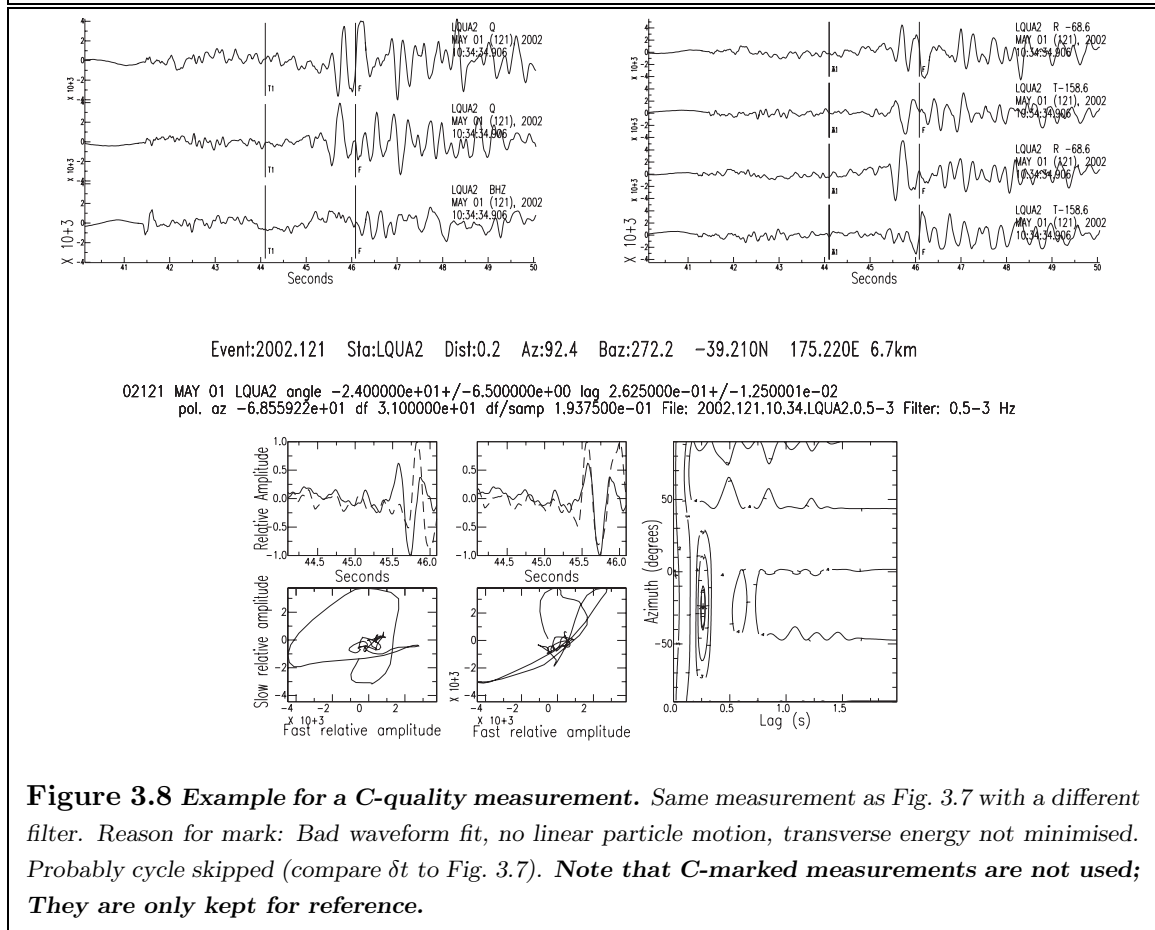
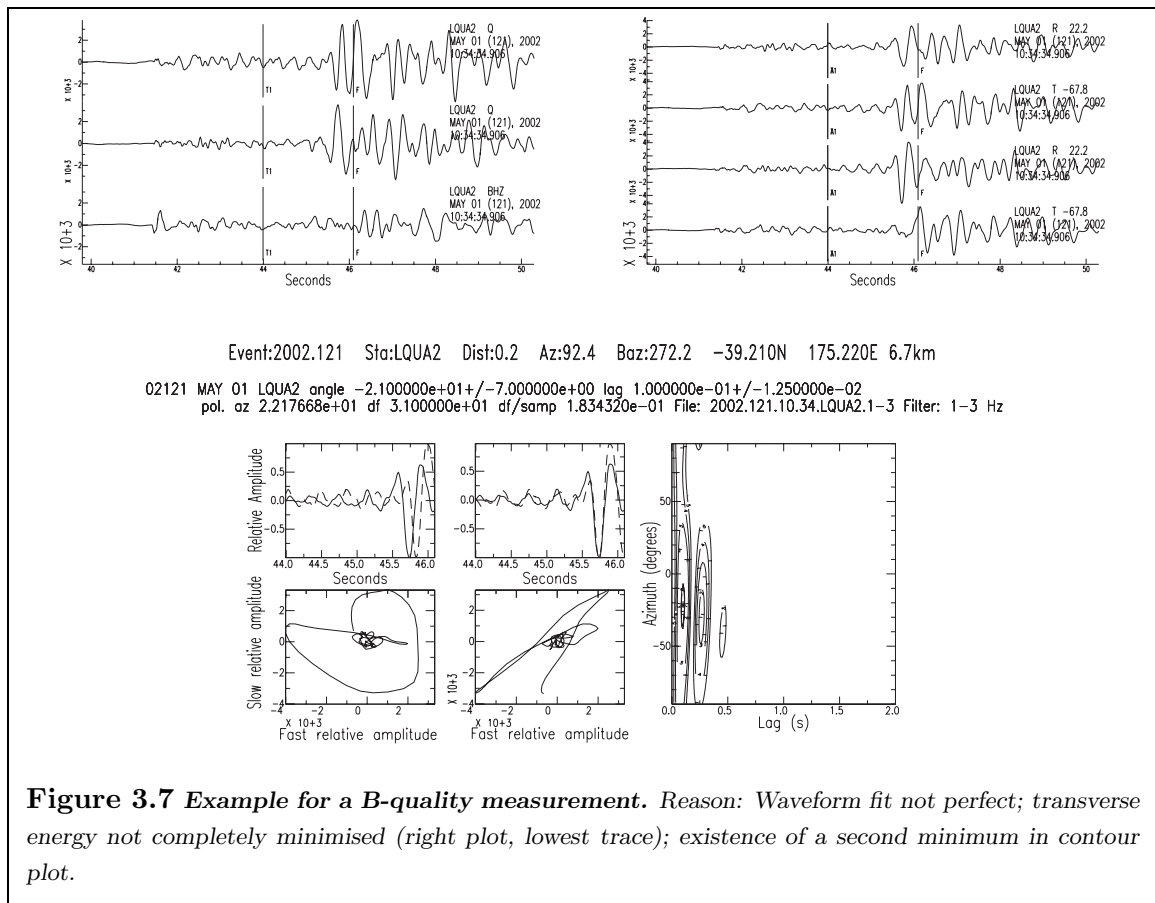


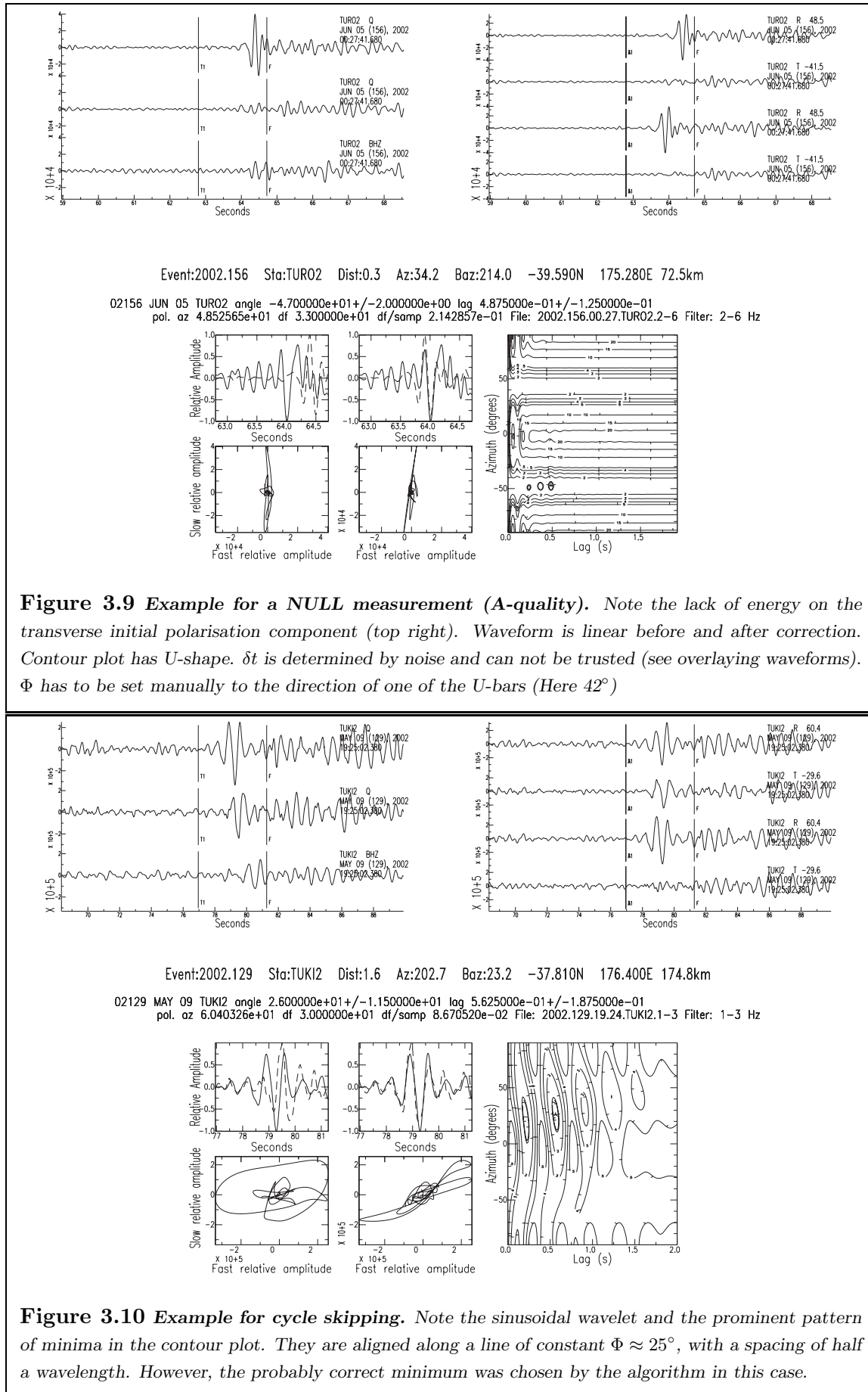
Figure 3.4 Example for an A-quality measurement. This measurement was recorded at station TUR02 (=TUR2). Information about the obtained parameters can be found in the header of the lower picture. $\Phi = 31^\circ$, $\delta t = 0.3$ sec, initial polarisation $\alpha = 62^\circ$.

- (1) Original seismogram, rotated into direction of back azimuth.
- (2) Original seismogram, rotated 90° to back azimuth.
- (3) Original seismogram, vertical component.
- (4) Original seismogram, rotated into direction of initial polarisation.
- (5) Original seismogram, rotated 90° to initial polarisation.
- (6) Corrected seismogram, rotated into direction of initial polarisation.
- (7) Corrected seismogram, rotated 90° to initial polarisation.
- (8) Original seismogram, fast and slow components in overlay wave form plot.
- (9) Corrected seismogram, fast and slow components in overlay wave form plot.
- (10) Original waveform, hodogram (horizontal particle motion). Axes are the fast and slow directions.
- (11) Corrected waveform, hodogram (horizontal particle motion).
- (12) Contour plot (Φ vs. δt), solution is marked as a star. Innermost contour outlines the 95% confidence region.

The criteria for judging the quality of a measurement are shown at the end of Section 3.2.2.







3.3 The slope corrected shear wave angle

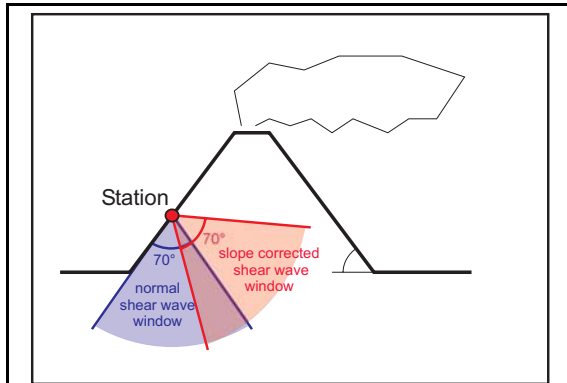


Figure 3.11 *The slope corrected shear wave window.* Note that a wave coming from the left side of the blue window would strike the surface at the station at a very shallow angle, which would cause strong distortion of the measured wavelet. This can be avoided by defining a slope corrected shear wave window (red) which only allows events that strike the surface at an angle of max. 35° .

Section 2.1.7 described why it is necessary to select events with a steep angle of incidence at the receiving station. This is especially difficult when the stations are positioned on the slope of a mountain, as was the case during all deployments at Mt. Ruapehu. The slope-angle δ varied from 2.3° at LHOR to 14.0° at LHUT (see Table 3.4). The determination of this slope angle is also not trivial. Based on the length of the scale, this angle is highly variable at any given station. For example, when the steepness of the surface close to a station is measured, the result could be 90° if the station is placed at the base of a cliff face. On the other hand, if the whole mountain is considered, the angle would certainly be very shallow when it is

calculated only by the height and the width of the base of the mountain. The answer to this question is choosing the right length of scale. Thus it is important to know the main wavelength of the incoming waves. With an assumed surface S-wave velocity of around 1.3 – 1.6 km/s (Latter, 1981) and main frequencies of around 1 Hz and lower, a scale length of 2 km was chosen.

For Table 3.4, the direction of the steepest gradient was determined and then the altitude difference between a point 1 km downslope and 1 km upslope of the station along that direction was measured on a map. The resulting slope angle allows the experimenter to calculate the incidence angle at the slope surface. However, the incidence angle on an assumed horizontal surface has to be calculated first. This is done by using the ray parameter for the event. It is given by the IASPEI earth model (Kennett, 1991), which is assumed to be a valid model **under** the low velocity layers of the volcanic edifice. To calculate the incidence angle at an assumed

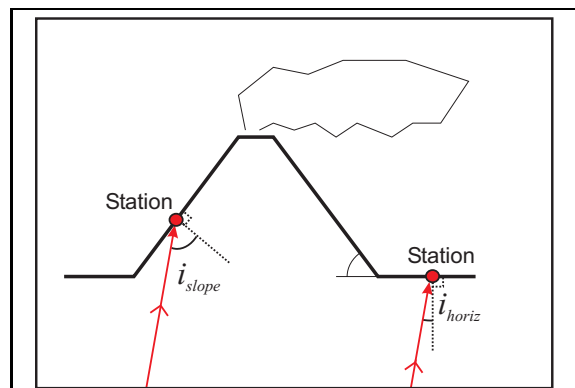


Figure 3.12 *Incidence angle on a slope.* For the same incoming wave, the incidence angle at a station on the slope can be substantially different from that of a station on a horizontal surface.

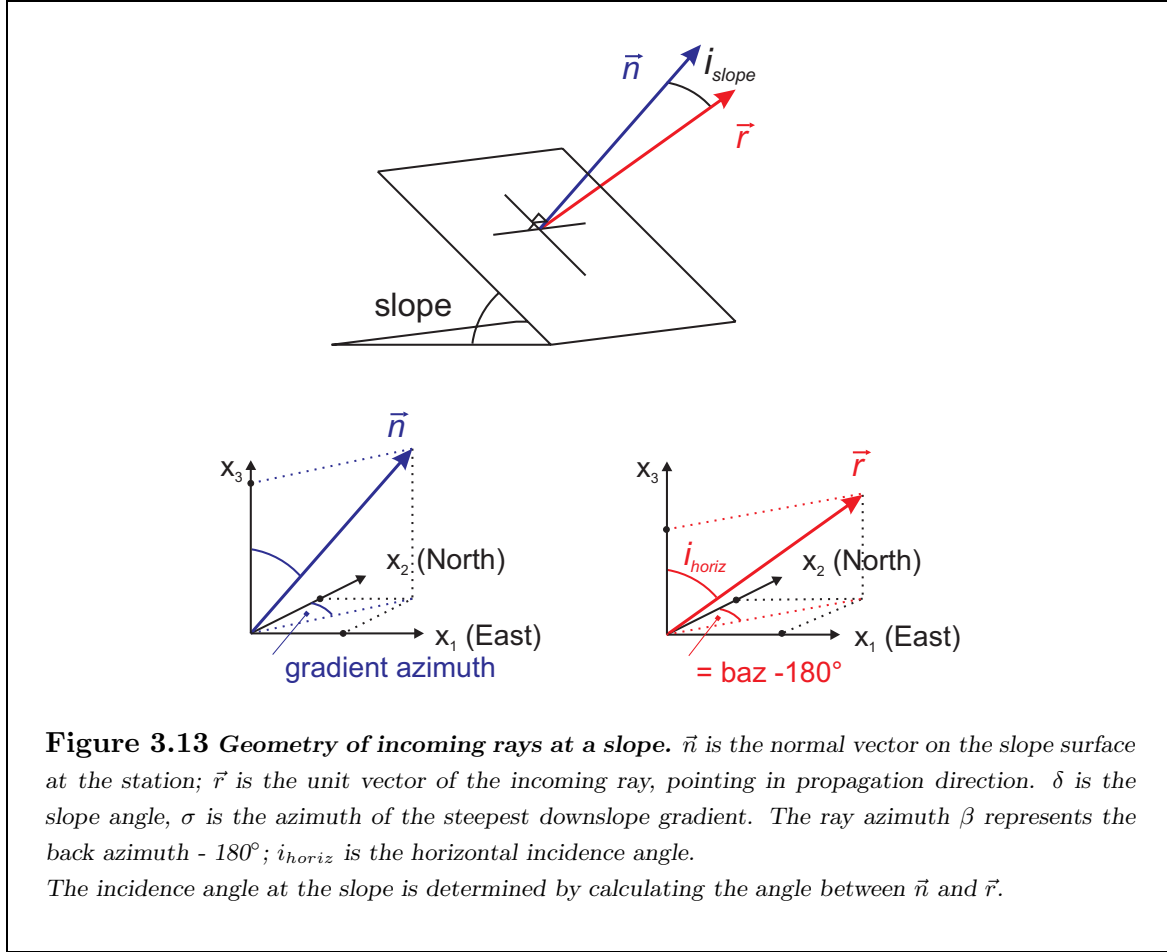
To calculate the incidence angle at an assumed

horizontal surface, the following formula was used (Lay and Wallace, 1995):

$$i_{horiz} = \arcsin\left(\frac{p v_s}{R}\right) \quad (3.3)$$

where

- i_{horiz} : incidence angle on a horizontal surface [°]
- p : ray parameter (slowness) [s/rad]
- v_s : S-wave velocity at or near the surface [km/s]
- R : Earth's radius (6371 km)



The incidence angle at the slope surface can be obtained by calculating the angle between an incoming ray \vec{r} and the normal vector on the slope \vec{n} . Both vectors have the length 1 and are defined by:

$$\vec{r} = \begin{pmatrix} r_x \\ r_y \\ r_z \end{pmatrix} = \begin{pmatrix} \sin(i_{horiz}) \sin \beta \\ \sin(i_{horiz}) \cos \beta \\ \cos(i_{horiz}) \end{pmatrix}; \quad \vec{n} = \begin{pmatrix} n_x \\ n_y \\ n_z \end{pmatrix} = \begin{pmatrix} \sin \delta \sin \sigma \\ \sin \delta \cos \sigma \\ \cos \delta \end{pmatrix},$$

where β is the back azimuth minus 180° ; δ is the slope angle and σ is the azimuth of the steepest downslope gradient (see Figure 3.13). The incidence angle is then defined by the

Station name	Azimuth of steepest gradient (downslope) σ	Altitude difference within 2 km	Resulting slope angle δ
FWVZ	340°	500 m	14.0°
LHOR2	255°	80 m	2.3°
LHUT2	340°	500 m	14.0°
LQUA2	0°	220 m	6.3°
LTUR2	240°	300 m	8.5°
TUKI2	90°	320 m	9.1°
TUK2	80°	160 m	4.6°
TURO2	240°	300 m	8.5°

Table 3.4
Slope angles for recording stations.

angle between \vec{n} and \vec{r} , which in a cartesian coordinate system is defined by:

$$\begin{aligned}
 i_{slope} &= \arccos \left(\frac{\vec{n} \cdot \vec{r}}{|\vec{n}| \cdot |\vec{r}|} \right); \quad |\vec{n}| = |\vec{r}| = 1 \\
 &= \arccos \left(\sin(i_{horiz}) \sin \beta \sin \delta \sin \sigma + \right. \\
 &\quad \left. + \sin(i_{horiz}) \cos \beta \sin \delta \cos \sigma + \cos(i_{horiz}) \cos \delta \right) \\
 &= \arccos \left(\cos(i_{horiz}) \cos \delta + \sin(i_{horiz}) \sin \delta \left(\sin \beta \sin \sigma + \cos \beta \cos \sigma \right) \right) \\
 &= \arccos \left(\cos(i_{horiz}) \cos \delta + \sin(i_{horiz}) \sin \delta \cos(\beta - \sigma) \right).
 \end{aligned} \tag{3.4}$$

which can be expressed as:

$$i_{slope} = \arccos \left(\cos(i_{horiz}) \cos \delta - \sin(i_{horiz}) \sin \delta \cos(baz - \sigma) \right). \tag{3.5}$$

This formula was used to calculate the incidence angle at the slope surface, where

i_{slope} : incidence angle on the slope surface [°] (= corrected arrival angle)

i_{horiz} : incidence angle on a horizontal surface [°]

δ : slope angle [°]

σ : azimuth of the steepest downslope gradient [°]

baz : back azimuth of the event [°].

Once this value was calculated, only events with an i_{slope} incidence angle smaller than 35° were selected for the further visualisation and interpretation of the data. A program has been developed to automatically calculate the normal and corrected S-wave incidence angles from a measurement file (See Appendix D.2 for more details).

3.4 Mean value and error analysis

In this study, most of the data consists of measurements of the fast anisotropic direction, which can be classified as directional data. When handling directional data, a normal error statistic can not be used for two reasons:

1. The range of directional data is wrapped and has a maximum of 360° . In a normal statistic, the maximum possible range is $[-\infty \dots + \infty]$.
2. Splitting data has a bimodal distribution. This means that a fast direction of 1° is at the same time also 181° . Thus, every measurement is ambiguous by 180° , which constrains the effective maximum possible range of data to only 180° .

Mardia (1972) and Davis (1986) describe methods for handling this special type of data, which will be presented in the following sections.

3.4.1 Obtaining the mean value of splitting measurements

In order to obtain the mean value of all splitting measurements, every measurement is treated as a normalised vector with the direction Φ_i ($i = 1, \dots, n$), which represents the measured fast direction. All vectors are added up and the length of the resultant vector is divided by the number of measurements (n). Equation 3.6 shows how the individual vectors are added up. The factor l ($l = 2$) represents the fact that the distribution is bimodal, and will be explained in Section 3.4.2.

$$\vec{R} = \frac{1}{n} \begin{pmatrix} X_r \\ Y_r \end{pmatrix} = \begin{pmatrix} \frac{1}{n} \sum_{i=1}^n \cos(l \Phi_i) \\ \frac{1}{n} \sum_{i=1}^n \sin(l \Phi_i) \end{pmatrix} \quad (3.6)$$

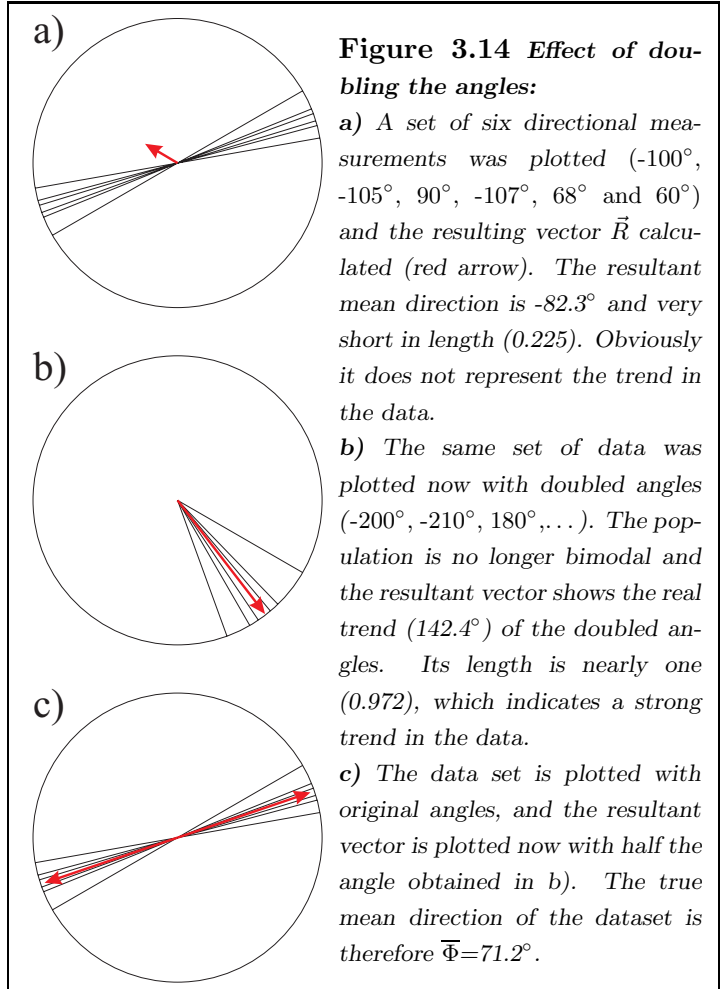
The direction of this resultant vector \vec{R} represents the mean direction Φ of all measurements, and its length is related to the variance. Equation 3.7 shows how it is obtained:

$$\begin{aligned} \bar{\Phi} &= \arctan(Y_r/X_r) / l \\ &= \arctan \left(\frac{1}{n} \sum_{i=1}^n \sin(l \Phi_i) \middle/ \frac{1}{n} \sum_{i=1}^n \cos(l \Phi_i) \right) \middle/ l \end{aligned} \quad (3.7)$$

(adapted from Davis (1986)), again, $l = 2$ (see Section 3.4.2).

3.4.2 Why angles have to be doubled

Since splitting data has a bimodal distribution (i.e. 180° ambiguity), simply adding up all vectors would lead to the wrong result. For example, two measurements of -90° and $+90^\circ$ represent the same fast direction, but adding them up will result in a vector with zero length and an undefined direction. A way of avoiding this is to double the angles of all measurements before the vectors are added up (Krumbein, 1939), hence the factor $l = 2$ in the sine and cosine of Equation 3.6 and 3.7. This, of course, will lead to an average direction that is also multiplied by the factor two. Thus, the mean direction of the resultant vector has to be divided by this factor in Equation 3.7 (Davis, 1986). See Figure 3.14 for an example. In the case of a higher order of multi-directional data, the factor l also rises. For example, if the directions of NULL measurements are added up (which have a $\pm 90^\circ$ ambiguity), then l would be four.



3.4.3 Calculating standard deviation and errors : The Von Mises Statistics

For the evaluation of the data quality, it is important to obtain information about the errors and deviations of the dataset. Every statistic uses certain assumptions about the probability model of the data involved, and a special kind of distribution has to be used for directional data. The *Von Mises distribution* is a circular analog to the normal distribution (Mardia, 1972) and will be used as a basis for the following calculations. It is defined by the two parameters Φ (mean direction) and κ , which is called the concentration parameter. Figure 3.15 shows the distribution of the 2002 deep events with the expected Von Mises and Normal distributions. It is shown that a Von Mises distribution fits well to the data in this study. Its

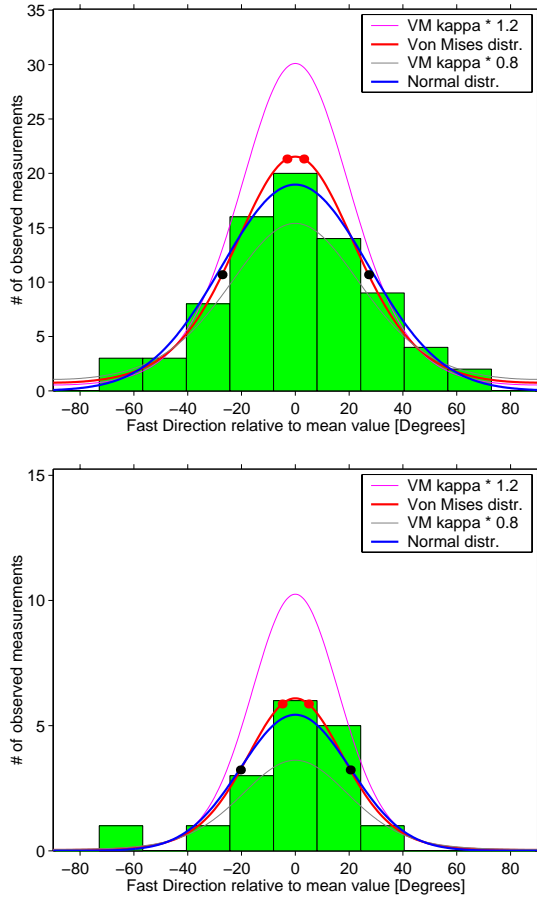


Figure 3.15 Validity of the Von Mises Distribution

top: 2002, deep events. Number of observed measurements vs. the fast direction (relative to the mean fast direction). The blue curve represents a normal distribution, the red curve a Von Mises distribution. Considering the fact that the dataset consists of data from several different stations that sample different regions of the crust, a broad distribution can be expected. This also means that the centre column will be smaller than the theoretical value for a Von Mises distribution. The red curve is only determined by the concentration parameter of the distribution (κ) and the total number of measurements. Note that the curve was not fitted to the data. Yet it predicts the probabilities surprisingly well. For the other two curves, κ was manually altered to display the dependency on this parameter. In this example, only measurements of A and AB quality are included. The red dots on the curve represent the standard error interval and show how well constrained the mean value is. The black dots represent the standard deviation and show how spread the data is. It is clear that a Von Mises distribution is a valid assumption for the data.

bottom: 2002, deep events recorded at TURO2. This plot shows that the Von Mises distribution is also a valid assumption for data that is recorded at only one station.

probability density function is given by Mardia (1972):

$$g(\Phi_i; \bar{\Phi}, \kappa) = \frac{1}{2\pi I_0(\kappa)} e^{\kappa \cos(\Phi_i - \bar{\Phi})}, \quad 0 < \Phi_i \leq 2\pi, \quad \kappa > 0, \quad 0 \leq \bar{\Phi} < 2\pi, \quad (3.8)$$

where $I_0(\kappa)$ is the modified Bessel function of the first kind and order zero:

$$I_0(\kappa) = \sum_{r=0}^{\infty} \frac{1}{(r!)^2} \left(\frac{1}{2}\kappa\right)^{2r}. \quad (3.9)$$

$\bar{\Phi}$ is the mean direction; κ is the concentration parameter and a direct function of R ; it will be described in a paragraph later in this section.

Standard deviation

The above calculated resultant vector \vec{R} also carries information about the spread of the data.

The longer \vec{R} is (with a maximum of 1), the more homogeneous is the data. If all measurements point in the same direction, then the length of the vector will be one. If the measurements are randomly dispersed in all directions, then the resultant vector will be of

almost zero length. Mardia (1972) provides a more quantitative formula for this. First, the length of \vec{R} has to be calculated:

$$\begin{aligned} R &= |\vec{R}| \\ &= \sqrt{X_r^2 + Y_r^2} \\ &= \sqrt{\left(\frac{1}{n} \sum_{i=1}^n \cos(l \Phi_i)\right)^2 + \left(\frac{1}{n} \sum_{i=1}^n \sin(l \Phi_i)\right)^2} \end{aligned} \quad (3.10)$$

From this value, the so called *circular variance* S_0 can be derived:

$$S_0 = 1 - R. \quad (3.11)$$

Since R lies in the Range $[0, 1]$, the following formula of a wrapped normal distribution is valid (Mardia, 1972):

$$1 - S_0 = e^{-\frac{1}{2}l^2 s_0^2}, \quad (3.12)$$

with the *circular standard deviation* s_0 . Thus

$$s_0 = \sqrt{-2 \ln(1 - S_0)} / l \quad (3.13)$$

The circular standard deviation describes the width of an interval around the mean value, in which a random measurement will fall with a 68% probability. However, before this value can be trusted, it has to be shown that the sample of measurements is not uniformly distributed.

Test for Non-Randomness (Rayleigh's Test)

In order to use error statistics on a sample of data, it has to be proven that the data is not random (uniformly distributed). This can be achieved by applying Rayleigh's test, which assumes that the measurements are sampled from a Von Mises distribution. This test is very simple, and only the number of measurements n and the calculation of R is needed. For every value n , there is a critical value for non-randomness at a certain level of significance. Tables for this are provided in Mardia (1972) and Davis (1986). Since the value of R rises with the uniformity of the data, it has to be larger than the critical value specified by the number of measurements. Also the level of significance has to be specified, which gives the likeliness of the test being wrong. For example, the dataset described in Figure 3.14 has a value of $R = 0.972$, $n = 6$. Assuming that the observer wants to be 99% sure that this dataset is not random, he or she would look up the critical R -value for $n = 6$ and a significance level of 1% ($= 100\% - 99\%$). This value is 0.825, which is exceeded by the R -value of the dataset

(0.972). This means that the observer can be at least 99% sure that the data in this example is not random.

Concentration parameter

Another parameter that can be derived from \vec{R} is the concentration parameter κ . It behaves similarly to R , i.e. it is zero for random data, and its value rises with the homogeneity of the data. However, its maximum value approaches infinity for homogeneous data, i.e. when all measurements are pointing into the same direction ($R = 1$ in this case). The relationship between R and κ is not trivial, as it is described by two Bessel functions:

$$R(\kappa) = I_1(\kappa)/I_0(\kappa). \quad (3.14)$$

Mardia (1972) provides charts, tables and also several approximations for this relation. For example, an approximation for $R > 0.8$ is given by:

$$\frac{1}{\kappa} \approx 2(1 - R) - (1 - R)^2 - (1 - R)^3 \quad (3.15)$$

A program called *kappa* was developed which combines different approximation methods to provide an accurate estimation for $\kappa(R)$.

Standard error

With a given dataset, a mean direction can be calculated as described above. The standard deviation of the measurements describes how spread the data are around this mean value. However, it does not give any information about how accurate this mean value represents the true fast direction. This information is given by the *standard deviation of the mean*, which is also called the *standard error*. Assuming that a true fast direction in the ground exists, the standard error can be derived from Equation 3.8. The exact derivation will not be shown here, as it is of considerable length, and is also shown in Mardia (1972). A key part of it is the relation of the expected value $E\{\cos(\Phi_i - \bar{\Phi})\} = R$, which eventually leads to:

$$\boxed{s_e = \frac{1}{l \sqrt{n R \kappa}}}, \quad l = 2 \quad (3.16)$$

where

- s_e : standard error [rad]
- n : number of measurements
- R : resultant vector length
- $\kappa(R)$: concentration parameter

With this parameter known, it can be expected that the true mean of the population is contained in the interval

$$\Phi = \bar{\Phi} \pm Z_{\alpha} s_e \quad (3.17)$$

where Z_{α} is a factor that specifies the level of significance. E.g. $Z_{68\%} = 1$ and $Z_{95\%} = 1.96$. For the dataset in Figure 3.14, the standard error calculates to $s_e = 3.0$. This means that the probability is 95% that the true mean value is contained in the interval $71.2^{\circ} \pm 1.96 \cdot 3.0^{\circ}$ (i.e. from 65.32° to 77.08°). These values can also serve to test whether two sets of samples are drawn from the same population. In other words: is the set of measurements from one station sampling the same region of anisotropy as the measurements from the next station? With a specified standard error value, the answer is easily obtained: if the standard error intervals of the two stations do not overlap, then it can be excluded with the specified significance that the measurements of the two stations represent the same region of anisotropy. For a more quantitative evaluation of this, an F-Test statistic can be computed (Davis, 1986). During this study, software was developed which calculates the above mentioned error parameters (std. deviation, std. error, R , n , $\bar{\Phi}$, ...) for a given measurement file (see Appendix D.2 for more details).

3.4.4 The difference between standard deviation and standard error

When a physical property is measured a certain number of times (e.g. 10), then the measurements will suffer from the same statistical error sources as every measurement, i.e. the results will form a gaussian, bell shaped curve around the true value. Out of this shape, a standard deviation interval for the measurements can be estimated, which means that the random chance for the next measurement falling into this interval is 68%. The mean value of the measurements is an estimate of the true value (assuming that no systematic errors were made), but due to only 10 measurements it will have a limited accuracy. This accuracy is given by the *standard deviation of the mean value*, which is also called the *standard error*. It means that there is a 68% probability for the true value being contained in the standard error interval around the mean value. For a normal distribution this is the standard deviation of the measurements divided by the square root of the number of measurements. So in this case the standard deviation of the mean value is $\sqrt{10}$ (~ 3.2) times smaller than the standard deviation of the measurements.

$$s_e = \frac{s_0}{\sqrt{n}} \quad (3.18)$$

This means that if not only 10 measurements, but 10,000 measurements were obtained, the standard deviation of the mean value is $\sqrt{10,000}$ ($= 100$) times smaller than the standard

deviation of the measurements. Thus the error interval for the mean value becomes substantially smaller. Yet the measurements will still form the same gaussian curve around the mean value as before. The width of the curve and therefore the standard deviation of the measurements will be the same as with only 10 measurements, since the error sources have not changed.

CHAPTER 4

DATA ACQUISITION

This chapter provides information about the data collection during the CHARM 2002 experiment and the instrument deployments from 1994 and 1998. Details about sensors and recording equipment will be given, as well as about logistical aspects.

4.1 The CHARM experiment

CHARM (CHanges of Anisotropy at Ruapehu Mountain)

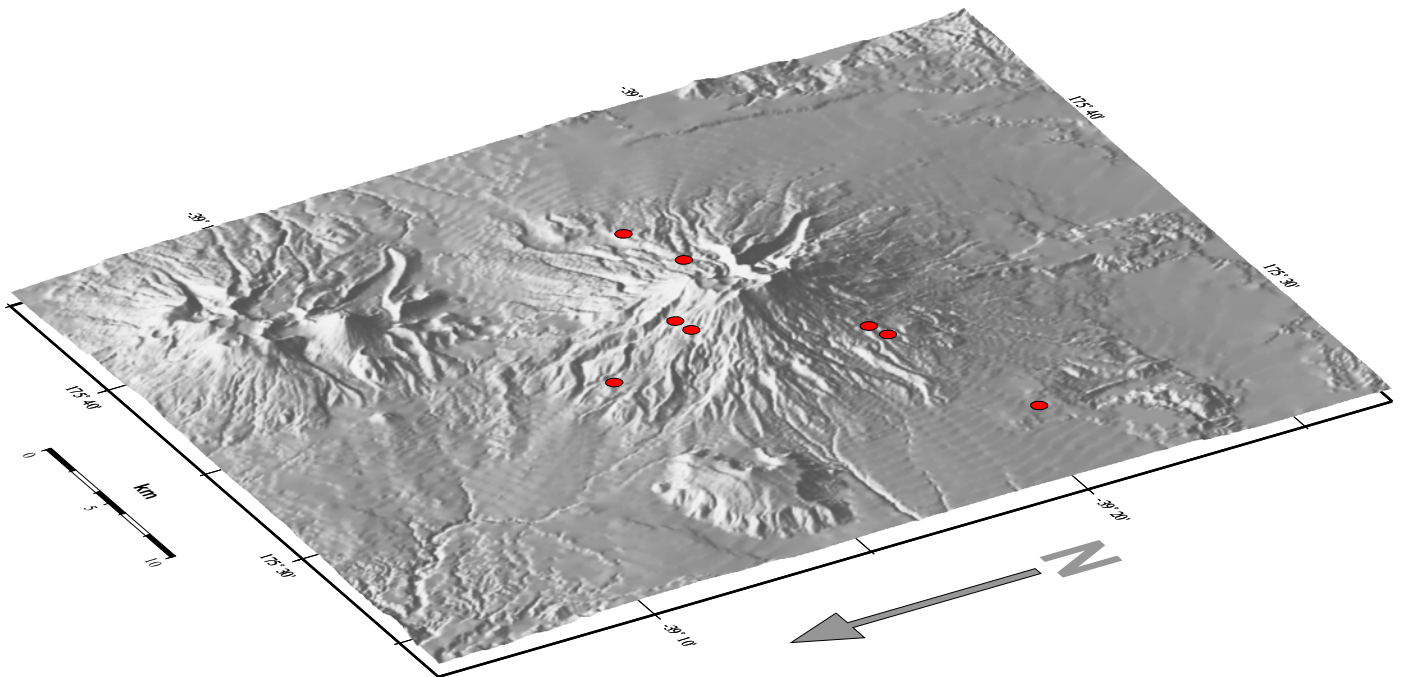


Figure 4.1 Real scale digital elevation model of Mt. Ruapehu with the CHARM stations shown in red

Station	Latitude	Longitude	Alt.	Serial #	Sensor	SENSOR #
FWVZ	-39.2564°	175.5518°	2000 m	Q-980306	CMG-40T	T4605
LHOR2	-39.3391°	175.4382°	1022 m	ORION 251	CMG-40T	T4788
LHUT2	-39.2542°	175.5606°	2066 m	ORION 253	CMG-40T	T4C49
LQUA2	-39.2216°	175.5403°	1364 m	ORION 252	CMG-40T	T41076
LTUR2	-39.3156°	175.5153°	1483 m	ORION 162	CMG-40T	T4431
TUKI2	-39.2795°	175.6097°	1746 m	ORION 177	CMG-40T	T4432
TUK2	-39.2725°	175.6458°	1525 m	ORION 177	CMG-40T	T4432
TURO2	-39.3122°	175.5241°	1571 m	ORION 178	CMG-40T	T4430
TUR2	-39.3125°	175.5235°	1565 m	ORION 178	CMG-40T	T4430

Table 4.1

Station locations and equipment of the CHARM project. Note that all station coordinates are given in the international lat/long geodetic system (Hayford 49).

4.1.1 Setup

In order to obtain the data for this experiment, six NANOMETRICS ORION digital seismograph recorders were deployed on Mt. Ruapehu in January 2002, with GURALP CMG-40T three component broadband sensors connected (see Figures 4.1-4.3). The power supply consisted of a 70 Watt solar panel and three to four 60 Amp-h batteries per station. Where possible, the sensors were placed on rock, protected by a plastic casing and several layers of insulation. The plastic case was then buried under a pile of rocks (TUKI2, TURO2). Where this was not possible, the sensors were placed in a pit in the ground, sitting on a concrete pad, protected by several layers of insulation and a plastic casing. These were then covered with at least 20 cm of soil as additional noise protection (LQUA2, LHUT2, LTUR2, LHOR2). A seventh station (FWVZ, the station formerly known as FWTB) is now permanently installed in the Whakapapa ski field area at the “Far West T-Bar” and is run by the Institute of Geological and Nuclear Sciences as part of the Eruption Detection System and the GEONET program (Sherburn and Bryan, 1999). It uses a QUANTERRA Q730-4G-CW data recorder, which is a 4 channel 24-bit diskless unit, running with a sampling rate of 40 Hz. The sensor is a Gralp CMG-40T three component, broadband seismometer which is enclosed in a concrete and polystyrene vault. The data from this station is telemetered via spread-spectrum radio to the Chateau Mountain Observatory and then sent via VSAT to IGNS at Gracefield and Wairakei. See Table 4.1 for exact station locations. Note that there are nine stations described in Table 4.1. The additional two stations were TUR2 and TUK2, which were deployed for one month and then relocated to TURO2 and TUKI2.

The CHARM stations were recording from January 2002 to July 2002 (for a detailed time chart, see Appendix B.2, figure B.3) with a sampling rate of 80 Hz. The data was stored on

2 GByte hard drives, which were swapped while servicing the stations every six weeks. A total number of 830 events in the proximity of Mt. Ruapehu were recorded (see Table 3.1 for selection criteria). The hypocentres of all available events, recorded by the IGNS/GEONET network during the time of the three deployments are shown in Figure 4.4.

The sensor orientation was adjusted with a magnetic compass, and then checked with a sun azimuth compass to detect possibly wrong declinations caused by magnetised volcanic rock. All but one of the obtained errors for the north components are under 6° , which is about the accuracy threshold for this method (for the individual values, see appendix table B.1). Pictures of the sensors in the ground together with a compass were taken to allow later verification of the correct sensor orientation. Also, a huddle test with all sensors and instruments was carried out prior to the deployment in order to ensure a correct sensor response and component orientation.

The recording units of the three VUW owned stations were placed in a lockable aluminium box and anchored to the ground. Attached to the boxes were the poles for the solar panels and GPS antennae (see Figure 4.2). The three IGNS owned instruments had a lighter setup which enabled them to be carried to more remote locations. The recording units were placed in an open A-frame construction, to which the solar panel and the GPS antenna was attached.

4.1.2 Relation to previous deployments

The aim of the CHARM project was to investigate the exact nature of the changes in anisotropy directions. Since the idea was to eliminate the possibilities of lateral inhomogeneities and site effects as cause of misinterpretation, it would have been ideal to reoccupy all the sites of the previous two deployments (1994 and 1998). However, availability of recording instruments and financial considerations restricted the number of CHARM stations to six, plus one now permanent station at the Far West T-Bar location (FWVZ). Since it is important to compare the results of the previous deployments to the current state, the most practical solution was to reoccupy the sites that delivered the most results. The name convention was chosen so that a reoccupied site would get the same name as before, with the number “2” added at the end. Only the former FWTB station is now called FWVZ as part of the GEONET programme.

Of the 1994 deployment, which originally had more than the five stations that are shown in the maps, only those five stations delivered usable shear wave splitting measurements. Two other stations were situated in the summit and crater area of Mt. Ruapehu, but the ambient noise level and the scattering of waves in the volcanic structure prevented any reasonable measurements. These two stations were not reoccupied in the CHARM deployment. Another 1994 station, at the Pukeonake scoria cone (LPUK), was also not reoccupied. Only six deep and one of the shallow events resulted in a usable splitting measurement. However, those six



Figure 4.2 *Field picture of LTUR2 station*

deep measurements lie within the trend of the others and do not show any surprising results, thus they are not very significant to the overall result. The other four stations of the 1994 deployment were reoccupied in the same spots (± 3 m) as before. At the stations LTUR and LHOR the sensors were probably even placed in the same pits as before.

All three stations of the 1998 deployment were reoccupied. At TURO2 and TUKI2 the sensors are placed on the same concrete platforms as during the previous deployments. Both concrete platforms sit directly on andesite rock. The third station, FWVZ is now placed on a concrete basement in a hut at the Far West T-Bar lift on Whakapapa ski field. Its relation to the old spot is not exactly known but is very likely not more than 10 metres away from the old spot.

The stations TUK2 and TUR2 were previously not occupied by broadband 3D instruments. They were only installed for one month, and were then relocated to TUKI2 and TURO2, respectively. The reason for this was that at the time of the deployment they were mistakenly installed at previous short-period sites. The distance between TUK2 and TUKI2 is 3.2 km, whereas the distance between TUR2 and TURO2 is only 50 m. Due to the close proximity of TUR2 and TURO2, which is negligible compared to the wavelength of the signal, the results of TUR2 were included in the results of TURO2 during the data processing.

However, the results of the two stations were compared before and combining them showed no significant differences in Φ or δt .

4.1.3 Equipment

The recording instruments were Canadian built NANOMETRICS ORION recorders (see table 4.1 for serial numbers) with the following recording parameters:

Model:	ORION-3S
Channel sensitivity:	~ 800 nV/Bit
Sample rate:	80 Hz
DC Filter:	none applied
Recording mode:	continuous
GPS duty cycle:	5 out of every 60 minutes
Disk capacity:	2 GigaByte

The sensor parameters were the following:

Sensor Model:	Güralp CMG-40T
No. of components:	3
Velocity Output:	VUW Sensors (T4431, T4432, T4433): $\sim 2 \times 1600$ V/m/s IGNS Sensors (T4788, T41076, T4C49): $\sim 2 \times 400$ V/m/s
Norm factor at 1 Hz:	VUW: -0.314 IGNS: -0.346
Poles:	VUW: $-23.56 \cdot 10^{-3} \pm i23.56 \cdot 10^{-3}$ Hz; -50 Hz IGNS: $-11.78 \cdot 10^{-3} \pm i11.78 \cdot 10^{-3}$ Hz; -48.4 Hz
Zeros:	VUW: 0 Hz; 0Hz; 159 Hz IGNS: 0 Hz; 0Hz; 140 Hz

4.1.4 Logistics

Since many of the sites are located in remote areas, the stations had to be portable. The IGNS owned A-frame constructions were especially suitable for these areas. Access to the LHUT2 site was only possible by foot, since it is situated in the Whakapapa ski field. The altitude difference between the closest possible road and the station is 750 m, but a chairlift could be used during good weather to transport equipment to a point 1 km away from the station and about 100 m lower in altitude. Special backpacks for carrying the 100 Amp-h truck batteries were used and are highly recommended for future deployments. This site is situated on a ridge and was covered with about 1.5 m of snow and solid ice in the winter.

Abnormal weather conditions delayed the removal of the instrument for about 6 months into the summer of 2002/2003.

Several other sites required access via roads that are only usable by four wheel driven vehicles. TUKI2 is situated in the Tukino ski field, which is only accessible in low snow conditions during the autumn and winter months. 4WD and snow chains are required.

LHOR2 is situated on a forest clearing close to the Makotuku river, which has to be crossed by foot in order to access the station. After heavy rain and during the spring time the river becomes unpassable, so the station is not accessible during this time. Also, the road to the site crosses the private property of a farm and permission to enter the property had to be obtained.

The stations LQUA2, LTUR2 and TUKI2 are all in the vicinity of roads, so the equipment had to be carried for only a few hundred metres. In these cases, the heavier and sturdier VUW stations were used, which provide a better protection against theft and vandalism with their lockable aluminium box.

Since all the stations are located in the Tongariro National Park, a permit from the New Zealand Department of Conservation (DOC) to install the stations in the field was obtained prior to the deployment. This permit specified the exact location, setup and deployment time for each station.

Two field teams of two to three people each were involved in the installation and the removal of the stations. Six - weekly service runs were usually carried out by a team of two, sometimes by a single person. The base for all operations was the IGNS volcano observatory hut in Whakapapa village.

4.2 Information about previous deployments at Mt. Ruapehu

4.2.1 The 1994 deployment

The deployment in 1994 was conducted by Leeds University, the University of Memphis and the New Zealand Institute of Geological and Nuclear Sciences (IGNS). 14 broadband 3D seismographs were installed around the Tongariro National Park and Mt. Ruapehu between 28 January and 13 March 1994 (Hurst, 1998). The recorders were 9 Lennartz MARS-88 dataloggers and 5 REFTEK systems, provided by Jer-Ming Chiu from the IRIS PASSCAL pool. All stations were equipped with Gralp CMG3 sensors and operated with a sampling rate of 62.5 Hz. The REFTEK sets were stationed further away from the mountain but did not produce valuable data in most of the cases (Hurst, pers. comm.). Also, the stations located close to the summit and crater lake on Mt. Ruapehu did not produce valuable S-wave splitting measurements (Miller, 2000).

The data that was used is shown in Chapter 5, the station locations are described in Table 4.2 and plotted in Figure 4.3. During the time of this deployment, a total number of 272 earthquakes were recorded by the IGNS network, and their locations determined using CUSP (Caltech-USGS Seismic Processor) (Maunder, 1999). These earthquakes produced 99 splitting measurements (note that most earthquakes produce measurements at more than one station).

Station	Latitude	Longitude	Alt.
LHOR	-39.3391°	175.4382°	1022 m
LHUT	-39.2542°	175.5606°	2066 m
LQUA	-39.2216°	175.5403°	1364 m
LTUR	-39.3156°	175.5153°	1483 m
LPUK	-39.1408°	175.5526°	1010 m

Table 4.2

Station locations and equipment of the 1994 deployment.

4.2.2 The 1998 deployment

This deployment was also conducted by Leeds University (Neuberg et al., pers. comm.) between February and July 1998. Three Lennartz MARS-88 dataloggers were installed with Gralp CMG3 3D broadband seismometers with a sampling rate of 62.5 Hz at station locations specified in Table 4.3. A map with station locations is shown in

Station	Latitude	Longitude	Alt.
FWVZ	-39.2564°	175.5518°	2000 m
TUKI	-39.2795°	175.6097°	1746 m
TURO	-39.3122°	175.5241°	1571 m

Table 4.3

Station locations and equipment of the 1998 deployment.

Figure 4.3. During the time of this deployment, a total number of 997 earthquakes were recorded and located by the IGNS network, which produced 126 splitting measurements.

To confirm a correct sensor orientation for the 1994 and 1998 deployments, the components of each sensor were individually checked by comparing the first motion of arriving P-waves with the expected first motion for a certain back azimuth of the incoming wave (results shown in Miller, 2000, Appendix A). In all cases the observed first motion matched the expected one. Thus it is ruled out that the sensor orientations were substantially wrong, or that internal components of the sensors had a switched polarity. For an illustration of this method, see Appendix B.3.1.

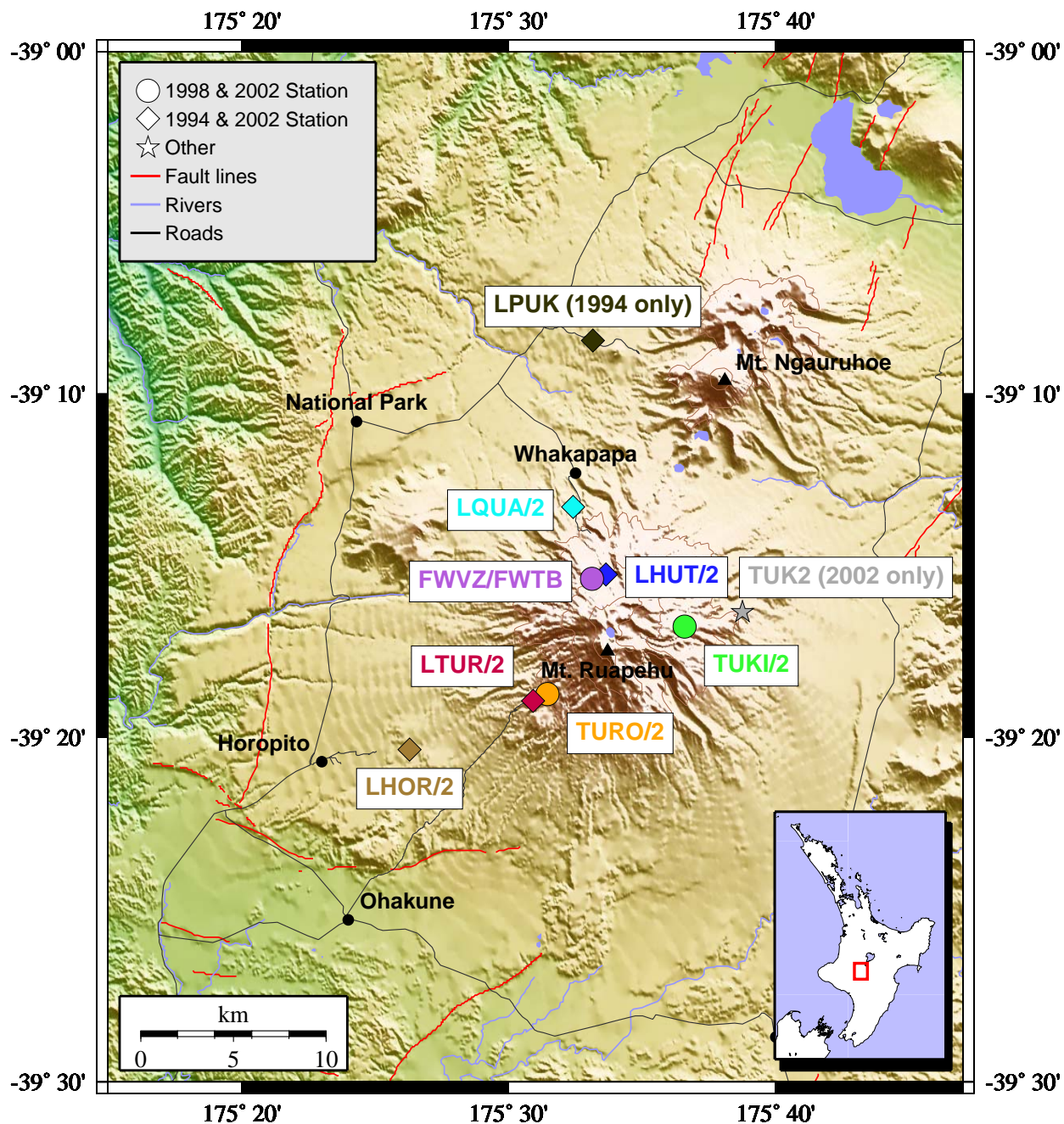


Figure 4.3 Station locations of all deployments. Circular outlines show stations that were deployed in 1998 and 2002. Diamond shaped outlines show stations that were deployed in 1994 and 2002. The station LPUK was only deployed in 1994, the station TUK2 recorded only in 2002. Note the predominant NE-SW alignment of fault lines (mostly normal faults; shown in red).

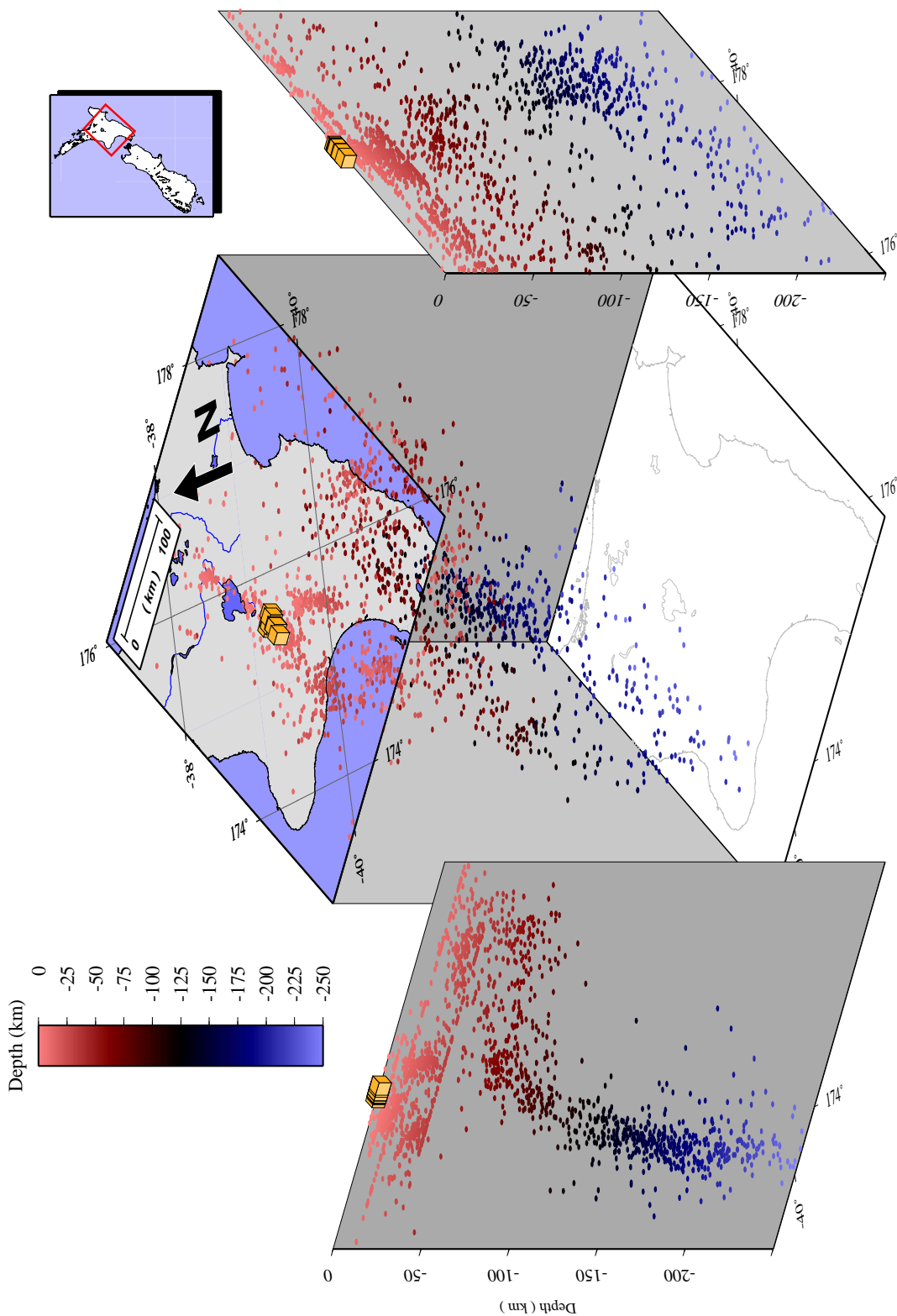


Figure 4.4 A 3D perspective view of the North Island with all earthquakes sources that were available in the three deployments. Coloured dots are plotted at the hypocentres of all earthquakes. The colours indicate the depth of the hypocentre. It is clearly visible that the deep earthquakes follow the shape of the subducting pacific plate under the North Island (left). All station locations and their projections are marked by yellow cubes. The depth of this model is 250 km and is not vertically exaggerated. For a figure with all EQ that were actually used in the data processing, see Figure 5.14 on page 90.

CHAPTER 5

RESULTS

This chapter will report the results of the three deployments at Mt. Ruapehu. In the first part, an overview of all measurements will be given in the form of maps and tables. In the second part, detailed investigations for dependencies on different parameters will be carried out.

5.1 General results of the deployments

The aim of this project is to investigate changes in the fast directions between the three deployments at Mt. Ruapehu. In order to achieve an unambiguous result, a high data quality is necessary. Therefore only results with the highest quality marks are included in the following results. Generally, the obtained splitting parameters are divided into shallow (i.e. crustal) events with a depth < 35 km, and deep events (originating from the subducting slab) with a depth > 55 km. It was found that events in these “subsets” show similar splitting parameters and are therefore often treated as a group*. In several cases, however, the results from different stations behave differently, and the stations have to be distinguished. There are very few earthquakes between 35 km and 55 km depth, and their behaviour is somewhat in between the shallow and the deep earthquakes. These few events are not included in the map results, but are shown in all figures of Section 5.3.

Only events within a slope corrected shear wave window of 35° to the normal vector at the slope were included. For obtaining a high data quality, a surface S-wave speed of 1.6 km/s was assumed. This is a significantly higher speed than was proposed for the surface material at Mt. Ruapehu (Section 1.3.3), therefore the shear wave window criterion is more conservative than with a lower surface S-wave speed (Section 2.1.7). The difference in the results between using a slope corrected shear wave window and a conventional shear wave window was found to be minor in this study. The results were also stable with respect to changing the width of the window in either direction.

*These groups of shallow and deep earthquakes of the different deployments are from now on referred to as shallow and deep *subsets*.

Since the data quality in the 2002 deployment was very high, measurements of A, AB and B quality are included in the results. The data quality in 1998 was not as high as in 2002, and B-quality events are often ambiguous. Therefore, only A and AB quality events are included in both shallow and deep subsets. In 1994, shallow events were not reprocessed, and the same events as in the previous study (Miller, 2000) were included. These had qualities of A and AB. Deep events from 1994 were reprocessed, and a high data quality was found, which allowed the inclusion of A, AB and B quality events. Generally, it was found that including C quality events increases the scatter in the data, but does not affect the overall trends.

Different frequency filters were applied to the data in order to maximise the signal to noise ratio, and the most successful filter was chosen for the measurement. In some cases, two separate frequency filters (i.e. 0.1-1 Hz and 3-10 Hz) that were applied to the same event on a certain station resulted in significantly different wavelet shapes, which both led to valid measurements. In these cases both measurements were included in the results, which effectively means that the event acquires a double weight. The reason for this practice is that when different fast directions were obtained, none of them should be favoured over the other. When the two fast directions are similar despite their different waveform, then it can be assumed that the measured fast direction has a low error and is not influenced by noise. In this case, a double weight enhances the data quality. Therefore it can be argued that this practice is the most objective way of handling different frequency filters. However, one might also argue that introducing weighted data is not objective by itself. Therefore, Appendix B shows the same data as presented in this chapter, but with only one measurement per station and event included (similar to Figures 5.2 to 5.4, and 5.5). The chosen measurement was always the one with the highest quality; in the case of two measurements with the same quality the choice was randomly made by the computer. It is clear that no significant differences to the data with multiple filters are present.

Table 5.1 shows the results, grouped for different stations. Shallow and deep events are shown separately, and a summary for all stations of each deployment is also included. The measured splitting parameters are:

1. Mean fast direction ($\overline{\Phi}$).
2. Standard error s_e of the mean fast direction ($\pm\overline{\Phi}$).
3. Standard deviation s_0 of the fast directions ($\pm\Phi$).
4. Mean delay time ($\overline{\delta t}$).
5. Standard deviation of the delay times ($\pm\delta t$).
6. Mean wavelet main frequency (\overline{f}).
7. Standard deviation of the main frequencies ($\pm f$).
8. Number of contributing measurements (#)

Year/Station/Depth	$\bar{\Phi}$ [°]	$\pm\bar{\Phi}$ [°]	$\pm\Phi$ [°]	$\bar{\delta t}$ [s]	$\pm\delta t$ (s)	\bar{f} [Hz]	$\pm f$ [Hz]	#
94 ALL shallow	-28.3	3.9	23.3	0.108	0.060	N/A	N/A	36
94 ALL deep	-42.8	3.6	22.3	0.231	0.129	2.48	0.86	37
98 ALL shallow	13.4	5.8	33.0	0.113	0.058	3.82	1.40	39
98 ALL deep	37.4	7.5	28.9	0.118	0.063	N/A	N/A	16
02 ALL shallow	-30.0	2.4	26.2	0.107	0.053	4.10	1.91	123
02 ALL deep	19.2	2.7	28.6	0.272	0.175	2.44	1.33	117
94 LHOR shallow	-14.5	11.4	29.1	0.076	0.048	N/A	N/A	7
94 LHOR deep	-41.0	3.4	14.0	0.258	0.121	2.69	0.76	17
94 LHUT shallow	-40.6	10.7	27.7	0.076	0.026	N/A	N/A	7
94 LHUT deep	-74.9	13.5	23.6	0.213	0.080	2.05	0.21	3
94 LPUK shallow	8.0	N/A	N/A	0.080	N/A	N/A	N/A	1
94 LPUK deep	-48.1	8.1	20.0	0.175	0.127	2.01	0.54	6
94 LQUA shallow	-35.1	6.2	17.9	0.109	0.041	N/A	N/A	8
94 LQUA deep	-11.1	19.1	34.0	0.315	0.133	2.17	1.12	4
94 LTUR shallow	-27.1	3.9	14.3	0.143	0.070	N/A	N/A	13
94 LTUR deep	-42.4	6.3	17.0	0.174	0.120	2.70	1.02	7
98 FWTB shallow	-7.1	12.1	37.5	0.117	0.065	3.59	1.27	14
98 FWTB deep	38.0	17.6	34.6	0.094	0.020	N/A	N/A	5
98 TUKI shallow	42.2	15.8	26.9	0.133	0.021	2.06	0.55	3
98 TUKI deep	46.4	9.8	24.1	0.117	0.060	N/A	N/A	6
98 TURO shallow	17.8	5.5	25.5	0.107	0.056	4.21	1.33	22
98 TURO deep	26.0	10.9	24.3	0.144	0.083	N/A	N/A	5
02 FWVZ shallow	-8.3	10.2	29.4	0.090	0.030	3.35	1.16	9
02 FWVZ deep	39.5	8.7	29.1	0.305	0.182	2.12	0.55	12
02 LHOR2 shallow	-14.1	5.4	26.3	0.150	0.042	3.91	1.80	24
02 LHOR2 deep	-5.3	6.8	28.7	0.224	0.104	2.94	1.42	19
02 LHUT2 shallow	-45.4	3.0	16.9	0.075	0.038	5.27	1.57	31
02 LHUT2 deep	37.8	9.2	33.9	0.240	0.209	3.03	1.27	17
02 LQUA2 shallow	-24.9	4.0	17.8	0.110	0.030	3.29	1.26	19
02 LQUA2 deep	24.5	3.2	11.2	0.367	0.152	1.36	0.71	12
02 LTUR2 shallow	-17.9	3.7	12.3	0.122	0.054	2.83	0.27	11
02 LTUR2 deep	7.4	5.8	25.6	0.252	0.077	2.24	0.95	20
02 TUK2 shallow	10.0	13.8	19.8	0.140	0.030	1.97	0.95	2
02 TUK2 deep	-8.5	5.3	7.5	0.200	0.060	1.59	0.24	2
02 TUKI2 shallow	-73.1	7.7	23.2	0.112	0.080	4.16	3.31	9
02 TUKI2 deep	33.4	6.0	20.1	0.392	0.243	2.15	1.10	11
02 TURO2 shallow	-31.1	3.3	14.0	0.095	0.057	4.58	1.78	18
02 TURO2 deep	18.7	3.7	18.3	0.237	0.181	2.69	1.69	24

Table 5.1

Results of individual stations and deployments. Shallow events have a source depth of < 35 km, deep events have a source depth of > 55 km. $\bar{\Phi}$ is the mean fast direction; $\pm\bar{\Phi}$ is the standard error of the mean fast direction (s_e), whereas $\pm\Phi$ is the standard deviation of the fast directions (s_0). $\bar{\delta t}$ and $\pm\delta t$ are the mean delay time and the standard deviation of the delay times. \bar{f} and $\pm f$ are the mean frequency of the wavelet and the standard deviation of the frequencies. # shows the respective number of measurements. Note that the datasets 1994-shallow and 1998-deep were not reprocessed, so no frequency measurements were obtained for these datasets.

A list of all individual measurements with A, AB, B and C marks of all three deployments is given in Appendix C.

When considering only the total results of the different subsets (Table 5.1, top part), it is clear that the fast directions vary substantially between the three deployments (Figure 5.1). In 1994, both shallow and deep events show fast directions strongly aligned in NW-SE direction. In 1998, shallow events show considerable scatter, with a mean fast direction of about NNE-SSW. The fast directions of the deep 1998 events are much more aligned, and point in a NE-SW direction, which is 80° from the deep 1994 fast directions (however, station locations in 1994 and 1998 were different). In the 2002 dataset, shallow and deep events yield different fast directions. The deep 2002 events have a fast direction that is aligned in a NNE-SSW direction, similar to the 1998 deep results. The shallow 2002 events however, have a mean fast direction that is aligned in a NNW-SSE direction, similar to the 1994 shallow events. The station locations in 2002 include both 1994 and 1998 stations.

Figures 5.2 to 5.4 show the individual splitting measurements plotted as bars in a map, where the direction of the bar points in the fast direction of this measurement, and its length is in scale with the delay time. For visual reasons, the splitting bars were plotted where a straight line between source and receiver intersects 5 km depth (for shallow events) and 10 km depth (for deep events). In all three deployments, the strong alignment of fast directions is visible, with the exception of the 1998 shallow fast directions, that seem to align in two distinct directions and also show scatter. In the 2002 results (Figure 5.4), stations that were previously installed in 1994 do not yield significantly different results from stations that were installed in 1998 (e.g. TURO2 and LTUR2).

The behaviour of fast directions from different stations was also investigated, and a station-histogram was plotted for each station (Figure 5.5, see also large foldout at end of thesis). In 1994, fast directions of all stations are subparallel, although some stations represent merely one to three measurements. In the shallow 1994 subset, station LHOR yields fast directions that are slightly more oriented towards North than the others.

In 1998, the FWTB station is mainly responsible for the large scatter in the shallow data. Figure 5.6 b shows this subset again, but only events with a main frequency under 3.5 Hz were included. Also, a set with low frequency events inside a 30° shear wave window is shown (Figure 5.6 c). This causes the fast directions to show a stronger alignment in a NNE-SSW direction (see also Table 5.2). The deep 1998 events do not show as much scatter as the shallow events, possibly because the incidence angles of the deep events are generally steeper, and therefore further inside the shear wave window.

In the 2002 deep subset, most stations yield subparallel fast directions, with the exception of LHOR2 and TUK2. These two stations show mean fast directions that are oriented slightly more towards North than the others (similar to the behaviour of LHOR in the shallow 1994

Year/Station/Depth	$\bar{\Phi}$ [°]	$\pm\bar{\Phi}$ [°]	$\pm\Phi$ [°]	$\bar{\delta t}$ [s]	$\pm\delta t$ (s)	\bar{f} [Hz]	$\pm f$ [Hz]	#
98 ALL shallow	13.4	5.8	33.0	0.113	0.058	3.82	1.40	39
98 ALL shallow L	13.4	6.6	27.6	0.125	0.057	2.56	0.57	18
98 ALL shallow LN	20.8	6.0	23.2	0.114	0.053	2.47	0.56	15
02 ALL shallow	-30.0	2.4	26.2	0.107	0.053	4.10	1.91	123
02 ALL shallow L	-26.5	3.5	26.7	0.123	0.053	2.60	0.55	61
98 FWTB shallow	-7.1	12.1	37.5	0.117	0.065	3.59	1.27	14
98 FWTB shallow L	7.4	7.9	21.3	0.153	0.059	2.50	0.53	7
98 FWTB shallow LN	17.8	5.5	12.3	0.150	0.068	2.38	0.56	5
02 FWVZ shallow	-8.3	10.2	29.4	0.090	0.030	3.35	1.16	9
02 FWVZ shallow L	-26.6	11.8	26.2	0.110	0.024	2.49	0.54	5

Table 5.2

Special results of the 1998 and 2002 shallow data. For the 1998 and 2002 shallow results, only events with main frequencies lower than 3.5 Hz were included (marked as L). In addition to this, the 1998 shallow events are shown with only events inside a narrow (30°) shear wave window and with frequencies lower than 3.5 Hz included (marked as LN). A significant change in the fast directions is visible, especially at FWTB/FWVZ. However, choosing a narrow shear wave angle in 2002 had no significant effect on the fast directions (not shown). Generally, all other subsets and stations did not show any significant changes with respect to changing the selection criteria (not shown).

data). Again, there is a strong consistency of fast directions between stations that had also been installed in 1994 and stations that had also been installed in 1998.

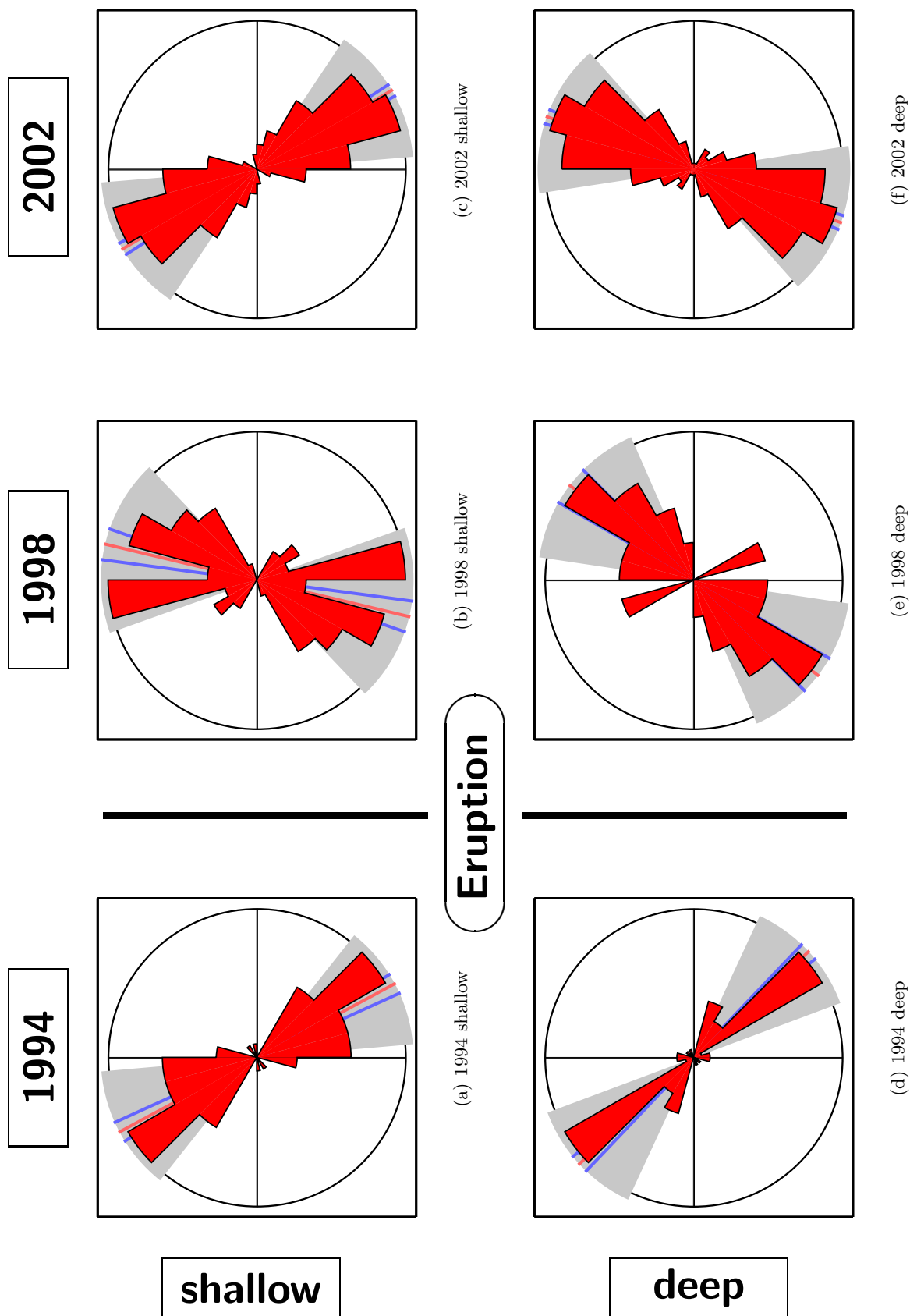


Figure 5.1 Overview of the splitting results: Combined results. The fast direction of the shallow events is aligned NNW-SSE in 1994 (a), scatters in 1998 (b), and is realigned in 2002 (c). The fast direction of the deep events in 1994 (d) shows the same orientation as the fast direction of the shallow 1994 events; in 1998 (e) it is different by almost 90° from the 1994 deep fast direction. The orientation of deep fast directions in 2002 (f) is only slightly different from the orientation measured in 1998.

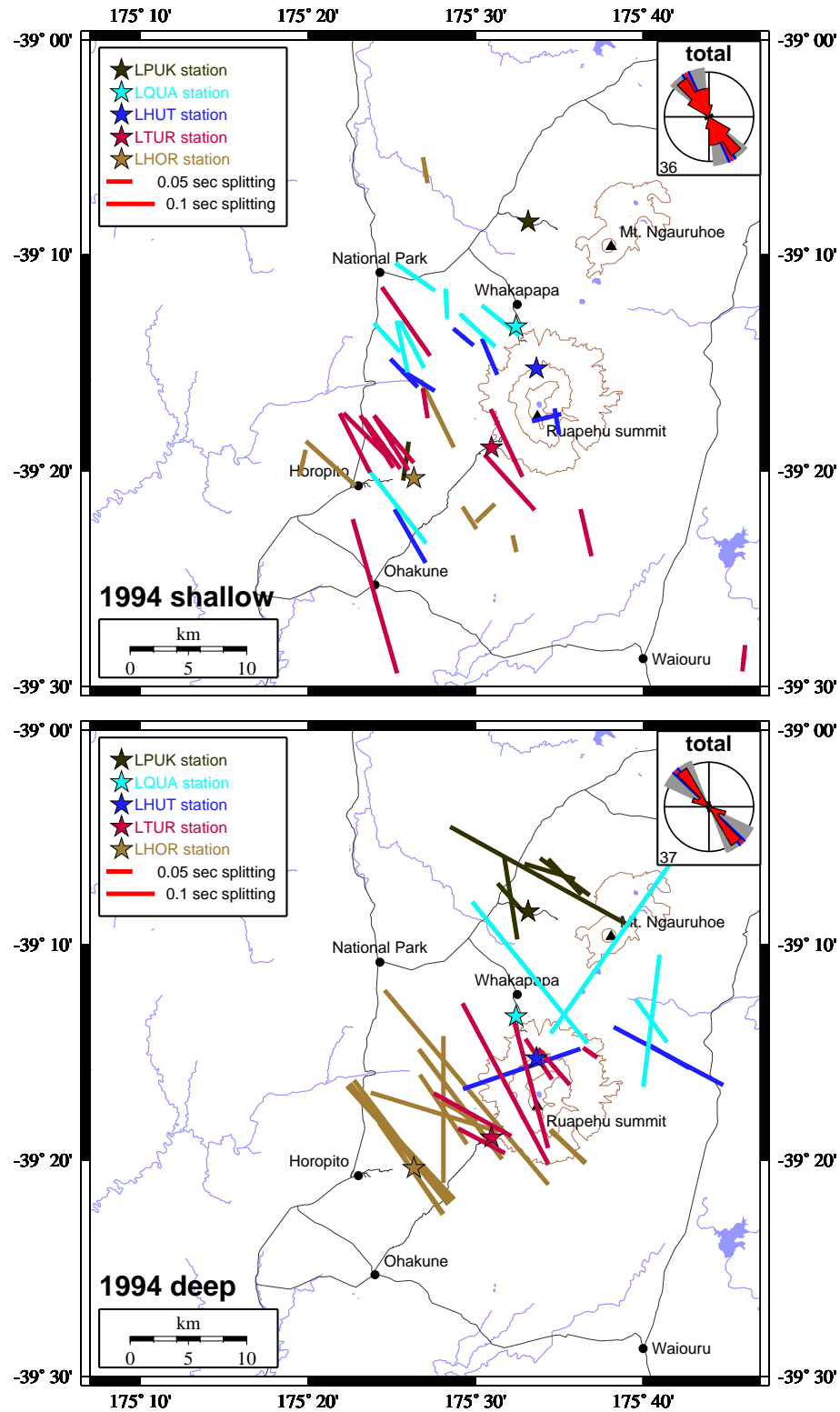


Figure 5.2 Map of individual splitting results, 1994. Top: shallow earthquakes, bottom: deep earthquakes. The splitting bars are scaled in length to their delay time and are plotted at a point where a straight line between source and receiver intersects 5 km (shallow) and 10 km (deep) depth. The histogram in the corner shows the total distribution of measurements for each plot, as well as the total number of measurements. Note the strong NNW-SSE alignment of fast directions for both shallow and deep events.

Changes between 1994 and 2002

From Figure 5.5, it is clear that the stations LQUA, LHUT, LTUR and LHOR in the 1994 shallow subset show subparallel fast directions to the respective stations in the 2002 shallow dataset (LQUA2, LHUT2, LTUR2 and LHOR2). However, the fast directions of the deep events in 1994 are significantly different from the fast directions of the deep 2002 events at the corresponding stations. Station LQUA shows a 36° change, LHUT changes by around 70° , although only 3 and 4 measurements respectively were obtained in 1994, which means that these values do not have a high statistical significance. Station LTUR changed by 50° , station LHOR only by 35° . These two stations have 7 and 17 measurements respectively in 1994, and the numbers are therefore more significant.

In total, the fast direction of the 2002 deep subset is different from the fast direction of the 1994 deep subset by 62° . The 99.9% confidence intervals of the mean fast directions of these two subsets do not overlap ($Z_{99.9\%} = 3.29$, i.e. the 99.9% confidence interval is an interval around $\bar{\Phi}$ with a width of $\pm 3.29 \cdot s_e$). Therefore, the hypothesis that the two subsets have the same fast direction can be rejected with a statistical significance of more than 99.9% (e.g. Davis, 1986).

The shallow fast directions changed by only 1.7° between 1994 and 2002. This change is not statistically significant ($< 50\%$).

Changes between 1998 and 2002

All three stations that recorded deep events in 1998 show subparallel fast directions to the deep 2002 events, i.e. the standard error bars overlap. Shallow events, however, have different fast directions. Station TUKI changed by 65° , and station TURO changed by 49° . Station FWVZ, which is located at the same place as FWTB in 1998, shows strong scatter in the 2002 shallow data. However, this scatter only seems to be present at high frequencies, and disappears when only measurements with a main frequency under 3.5 Hz are included (Figure 5.6 a and Table 5.2). Without these special selection criteria, the fast directions of the shallow events at FWTB/FWVZ are scattered, and no significant change between 1998 and 2002 can be seen. When selecting only frequencies below 3.5 Hz, then the fast directions from 1998 and 2002 at this station are different by 34° . In addition to this, the fast directions of FWVZ in 2002 then become subparallel to the fast directions at the station LHUT2 at a distance of 1 km. At frequencies under 3.5 Hz, the Fresnel zones of rays travelling to FWVZ and LHUT2 overlap, therefore similar results are expected. However, at frequencies higher than 3.5 Hz, an assumed local heterogeneity under the FWVZ station alters the results significantly. No other subsets and stations show any significant changes when specifying these or other selection criteria, so it can be considered a local effect at the station FWTB/FWVZ.

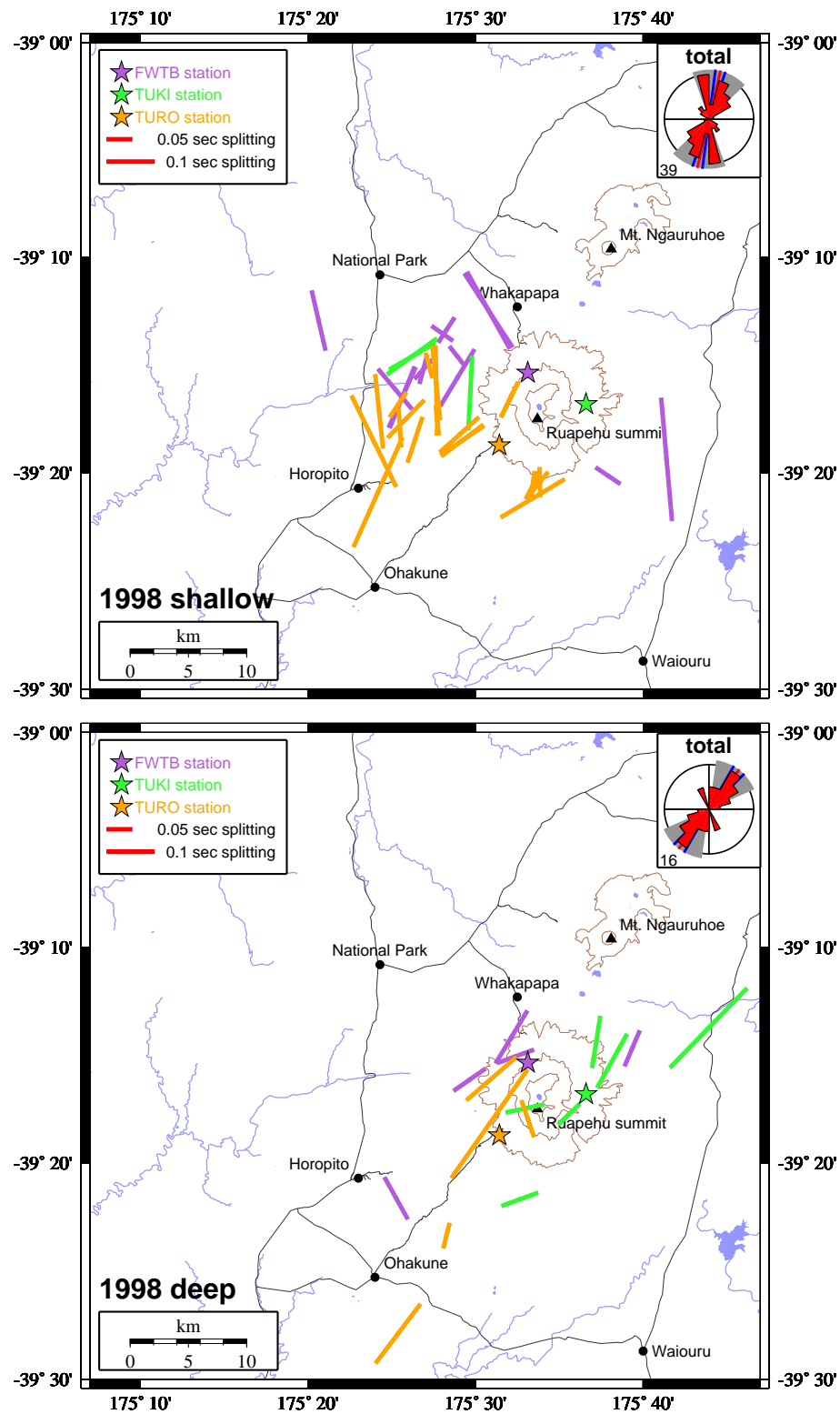


Figure 5.3 Map of individual splitting results, 1998. Top: shallow earthquakes, bottom: deep earthquakes. For a description of the annotation scheme, see Figure 5.2.

The alignment of the deep events is now NE-SW, while the shallow events show a more random pattern with a slight tendency to NE-SW.

In summary, the fast direction of the 2002 shallow subset is different from the fast direction of the 1998 shallow subset by 43.4° . The statistical significance (as explained above) is larger than 99.9%. When choosing frequencies under 3.5 Hz, the difference is 39.9° with the same confidence level.

The deep fast directions changed by 18.2° between 1998 and 2002. The hypothesis that no change occurred can be rejected with a confidence level of $\approx 90\%$.

Changes between 1994 and 1998

Assuming that station, frequency, and back azimuthal effects are not responsible for the difference in the fast directions, the shallow fast direction changed by 41.7° between 1994 and 1998, with a confidence level of $>99.9\%$.

The deep fast directions changed by 80° between 1994 and 1998, with a confidence level of $>99.9\%$. When choosing a specific statistical significance, the error boundaries of this change can be given. For example, with a confidence of at least 95%, this change of fast direction was between 58° and 102° .

NULL measurements

NULL measurements were obtained in 2002 and in the reprocessed datasets, i.e. the 1994 deep events and the 1998 shallow events. Records from NULL measurements from the old processing are not available. Figures 5.7 and 5.8 show these NULL measurements from 1998 and 2002. Since a fast direction that is obtained by a NULL measurement is ambiguous by 90° , not only one, but two bars are plotted for each measurement, pointing in perpendicular directions and resembling a cross (see Section 3.2.3). A strong alignment of these crosses in NE-SW/NW-SE direction can be seen both in 1998 and 2002.

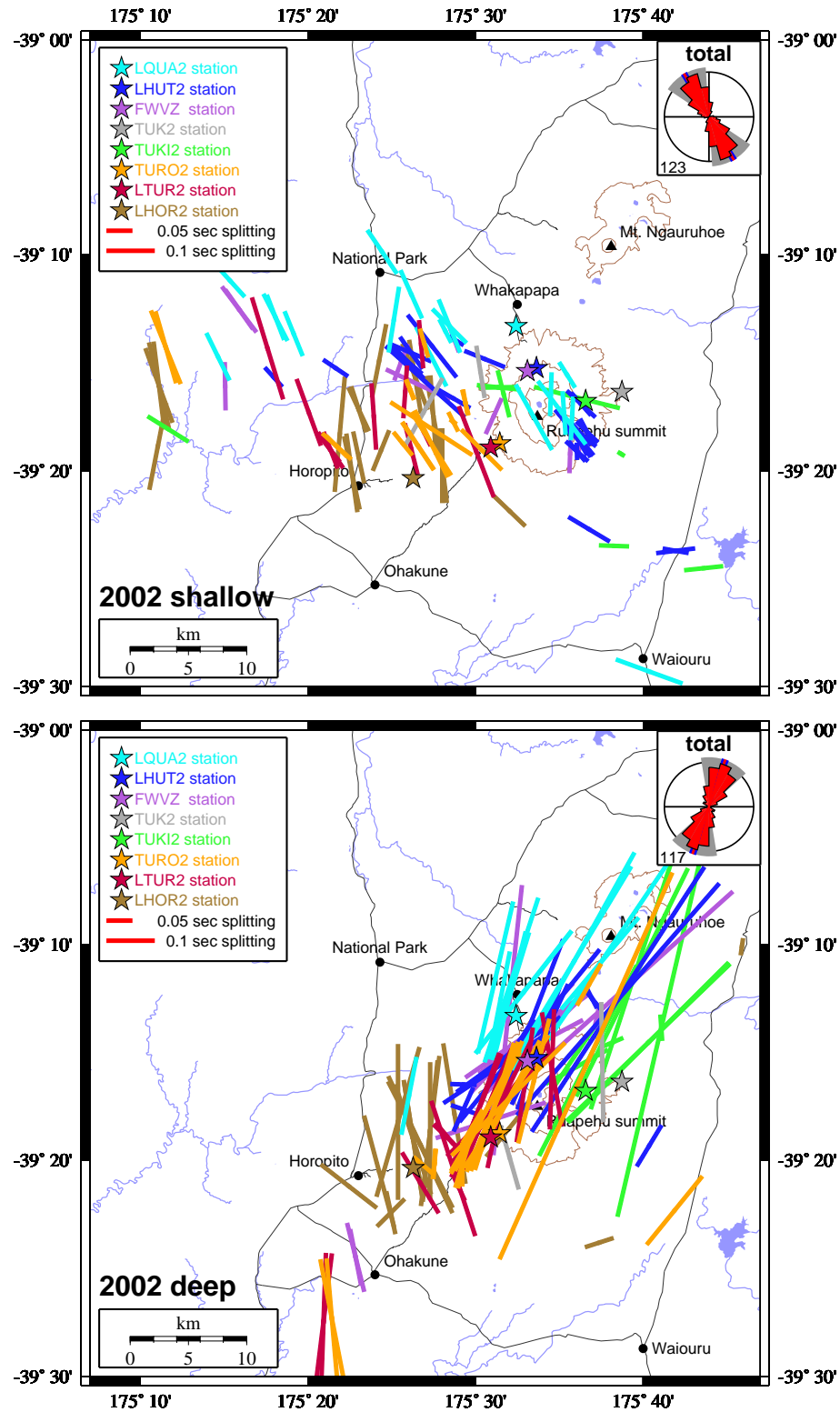


Figure 5.4 Map of individual splitting results, CHARM 2002. Top: shallow earthquakes, bottom: deep earthquakes. For a description of the annotation scheme, see Figure 5.2.

Note that the alignment of the deep events is similar to 1998, and the alignment of the shallow events is NNW-SSE again (similar to 1994). The figures are plotted in a way that the changes become obvious when flipping through the last two pages in quick succession

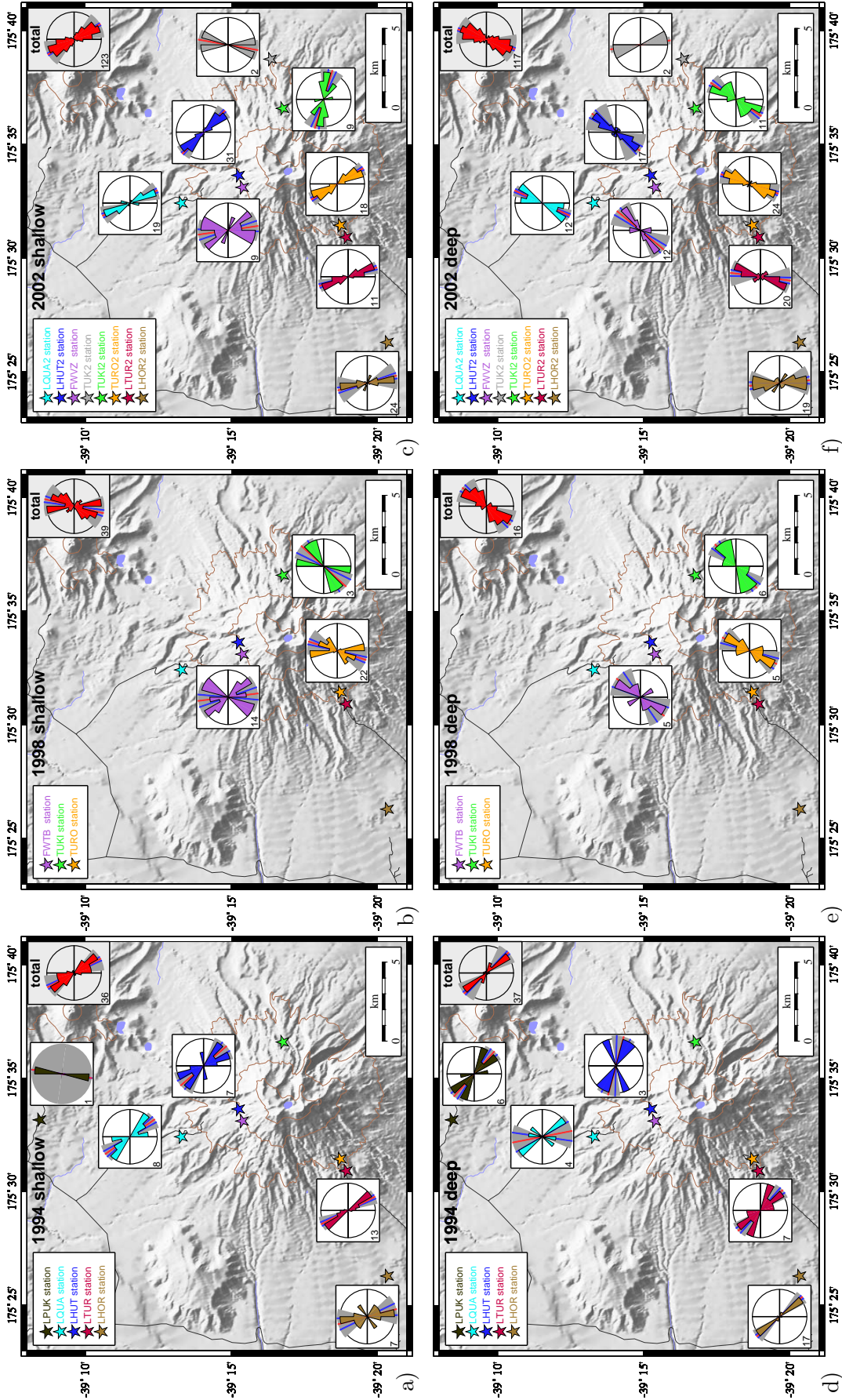


Figure 5.5 Overview of the splitting results. The histograms visualise the number of measurements in every 15° angle segment of the fast direction for each station. In each histogram, the underlying grey area shows the standard deviation of the fast directions, the red bar shows the mean fast direction, the blue bar shows the standard deviation of the mean fast direction (= std. error). The numbers in the corner of the histograms show the number of measurements that were taken into account. **This figure is printed as a large fold out map on the last page of this thesis for better reference.**

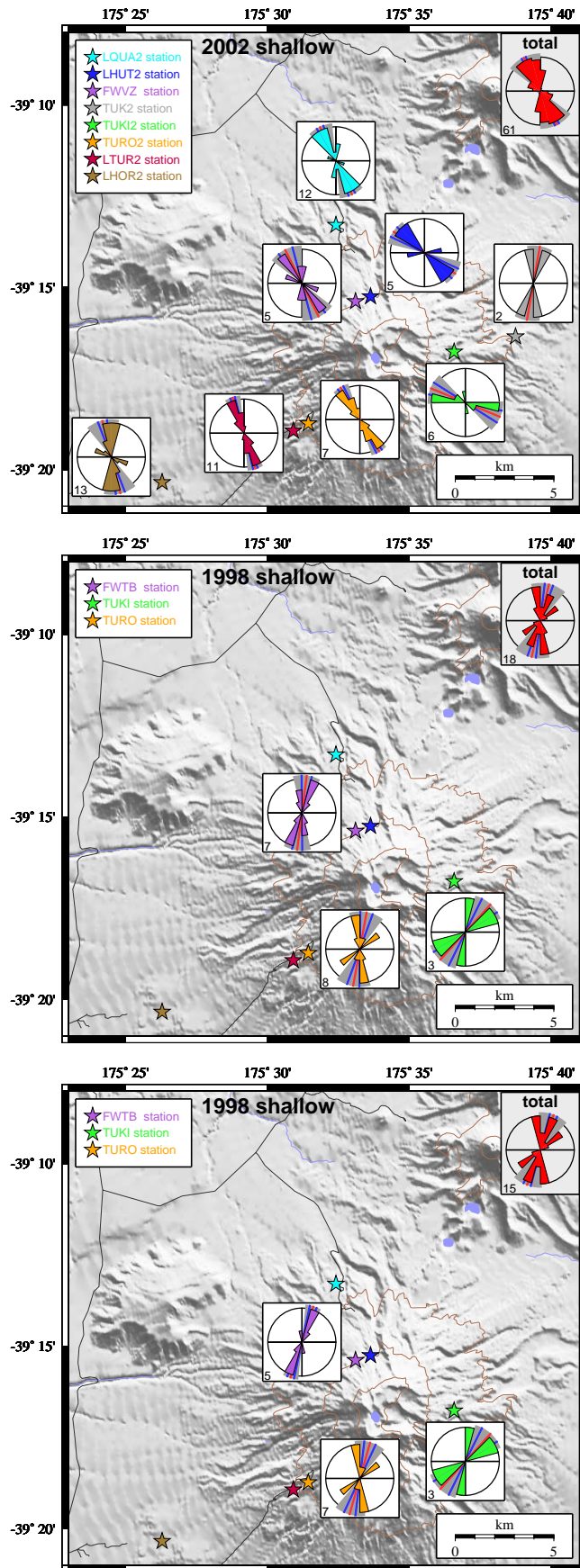


Figure 5.6 Shallow events from 1998 and 2002 with special data selection criteria

a) 2002 shallow, frequencies <3.5 Hz:

In this plot, only events with a main frequency (the frequency of the split wavelet) under 3.5 Hz were included. This strongly alters the mean direction of the FWVZ station, which is then similar to the other stations, and especially to the LHUT2 station at a distance of only 1 km. None of the other stations show significant changes. Selecting events from a narrower shear wave window does not significantly affect the results (not shown).

b) 1998 shallow, frequencies <3.5 Hz:

This plot shows the shallow 1998 data, with the same selection criteria as a). It is visible that after selecting only events with a frequency under 3.5 Hz, the remaining events show a stronger NE-SW trend. This effect is strongest at FWVB, with a fast direction now similar to the 1998 deep events (see Figure 5.5 or fold-out map).

c) 1998 shallow, narrow S-wave window:

This plot shows the shallow 1998 data again, but only events with frequencies <3.5 Hz in a narrow shear wave window were selected, i.e. with an angle of incidence < 30°. In comparison with b), an even stronger alignment of the FWVB fast directions into NE-SW direction is visible.

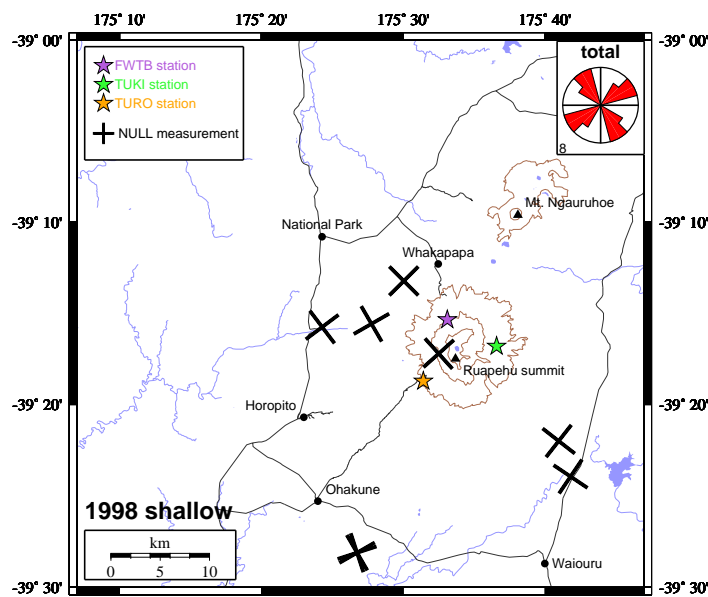


Figure 5.7 Map of obtained NULL measurements for the shallow 1998 measurements. The bars are oriented in (and perpendicular to) the direction of the initial polarisation. Therefore they represent a fast direction which is ambiguous by 90° . The bars are plotted at a point where a straight line between source and receiver intersects 5 km (shallow) and 10 km (deep) depth. The histogram in the corner shows the total distribution of NULL measurements for each plot. If there were no common fast direction present, the histogram would be expected to show a random pattern of directions. However, the clear alignment suggests that a relatively uniform fast direction is present in the area around the stations.

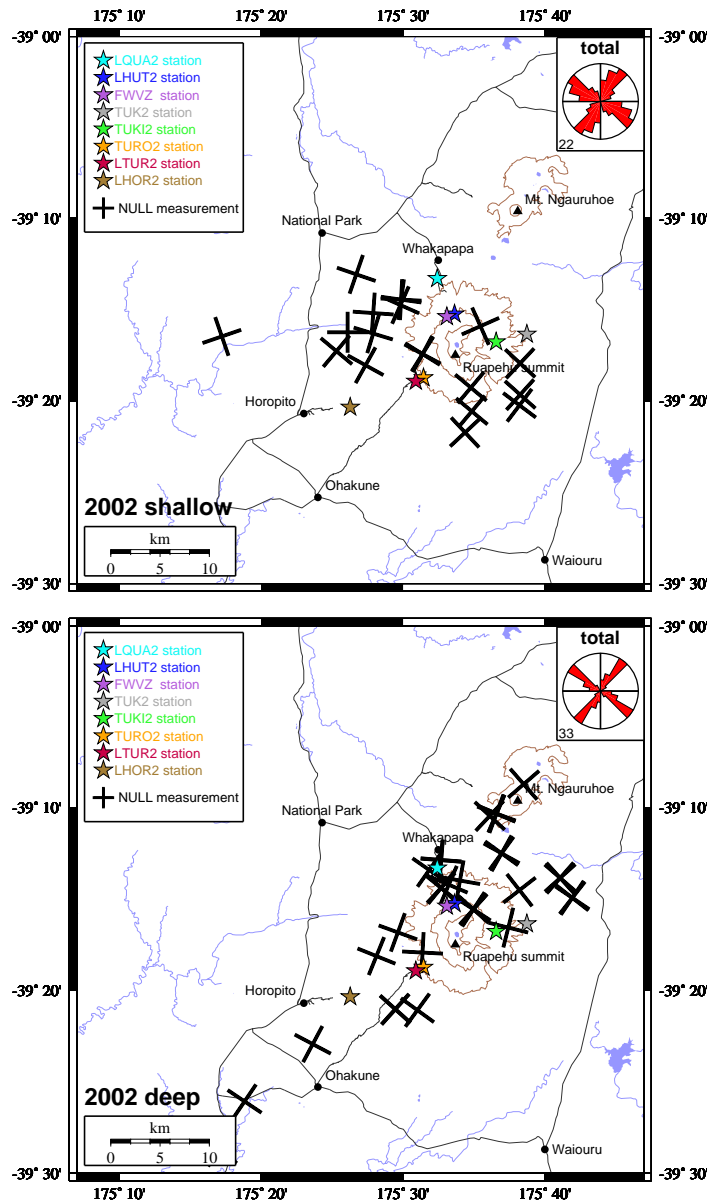


Figure 5.8 Map of obtained NULL measurements, CHARM 2002. Top: shallow earthquakes, bottom: deep earthquakes. The bars are oriented in (and perpendicular to) the direction of the initial polarisation. Therefore they represent a fast direction which is ambiguous by 90° . The bars are plotted at a point where a straight line between source and receiver intersects 5 km (shallow) and 10 km (deep) depth. The histogram in the corner shows the total distribution of NULL measurements for each plot. If there were no common fast direction present, the histogram would be expected to show a random pattern. However, the clear alignment suggests that a relatively uniform fast direction is present in the area around the stations.

5.2 Raypaths and source locations

When examining the 2D map of the earthquake epicentres (Figures 5.9 and 5.10), it is clear that largely the source regions for shallow and deep earthquakes do not overlap. They are therefore not only separated by their depth, but also by their back azimuth. Yet in all three deployments, all shallow earthquakes originate in the same source regions. The same is valid for the deep earthquakes, thus there is no systematic shift between the source regions of the different deployments.

The 3D perspective view (Figure 5.12) shows that the deep events exclusively follow the shape of the subducting slab, while the shallow events originate in the crust around Mt. Ruapehu. Splitting bars are printed at the earthquake hypocentres for visualisation reasons, but the splitting may occur anywhere along the path from the source to the receiver.

When plotted in a 2D vertical cross section (Figures 5.11 to 5.15), the changes between the three deployments become very clear. Two cross sections are shown for each deployment, one perpendicular to the subducting slab, and one parallel to it. Splitting bars in 1994 show a uniform fast direction, which changes by almost 90° in 1998. 2002 shows a mixture of both (shallow events as in 1994 and deep events as in 1998). The figures are plotted in a way so the changes can be visualised by turning the pages forth and back in quick succession.

A 3D plot of all events that were used in the three deployments shows the source regions of each deployment (Figure 5.14). Different coloured dots represent earthquake hypocentres from different deployments. It is clear that the respective source regions of the three deployments coincide, as the dots are well mixed up and show no systematic differences.

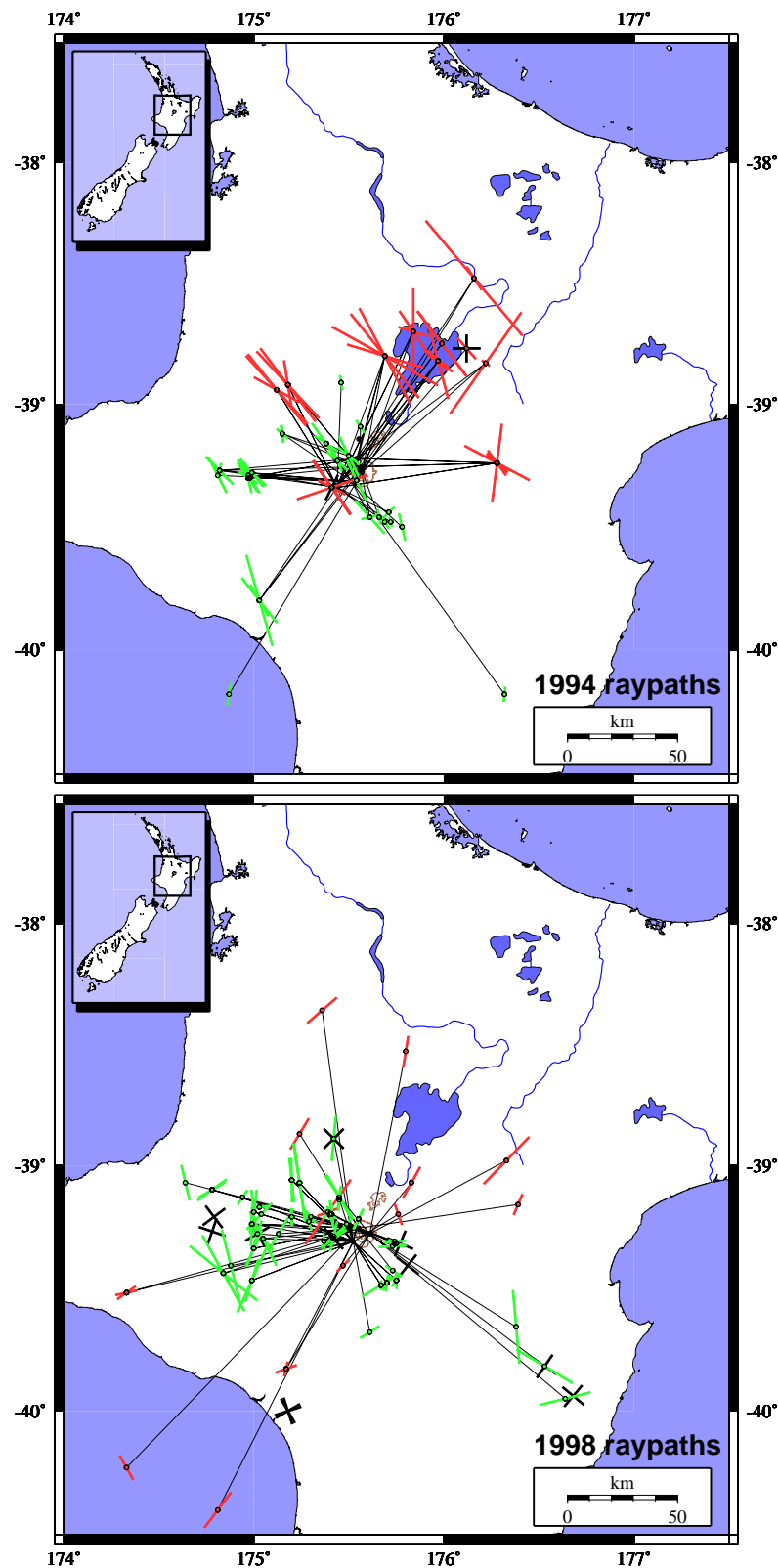


Figure 5.9 This map of the North Island shows the raypaths and epicentres of the 1994 (top) and 1998 (bottom) measurements. Green bars show the shallow earthquakes (<35 km), and red bars show the deep earthquakes (>55 km). Null measurements are shown as black crosses. The source regions for shallow and deep events are largely separated. However, the splitting bars in this figure are only printed at the epicentre for visual reasons – this is not where the splitting of the wave actually occurred. Under the stations, the rays arrive on a steep raypath and therefore all rays sample this region.

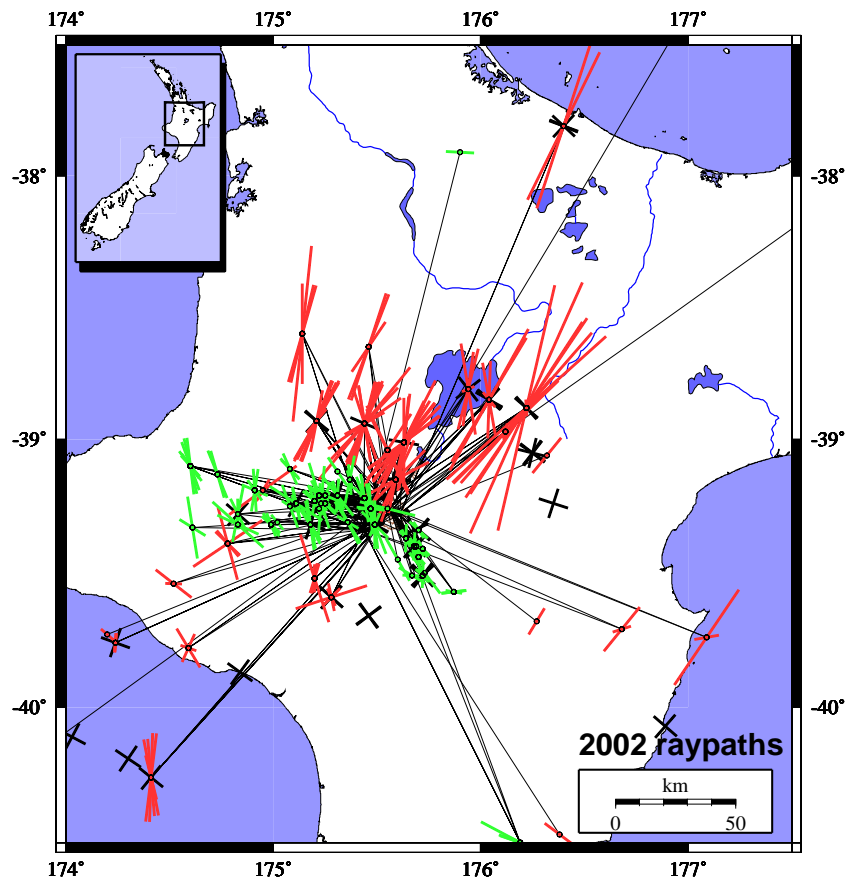
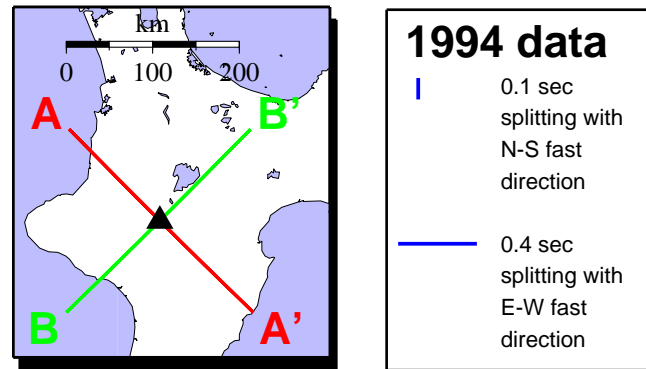


Figure 5.10 This map of the North Island shows the *raypaths* and *epicentres* of the 2002 measurements. Green bars show the shallow earthquakes (<35 km), and red bars show the deep earthquakes (>55 km). Null measurements are shown as black crosses. The source regions for shallow and deep events are largely separated. However, the splitting bars in this figure are only printed at the epicentre for visual reasons – this is not where the splitting of the wave actually occurred. Under the stations, the rays arrive on a steep raypath and therefore all rays sample this region. The lack of usable shallow earthquakes from the North can be attributed to strong attenuation in the Taupo Volcanic Zone.

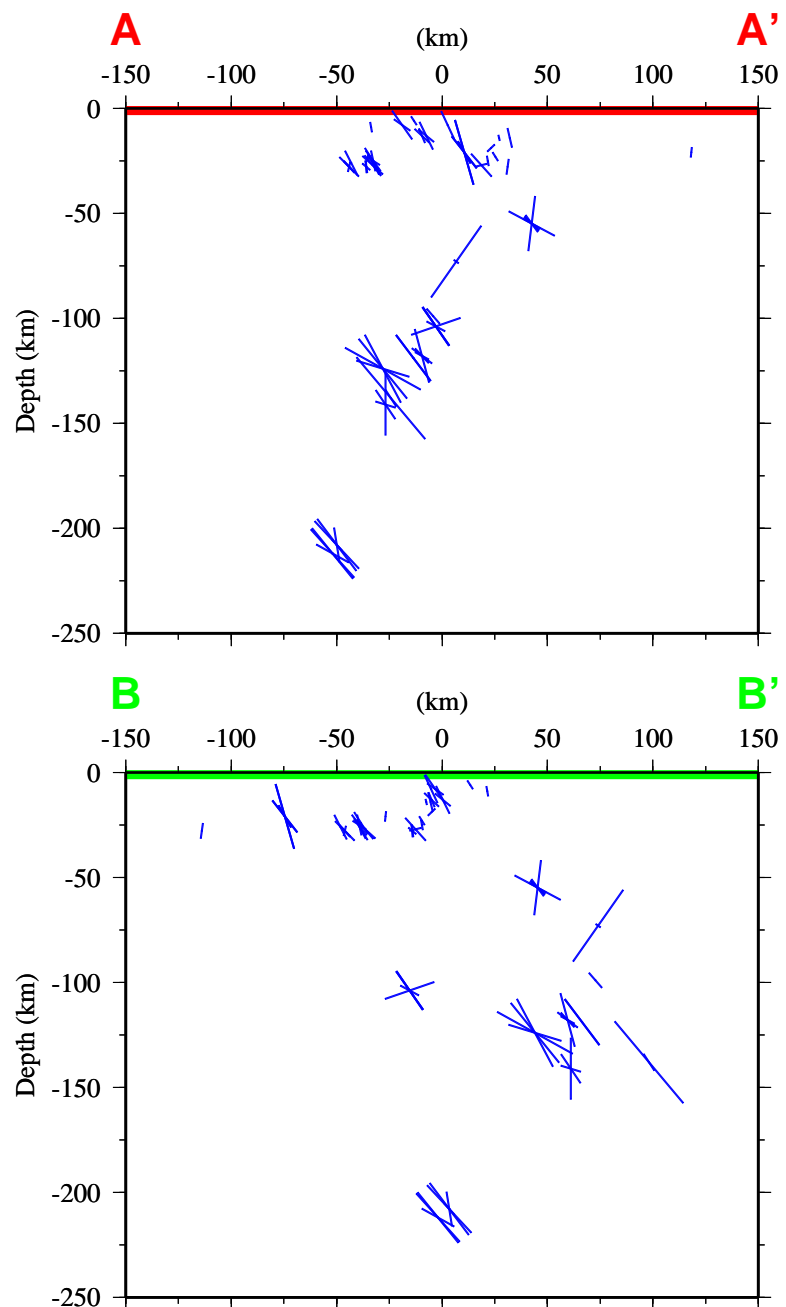
Figure 5.11

Vertical cross section of the 1994 results. The trace of the cross section is shown in the overview map. A-A' represents a cut perpendicular to the subducting slab. It is clear that the deep events follow the shape of the slab under the North Island. B-B' cuts the slab along its strike.



Note that the orientations of the splitting bars do not lie in the cross section plane; they merely indicate the horizontal fast direction as in a map projection, i.e. a vertical bar means a N-S oriented fast direction (unlike in Figure 5.12, where they are shown in perspective view). The length of the bars is proportional to the measured delay time. This and the following two figures are printed in a way that the changes can be visualised by turning the pages forth and back in quick succession.

Also note that the splitting bars are only plotted at the hypocentre for visual reasons. This location is probably not where the fast directions were acquired.



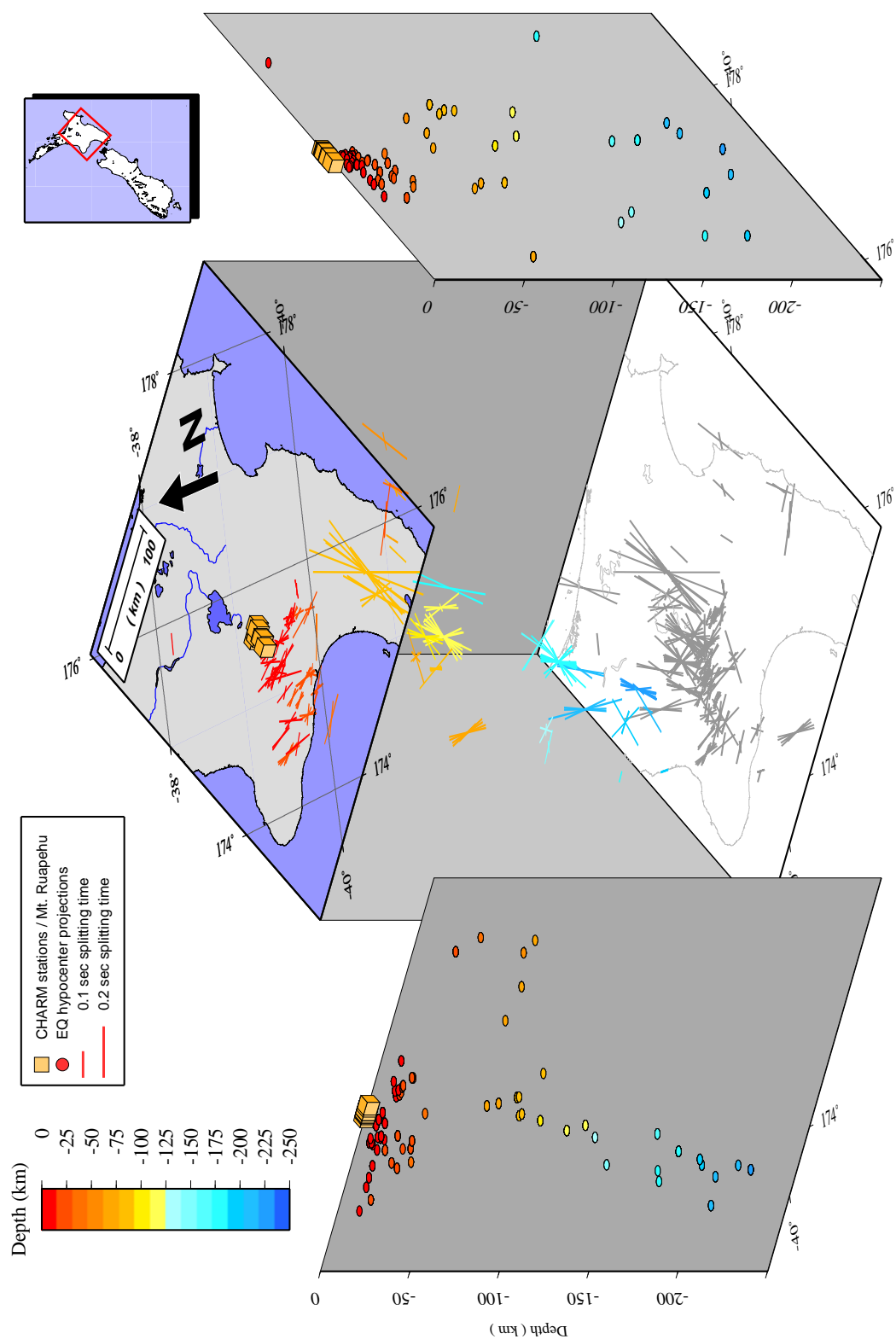
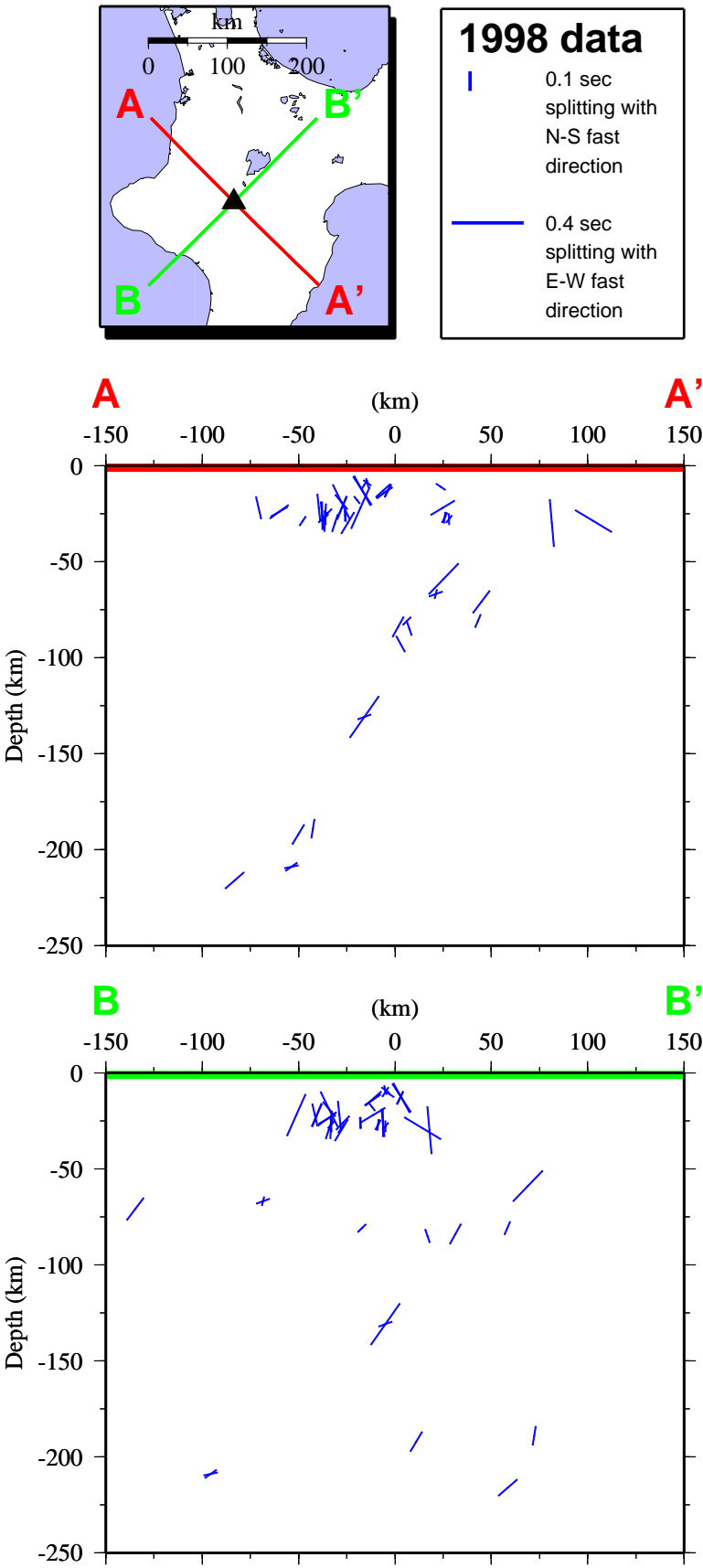


Figure 5.12 This map of the North Island shows the **measurements of the 2002 deployment** plotted at the earthquake hypocentres for visualisation purposes. The colours of the perspective splitting bars indicate the depth of the hypocentre. Underlying grey shadows represent their vertical projections. The dots on the walls are projections of the hypocentres. The depth of this model is 250 km and is not vertically exaggerated. Note that the deep events clearly follow the shape of the subducting slab (projections on the left wall), while the shallow ones originate from the crust around Mt. Ruapehu. The splitting bars are also shown in perspective view, they are therefore not exactly to scale.

Figure 5.13
Vertical cross section of the 1998 results. For the complete figure caption, see Figure 5.11.



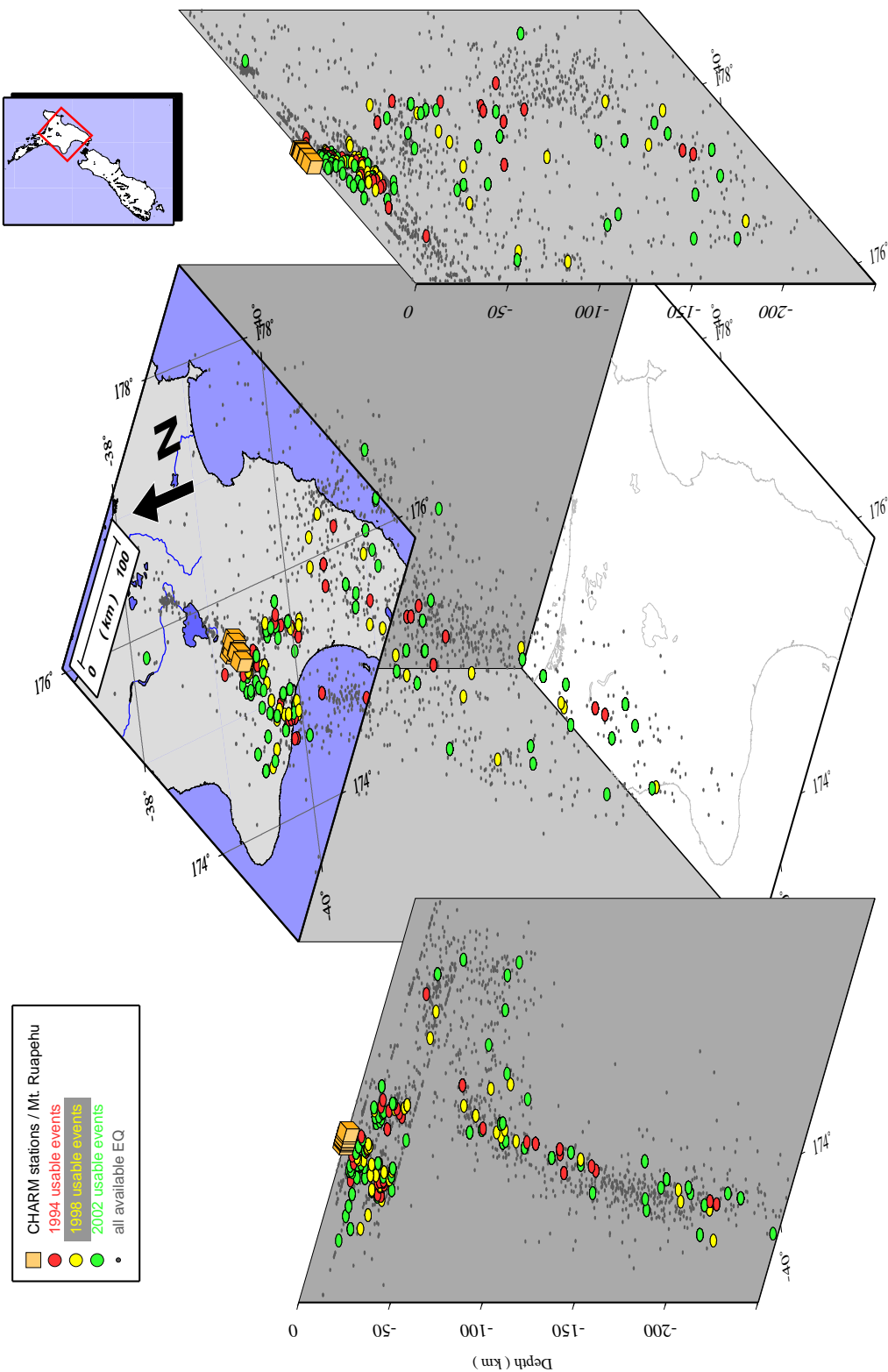
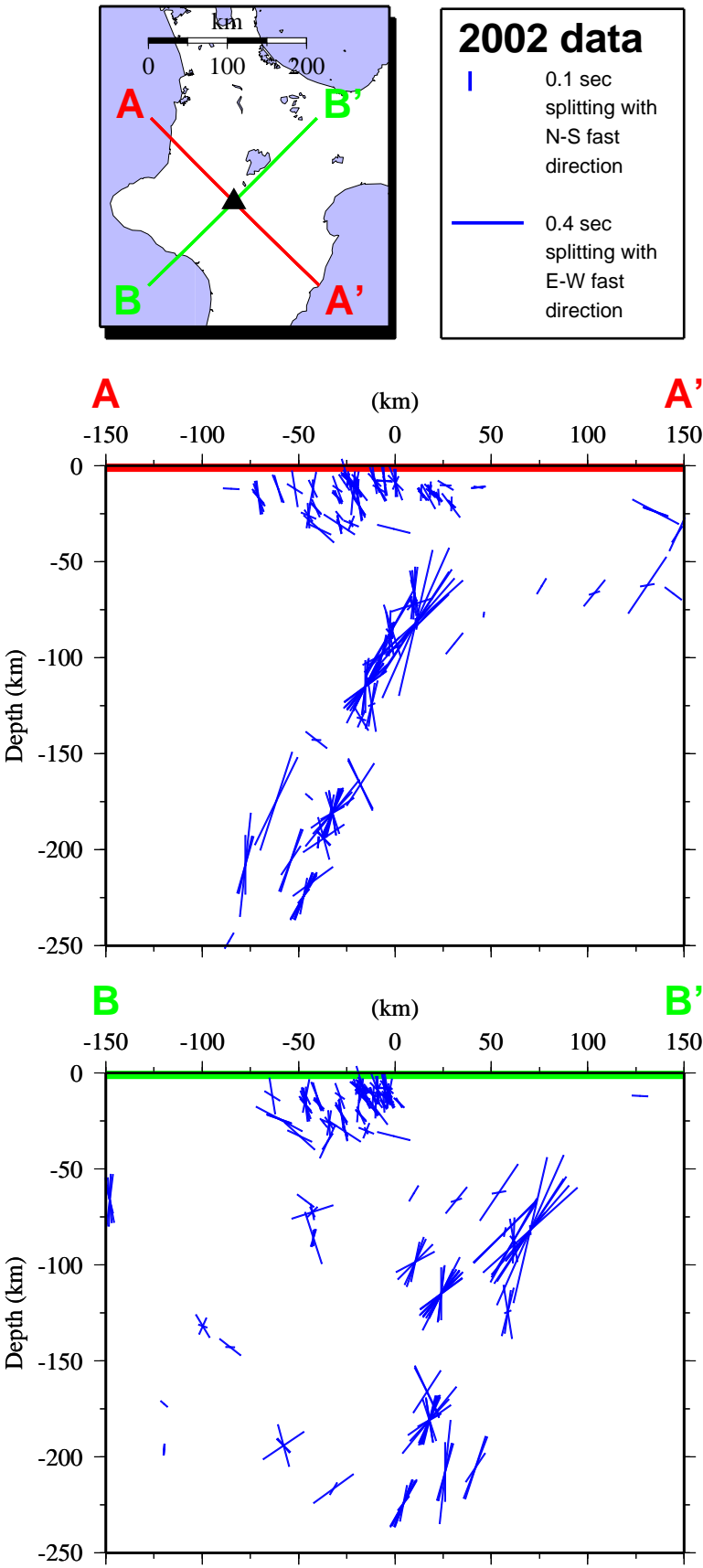


Figure 5.14 A 3D perspective view of earthquakes that were used in the three deployments. Coloured dots are plotted at the hypocentres of all earthquakes used in the analysis. The colours indicate in which deployment they were used. The grey dots are the hypocentres of all available earthquakes. The figure shows that the source regions of the different deployments coincide and that no systematic differences in the used EQ source locations are present. The depth of this model is 250 km and is not vertically exaggerated. For a figure with all available EQ only, see page 67.

Figure 5.15
Vertical cross section of the 2002 results. For the complete figure caption, see Figure 5.11.



5.3 Examination for dependencies on different parameters

Dependency on depth and frequency

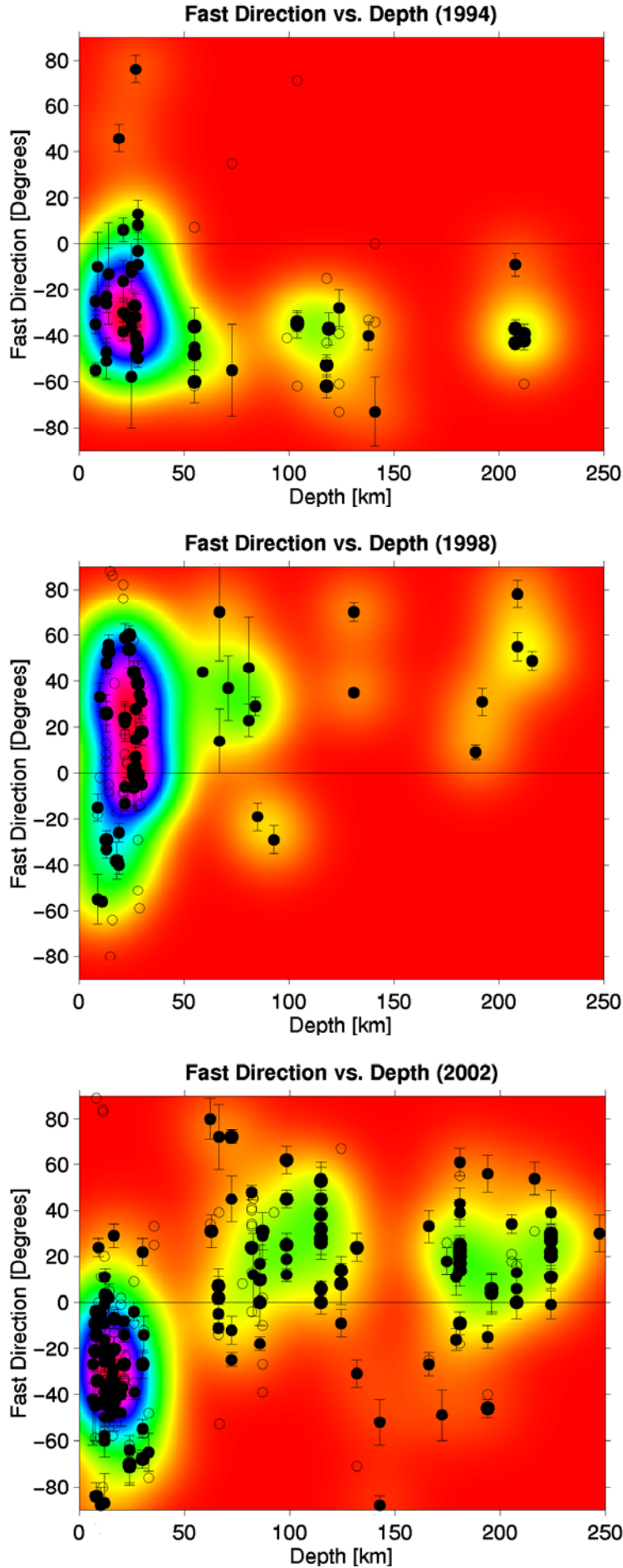
When plotting the observed fast directions versus the depth of the earthquakes, it is clear that in 1994 there is a mostly constant fast direction for all depths (Figure 5.16 top). In 1998, this is also the case, but with slightly more scatter in the shallow fast directions (Figure 5.16 centre). However, in 2002, most of the shallow events show a fast direction that is different from the majority of the deep events (Figure 5.16 bottom).

A plot of the observed main frequencies of the wavelet versus the depth also reveals a prominent depth dependence of the frequencies (Figure 5.17). Shallow earthquakes have frequencies mainly in the range from 2 to 6 Hz (some of them up to 9 Hz), while deep earthquakes only range from 1 to 3 Hz. This can be explained by the fact that for deep earthquakes, only strong ones have enough energy to be observed at the surface. Strong earthquakes naturally have lower frequencies due to a longer rise time in the fracture process (Lay and Wallace, 1995). In addition, while travelling through the ductile mantle above the slab, high frequencies get attenuated more strongly than low frequencies (Aki and Richards, 1980).

A strong dependence of the observed delay times on the depth is also observed (Figure 5.18). It is clear that frequencies and delay times of shallow and deep earthquakes appear in two distinctive bands. The shallow earthquakes (with their frequencies of mainly 2 to 6 Hz, see above) yield delay times of around 0.1 s to 0.2 s, while deep earthquakes (with frequencies around 1 to 3 Hz) yield delay times of around 0.3 s. Some low-frequency deep events show delay times as high as 0.9 s. Another feature of this plot is a distinct cutoff at the top of the samples, where the delay time is larger than the wavelet period. This probably reflects the tendency of the algorithm to interpret wavelets with a very large splitting time as NULL measurements, since the slow wavelet may not be included in the processing window, or it may be obscured by noise (see also Figure 5.19).

When plotting the delay times vs depth (Figure 5.20), it becomes clear that even the shallowest A or AB quality earthquakes (with depths around 6 km) show delay times of up to 0.2 s. This value seems to be constant for all shallow earthquakes, with only occasional B quality events having delay times larger than 0.2 s. Delay times of deep events also seem to be constant with depth, mainly ranging around 0.3 s, but with a second band of delay times of around 0.1 s.

The dependency of the fast directions on the frequency seems to be random for all shallow events (the 1998 and 2002 shallow events are plotted in Figure 5.21). However, the deep events in 2002 show an interesting correlation: for frequencies under 2 Hz, the fast direction seems to be constant at around 10° to 30° . For frequencies above 2 Hz, the fast directions become

**Figure 5.16**

Fast directions vs. depth in a density plot.

Large black dots represent A quality measurements, the slightly smaller black dots are AB quality. Outlined dots represent B-quality measurements. Every measurement of A and AB quality has an error bar, and is the centre of a weight function. This weight is 1 at the point of the measurement, and decays exponentially when moving away from the measurement in either depth- or Φ -direction. The underlying colour map is the representation of the sum of all weight functions, its colour therefore indicates the density of the measurements.

Note the different fast directions during the three deployments. Also note that in 1994 (top) and 1998 (centre), the deep events yield approximately the same fast directions as the shallow events in the respective deployment. In 2002 (bottom) however, the deep events show a different fast direction from the shallow ones.

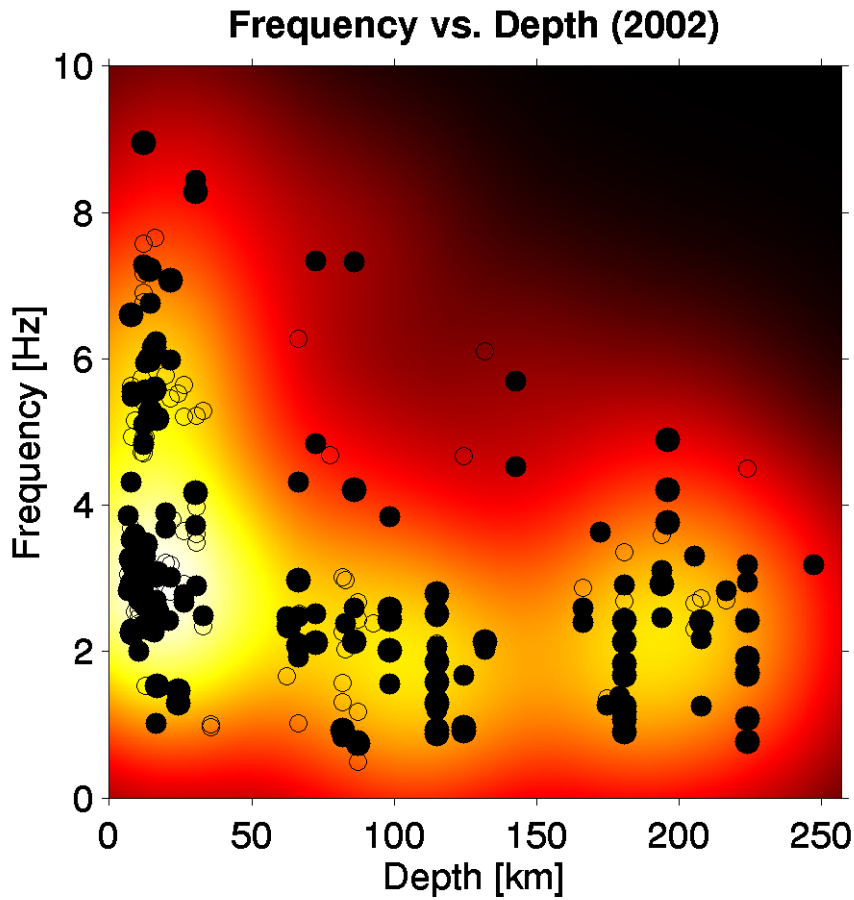


Figure 5.17 *Main frequency of the measurements vs. depth (2002 data).* The density map was generated in the same way as in Fig. 5.16, although a different colour map was used. Note that the measured frequencies of the wavelets strongly decrease with the depth of the source. The different sized black dots represent A and AB quality measurements, the outlined dots represent B quality measurements.

increasingly scattered, and show a broad range of fast directions. The stations were plotted in different colours, so the behaviour of individual stations could be investigated. Most stations seem to follow the general trend, even though a slight frequency dependence of the shallow 2002 FWVZ measurements can be seen (Figure 5.21 centre; purple dots). This observation is consistent with the observation made earlier that the FWTB/FWVZ station yields different fast directions at high frequencies (see Figure 5.6) to the ones at low frequencies.

In general, it can be noted that delay times strongly depend on the observed frequencies and depths (and therefore also on frequency filters and earthquake magnitudes). Since the shallow 1994 events and the deep 1998 events were not reprocessed, it is deceptive to compare delay times from these subsets. Yet for the rest of the dataset, the average delay times of shallow events range around 0.1 s, and the average delay times of the deep events range around 0.25 s (Table 5.1). An exception to this is the deep 1998 subset with an average delay time of 0.12 s. This low average reflects the fact that no low frequency filters were used in the

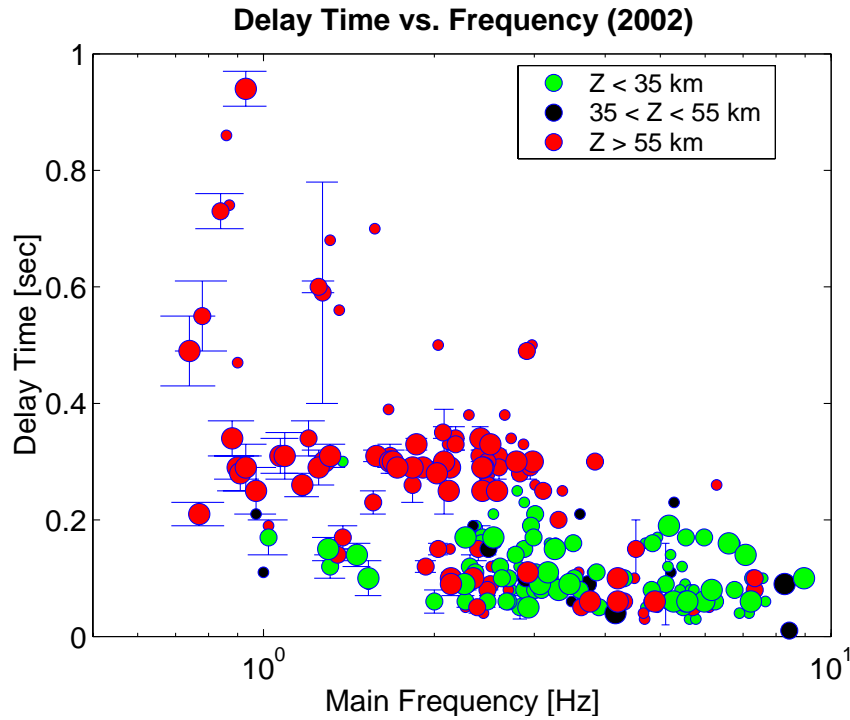


Figure 5.18 *Delay time vs. main frequency of the measurements (2002 data).* Green dots represent shallow measurements, red dots represent deep measurements. The size of the dots refers to the quality, where large means A, medium size means AB, and small means B quality. Error bars were drawn at all A and AB measurements, but are often hidden behind the dots. Note the difference in frequencies and delay times between the shallow and deep events. The distinct cutoff at the top of the samples is likely to be an artefact of the algorithm, since measurements with a delay time of more than one period may have been interpreted as NULL measurements (See Figure 5.19). The shallow events (green dots) do not show any frequency dependence.

old processing, which tends to allow measurements of low frequency events that yield long delay times. Also, a narrow processing window was used in the old processing, so events with very long delay times were probably interpreted as NULL measurements.

The frequency contents of the reprocessed shallow subsets (1998 & 2002) match, as do the frequency contents of the reprocessed deep subsets (1994 & 2002). Therefore the datasets that show differences in the fast direction do not show differences in the frequency content.

Dependency on hypocentral distance

Figure 5.22 shows delay times with respect to the hypocentral distance of the earthquake. It is clear that the delay times of the shallow events do not increase with depth in 1994 and 2002, which suggests a local source of shallow anisotropy (i.e. closer to the stations than the closest earthquakes). In 1998, however, the delay times of the shallow events seem to increase with depth, and reach up to 0.3 s. This suggests a more regional source of shallow anisotropy in this case.

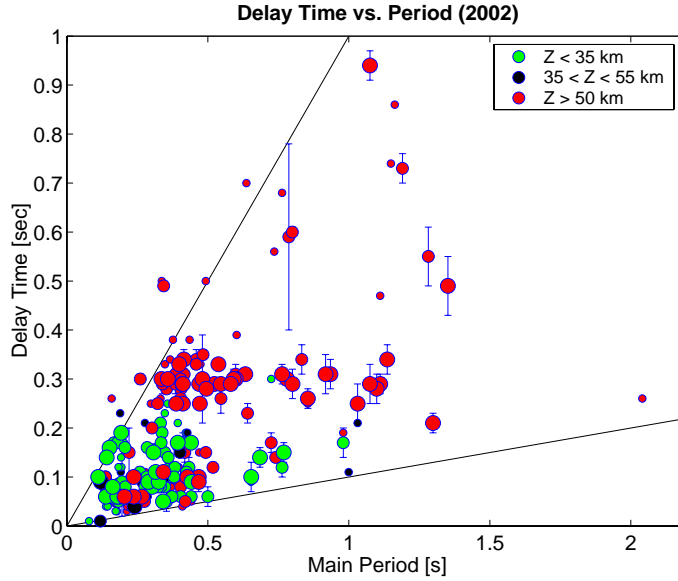


Figure 5.19 *Delay time vs. main period of the measurements (2002 data).* The annotation scheme is similar to Figure 5.18. Only a few measurements yield delay times that are longer than one period (upper line). Generally, the algorithm tends to interpret these as NULL measurements. In addition, the algorithm detects only a few delay times under $1/10$ of a period (lower line). These are mainly NULL measurements, and ambiguities are large (due to noise interference).

Dependency on back azimuth and initial polarisation

A plot of the fast directions versus the back azimuth reveals no obvious relation (Figure 5.23). It was shown above that shallow and deep events have different back azimuths respectively. Since they also yield different fast directions, this plot shows different areas occupied by shallow and deep events. However, no characteristic 2π -, π -, or $\pi/2$ -variation is observed, as may be expected in the case of an inclined axis of symmetry, or with large deviations from vertical incidence, for example (see Section 2.1.7).

Also, a plot of the observed fast direction versus the initial polarisation reveals no relation, as already shown in Section 3.2.3, Figure 3.3.

Dependency on time

Apart from the already mentioned variations of the splitting parameters between the deployments, all but one of the parameters showed no obvious variation *during* the time of the individual deployments. These plots are not all shown, only Figure 5.24 is given as an example. However, in one case there is weak evidence for a temporal change during the time of a deployment: Figure 5.25 shows the variation of delay times of the shallow 1994 events over the time of the deployment. The delay times seem to slightly increase towards the end of the deployment, but it could also represent a random variation.

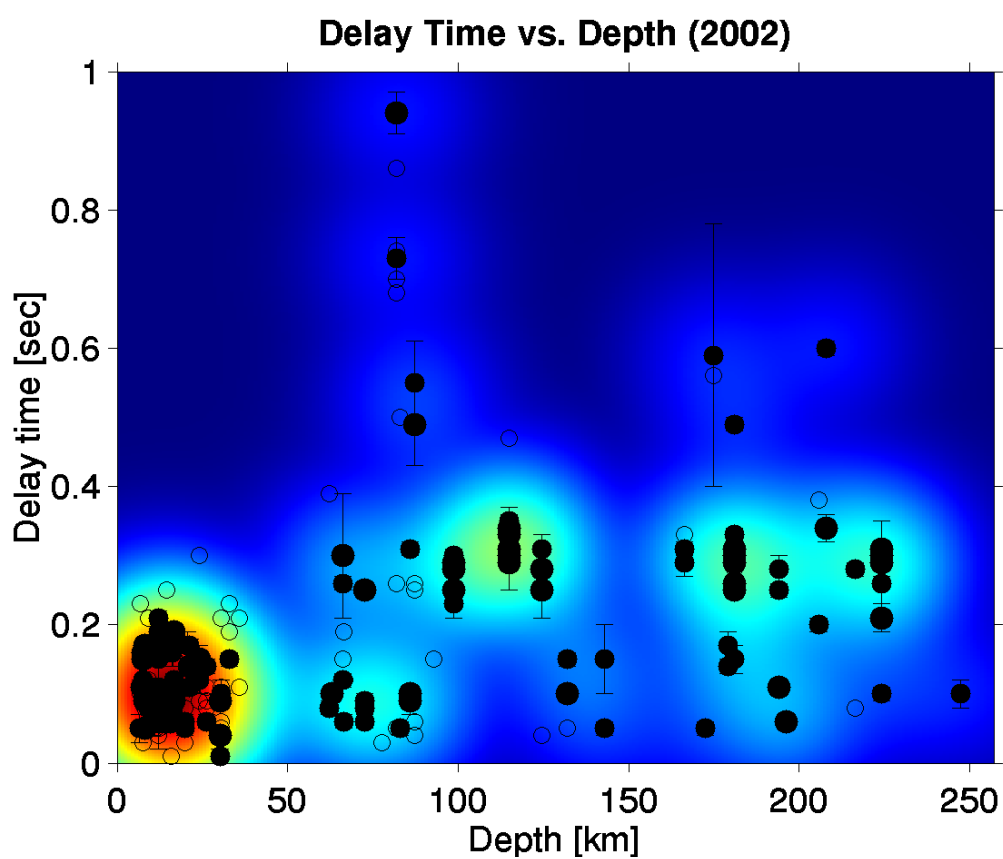
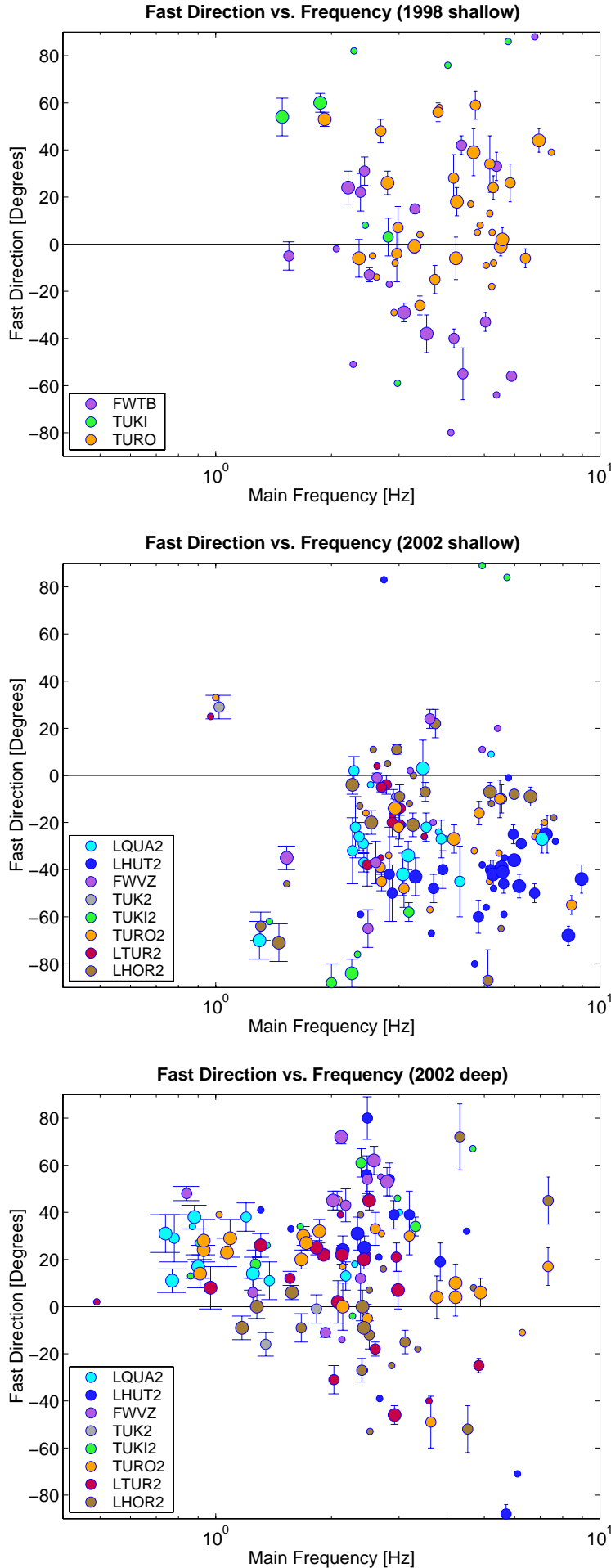


Figure 5.20 *Delay time vs. depth (2002 data).* Note that the shallow events (<35 km) have delay times of up to 0.2 s. The delay times of the deep events mainly lie around 0.3 s, with a second cluster just under 0.1 s. They do not correlate with depth. The density map was generated in the same way as in Fig. 5.16.

**Figure 5.21****Fast direction vs. frequency.**

In these plots, the colour of the dots represent the station at which the measurement was obtained. Large dots represent A quality measurements, medium sized dots are AB-quality, small dots represent B-quality measurements. Error bars were drawn at all A and AB measurements.

For the 1998 shallow (top) and the 2002 shallow (centre) measurements, there seems to be no overall correlation between the measured fast directions and the frequencies. However, the 2002 deep measurements (bottom) show a strong alignment of the fast directions (around 10° to 30°) at frequencies under 2 Hz, but show significant scatter above 2 Hz.

Note also that the 2002 shallow FWVZ fast directions seem to align towards NE-SW with increasing frequencies (centre plot, purple dots).

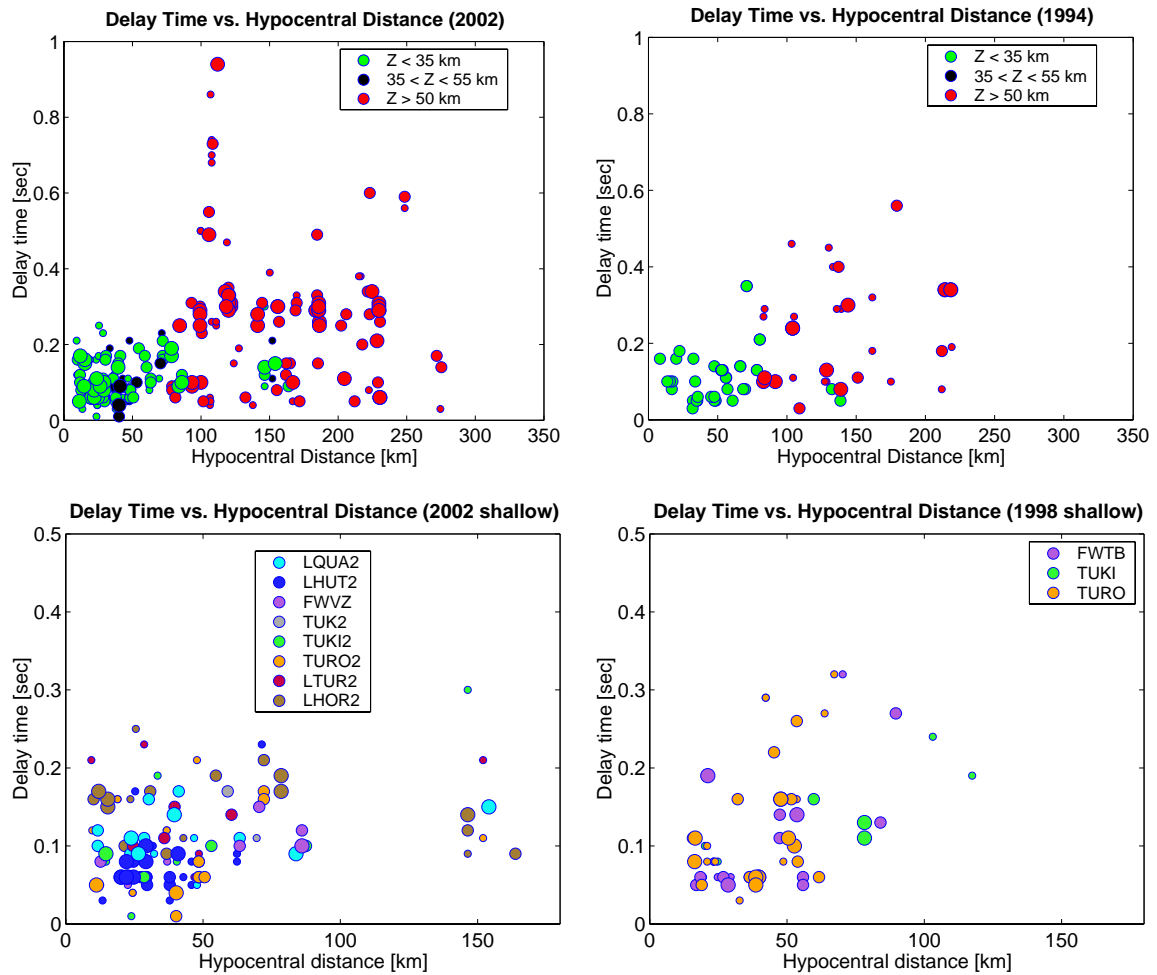


Figure 5.22 Delay time vs. hypocentral distance.

The two figures on the top show the 2002 delay times (top left) and the 1994 delay times (top right) as a function of the earthquake hypocentre distance. The colours of the dots indicate the depth, where green dots have a source depth < 35 km, and red dots have a source depth of > 55 km. The dot size refers to the quality (similar to Fig. 5.18). Note that in both deployments (1994, 2002), the delay times of the shallow events do not increase with the distance.

The two bottom figures show the 2002 shallow delay times (bottom left) and the 1998 shallow delay times (bottom right). In these cases the colours indicate the recording station. Note that the 2002 shallow delay times do not correlate with the distance, whereas the 1998 shallow delay times seem to increase with the distance.

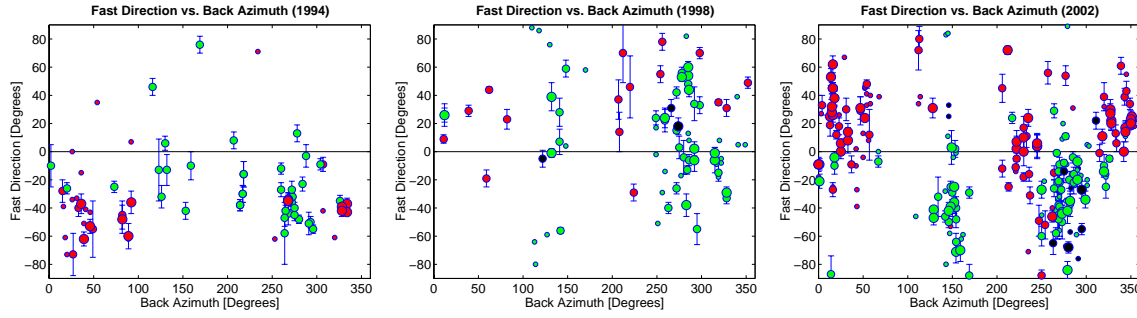


Figure 5.23 Fast direction vs. back azimuth. This figure shows the variation of the fast directions of the 1994 (left), 1998 (centre) and 2002 (right) measurements with the back azimuth. In the case of an inclined axis of symmetry, a typical 2π -variation of the fast directions can be expected (see Section 2.1.7). Note that there is a systematic difference in the back azimuth of shallow (green dots) and deep events (red dots) due to different source locations. Since shallow and deep events also have different fast directions, an apparent correlation between Φ and back azimuth emerges. However, this is not a true dependence on the back azimuth, and no systematic variation is visible otherwise. The annotation scheme in this figure is similar to Fig. 5.18.

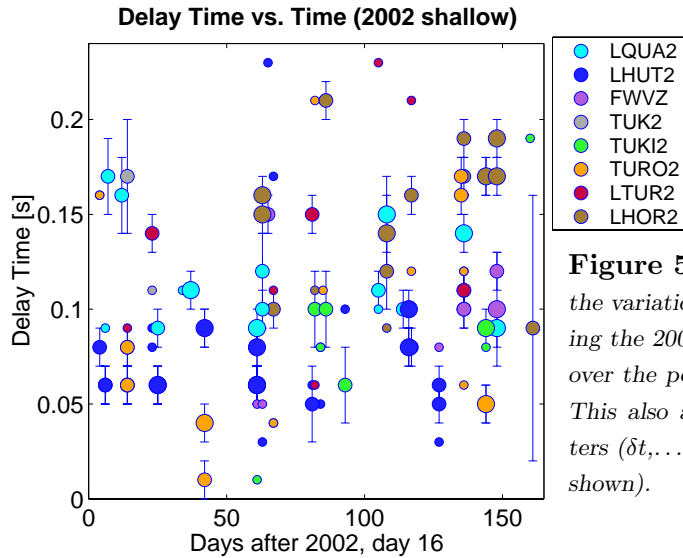


Figure 5.24 Delay time vs. time. This figure shows the variation of the delay times of the shallow events during the 2002 deployment. No variation of the delay times over the period of the deployment can be found in 2002. This also applies for the variation of the other parameters ($\delta t, \dots$), and the results of the 1998 deployment (not shown).

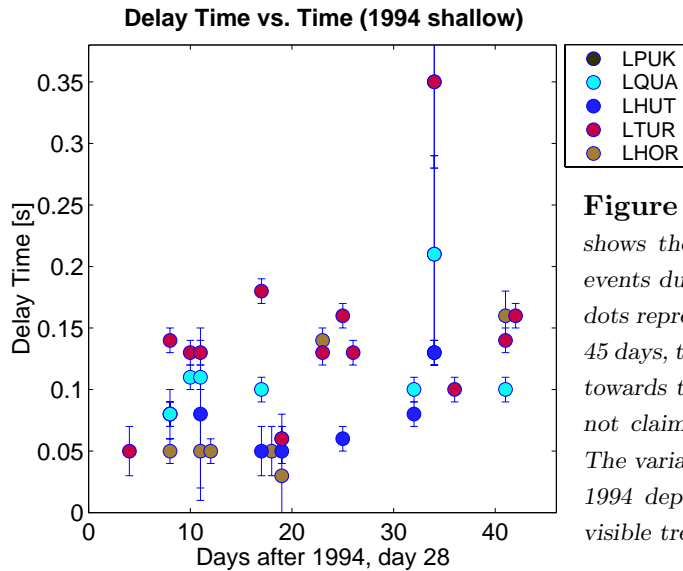


Figure 5.25 Delay time vs. time. This figure shows the variation of the delay times of the shallow events during the 1994 deployment. The colours of the dots represent the recording station. Over the period of 45 days, there seems to be a slight increase in delay times towards the end. However, due to the lack of data it is not claimed that this trend is statistically significant. The variation of the fast directions over the time of the 1994 deployment was also investigated, but yields no visible trend (not shown).

CHAPTER 6

DISCUSSION

This chapter aims to provide a logical explanation for the phenomena that were described in the last chapter. Questions about the authenticity of the changes in anisotropy will be addressed, as well as about the source of the anisotropy. A model will be proposed to explain the mechanism of the changes, and a numerical implementation of this model will be presented.

6.1 Authenticity of the changes in anisotropy

The first question that needs to be answered is whether the differences in anisotropy were truly due to temporal changes, or whether they are effects of differences in station locations, frequency effects, or effects of back azimuth and polarisation dependence. These questions will be addressed in the following.

Station effects

In order to test for station effects, the 2002 deployment consisted of stations that were either previously deployed in 1994, or previously deployed in 1998. If the different stations in 1994 and 1998, combined with lateral heterogeneities in anisotropy were responsible for the observed change in fast directions, they would be expected to also yield substantially different results from each other in 2002. However, Figures 5.2 to 5.5 show that these stations yield similar fast directions. At the stations FWVZ and LHUT2, which are around 1 km apart, the difference in the average fast direction of deep events is only 1.7° in 2002. Shallow events at FWVZ show strong scatter at high frequencies; the average of measurements under 3.5 Hz differs by 18.8° from the average of fast directions measured at LHUT2. However, only 5 measurements contribute to the average at FWVZ, and the uncertainty of this value is larger than 10° .

A further example is the station pair TURO2–LTUR2. These two stations are 1 km apart, and show average fast directions that are different by only 13.2° for shallow events, with a

standard error of 3.3° and 3.7° respectively, and standard deviations of 14.0° and 12.3° . The average fast directions of deep events are different by -11.3° with standard errors of 3.7° and 5.8° respectively, and standard deviations of 18.3° and 25.6° .

The difference of the average fast directions measured at this station pair between 1994 and 1998 was 44.9° for shallow events, and 68.4° for deep events. The 2002 data shows that in 2002, the hypothesis that the average fast directions of the two stations differ by these amounts can be rejected with a confidence level of more than 99.9%. Therefore it has to be assumed that the differences in the average fast direction at the two stations can not account for a difference of 44.9° and 68.4° respectively. Thus the difference in station locations (and therefore the difference in the shallow part of the ray path) can not be responsible for the observed changes in anisotropy.

Frequency effects

Figure 5.20 shows that the observed delay times are dependent on the depth of the source. Since the observed frequencies also depend on the depth (Figure 5.17), a frequency dependence of the delay times is observed (Figure 5.18). When considering only the shallow events, no frequency dependence of delay times is present.

Even more importantly, Figure 5.21 shows that the fast directions of the individual subsets do not show a correlation with the frequency. Only the deep 2002 fast directions show an increase of scatter above 2 Hz, as do the shallow fast directions at station FWVZ above 3.5 Hz. This scatter at high frequencies can be interpreted as a slight form of frequency dependence, but not as a systematic change of fast directions, depending on the frequency. Therefore, a systematic difference in frequencies between the deployments would not cause a difference in the measured fast directions.

In addition to this, Figure 5.21 and Table 5.1 show that the average frequency content of the wavelets did not change significantly between the deployments (≈ 2.5 Hz for deep events of the different deployments, and ≈ 4 Hz for shallow events). Therefore, frequency effects can not account for the observed changes in anisotropy. However, note that shallow and deep events behave fundamentally differently in 2002, which is partially related to their different frequency content, and will be explained in Section 6.3.1.

Back azimuth, polarisation, source and path effects

Figure 5.23 shows that shallow and deep events have largely different back azimuths. Since shallow and deep events also yield different fast directions in 2002, an apparent dependence on the back azimuth emerges. This behaviour can not be distinguished from a real dependence on the back azimuth when only 2002 events are considered. However, the plots with the

1994 and 1998 events show that a similar fast direction is measured for all back azimuths. Therefore a back azimuth dependence can be excluded.

This study did not investigate the focal mechanisms of the earthquake sources. However, other studies show that focal mechanisms in the CVR, TVZ (e.g. Cole et al., 1995), and in the vicinity of Mt. Ruapehu (Hurst and McGinty, 1999) show a wide variety of focal mechanisms. Therefore it is not likely that the focal mechanisms of earthquakes (and with them the initial S-wave polarisations) show a systematic change between 1994, 1998 and 2002. Furthermore, in Section 3.2.3 (Figure 3.3), it was shown that the fast directions do not depend on the initial polarisations of the waves. Therefore the measured fast directions are not affected, even in the unlikely case of a systematic difference in focal mechanisms.

Figure 5.14 shows that the source regions of the three deployments do not show any systematic differences, as can also be seen in the cross section plots (Figure 5.11 to 5.15). This means that there are no systematic differences in the ray paths between source and receiver. Therefore back azimuth, polarisation, source and path effects did not cause the fast direction to change.

Summary

Neither station, frequency, back azimuth, polarisation, source nor path effects can explain the observed changes in the fast direction between the three deployments. Therefore it must be assumed that the changes reflect a temporal change in the anisotropic medium somewhere on the path of the incoming waves.

6.2 The source region of the anisotropy

Since the authenticity of the changes in fast direction is now established, the question arises of where the shear wave splitting originates, and what processes can change the behaviour of the anisotropic medium. The first question will be answered in this section.

Several studies on the North Island showed that shear wave splitting of deep events (e.g. teleseismic events or events from the subducting slab) is mostly influenced by mantle anisotropy (e.g. Audoiné, 2002; Marson, 1997; Marson-Pidgeon et al., 1999). In the case of the deep events at Mt. Ruapehu, this shear wave splitting is acquired on the path through the mantle wedge above the subducting slab. Since there are no known processes that could change the fast direction over a large region of the mantle in the time scales involved (i.e. in less than a few years), an explanation is needed that invokes only a small region in the crust. This implies that at depths greater than the crustal thickness, the polarisation of the fast S-waves has not changed during the three deployments, but was constant and subparallel to the common deep fast direction that is observed over the central and southern part of the

North Island (around NNE-SSW; Audoine, 2002). This is consistent with the data in this study. Therefore, in the cases where a fast direction different to NNE-SSW was observed for deep events, the fast direction must have been altered while passing through the crust. A further implication of this is that at least two independent layers of anisotropy must be present: one in the above mentioned mantle wedge, and a hitherto unspecified region in the crust.

This region will be the subject of the next part of the discussion. Figures 5.20 and 5.22 show that shallow earthquakes have delay times between 0.05 and 0.2 s, which are not increasing with depth or hypocentral distance. The only exception are the shallow 1998 events, which will be discussed later. This behaviour implies that the anisotropic body in 1994 and 2002 must be closer to the stations than the closest earthquakes, otherwise an increasing delay time with depth or distance would be expected. The path length of the closest earthquakes is just under 10 km, with delay times of up to 0.2 s. Assuming that the whole path lies in the anisotropic medium, and assuming an average S-wave speed of 2.5 km/s, Equation 2.20 gives a percent anisotropy of about 5% for delay times of 0.2 s. This can only be a rough estimate, because the error of each individual earthquake depth might be as large as several km, and therefore the hypocentral distance is not well known for events close to Mt. Ruapehu. Also, errors in the measured delay times (in the order of 0.05 s for individual measurements; Table 5.1) lead to uncertainties in the percent anisotropy. However, since many of the closest events show a path length of 10 km (none of them is closer) and delay times of up to 0.2 s, these values are assumed to be good estimates for the correct values.

The initially almost horizontal raypaths of incoming waves from shallow earthquakes strongly curve upwards in the volcanic system due to a strong velocity contrast. This implies that the depth region that is common to all observed raypaths must be very shallow, possibly significantly less than 10 km. In case of a shallower source region, the percent anisotropy must be accordingly higher.

With typical frequencies of around 4 Hz and S-wave speeds of around 2.3 km/s in the upper 5 km of the crust, the Fresnel zones* of the incoming rays have radii of only about 300 metres. An implication of this is that stations with a distance of more than 300 metres sample different regions of the shallow crust, since the Fresnel zones of the raypaths do not overlap. This means that the changes in the fast directions must have occurred in a region that is at least as wide as the area spanned by the stations measuring the changes. At Mt. Ruapehu, this area is around 100 km² (e.g. Figure 4.3). From the data that is available in this study, the maximum size of the affected area can not be constrained with a high statistical significance. However, there are indications that suggest that the stations LHOR2

*The Fresnel zone is the area around a ray that is assumed to influence its behaviour. Its radius is half a wavelength.

and TUK2 are close to the edge of the affected area in 2002. This will be discussed in more detail at the end of Section 6.3.2.

Figure 5.22 shows that in 1998, the delay times of shallow events show indications for an increase with the hypocentral distance. Some events show up to 0.3 s delay time with a hypocentral distance of around 80 km. This suggests that the shear wave splitting in 1998 was not acquired while travelling through a narrow local region of strong anisotropy, but rather while travelling through a wide region of pervasive anisotropy.

Summary

There must be at least two regions of anisotropy, one in the mantle wedge above the subducting slab (“lower layer”), and another in the shallow crust (<10 km), directly beneath Mt. Ruapehu (“upper layer”). Changes in anisotropy originate from the upper layer, and influence the fast directions from deep earthquake waves travelling through the upper layer. This layer yields a minimum of 5% anisotropy in 1994 and 2002, while a locally less strong but more pervasive anisotropy is observed in 1998.

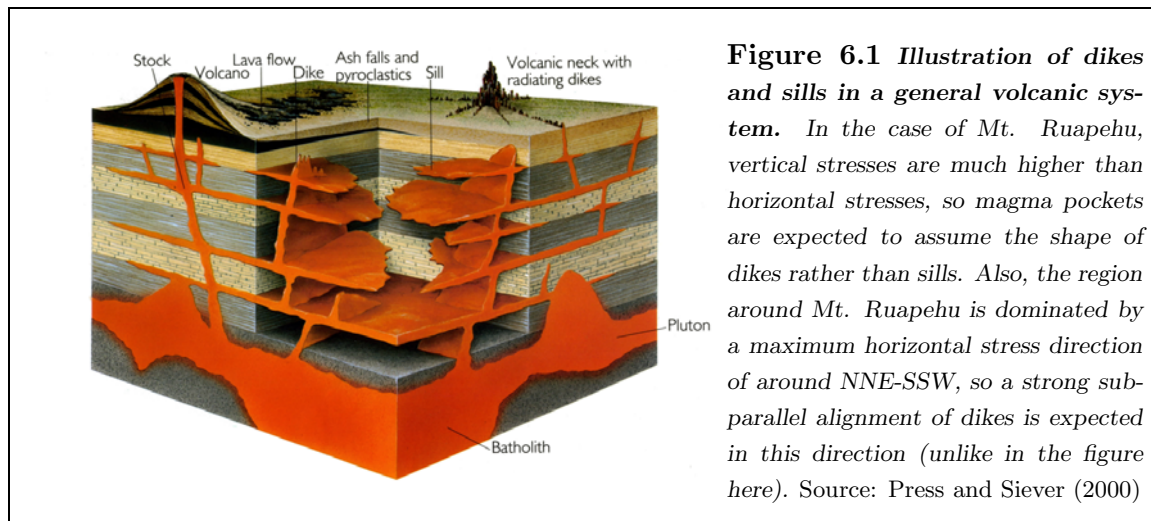
6.3 The model

“All models are wrong – but some models are useful.”

George E. P. Box

As shown above, a model is needed that can explain the presence of a shallow anisotropic body beneath Mt. Ruapehu, that changes its fast direction in a maximum time scale of a few years. Apart from earthquakes, the only processes known to generate changing conditions in the earth within these time scales involve either liquids, or gas (e.g. volcanic activity, drainage of a reservoir, hydraulic fracturing, etc.). These processes only act locally, and not over great distances. Therefore, in addition to a rapidly changing “anisotropy source” process, a way of transporting the change of conditions has to be found. A process capable of acting fast and over great distances in the earth is a changing stress field.

Latter (1981) finds evidence of bodies of partially molten rock under Mt. Ruapehu by means of S-wave attenuation. Anomalously high attenuation was found under Ruapehu Crater Lake in depths between 2 and at least 10 km under the surface of the lake. He proposes the presence of three principal intrusions, which are steeply dipping structures, aligned with the regional stress field (NNE-SSW to NE-SW) and the main axis of volcanic vents. Petrologic evidence suggests that these intrusions are about 70% molten. Under the given stress conditions ($\sigma_V \gg \sigma_H > \sigma_h$), they strongly resemble the expected shape of a magma intrusion in the shallow crust, which is basically a hydraulic fracture: one or



multiple volcanic dikes, aligned with the principal horizontal stress direction. Many studies report dikes of similar sizes and alignment, one of the most recent of which is presented by Gudmundsson (2002). Regional magma dike swarms are found in Iceland with dike lengths between 4 to 22 km and an average thickness of around 10 metres. The average length is 8 km. These dikes are extension fractures (mode I cracks), and are oriented perpendicular to the minimum compressive principal stress; their strike is therefore parallel to the maximum horizontal stress direction.

Several exposed dikes and faults are mapped on Mt. Ruapehu and in the Tongariro Volcanic Centre. The majority of them has a strong NNE-SSW alignment, parallel to the inferred maximum horizontal stress direction (See Section 1.3 and Figure 1.7).

Following these observations, we propose a magma intrusion in the form of a dike or a swarm of parallel dikes under Mt. Ruapehu, aligned perpendicular to the inferred minimum principal stress, and therefore parallel to the maximum horizontal stress σ_H (approximately NNE-SSW). The length of the dike system is unknown, but is at least 5 km in either direction from Crater Lake, considering the results from Latter (1981). The thickness is also undetermined, but is assumed no more than a few hundred metres, following suggestions made by Gudmundsson (2002).

Such an intrusion of volume in the crust exerts pressure on the surrounding rock, therefore generating a local stress field which is superimposed on the regional stress field. The stresses of this elongated structure will mainly be oriented perpendicular to the strike axis and are therefore parallel to the regional minimum principal stress (See Figure 6.2).

It is suggested that prior to an eruption, the dike system is pressurised by uprising magma from a deeper reservoir, with this pressure eventually triggering an eruption at the volcano.

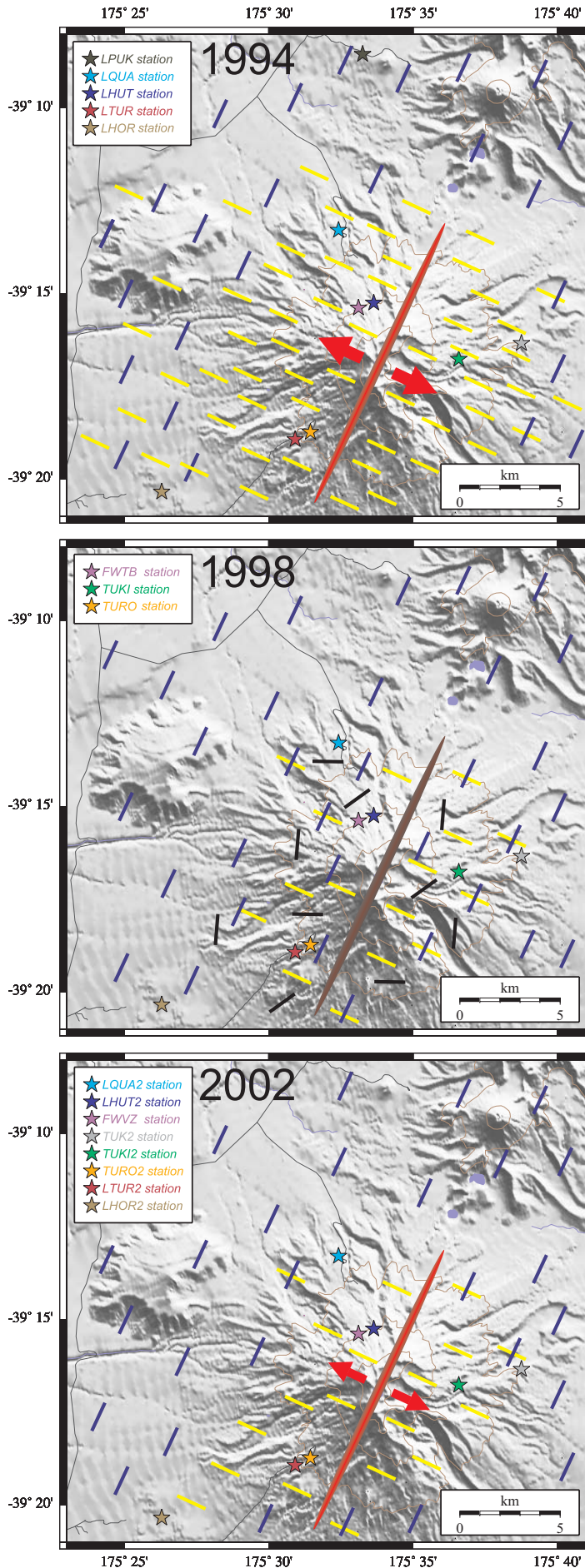


Figure 6.2 Anisotropy model for 1994, 1998 and 2002

In 1994 (top), a pressurised system of subparallel dikes (visualised as only one dike) creates a local stress field with a main horizontal stress direction aligned between WNW-ENE and NW-SE (red arrows). Within the anomalous region in the reach of this local stress field, EDA cracks realign by changing their aspect ratios, i.e. cracks that are perpendicular to the new σ_H close (blue bars), while the ones parallel to the new σ_H open up (yellow bars).

In 1998 (centre), after the eruption, the dike system is depressurised and the main horizontal stress direction in the anomalous region partially returns back to the regional trend (between NNE-SSW and NE-SW). EDA cracks therefore also partially realign in NE-SW direction, but a large part assumes a random alignment (black bars). The anisotropy in the anomalous region is more heterogeneous than in 1994.

In 2002 (bottom), the dike system is refilling, and the stress field in the anomalous region is dominated by the dike again. However, the alignment of EDA cracks is not yet as strong as in 1994, so the overall strength of the anisotropy in the anomalous region is not strong enough to affect fast directions from low frequency, deep events.

Note that the true length of the dike is unknown; this figure only shows the dike with its minimum length, therefore stress effects from the tips of the dike were not included (See Figure 6.5).

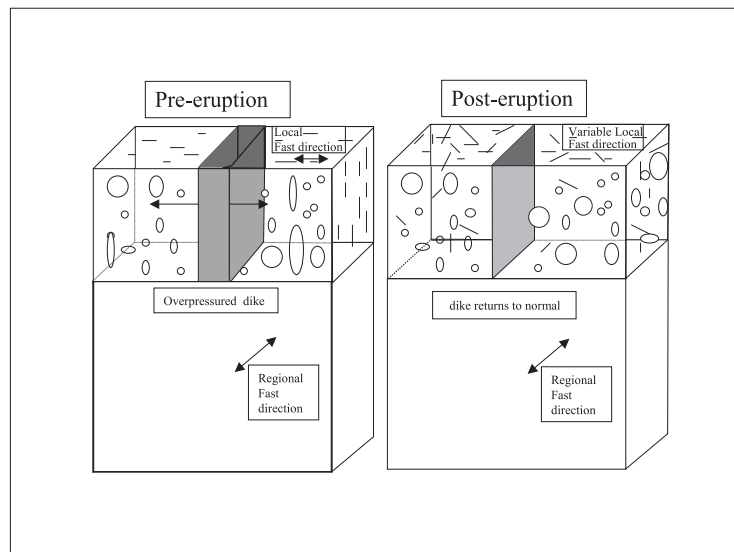


Figure 6.3 *Model of crustal crack orientation before and after the 1995/96 eruption. Before the eruption (left), a system of magma dikes pressurised the surrounding rock and closes cracks that were oriented parallel to the dike. After the eruption, the pressure went back to normal and cracks in all directions could open up again, preferably the ones parallel to the regional stress direction (NE-SW).*

6.3.1 How can a dike change the fast direction?

It was shown that there are no systematic variations of the fast direction with frequency, back azimuth, polarisation, or hypocentre location. The most plausible explanation for the observed temporal changes in shear wave splitting is stress-induced changes to EDA crack geometry (e.g. Peacock et al., 1988; Crampin et al., 1990; Savage, 1999). Below a depth of a few hundred metres, the minimum stress is typically horizontal and therefore causes EDA cracks with vertical crack planes (Crampin, 1994). This system yields a hexagonal or orthorhombic symmetry system with a horizontal symmetry axis (See Section 2.1.1). The fast direction is commonly observed parallel to σ_H .

These EDA cracks are widely observed fluid filled inclusions in the crust. They are not necessarily connected to volcanic processes in any way, and only act as indicator for stresses in the crust. It is assumed that the proposed dike system itself due to its restricted thickness does not influence the incoming S-waves as much as the EDA cracks. Thus, it is important to separate these two processes: the dike system as source of the stress field, and the EDA cracks as source of the anisotropy.

Changes in the stress field, triggered by pressurisation of the proposed dike system, could alter the effective maximum horizontal stress direction and therefore the polarisation direction of the leading S-wave (See Figure 6.3). This process will now be described in detail:

It is assumed that prior to the eruption (i.e. in 1994), a recently pressurised magma dike system generated a local stress field beneath Mt. Ruapehu. This local stress field would have

been superimposed on the regional stress field, and therefore added to the regional stress. As typical hydraulic fractures, dikes mainly pressurise the surrounding crust perpendicular to their strike. When the pressures in the dike system are high enough, this stress direction then becomes the maximum horizontal stress direction in a certain region around the dike. This region is from now on referred to as *anomalous region* (See Figure 6.2). If such a region existed around Mt. Ruapehu before the eruption, then the direction of σ_H within this region would be expected to be subparallel to the direction that was previously the minimum horizontal stress direction σ_h (NW-SE), i.e. the maximum and the minimum stress directions would be basically swapped. The EDA cracks in the region would react to these changing stress conditions, and cracks that were open perpendicular to the new σ_H would be forced to close, with their pore fluid migrating into cracks that were previously closed (and which are now able to open due to being oriented perpendicular to the new minimum stress direction). Effectively, the alignment of the cracks would be expected to adjust to the new stress field, and to orient parallel to the new σ_H . Zatsepin and Crampin (1997) show that the time scale for these changes is dependent on the rock permeabilities. Estimates for applied differential stresses of 10 MPa range from seconds to several minutes, assuming reasonable rock permeabilities of 10^{-9} to 10^{-6} Darcy (Zatsepin and Crampin, 1997).

Such a change in the alignment of EDA cracks would be expected to cause a near 90° change in fast directions obtained within the anomalous region – which is observed in the data. Below it is described in detail how the model explains the observed measurements.

Influence on the shallow measurements

Events that originate in the crust have a polarisation direction that is dependent on their focal mechanism, and a wide variety of these can be expected. On their way to the receiver, the waves travel through the mostly isotropic lower crust, until they enter a region of EDA cracks at a depth of approximately 15 km. With no anomalous stress field present, the S-waves split, with a fast direction that is expected to be parallel to the regional stress field (in this case around NE-SW or NNE-SSW).

However, prior to the eruption (1994), subparallel fast directions from shallow events were strongly oriented in \approx NW-SE direction (see Figure 5.1 and the supplementary plot). This observation is consistent with the model, as the dike was pressurised prior to the eruption, causing the fast direction within the anomalous region to change to NW-SE. The earthquake waves that crossed this region on the way to the receivers would have acquired shear wave splitting with a NW-SE fast direction.

In 1995 and 1996, a phreatomagmatic eruption sequence occurred at the main crater of Mt. Ruapehu, which ejected material with an overall volume of around 0.02 km^3 to 0.05 km^3 (e.g. Bryan and Sherburn, 1999; Nakagawa et al., 1999; Nairn and Scott, 1996). This

might have lowered the pressure in the proposed dike system enough to let the majority of the EDA cracks partially change back to their inferred original alignment: approximately parallel to the regional crustal σ_H (around NE-SW, but with significant scatter; see Audoiné, 2002). In this case, earthquake waves that travelled through this region *after* the eruption would have been expected to acquire the regional fast direction. This is consistent with the observed shallow fast directions in 1998 (mainly NE-SW, with strong scatter). It is not known to what degree the EDA cracks realigned to their original orientation after the eruption. However, the increased scatter and several different alignment directions in the 1998 shallow dataset suggest that only some of the cracks realigned, while some of them were possibly still under the influence of an only partly depressurised dike system, or a very heterogeneous stress field around Mt. Ruapehu. Furthermore, the observation of increasing delay times with an increasing hypocentral distance of the 1998 shallow events suggests that the splitting parameters were acquired over a large part of the path, rather than only in the inferred anomalous region (See Figure 5.22 and Section 6.2)

In 2002, fast directions of shallow events are found to be aligned NW-SE and NNW-SSE, similar (within 2°) to the fast direction observed prior to the eruption (1994). This can be explained by a currently refilling dike system that is re-pressurising the surrounding crust. Such a re-pressurisation would cause the EDA cracks in the anomalous region to align perpendicular to the dike again, and therefore to generate fast directions in a NW-SE direction.

Influence on the deep measurements

Generally, the behaviour of the deep events is more complicated in this study, since the deep events have already acquired a NE-SW fast direction from the mantle anisotropy by the time they enter the inferred anomalous region beneath Mt. Ruapehu. Therefore they behave similar to a two layer problem. As shown in Section 2.1.6, the faster S-wave entering the upper anisotropic medium might simply split again into a new fast and slow S-wave, oriented parallel and perpendicular to the fast direction of the upper layer (Silver and Savage, 1994). In this case, the fast direction of the lower layer is lost, and only the fast direction of the upper layer is measured at the surface.

Generally, there are two conditions that have to be fulfilled in order to re-split the S-wave upon entering the upper layer:

1. The wavelength of the incoming wave has to be sufficiently small to be affected by the upper layer. This means it should not be longer than the thickness of the layer. In the case of a longer wavelength, the upper layer is simply “overlooked”. Therefore, low frequency waves tend to show the parameters ($\delta t, \Phi$) of the (thicker) lower layer, and high frequency waves show the parameters of the upper layer. Also, since low frequency

waves have a longer wavelet period, their fast and slow wavelets are not as separated (in relation to the period) as those of high frequency waves with the same delay time. This means that for high frequency waves, the fast wavelet entering the upper layer is more likely to be “cleared” from the slow wavelet and can therefore more easily be re-split without complicating the waveform.

2. The anisotropy in the upper layer has to be strong enough to split the entering wave by a sufficient amount. Figure 5.19 showed that delay times under $1/10$ of a period can not be detected by the algorithm. Therefore, waves with a period longer than $10 \cdot \overline{\delta t}$ will yield either no splitting parameters, or the ones from the lower layer. When the strength of the anisotropy in the upper layer rises beyond a certain point (e.g. by dike pressurisation), then waves that previously showed the parameters of the lower layer will suddenly show the parameters of the upper layer.

Figures 5.17, 5.18 and 5.20 show that deep events generally have lower frequencies (i.e. longer periods and wavelengths) than shallow events. They also yield longer delay times due to a long path in the anisotropic mantle wedge.

In 1994, prior to the eruption, fast directions from the deep events were strongly aligned NW-SE (similar to the shallow events in this deployment; see Figure 5.5, or foldout map). This can be explained by a highly pressurised dike system before the eruption, causing EDA cracks in the anomalous region to strongly align NW-SE. The resulting anisotropy would have been high enough to re-split waves from deep earthquakes that entered the anomalous region (condition 2), and would have caused the fast directions to be observed in a NW-SE direction.

In 1998, after the eruption, the fast directions of the deep events were aligned NE-SW to NNE-SSW. This is consistent with a depressurised dike system after the eruption, causing EDA cracks to show more or less random directions, with a tendency towards the regional σ_H (NNE-SSW). The resulting anisotropy would have been significantly less strong than with highly aligned EDA cracks. Thus, condition 2 would have not been fulfilled, and the incoming deep waves would have not been re-split. The measured parameters of the deep events were therefore the ones from the lower layer: a fast direction around NE-SW, resulting from the mantle anisotropy (long delay times would also be expected, but since the 1998 deep subset was not reprocessed, long delay times were not recognised by the algorithm).

In 2002, deep events yielded fast directions aligned NNE-SSW, together with large delay times (up to 0.8 s and more). Even though this alignment is similar to the deep fast directions in 1998, it is still consistent with the model of a refilling and repressurising dike system (as inferred from the realigning 2002 shallow events), where the resulting realignment of EDA cracks is not yet strong enough to re-split the deep events. The situation for the 2002 deep

events is assumed to be similar to the 1998 deep events, where the splitting parameters from the lower layer are measured at the surface: a fast direction around NE-SW and longer delay times than those from shallow events. However, the slight difference of 18° between 1998 and 2002 might be an indicator of the onset of re-splitting of the deep events in 2002. When the inferred pressurisation of the dike continues in the future to a similar stage as that before the eruption (1994), then the reorientation of measured fast directions from deep events would be expected (similar to 1994). This might be an important indicator for the current pressure in the dike system.

A simple test for this hypothesis is plotting all initial polarisations of deep events on a map. Since the polarisation of the wave before entering the upper layer is the fast direction of the lower layer, this direction should be automatically calculated by the algorithm as initial polarisation of the split wave. Figure 6.4 shows such a plot. Initial polarisations of all deep events show a strong alignment in the NE-SW direction, which coincides with the fast direction of the mantle anisotropy (lower layer), as expected.

6.3.2 Further observations that agree with this model.

In addition to the observations described above, there are further observations that agree with the model:

- In the 2002 deep subset, the majority of events are aligned NE-SW and show long delay times. This is consistent with the deep events being aligned by the mantle wedge. However, not all measurements are aligned in this direction (Figure 5.4 bottom, eg. stations LHOR2 and TURO2). These few measurements, aligned more towards NW-SE, have shorter delay times (around 0.1 s) than the NE-SW aligned measurements, and might represent deep events that were re-split in the upper layer by the same process that split the 2002 shallow events (repressurising dike). However, due to the small number of these events, normal scatter can not be excluded as an alternative explanation.
- In 1998, a large variety of delay times is observed in the deep subset (Figure 5.3 bottom). This is consistent with the dike system being depressurised, causing none of the deep events to re-split. Very long delay times were not detected in this subset, since it was not reprocessed.
- In 1994, all deep events with short delay times are aligned NW-SE; they are re-split. However, three events (aligned NE-SW) do not seem to be re-split, all of which have delay times longer than 0.2 s (Figure 5.2, bottom). This is consistent with the pressurised dike system in 1994 being strong enough to re-split the shorter period deep

waves, but nevertheless not being strong enough to re-split waves with long periods and long delay times. However, this effect could also be attributed to scatter as an alternative explanation.

- The reason for the absence of delay times >0.4 s (which are usually yielded by low frequency waves) in the 1994 deep subset can be explained by their partial re-splitting in the strongly anisotropic upper layer. This would cause their waveforms to become complicated since they can not be re-split completely due to their long period. Therefore no valid measurements from these events would be obtained.

In addition to these observations, there are indications of a constraint on the size of the affected area. Figure 5.5 shows that in 2002, the overall fast directions of shallow events are significantly different from the fast directions of deep events. However, the stations LHOR2 and TUK2 do not show such strong differences between shallow and deep events. At station LHOR2, 24 and 19 measurements were obtained from shallow and deep events respectively. Shallow and deep fast directions at this station are different by only 8.8° , with the standard error intervals overlapping each other. At station TUK2, only 2 measurements each were obtained from shallow and deep events respectively, therefore the results are statistically not as significant as the results from LHOR2. Shallow and deep fast directions at this station are different by 18.5° , also with their standard error intervals overlapping each other.

It was argued above that the overall NW-SE alignment of the 2002 shallow events, and the difference between shallow and deep events, is caused by the realignment of EDA cracks in the anomalous region around the dike system. Only stations LHOR2 and LTUK2, which are the ones furthest away from the proposed dike system (Figure 6.2), show different behaviour. These two stations (at a distance of >5 km from the dike axis) show neither a NW-SE alignment, nor different fast directions between shallow and deep events due to being outside the reach of the anomalous region in 2002. This would constrain the size of the anomalous region in 2002 to within approximately 5 km from the dike. Station LHOR2 might also be too far south to be affected by the dike system.

It is not clear to what amount the size of the anomalous region is increasing with the pressure of the dike system, and whether LHOR2 was inside the anomalous region in 1994. Figure 5.5 shows that for the 1994 deep events, fast directions from LHOR2 were strongly aligned in NW-SE direction, indicating that LHOR2 was inside the anomalous region. However, the shallow fast directions at LHOR2 in 1994 show a more northerly direction than fast directions from shallow events at other stations, indicating that LHOR2 might be close to the edge of the anomalous region.

Even though these observations and their above interpretation are consistent with the model, the possibility exists that they are merely the result of hitherto undiscovered station

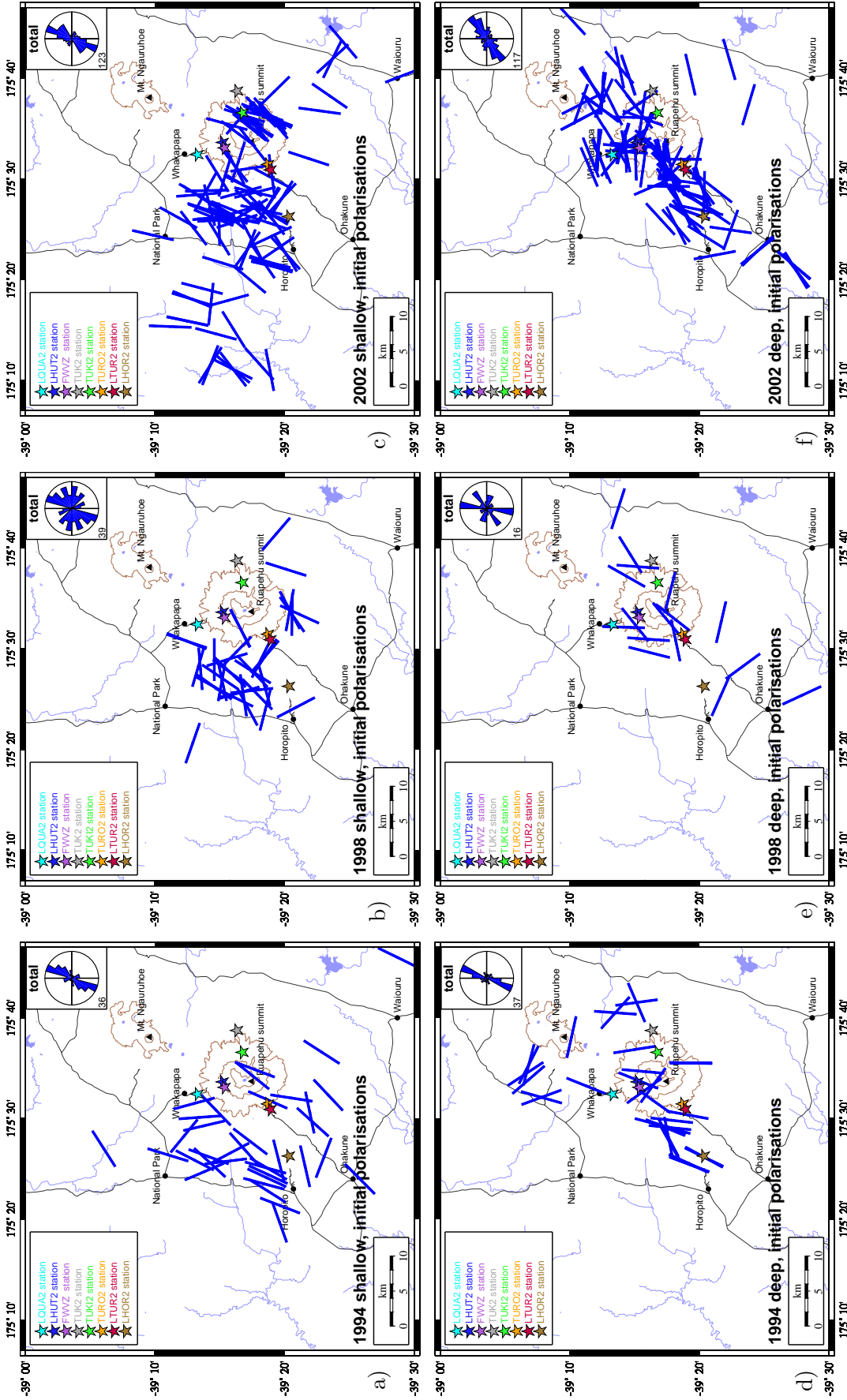


Figure 6.4 Initial polarisations of 1994 (left), 1998 (centre) and 2002 events (right). In 1994 and 2002, both shallow (top) and deep (bottom) events show a strong alignment of initial polarisations in NNE-SSW to NE-SW directions (see histograms in the maps). Consistent initial polarisations emphasise the quality of the obtained fast directions, since initial polarisations are a subsequent byproduct of the splitting algorithm (e.g. it is unlikely that one obtains the correct initial polarisation when the fast direction is wrong). It is remarkable that the deep 1994 events show this alignment. It shows that the majority of earthquake waves have a NNE-SSW alignment when entering the upper layer of anisotropy. This indicates that waves leaving the lower layer (mantle wedge) have constant fast directions. In 1998, initial polarisations are scattered, possibly due to the depressurised dike (see explanation at the end of Section 6.3.3).

effects at LHOR2, combined with the lack of a significant number of measurements at TUK2. Thus, even though indications exist, it must be stated that the available data yields no compelling constraint on the maximum size of the anomalous region.

6.3.3 Observations that require further refinement of the model.

The model, as hitherto described, explains all observed phenomena that were mentioned up to this point. For the time prior to the eruption, it consists of two layers of anisotropy with different fast directions that are separated by an isotropic (or weakly anisotropic) region (i.e. the lower crust between the anisotropic mantle wedge and the upper layer). The interfaces of these layers were not described above, but have been assumed to be abrupt. It was shown that all events (shallow and deep) originate from *below* the upper layer, i.e. the shallow earthquakes ($10 \text{ km} < Z < 35 \text{ km}$) in the crust, and the deep earthquakes ($Z > 55 \text{ km}$) in the subducting slab, below the anisotropic mantle wedge.

In this case there are three possibilities for the behaviour of the deep events:

1. The wave period is short enough to “see” the upper layer and to acquire the splitting parameters of the upper layer.
2. The wave period is long enough not to “see” the upper layer and to therefore keep the splitting parameters of the lower layer.
3. A situation in between 1. and 2., where the waveform becomes complicated and either no valid measurement can be obtained, or, less likely, polarisation-dependent splitting parameters can be observed (see Section 2.1.6).

A logical consequence of this is that in case 1, all measurements from shallow and deep events are expected to show approximately the same delay times. However, even though case 1 applies to the majority of the 1994 deep events, they show longer delay times than the 1994 shallow events[†], and also longer delay times than the 2002 shallow events. This behaviour is not explained by the above mentioned model.

It is therefore proposed that the layer boundary between the upper layer and the isotropic part is not an abrupt change in the anisotropic medium, it rather is a smooth change over several kilometres of distance: from a fast direction parallel to the regional stress direction (NE-SW) *below* the dike system (e.g. at around 10 to 15 km depth) to a fast direction that is

[†]It was argued before that the delay times of the 1994 shallow and deep subsets should not be compared due to the fact that the 1994 shallow events were not reprocessed. However, the 1994 deep events not only show longer delay times than the 1994 shallow events, but also show longer average delay times than the 2002 shallow events, which were newly processed, and are assumed to be similar to the 1994 shallow events. This phenomenon can not be explained with a strict 2 layer model.

determined by the dike system closer to the surface (NW-SE in 1994 and 2002, and NE-SW with scatter in 1998).

Saltzer et al. (2000) show that in this case, waves that enter the upper layer when the dike system is pressurised do not simply re-split into the new fast and slow direction, but can under certain circumstances smoothly rotate into the new fast direction. The delay time, which was acquired in the lower layer, is partly preserved while travelling through the upper layer. In this case, the measured parameters at the surface are the fast direction of *mainly the upper part of the upper layer* (determined by the dike system) and a delay time that is influenced by both layers[‡].

Thus, long delay times of realigned deep events are not contradictory to the extended model. The theory, which was backed up by numerical tests, also predicts that waves with increasingly lower frequencies sample regions from an increasing depth (Saltzer et al., 2000). This provides a further possible explanation for the observation that the fast directions of the low frequency deep events in 2002 show a better alignment in NNE-SSW direction than the high frequency deep events, which show more scatter (Figure 5.21).

Similar examples of frequency dependent behaviour of shear wave splitting were observed by Marson-Pidgeon and Savage (1997), with a theoretical framework developed by Silver and Savage (1994), and Rümpker and Silver (1998).

A further argument for the need of the extended model (instead of only two sharply defined anisotropic layers) is the consistent initial polarisation that is observed in the shallow events of the 1994 and the 2002 deployment (Figure 6.4). In the case of a sharply defined upper layer, the *deep* events would be expected to show the fast direction of the lower layer as initial polarisation (as observed), whereas the *shallow* events should show their source polarisation, determined by the focal mechanism. These polarisations should show a much wider variation than observed in 1994 and 2002. Such consistent initial polarisations in NE-SW direction can be explained by a fast direction parallel to the regional stress (NE-SW) at the base of the upper layer, which was then rotated into NW-SE by the dike system. This is consistent with the “rotation” theory. In 1998, the shallow initial polarisations are more or less random, which might reflect the fact that they travelled through only one layer of anisotropy. In this case the initial polarisations are expected to represent the source polarisations (determined by the focal mechanisms), which show a wide variety of possible polarisations. This is consistent with the fast directions not having been rotated due to a de-pressurised dike system.

In summary, it can be stated that the basic model needed refinement in order to accommodate the observations described in this section. All observations can be explained when allowing a smooth change of fast direction in the upper layer.

[‡]Considering the smooth change between the layers, it would be more appropriate to refer to them as regions instead of layers. Nevertheless, the term will be used for convenience

6.3.4 Numerical modelling

In order to test whether an opening dike could affect the stress field in the crust sufficiently to change the fast direction, a numerical model was used to calculate the expected stress changes in the surrounding crust. It is assumed that all stress related effects in the crust are linear, i.e. the stress field of the injected dike can be added to the regional stress field to calculate the total stress field. Therefore, opening up a dike by a certain amount in a previously undisturbed elastic half space is equivalent to widening an existing dike by the same amount.

In order to change the fast direction, the condition that the total stress in the direction perpendicular to the dike (x-direction) exceeds the regional maximum horizontal stress σ_H parallel to the dike (y-direction) has to be fulfilled: $\sigma_{x,dike} > \sigma_{H,regional} - \sigma_{h,regional}$. In other words, the dike has to be strong enough to overcome the difference between the two horizontal stresses, and therefore to locally swap σ_h with σ_H . Since the exact dimensions of the dike system are unknown, this analysis will concentrate on the solution well between the tips of the dike (e.g. a region $-5 \text{ km} < y < 5 \text{ km}$ in Figure 6.5), where the stress field can be presumed to vary only in the x-direction and the y-component of the dike stress field can be neglected.

The software that was used to calculate the stress changes is Coulomb 2.3, and was developed by Toda et al. (1998). It implements the elastic dislocation formulae of Okada (1992) and the boundary element formulae of Crouch and Starfield (1983). All calculations are made in a half space with uniform elastic properties, namely a Young's modulus of 40 GPa and a Poisson's ratio of 0.25.

Okada's dislocation formulae are used to calculate the 3D displacement field of a shear or a tensile fault in a homogeneous elastic half space. They are based on the formulae for a displacement field caused by a single (point) dislocation in the half space (*displacement Green's function*). Since the medium is elastic, the solution for a single dislocation can be integrated over the area of the modelled "fault" (in the case of a dike, the fault is purely tensile). The solutions of this integral are Okada's dislocation formulae, and represent the complete dislocation field produced by the fault (or dike) in the half space. They can also be expressed as a stress field, derived from the elastic parameters of the medium. Such a stress field is shown in Figure 6.5.

It is assumed that the erupted volume during the 1995/96 eruptions at least equals the volume of material that was injected into the dike system shortly before the eruption, and is therefore responsible for the modelled stress changes. Estimates of the total erupted volume are approximately 0.05 km^3 or less (e.g. Bryan and Sherburn, 1999; Nakagawa et al., 1999; Nairn and Scott, 1996). Geophysical evidence from Latter (1981), together with surface

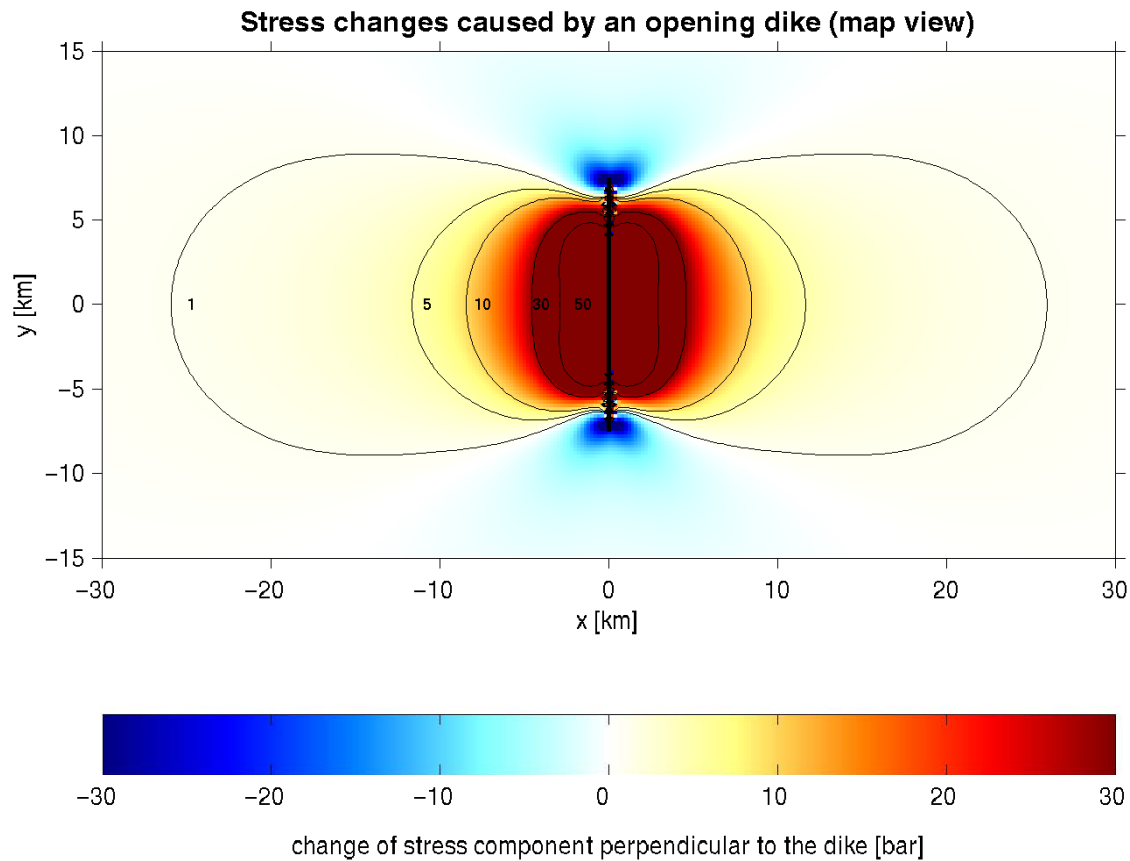


Figure 6.5 Stress changes caused by an opening dike. This 3D numerical model shows the changes of the stress component perpendicular to the opening dike (σ_{xx}). The dimensions of the dike are 15 km in length, 6 km in height (2 – 8 km depth), and it has a thickness of 1 m (the amount of opening). The plane that is shown here is horizontal and lies in the centre of the dike at a depth of 5 km. All edges of the dike are linearly tapered, so that an overall volume of $\approx 0.05 \text{ km}^3$ is injected into the elastic half space. The parameters of the elastic medium are: Poisson's ratio: 0.25; Young's modulus: 40 GPa. The contours show the stress change in bar [kg/cm^2], where 10 bar $\approx 1 \text{ MPa}$. Note that stress changes of 10 bar (1 MPa) reach as far as 10 km away from the dike axis. Changes in the order of >50 bar can be expected within 3 km of the dike.

observations of old eroded dike systems in the Ruapehu area constrain the dimensions of the dike system (see Section 6.3). Combining these values with the injected volume, the following single dike is assumed to be representative of the dike system under Mt. Ruapehu: a vertical “crack” with a length of 15 km and a height of 6 km, ranging from 2 to 8 km depth. The amount of opening in the dike is 1 metre in the centre. This amount of opening is linearly tapered at the edges of the dike, where no opening is assumed. The total injected volume is approximately 0.05 km^3 . Figure 6.5 shows the resulting changes in the x-component of the 3D stress field, which is perpendicular to the dike and therefore exhibits the strongest changes. The figure represents a horizontal plane at 5 km depth. Figure 6.6 shows the displacement of the grid cells, where every cell has a base length of 200 m.

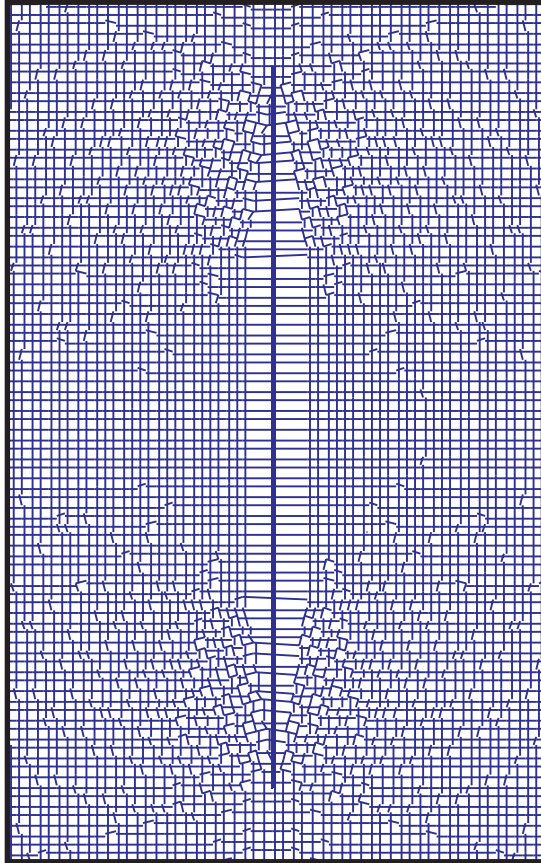


Figure 6.6 *Grid displacement by the numeric dike model.* Every cell in the 3D grid is 200 m by 200 m in area. The plane shown here lies at 5 km depth, which is the centre of the dike. The length of the dike (blue bar in the centre) is 15 km, the amount of opening is 1 m in the centre part of the dike. Within 3.5 km (horizontally) and 1.5 km (vertically) of all edges of the dike, the amount of opening is linearly tapered to zero. In this figure, the amount of opening is exaggerated by a factor of 3000 for visual reasons. The complete model is 30 km by 60 km in size, and consists of a total of 45000 grid cells.

The model presented here is different from the one initially proposed by Miller and Savage (2001) for several reasons:

1. A dike-shaped magma chamber is assumed, instead of a spherical magma chamber, which does not conform to the expected shape in the local stress regime. Also, assuming a spherical pressure source leads to an unrealistic decay of the stress in the near field ($1/R^2$, where R is the radius from the source). The stress decay of a dike (on the symmetry axis perpendicular to the strike) is significantly weaker than this in the near field (e.g. if the distance is smaller than the length of the dike).
2. The stress in the magma chamber and in the rock around it is not determined by the compressibility of magma in a static magma chamber, but rather by the compressibility of the elastic medium surrounding a (quasi-statically) expanding magma chamber (dike). The latter model must be considered more realistic since injecting magma into a chamber will inevitably lead to an expansion of the chamber. The pressures determined from the former model are unrealistically high. That is, the resulting 280 MPa pressure (Miller and Savage, 2001) at 5 km depth is almost twice as high as the lithostatic pressure, and would lead to an immediate rupture of the crust above and around the chamber.

The dike model reveals that even with an injected volume of only 0.05 km^3 , a 10 bar (1

MPa) change in the stress field[§] can be expected up to 10 km away from the dike axis. Stress changes mainly take place between the tips of the dike (in this case $-7.5 \text{ km} < y < 7.5 \text{ km}$). Considering that the whole station network is affected by changes in the fast direction (see Section 6.2), the length of such a dike system under Mt. Ruapehu would be expected to be at least 10–15 km, which is consistent with our assumptions.

Yet it must be pointed out that the results of the numerical modelling can not be regarded as the most probable state of the stress field under Mt. Ruapehu, rather than only as a clue of the magnitude of the expected stress changes. Sneddon (1946) provides a simple formula for the relation between crack opening (w), pressure (p), and crack diameter (a) of a penny shaped crack: $w = cpa/E$ in the center of the crack, where E is Young’s modulus and c is a constant. It shows that with a given amount of opening, the pressure inside a crack (and therefore also the pressure in the near field) is strongly influenced by the crack length (i.e. the diameter) and the elastic properties of the rock. This means that for calculating the pressure in or around a crack with a numerical model, it is necessary to constrain the crack dimensions (w , a) by geophysical or geological means, as it is the case here. The calculated pressure can only be as accurate as the crack dimensions.

Temporal changes in the fast direction were observed as far as 5 km from the inferred dike axis. At this distance, the stress change predicted by the model is approximately 30 bar (3 MPa), and even exceeds 80 bar (8 MPa) in the immediate vicinity of the dike. This means that for the dike to induce a 90° change of the maximum horizontal stress direction up to 5 km from the dike axis, the two horizontal stresses σ_H and σ_h would have to lie within 30 bar (3 MPa) of each other at this location. However, the true dimensions and expansion parameters of the dike are unknown, and the values presented here can only be viewed as preliminary estimates of the true values. Generally, pronounced alignment of EDA cracks can be expected at differential stresses as low as 0.1 MPa (Crampin, 1998) and as much as 300 MPa, when all cracks begin to close (Hrouda et al., 1993). However, this upper limit is far higher than the lithostatic pressure at 5 km depth and seems therefore too large to be reached at this depth in a normal faulting regime like the TVZ.

The magnitudes of the horizontal stresses in this region are not known. However, in a normal faulting regime, the maximum stress is vertical, and can be estimated by $\sigma_V = \rho g z$, where ρ is the average density of the rock, g is the gravitational acceleration, and z is the target depth. Townend and Zoback (2000) point out that the brittle crust appears to be in a state of failure equilibrium according to the Coulomb frictional failure criterium. This means, that if the fluid pressure of the regime is known, the least horizontal stress σ_h can be

[§]Note that this stress change relates to the total stress field of the dike. It is **not** the Coulomb stress field, which describes changes on assumed “receiver” faults with predefined orientations and friction coefficients, and which is used to investigate possible earthquake triggering on the receiver faults.

estimated using

$$\sigma_h = \sigma_V - \rho g z (\lambda - 1)(1 - F)/F \quad (6.1)$$

(Zoback and Townend, 2001); where

$$F = \left(\sqrt{\mu^2 + 1} + \mu \right)^2 \quad (6.2)$$

μ is the friction coefficient (≈ 0.75); λ is the ratio of the fluid pressure to the lithostatic load (vertical stress), i.e. $\lambda = p_f/S_V$. Using an average density of 2700 kg/m^3 and a hydrostatic fluid pressure ($\lambda \approx 0.37$), σ_V and σ_h are found to be 130 and 70 MPa, respectively, at a depth of 5 km. If the fluid pressure is slightly higher than hydrostatic ($\lambda = 0.5$), the resulting σ_h is approximately 80 MPa. Due to extensive fracturing and the permeable nature of volcanic sediments, the brittle crust around Mt. Ruapehu is presumed to be an open hydraulic system. Therefore, the hydrostatic fluid pressure is probably the more realistic case. Unfortunately, the maximum horizontal stress σ_H is not as easy to estimate as the other two stresses. Plausible estimates range from σ_H being the average of σ_V and σ_h , to a situation in which σ_H and σ_h are very close together. The latter case represents conditions consistent with the hypothesis of dike inflicted changes in anisotropy better than the former case, since the numerical model predicts stress changes of around 3 MPa in a few kilometres distance from the dike. It might also be assumed that the dike system had exerted pressure on the surrounding crust prior to the injection that led to the 1995/96 eruptions, since much of the injected magma remains in the crust and is not ejected. Therefore, a “pre-loaded” stress field in NW-SE direction may have existed in which σ_h was already close to σ_H before the 1995/96 injection. The above-mentioned stress changes would then merely be the final amount that is necessary to change the main horizontal stress directions.

Evidence for a small difference between σ_h and σ_H in the area comes from the shallow measurements made in 1998. If the difference between the two horizontal principal stress directions were large, then a much stronger alignment would be expected. Further evidence for the difference between σ_h and σ_H being in the range of stresses caused by a volcanic system comes from frequent observations of radiating dikes emerging from the centre of volcanoes (see also Figure 6.1). In this case, the pressure of the magma intrusion, together with the load of the volcanic edifice creates a local stress regime in which σ_H points radially towards the main magma intrusion. Furthermore, Takada (1994) argued that polygenetic[¶] volcanoes like Mt. Ruapehu are indicators of a small differential stress in the crust. However, the best way of obtaining quantitative stress and fluid pressure values in the crust is via careful earthquake focal mechanism analysis. Such an analysis has not yet been carried out in the region subject to this thesis.

[¶]Polygenetic volcanoes are volcanoes that repeatedly erupt from the same vent over periods of 10^4 to 10^5 years. Monogenetic volcanoes erupt only once over a short period of time.

Overall, it must be concluded that this model represents only a first attempt to model the complex behaviour of dike intrusion at Mt. Ruapehu. Many different combinations of injected volume, dike dimensions and opening amounts are plausible, all of which affect the changes in the stress field. Further modelling is thus necessary, but lies beyond the scope of this study. However, these preliminary results suggest that under certain circumstances, the stress changes inflicted by an opening dike in the crust can be large enough to affect the effective stress field in the vicinity, and to therefore change the alignment of EDA cracks.

6.3.5 Could the fast direction have changed by exactly 90° ?

When interpreting changes in the fast direction, the question arises whether the measured temporal changes (of the order of a maximum of 80°) in reality represent changes of 90° , masked by scattering or measurement uncertainties.

If – as a working hypothesis – the fast direction changed by exactly 90° between 1994 and 1998, then, according to the model, the fast directions of the upper and the lower layer must have been different by exactly 90° . In a situation where two layers lie on top of each other with perpendicular fast directions, the fast direction of the upper layer is equal to the slow direction of the lower layer. In this case, a wave entering the upper layer from below will already have its S-wave polarised in the new fast and slow direction – with the only difference being that the new slow S-wave enters the upper layer first, since it was the fast S-wave of the lower layer. Then the delay time of the wave from the lower layer will simply be reduced while travelling through the upper layer (Crampin and Lovell, 1991). The degree of this reduction depends on the thickness and grade of anisotropy in the two layers. When the upper layer yields a smaller delay time than the lower one (e.g. if it is thinner or only weakly anisotropic), then the delay time that was acquired in the lower layer will be reduced, and the polarisation of the first S-wave still shows the fast direction of the *lower* layer. If the upper layer yields a larger delay time than the lower one, then the delay time of the wave will get reversed, and the first S-wave polarisation shows the fast direction of the *upper* layer. If both layers yield the same delay time, then the two layers will exactly cancel each other out and no splitting is observed.

It could be argued that exactly this happened in 1994, when the dike system was pressurised and the upper layer had a fast direction in NW-SE direction. The anisotropy of the upper layer then must have been strong enough to completely reverse the delay time of the lower layer (with a fast direction of NE-SW), and then to imprint its own delay time (with a fast direction of NW-SE). However, such a strong anisotropy in the upper layer should have caused extremely long delay times in shallow events, which were not influenced by the strong mantle anisotropy and therefore did not have to be reversed. Also, the delay times of the deep events would then be expected to be smaller than the delay times of the shallow events.

These phenomena were not observed. Even though the 1994 shallow subset was not reprocessed and therefore very long delay times were not detectable, it still shows very consistent delay times around 0.1 s with a standard deviation of only 0.06 s (Table 5.1). This can only be explained by assuming that the upper layer in 1994 yielded an average delay time of 0.1 s, which is not enough to reverse the long delay times of the deep events.

Therefore the hypothesis that the fast directions of the two layers are different by exactly 90° has to be rejected if one assumes this simple model. Yet it could be argued that due to the proposed smooth “rotation” of the fast direction in the upper layer (as explained in Section 6.3.3), an exact 90° change is possible without reversing the delay times of the lower layer. In this case, the experimenter at the surface would not observe longer delay times for the shallow events than for the deep events. Thus the hypothesis that the fast directions of the two layers are different by exactly 90° can not easily be rejected on the basis of the extended model.

However, when comparing the measured average fast directions (Table 5.1), it is clear that none of the stations changed by exactly 90° . The average *deep* fast direction changed by 80.2° between 1994 and 1998; the hypothesis that this change was 90° can be rejected with a confidence level of around 90%. The average *shallow* fast direction changed by only 41.7° between 1994 and 1998; in this case it can be rejected with a confidence level of more than 99.9% that the change was in reality 90° .

The observed maximum change of 80.2° might be an indication for the regional fast direction in the mantle wedge being different from the regional fast direction in the crust by a small amount (e.g. in the order of 10° to 20°). In this case the maximum horizontal stress direction caused by the pressurising dike (which is perpendicular to the regional σ_H in the crust, and therefore also perpendicular to the regional fast direction in the crust) is slightly different from being perpendicular to the fast direction in the mantle. Therefore the observed changes in the fast direction are also slightly different from 90° in this case.

In summary, it can be stated that the observations do not allow a change by exactly 90° if the simple two layer model is assumed. If the refined model is assumed (Section 6.3.3), it is possible that the fast directions changed by exactly 90° but very unlikely according to the standard error intervals of the changes. The reason for the deviation from 90° might be a slight difference (e.g. 10° – 20°) between the regional fast direction in the mantle and the regional fast direction in the crust.

6.4 Alternative models

Even though the dike model explains the observations very well, alternative models must be considered. Such models would need to explain the temporal changes in anisotropy,

observed over short time periods, and the different behaviour of fast directions dependent on the earthquake depth. One possible scenario that explains some of the observations will be presented in this section.

Crampin et al. (1996), and Zatsepin and Crampin (1997) show that the theory of extensive dilatancy anisotropy (EDA) predicts a situation where the behaviour of waves travelling through a medium with aligned cracks is substantially different from the behaviour that was described so far. For high values of the excess pore pressure (i.e. the pore pressure in excess of the undisturbed equilibrium) in a cracked medium, it is predicted that the speed of a wave that is polarised perpendicular to the cracks becomes faster than the speed of the one that is polarised parallel to the cracks. This means that the leading (faster) split shear wave in near-vertical directions is polarised perpendicular to the maximum horizontal stress direction – which is the opposite behaviour to the normal case. It is also predicted that all vertical cracks are open in this case. This means that the pore (fluid) pressure has to be higher than the maximum horizontal compressive stress, which is assumed to be close to the vertical stress (and therefore lithostatic in a normal faulting regime) when the fluid pressures are high (see Equation 6.1). Thus a fluid pressure close to the lithostatic pressure is required to trigger the described behaviour.

However, these theoretical predictions are backed up by only a few observations, and to the knowledge of the author, no plausible physical explanation of the phenomenon has yet been given. Angerer, Crampin, Li, and Davis (2001) investigated anisotropy during overpressured fluid-injection experiments in a hydrocarbon reservoir, and report of 90° changes in the fast directions related to the injection. These changes are interpreted as the described 90°-flips due to anomalous pore pressure. Crampin et al. (2002), in a project that was designed to search for 90°-flips, measured fast directions at several seismic stations in Iceland, and find three stations above a fault zone with fast directions perpendicular to the regional trend. It is claimed that 90° flips due to high pore pressure in the fault zone are responsible for this effect. However, the alignment of fast directions at these stations is approximately parallel to the strike of the fault zone, which is in good agreement with observations of fault controlled anisotropy made elsewhere (e.g. Zinke and Zoback, 2000; Zhang and Schwartz, 1994). It is not explained why a 90°-flip should be assumed when conventional theories can explain the phenomenon (see Section 2.2.1).

In the case of Mt. Ruapehu, it can be argued that prior to the eruption, the pore fluid pressure in the surrounding rock (i.e. at least the area covered by the stations) increased drastically and caused the described 90° flip of the fast direction. This would then lead to fast directions that are oriented perpendicular to the normal fast direction (i.e. at normal pore fluid pressures). From this point on, the implications of this model are similar to the implications of the above described dike model, i.e. the influence on the shallow and deep

measurements would be approximately the same.

The model requires a large area ($>100 \text{ km}^2$) being affected by an almost lithostatic pore fluid pressure, and a mechanism to generate and maintain this pore fluid pressure over time scales in the order of months and years. It has to be considered that the crust in the affected region mostly consists of brittle volcanic sediments, underlain by some form of weathered and schistose greywacke at depths around two to three km (e.g. Latter, 1981). In such an open hydraulic system, the sustenance of an almost lithostatic pore pressure over such a large area is unlikely, and can not be explained by merely high pressurised feeder dikes, as suggested by Crampin et al. (2002) when interpreting Miller and Savage (2001).

Another implication of this model is that an observed change in fast directions should be very close to, or exactly 90° . However, it was shown above that with a confidence level of more than 90%, the fast directions at Mt. Ruapehu did not change by exactly 90° , but by around 80° and less.

In summary, the explanation for the temporal changes in the fast direction based on Crampin et al. (1996, 2002) seems unlikely. However, both this and the first model for the temporal changes in anisotropy have their source in the volcanic activity at Mt Ruapehu, and are related to the eruptions of 1995/96, therefore their differences do not affect the conclusions drawn from the first model.

6.5 Seismicity associated with the changes in anisotropy

Considering that between the deployments in 1994, 1998 and 2002, the parameters of the Earth's crust changed significantly over a wide area^{||}, the question arises whether these changes were accompanied by an increased seismicity in the area. Figures 6.7 and 6.8 show the shallow crustal seismicity from 1988 to 2002 within a radius of 20 km around Mt. Ruapehu. Figure 6.7 shows the number of events with $M_L \geq 0$ in a depth shallower than 10 km per month. Figure 6.8 shows all earthquakes with $M_L \geq 2$ in a depth of up to 25 km. The event data was supplied by the Institute of Geological and Nuclear Sciences in New Zealand.

Small earthquakes show a slight increase in seismicity shortly before the 1994 deployment, then a peak of activity between the eruptions of 1995 and 1996 and a further dominant peak of activity in the early months of 1997 is observed. During the time after the eruptions, the level of activity remained on a relatively low level. It is not clear whether the slight onset of activity in late 1993 and early 1994 is a real phenomenon or whether it is associated with the subsequent improvement of earthquake monitoring capabilities in the area.

^{||}the area spanned by the recording stations, over which the changes in the fast directions were observed, is larger than 100 km^2

The larger earthquakes ($M_L \geq 2$) show two small peaks of activity in 1989 and 1992 respectively, which are followed by a small increase of activity in 1994 and a distinctive peak several months before the 1995 eruption. Hurst and McGinty (1999) attributes this peak of activity to earthquake swarms some 15 to 20 km to the west of Mt. Ruapehu, with several large events up to a magnitude of $M_L = 4.8$. These earthquake swarms are followed by high activity during the time of the eruptions, and another dominant peak in late 1997, only several months before the 1998 deployment. It is remarkable that the two peaks of activity in 1997 for small and large earthquakes do not coincide but lie several months apart. Following the peak in late 1997, the number of large earthquakes decreased during 1998 and was followed by a last minor peak in 2001.

Since volcanic eruptions are almost always accompanied by seismic activity, it is not surprising to find increased seismicity between the deployments of 1994 and 1998. However, there is no evidence that the increased seismicity is directly connected to the change in the anisotropic parameters. Since it is not clear if the onset of seismicity in late 1993 and early 1994 is a real phenomenon or an artefact of improved earthquake monitoring, it can not be attributed to a pressurising dike or a change in fast direction. In addition to this, no information is available as to when the dike was pressurised before 1994. There is a medium sized peak of activity of larger events in 2002, which could possibly be accompanying a movement of magma into the dike system and therefore a pressurisation. However, such an assumption can only be speculative.

From the evidence presented here, it is not clear whether changes in anisotropy or a dike pressurisation coincide with an increased seismicity. Furthermore, Bryan and Sherburn (1999) report a lack of deep volcano-tectonic earthquakes during the 1995/96 eruption period, so that these can be excluded as indicators or precursors of stress changes in the dike. However, the question whether changes in seismic anisotropy are accompanied by increase seismicity can only be answered to its full extent by further and constant monitoring of seismicity and anisotropy at Mt. Ruapehu.

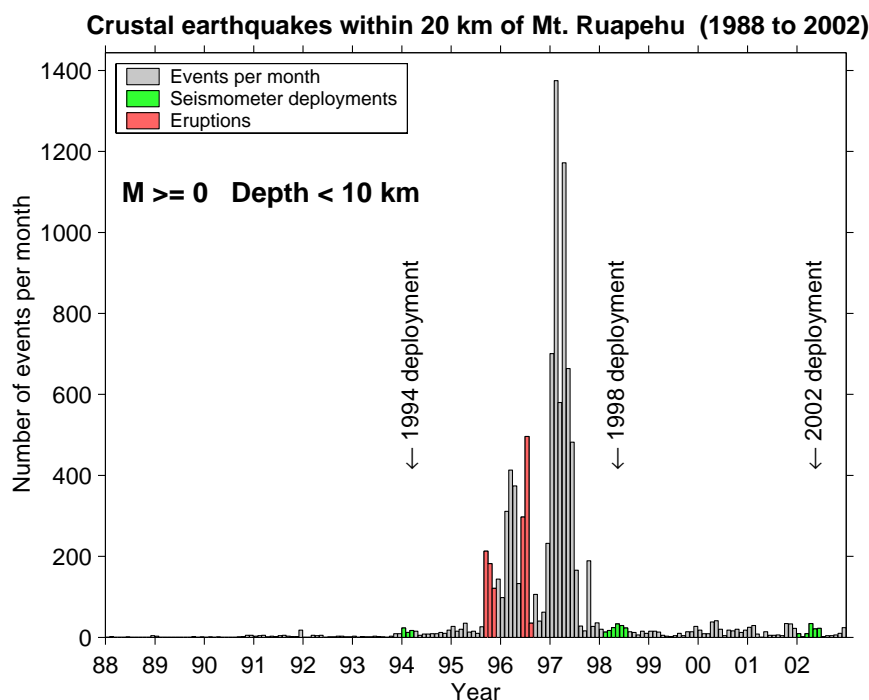


Figure 6.7 Shallow crustal seismicity rate ($M_L \leq 0$) within 20 km of Mt. Ruapehu between 1988 and 2002. Included are events with magnitudes ≥ 0 and a depth shallower than 10 km. The height of the bars indicates the number of earthquakes observed per month. Red bars mark the times of the eruptions in 1995 and 1996; green bars mark the times of the three deployments. An increased seismic activity is observed mainly during the eruptions and up to a year afterwards, with a dominant peak in the early months of 1997.

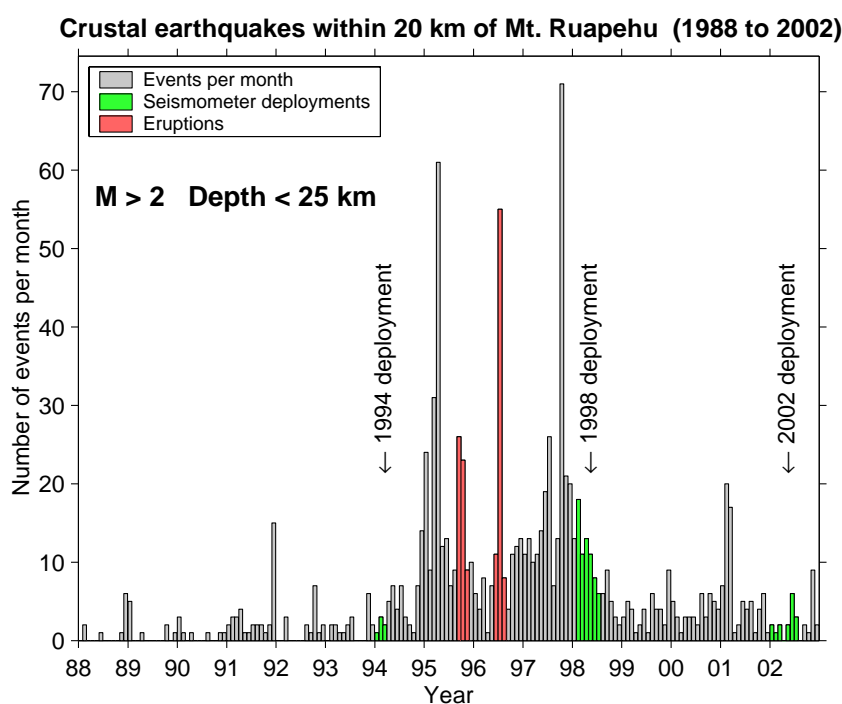


Figure 6.8 Crustal seismicity rate ($M_L \geq 2$) within 20 km of Mt. Ruapehu between 1988 and 2002. Included are events with magnitudes ≥ 2 and depths up to 25 km. The annotation scheme is similar to Fig. 6.7. Peaks of activity can be observed not only during and after the eruptions, but also several months before. No obvious correlation between the seismic activity and the changes in anisotropy can be observed.

CHAPTER 7

SUMMARY & CONCLUSIONS

The aim of this study was to investigate near 90° changes of seismic anisotropy beneath Mt. Ruapehu volcano, associated with a volcanic eruption in 1995/96. Three broadband seismic deployments were carried out on Mt. Ruapehu in 1994, 1998, and 2002, and polarisations of the leading shear wave from earthquakes up to a depth of 250 km were measured. The fast directions show a consistent alignment in all deployments, but differences between shallow crustal events (with a depth < 35 km) and deeper events from the subducted slab (with a depth > 55 km) are observed.

Before the eruption (in 1994), fast directions of both shallow and deep events were aligned approximately NW-SE, close to perpendicular to the direction of inferred maximum horizontal principal stress (σ_H) in the region. This orientation is also perpendicular to the average regional fast direction of shear waves, reported in a national study from nearby stations in the centre of the North Island. After the eruption (in 1998), the alignment of fast directions from shallow events is more scattered, with an overall trend of NNE-SSW, which is parallel to the direction of σ_H . The fast directions of shear waves from deep events in 1998 show a strong alignment of NNE-SSW, also parallel to the inferred direction of σ_H . Measurements of shear wave splitting from the most recent deployment (2002) yield different fast directions for shallow and deep events. Fast directions from deep events in 2002 are aligned NNE-SSW, similar to the deep events from 1998. Shallow events in 2002 show an alignment of NNW-SSE to NW-SE, and are therefore similar to 1994 (before the eruption).

The station locations in the 1994 and the 1998 deployment were different by at least 1 km, up to around 10 km; the station locations in 2002 covered all but one previously occupied station locations from both 1994 and 1998.

It was investigated whether the difference in station locations before and after the eruption, combined with lateral heterogeneities in the anisotropic medium could have caused the differences in the measured fast direction, and thus caused an apparent temporal change. The data was also tested for the influence of parameters like frequency, source location, ray path, back azimuth and initial polarisation. It was shown that none of these parameters are likely

to explain the observed changes. Also, differences in the station locations can be excluded as the source for the observed differences in fast directions.

It must therefore be concluded that the differences in the fast direction between 1994 and 1998 represent temporal changes, and that the anisotropic system further changed between 1998 and 2002.

The magnitude of these temporal changes is different for shallow and deep events, with the deep events changing by an average of 80° between 1994 and 1998, and the shallow events changing by around 42° . The hypothesis that these changes did not occur, and that the differences in the fast directions are only due to measurement uncertainties, can be rejected with a confidence level of more than 99.9%. Between 1998 and 2002, the shallow events show a change in the average fast direction by 43° . This change is also significant with more than 99.9% confidence level. The deep fast directions between 1998 and 2002 changed by only 18° , with a confidence level of approximately 90%.

Analogous to a wide range of studies elsewhere, the anisotropy in the shallow crust beneath Mt. Ruapehu is most likely caused by stress induced, preferred alignment of fluid filled cracks, microcracks, and pore space (*extensive dilatancy anisotropy*, EDA).

The measured delay times are not as consistent as the fast directions, and show a significant amount of scatter. Shallow events have average delay times of around 0.1 s, with some events showing up to 0.2 s. Deep events have long paths in the anisotropic mantle wedge, and therefore show much larger delay times, with an average of around 0.25 s and extreme cases of up to 0.8 s.

We proposed that the changes in anisotropy were a result of changes in the crustal stress field, caused by a (pre-eruption) pressurised and subsequently (post-eruption) depressurised magmatic dike or dike system under Mt. Ruapehu. This model explains all observed phenomena, and is consistent with the results from other geophysical and geological studies in the Mt. Ruapehu region and in other volcanic areas on Earth. The alignment of the dike is NNE-SSW, parallel to the regional stress field, and consistent with the alignment of mapped surface faults and dikes in the area. It coincides with a body of low-velocities and high S-wave attenuation, reported in a geophysical study (Latter, 1981). The proposed length of the dike (system) is at least 10 km to 15 km, with a height of around 6 km to 10 km, but reaching no deeper than 10 km depth.

Prior to the eruption, such a dike system would generate a local stress field with a new (local) σ_H perpendicular to both the old (regional) σ_H and the dike axis. It is inferred that these local stress conditions in 1994 led to a strongly (around 5%) anisotropic region beneath the volcano with a fast direction of NW-SE, which was imprinted on shallow and deep events that were travelling through the region.

We propose that, after the eruption, which ejected material with an overall volume of 0.02–0.05 km³, the dike system was depressurised, therefore causing the local stress field to relax and to return to the regional trend, around NNE-SSW, but with significant scatter. Fast directions of shallow events therefore showed considerable scatter in 1998, with an overall trend around NNE-SSW. Deep events in 1998, which have longer periods than the shallow events, yielded splitting parameters which we propose were acquired while travelling through the anisotropic mantle wedge above the subducted slab. These were long delay times (>0.2 s), and fast directions around NNE-SSW to NE-SW, which coincide with the regional fast directions in the crust.

The realignment of the shallow events in 2002 suggests that the dike system is refilling, therefore repressurising the crust, and causing a stress field similar to 1994. This causes the shallow events to acquire fast directions similar to 1994 (within 2°), around NW-SE. The fast directions of the deep events do not realign to NW-SE in 2002, still mainly showing the splitting parameters acquired in the mantle wedge, and suggesting that the pressure in the dike system is not (yet?) as high as in 1994 (long-period events, which are mainly deep events that have already experienced shear wave splitting on their path through the mantle wedge, do not acquire this new fast direction as easily as the shorter-period shallow events).

The maximum depth of the region affected by the temporal changes is 10 km, and the minimum affected area is around 100 km², spanned by the station network. There is weak evidence that suggests that in 2002, the affected area is not much larger than the area spanned by the network, limiting the observed changes to around 5 km within the dike axis. However, this assumption might be subject to review in future experiments at Mt. Ruapehu.

Numerical modelling shows that a dike of the proposed dimensions, forced to expand by an injection of around 0.05 km³ magma, causes stress changes in the crust in the order of 3 to 5 MPa or more at distances up to 5 km from the dike. Stress changes in the order of 0.1 MPa can be expected several tens of kilometres away from the volcano. Such stresses, which are only approximate values due to a strong dependency on the amount of injected material and the size of the dike, are well capable of altering the direction of σ_H when the differential horizontal stress in the region is small (i.e. in the order of the stress changes caused by the dike), as expected in this region.

An alternative model for the mechanism of the changes in anisotropy was considered. In this model, a wide zone of overpressured pore fluid causes the change in anisotropy, rather than a change in the direction of σ_H . Theoretical models show that above such a zone, the measured fast directions can flip by 90°. However, this model is unlikely for several reasons, one of them being that it requires the sustenance of a near-lithostatic pore fluid pressure over an area of approximately 100 km² in heavily fractured shallow volcanic sediments, which is unlikely.

7.1 Implications

If the cause for the newly aligned fast directions of the shallow events in 2002 is a refilling dike system, then the question immediately arises whether this process will lead to an eruption in the near future. It can be assumed that a refilling dike system will almost certainly lead to an eruption eventually. However, it is not known how early before an eruption the fast directions of the shallow earthquakes change, nor if the fast directions of the deep events always change before an eruption. Therefore there is no minimum or maximum constraint on the time to the eruption. This question can only be answered by continued monitoring of the fast directions over at least a full eruption cycle.

7.2 Answered questions

In the introduction of this thesis, several questions were raised about the changes in anisotropy and their relation to Mt. Ruapehu. With the data presented in this study, many of these questions can now be answered.

Did the direction of seismic anisotropy change between 1994 and 1998?

The shallow crustal seismic anisotropy at Mt. Ruapehu changed between 1994 and 1998. This change was most significant in the deep subsets, where the average fast direction changed by about 80° . Furthermore, it was shown that the fast direction of the shallow events changed again between 1998 and 2002, possibly indicating a refilling dike system under Mt. Ruapehu.

Where did this change in anisotropy occur?

Even though the overall trend of the fast directions is similar at almost all of the stations in 2002, there are significant differences between the different stations that can only be explained by local differences in the anisotropic medium. This and further arguments about the raypaths of shallow events and the delay time versus distance relationship lead to the conclusion that the change in anisotropy happened in a shallow region of the crust (< 10 km depth), which is at least as wide as the area spanned by the stations in the 2002 deployment, but possibly not much larger.

Can it be associated with a volcanic eruption at Mt. Ruapehu?

Even though there is no final proof that the changes in anisotropy are related to the eruptions of 1995 and 1996, it is the most likely explanation. Generally, processes in the earth's crust are slow and cover geologic time periods. The only known processes that significantly

change their surroundings in time periods of less than a few years are earthquakes and volcanic eruptions. Since no major earthquakes were observed between the three deployments, it must be assumed that the changes in anisotropy are of volcanic origin.

Will such a change happen again?

From the evidence presented here, it is inferred that the anisotropy is already in the process of changing, possibly towards a state that is similar to 1994, 1–2 years before the eruption sequence in 1995/96.

What are the processes that led to such a change?

A plausible mechanism for causing the observed changes in anisotropy is the pressurisation of the surrounding crust by a volcanic dike system under Mt. Ruapehu prior to an eruption. This change in the stress field changes the preferred alignment of fluid filled cracks, microcracks and pore space in the crust and therefore leads to a changing polarisation of the leading S-wave travelling through the upper crust.

Will this behaviour lead to a usable method for forecasting volcanic eruptions?

Unfortunately, this question can only be answered in part. While it was shown that changes in anisotropy occurred in association with an eruption sequence at Mt. Ruapehu, it is not clear whether this pattern will repeat before future eruptions.

It can be speculated that future eruptions are accompanied by changes in anisotropy. In this case, the method presented here has the capability of predicting eruptions in the mid term. This means that the forecasting period is a matter of months or years, but certainly not days or weeks. However, this question can only be answered by future monitoring of anisotropy at Mt. Ruapehu.

Another question is the efficacy of this method on other volcanoes. Since volcanoes exist in different kinds of stress regimes, it is possible that these changes can be observed at certain volcanoes in similar tectonic regimes to the one at Mt. Ruapehu. However, it is also possible that the observed phenomenon is unique to Mt. Ruapehu. This question can only be answered by monitoring anisotropy on other volcanoes in New Zealand and elsewhere.

7.3 Testable predictions

The described model predicts several phenomena that might be observed at Mt. Ruapehu in the future. While it is not claimed that these phenomena will occur, the possibility is provided to test the model and to readjust it, if necessary. Some of these predictions are:

- In the case of a refilling and repressurising dike system, the fast directions of the deep events should eventually realign towards NW-SE. The events that are aligned in this direction are expected not to show very long delay times (i.e. <0.3 s). However, no information is available whether this behaviour can be observed before every eruption cycle, or how long before an eruption the changes will take place.
- Even if the majority of the deep events realign, there should always be events with long enough periods (low frequencies) that can not be re-split by the upper layer. These events then yield either no valid measurement, or the fast direction and delay time of the lower layer (NE-SW, $\delta t > 0.3$ s). However, some of these events might partially get re-split in a strongly anisotropic upper layer, so that their waveforms might become complicated and no splitting measurement can be obtained.
- During or after a future eruption at Mt. Ruapehu in the order of the 1995/96 eruption, the fast directions of shallow events would be expected to realign towards NNE-SSW, accompanied by a large amount of scatter. The deep events would be also expected to change towards NNE-SSW.

7.4 The suitability of FWVZ as a long term monitoring station

The station FWVZ (formerly FWTB) is a permanent three component, broadband seismograph station that is installed at the Far West T-bar in the Whakapapa ski field on Mt. Ruapehu. It is part of the Eruption Detection System (EDS) and the GEONET programme. Such a permanently installed station provides a first step towards continuous monitoring of seismic anisotropy at Mt. Ruapehu. It is therefore proposed that a continuous processing system is established, which allows measurement of the fast direction of incoming waves at FWVZ in near real-time*. This might provide valuable data for the further refinement of the model and mechanism of the changes in anisotropy, and therefore towards a better understanding of the processes inside Mt. Ruapehu. Furthermore, in the case that a strong realignment of fast directions from deep events towards NW-SE is observed, an alert for a possibly increased risk of a volcanic eruption can be given.

However, when using FWVZ as a monitoring station, it must be considered that this station yields the most scattered results of all stations, combined with anomalous station effects above wavelet frequencies of 3.5 Hz. These effects might mask the changes in anisotropy, rendering the warning system less reliable. It must therefore be concluded that in order to improve and develop this new monitoring method, the installation of further 3D broadband stations on Mt. Ruapehu is required.

*The presently used algorithm is semi-automatic, i.e. it needs to be controlled by a human. The author is not aware of a fully automatic algorithm that obtains reliable splitting measurements at the present time.

7.5 Unanswered questions and future recommendations

Among the many answers that can be derived from the data in this study, there are also several unanswered questions that could not be addressed with the available data. Some other questions go beyond the scope of this study, and have to be answered by scientists working on other volcanoes. The most important of these questions are:

1. How soon before and after an eruption do these changes take place?
2. What is the horizontal extent of the region that is affected by the changes in the fast direction?
3. Is the observed behaviour between 1994 and 2002 a representative cycle in a repetitive pattern?
4. Is this process unique to Mt. Ruapehu, or can it be observed at other volcanoes elsewhere in the world?

These questions directly lead to the necessity of future studies on Mt. Ruapehu and on other volcanoes.

What should be done in the future – at Mt Ruapehu and on other volcanoes?

In order to obtain information about the repetitive pattern of changes in anisotropy, about the reliability of this method as eruption forecasting tool, and about the spatial extent of these changes, further monitoring is certainly necessary at Mt. Ruapehu.

Such further monitoring would require the long term installation of several three component, broadband seismograph stations at different distances and azimuths from the main eruptive vent, Crater Lake. An efficient configuration would be the alignment of stations on three radial lines outward from Crater Lake, with stations installed every three kilometres up to a distance of at least 20 kilometres. Such a network could also be implemented in the existing Eruption Detection System (EDS). At least one eruptive cycle should be covered by the installation, so the behaviour of the changes near the time of the eruption can be investigated. This configuration would allow investigation of the spatial extent of the anomalous area as a function of time. Ideally, the investigation should be combined with other stress monitoring methods like earthquake source mechanism studies and deformation measurement via the global positioning system (GPS), strain- and tilt-meters.

Such an experiment, combined with further modelling, might establish a relation between the size of the affected area and the pressure in the dike system. This would provide an indirect way of measuring the pressures inside a volcano, and therefore provide a direct handle on the processes that lead to volcanic eruptions.

APPENDIX A

MATHEMATICAL APPENDIX

A.1 Calculating the Christoffel matrix for the isotropic case

In Section 2.1, it was shown how to derive the Christoffel matrix and the respective wave velocities for an arbitrary anisotropic medium. Since the isotropic case is only a special kind of general anisotropy, it will now be used as an example for calculating the wave velocities.

The start of the derivation shall be the elastic tensor in the isotropic case (Babuška and Cara, 1991; Lay and Wallace, 1995, p.49):

$$c_{ijkl} = \lambda \delta_{ij} \delta_{kl} + \mu (\delta_{ik} \delta_{jl} + \delta_{il} \delta_{jk}), \quad (\text{A.1})$$

or:

$$(C_{ij}) = \begin{pmatrix} \lambda+2\mu & \lambda & \lambda & 0 & 0 & 0 \\ \lambda & \lambda+2\mu & \lambda & 0 & 0 & 0 \\ \lambda & \lambda & \lambda+2\mu & 0 & 0 & 0 \\ 0 & 0 & 0 & \mu & 0 & 0 \\ 0 & 0 & 0 & 0 & \mu & 0 \\ 0 & 0 & 0 & 0 & 0 & \mu \end{pmatrix}, \quad (\text{A.2})$$

where λ and μ are the two Lamé parameters. These are the only two independent parameters in the isotropic case. δ_{ij} is the Kronecker delta function, i.e. $\delta_{ij} = 1$ for $i=j$, otherwise $\delta_{ij} = 0$. Note that the Einstein summation convention is used throughout this example.

From Equation 2.11 follows:

$$m_{il} = \frac{1}{\rho} \left(\lambda \delta_{ij} \delta_{kl} n_j n_k + \mu (\delta_{ik} \delta_{jl} + \delta_{il} \delta_{jk}) n_j n_k \right), \quad (\text{A.3})$$

where n_i are the components of the propagation direction vector \vec{n} . If \vec{n} is parallel to the x_1 -axis [$\vec{n} = (1, 0, 0)^T$], then the term $n_j n_k$ is always zero, unless $j = k = 1$. This, however, means that all terms for m_{il} vanish, unless $i = l$. Therefore only diagonal elements remain

in (m_{il}) . In these diagonal elements ($i = l$), only terms with $j = k = 1$ (see above) remain. As a result of this, m_{il} reduces to:

$$m_{il} = \underline{M} = \frac{1}{\rho} \begin{pmatrix} \lambda + 2\mu & 0 & 0 \\ 0 & \mu & 0 \\ 0 & 0 & \mu \end{pmatrix}. \quad (\text{A.4})$$

This is the Christoffel tensor in the isotropic case under the condition that the propagation direction \vec{n} is parallel to the x_1 -axis. However, since isotropic conditions apply, the coordinate system (x_1, x_2, x_3) can always be chosen so that this condition is true. Therefore, the first eigenvector is always the propagation direction itself and (A.4) represents a general solution.

The eigenvalues of this diagonalised matrix can be read from the diagonal components. It is obvious that c_2^2 and c_3^2 are degenerate. They correspond to a set of eigenvectors in the $x_2 - x_3$ plane and therefore represent a polarisation in the $x_2 - x_3$ plane.

$$\begin{aligned} c_1^2 &= (\lambda + 2\mu)/\rho \\ c_{2,3}^2 &= \mu/\rho \end{aligned} \quad (\text{A.5})$$

Therefore $V_S = V_{S1} = V_{S2}$, and no S-wave splitting occurs:

$$\begin{aligned} V_P &= c_1 = \sqrt{\frac{\lambda + 2\mu}{\rho}} \\ V_S &= c_{2,3} = \sqrt{\frac{\mu}{\rho}} \end{aligned} \quad (\text{A.6})$$

The wave speeds thus obtained are the well known S- and P-wave speeds in an isotropic medium.

APPENDIX B

DATA PROPERTIES

B.1 Splitting results without multiple frequency filters

(see next pages)

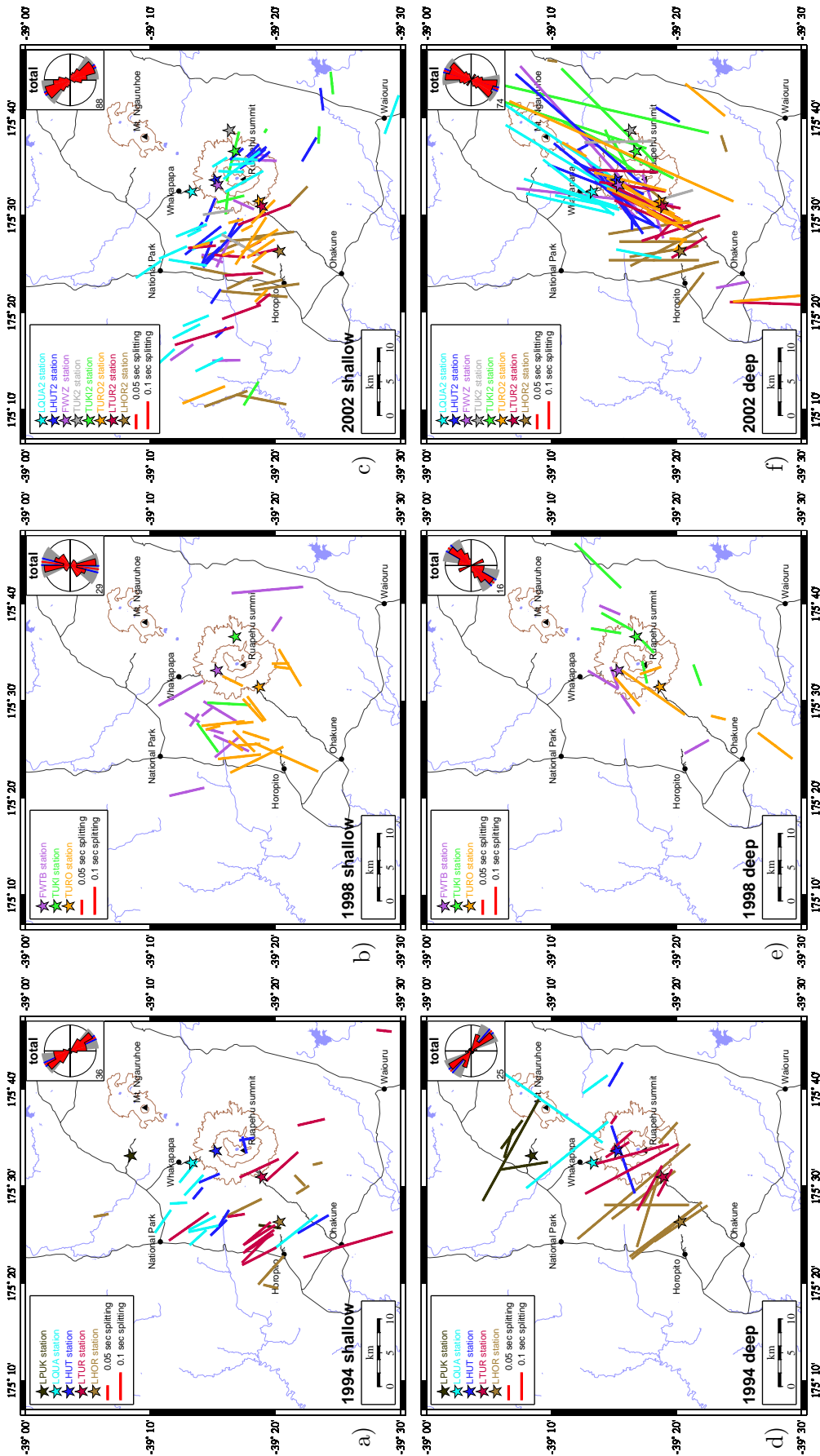


Figure B.1 Splitting measurements with only one measurement per event and station. This figure is a reprint of Figures 5.2 to 5.4, with the difference that only one measurement was included per station for every earthquake (i.e. no multiple measurements from one event with different filters). When comparing the two methods, it is clear that the difference between them is only minor and does not significantly affect the results.

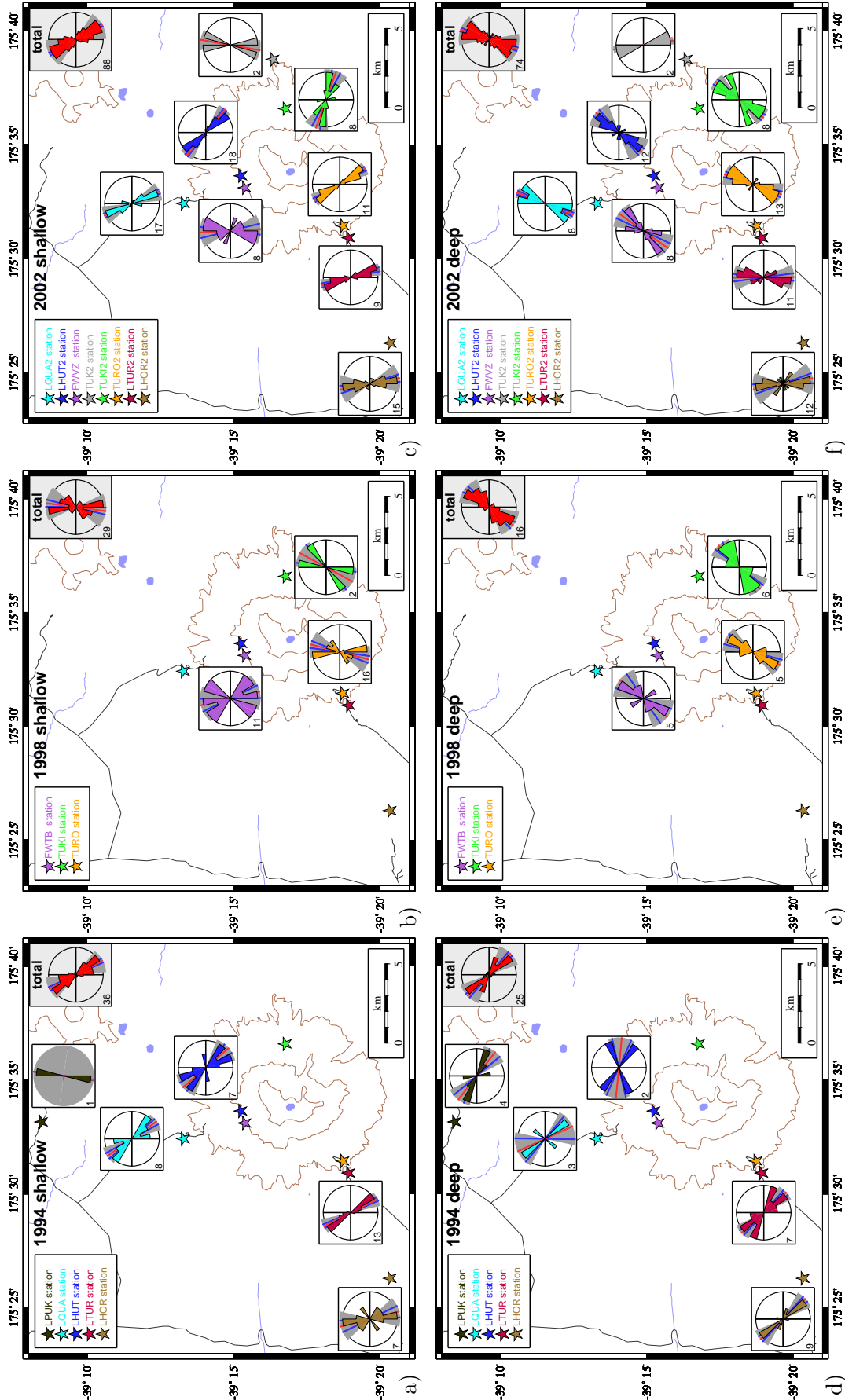


Figure B.2 Individual station histograms with only one measurement per event and station. This figure is a reprint of Figure 5.5, with the difference being that only one measurement was included per station for every earthquake, similar to Figure B.1 (i.e. no multiple measurements from one event with different filters). When comparing the histograms between the two methods, it is clear that the differences are only minor and do not significantly affect the results.

B.2 Instrument recording times

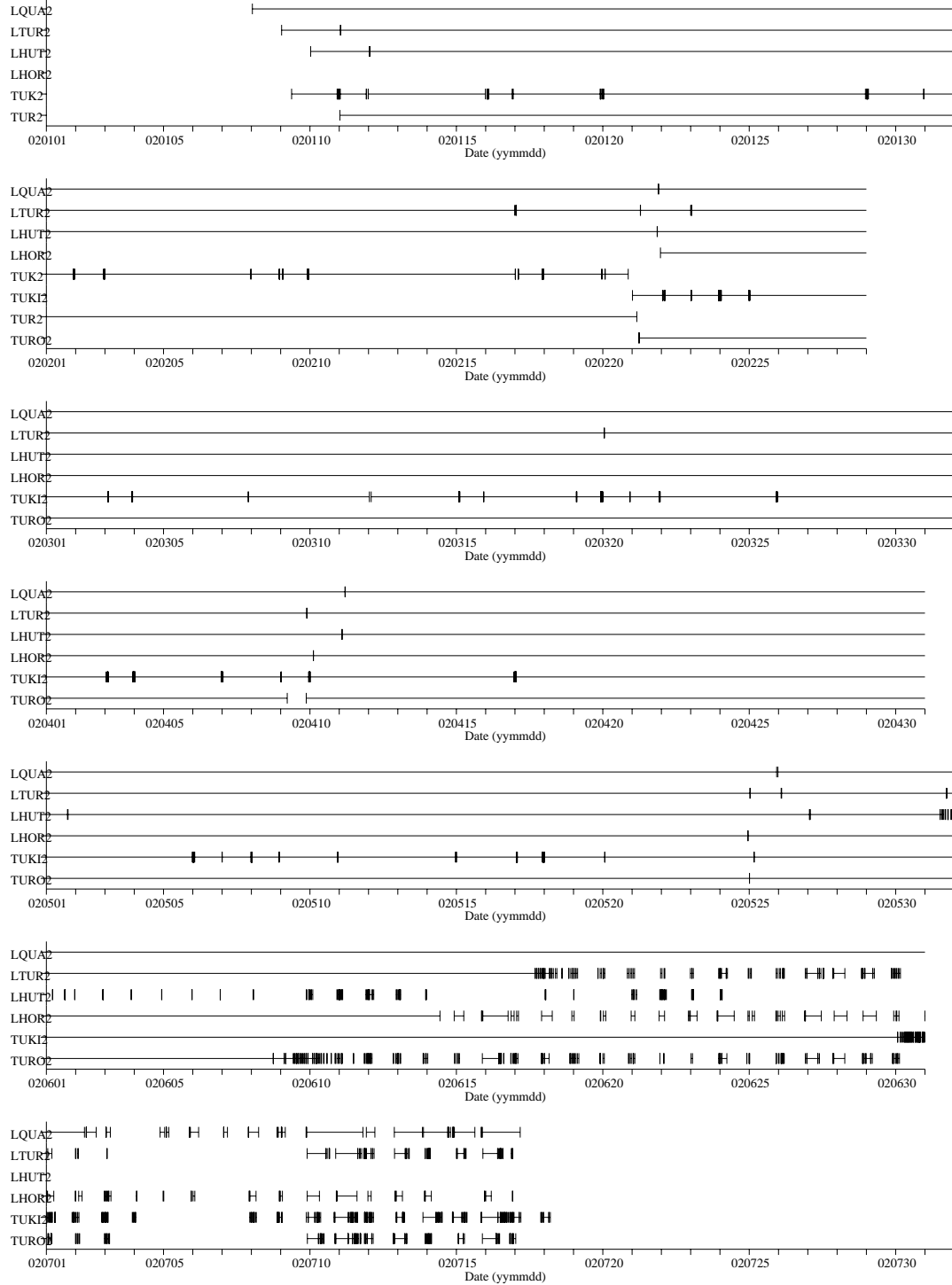


Figure B.3 Recording times of the CHARM instruments. Each row represents a month, starting with January 2000. A horizontal bar is drawn at times when the respective station was recording, terminated by vertical bars at the start and stop times. The long gap in January at the station LHOR2 is due to a disk failure. In the winter months (June/July), all the stations had frequent down times due to few daylight hours and snow cover on the solar panels

B.3 Data quality control

B.3.1 Check for rotated components

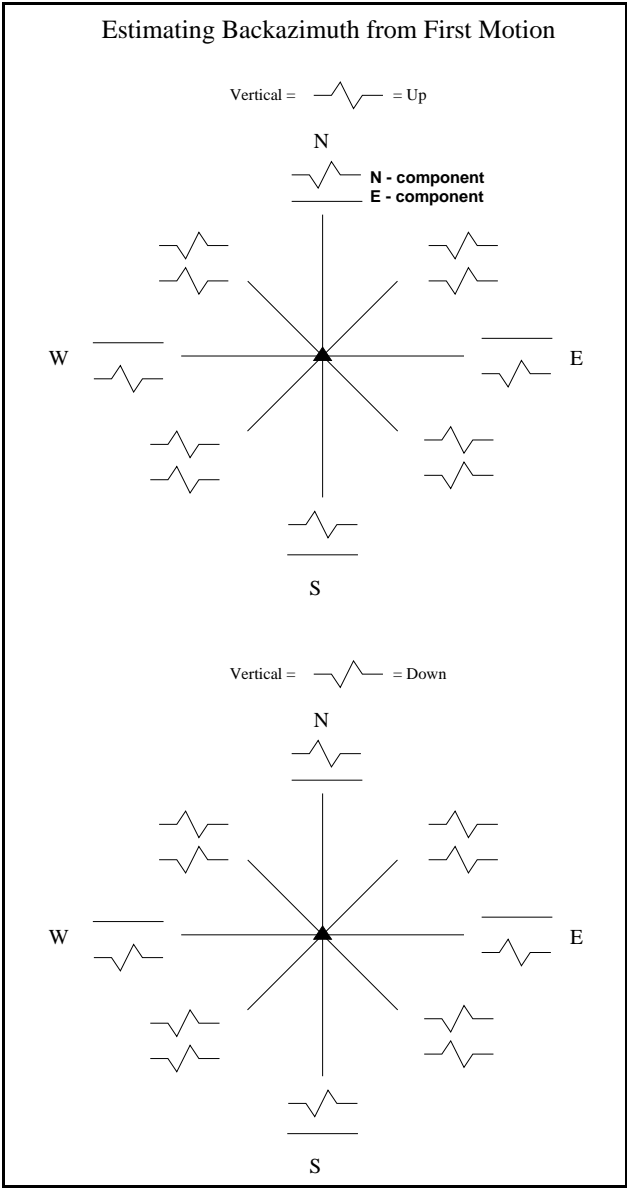


Figure B.4 *Check for rotated components by comparing the estimated back azimuth with the real one. When the estimated back azimuth of an event does not match its real one, then at least one component of this sensor is likely to be rotated.*

B.3.2 Sun compass test for correct orientation

Station	Sun azimuth to assumed true N [°]	date (UT)	time (UT)	date (NZ)	time (NZ)	rel. UTC	Lat [°]	Lon [°]	Sun Azimuth to true N [°]	Error of N comp. [°]
LQUA2	-27.0 = 333.0	8-Jan-02	1:10:00	8-Jan-02	14:10:00	+13	-39.2216	175.5403	326.8	-6.2
TUR2	-329.0 = 31.0	10-Jan-02	23:54:30	11-Jan-02	12:54:30	+13	-39.3125	175.5235	23.1	-7.9
LTUR2	-342.5 = 17.5	16-Jul-02	23:28:45	17-Jul-02	11:28:45	+12	-39.3156	175.5153	14.6	-2.9
TURO2	-359.0 = 1.0	17-Jul-02	0:35:00	17-Jul-02	12:35:00	+12	-39.3122	175.5241	357.1	-3.9
close to TUK12	-52.7 = 307.3	18-Jul-02	4:13:30	18-Jul-02	16:13:30	+12	-39.273	175.646	307.1	-0.2
LHUT2	-286 = 74.0	10-Jan-03	22:03:45	11-Jan-03	11:03:45	+13	-39.2542	175.5606	70.6	-3.4
LHUT2	-302 = 58.0	10-Jan-03	22:53:45	11-Jan-03	11:53:45	+13	-39.2542	175.5606	55.1	-2.9
LHUT2	-29.0 = 331.0	14-Sep-02	1:46:00	14-Sep-02	13:46:00	+12	-39.2542	175.5606	328.1	-2.9
LHUT2	-30.0 = 330.0	14-Sep-02	1:50:00	14-Sep-02	13:50:00	+12	-39.2542	175.5606	326.8	-3.2
LHOR2	-102.5 = 257.5	4-Jan-03	5:40:00	4-Jan-03	18:40:00	+13	-39.3391	175.4382	258.1	0.6
LHOR2	-103.5 = 256.5	4-Jan-03	5:46:00	4-Jan-03	18:46:00	+13	-39.3391	175.4382	257.3	0.8
LHOR2	-103.5 = 256.5	4-Jan-03	5:48:30	4-Jan-03	18:48:30	+13	-39.3391	175.4382	256.9	0.4

Table B.1
Sun compass test for rotated components. Calculated with NOAA Sun Position Calculator:
<http://www.srb.noaa.gov/highlights/sunrise/azel.html>
checked with the U.S. Naval Observatory Sun Azimuth Tables:
<http://aa.usno.navy.mil/data/docs/AltAz.html>
Please note that this is only a coarse test method for the correct orientation of the sensors. The sun compass is very hard to adjust, so that the uncertainty on this method has about the same range as the obtained results (5 to 10°).

APPENDIX C

LIST OF ALL MEASUREMENTS

This Appendix contains a full list of all measurements that were obtained in 1994, 1998 and 2002. The following parameters are listed in the tables: *

Event ID	A seven-digit number that identifies the earthquake source time, and consists of: <year><Julian day><hour><minute>
Station	Name of recording Station.
Φ	Fast direction [°].
$\pm\Phi$	68% confidence interval (error) of the fast direction [°].
δt	Delay time [s].
$\pm\delta t$	68% confidence interval (error) of the delay time [s].
Baz	Back azimuth of earthquake source [°].
Pol	Initial polarisation of wavelet [°].
RayP	Ray parameter [s/°].
Edepth	Earthquake depth [km].
Edist	Earthquake distance [°].
Elat	Earthquake latitude [°].
Elon	Earthquake longitude [°].
Filter	Applied frequency bandpass filter values [Hz].
Freq	Main frequency of the wavelet [Hz].
Quality	Quality mark of the measurement; Tag of NULL measurements.
Incid	Slope-corrected incidence angle at the station [°] (Assumes 1.6 km/s surface S-velocity).

*Note that the shallow events from 1994 and the deep events from 1998 were not reprocessed. Thus their frequencies were not measured, and the respective field shows “N/A”. All of these measurements have quality marks of either A or AB, and the respective field in the table shows “A-AB”. Measurements with B- and C-quality from these two groups are not included, since only good quality measurements (A, AB) were taken over from the old processing. B- and C- quality measurements in the old processing were both rated as ambiguous and therefore not usable (Miller, 2000), i.e. the definition for “B-quality” was different in the old processing.

Table C.1: List of individual measurements, 1994 deployment

Event ID	Station	Φ [°]	$\pm\Phi$ [°]	δt [s]	$\pm\delta t$ [s]	Baz [°]	Pol [°]	RayP [s/°]	Edepth [km]	Edist [°]	Elat [°]	Elon [°]	Filter [Hz]	Freq [Hz]	Quality	Incid [°]
19940360458	LHOR	-37	4	0.34	0.01	334	23	6.0	208.0	0.46	-38.92	175.18	0.5-3	2.11	A	5.8
19940360458	LHOR	-43	2	0.34	0.02	334	24	6.0	208.0	0.46	-38.92	175.18	2-6	3.60	A	5.8
19940360458	LHOR	-44	2	0.34	0.01	334	27	6.0	208.0	0.46	-38.92	175.18	4-100	4.19	C	5.8
19940362324	LHOR	13	6	0.05	0.01	278	70	27.7	28.0	0.48	-39.27	174.82	N/A	N/A	A-AB	25.6
19940381540	LHOR	-51	10	0.08	0.01	39	16	13.7	118.0	0.66	-38.82	175.97	2-6	4.17	B	9.6
19940381540	LHOR	-62	5	0.08	0.02	39	5	13.7	118.0	0.66	-38.82	175.97	1-3	2.90	A	9.6
19940390255	LHOR	-32	8	0.05	0.03	126	41	24.4	23.0	0.24	-39.48	175.69	N/A	N/A	A-AB	19.2
19940402050	LHOR	46	6	0.05	0.01	116	78	26.7	19.0	0.23	-39.44	175.71	N/A	N/A	A-AB	20.9
19940421323	LHOR	-34	4	0.18	0.02	26	78	12.5	141.0	0.71	-38.70	175.84	2-6	3.82	B	9.0
19940421323	LHOR	0	4	0.32	0.01	26	62	12.5	141.0	0.71	-38.70	175.84	1-3	2.80	B	9.0
19940461652	LHOR	-10	15	0.05	0.02	2	57	32.5	9.0	0.43	-38.91	175.46	N/A	N/A	A-AB	27.3
19940470141	LHOR	-13	22	0.03	0.04	123	46	28.9	14.0	0.26	-39.48	175.72	N/A	N/A	A-AB	23.1
19940470456	LHOR	-40	6	0.56	0.02	33	14	16.2	138.0	1.03	-38.48	176.16	1-3	1.72	AB	11.9
19940500737	LHOR	-34	4	0.24	0.02	268	25	0.6	104.0	0.02	-39.34	175.41	0.2-2	1.93	A	2.8
19940500737	LHOR	-35	2	0.24	0.01	268	28	0.6	104.0	0.02	-39.34	175.41	2-6	3.43	A	2.8
19940500737	LHOR	-35	6	0.24	0.01	268	26	0.6	104.0	0.02	-39.34	175.41	1-3	2.66	A	2.8
19940511320	LHOR	-48	3	0.14	0.01	280	20	25.9	27.0	0.35	-39.28	174.99	N/A	N/A	A-AB	24.0
19940600050	LHOR	-73	9	0.29	0.02	20	60	11.8	124.0	0.57	-38.80	175.69	1-3	1.82	B	8.7
19940620658	LHOR	-12	7	0.37	0.02	214	40	29.5	21.0	0.56	-39.80	175.03	1-3	2.39	C	26.9
19940620658	LHOR	-12	7	0.37	0.02	214	40	29.5	21.0	0.56	-39.80	175.03	1-3	2.39	C	26.9
19940651249	LHOR	-37	22	0.35	0.24	339	28	6.5	165.0	0.39	-38.97	175.26	2-6	3.40	C	6.1
19940691450	LHOR	-37	8	0.05	0.01	82	13	21.9	55.0	0.66	-39.24	176.28	4-100	9.20	C	16.1
19940691450	LHOR	-45	10	0.10	0.02	82	1	21.9	55.0	0.66	-39.24	176.28	1-3	2.74	AB	16.1
19940691450	LHOR	-48	10	0.10	0.02	82	0	21.9	55.0	0.66	-39.24	176.28	0.2-2	2.31	A	16.1
19940692342	LHOR	-26	4	0.16	0.02	20	37	24.1	13.0	0.14	-39.21	175.50	N/A	N/A	A-AB	19.1
19940710826	LHOR	-39	4	0.34	0.01	328	21	5.9	212.0	0.47	-38.94	175.12	0.5-3	1.71	A	6.0
19940710826	LHOR	-42	4	0.34	0.02	328	20	5.9	212.0	0.47	-38.94	175.12	2-6	3.03	A	6.0
19940711319	LHOR	-37	12	0.30	0.08	36	22	14.5	119.0	0.73	-38.75	175.99	2-6	3.23	B	10.4
19940711319	LHOR	-37	7	0.30	0.02	36	18	14.5	119.0	0.73	-38.75	175.99	1-3	1.81	A	10.4
19940362324	LHUT	-44	8	0.08	0.01	268	-7	28.8	28.0	0.57	-39.27	174.82	N/A	N/A	A-AB	31.6
19940390558	LHUT	-58	22	0.08	0.07	264	-27	28.6	25.0	0.46	-39.30	174.97	N/A	N/A	A-AB	30.7
19940421323	LHUT	54	4	0.34	0.02	22	-53	10.8	141.0	0.59	-38.70	175.84	1-3	1.71	C	21.5
19940451058	LHUT	-10	10	0.05	0.02	159	20	22.7	25.0	0.22	-39.46	175.66	N/A	N/A	A-AB	5.1
19940471421	LHUT	-50	4	0.05	0.01	293	-13	25.6	28.0	0.35	-39.12	175.15	N/A	N/A	A-AB	32.7

continued on next page...

Event ID	Station	Φ [$^{\circ}$]	$\pm\Phi$ [$^{\circ}$]	δt [s]	$\pm\delta t$ (s)	Baz[$^{\circ}$]	Pol[$^{\circ}$]	RayP[s/ $^{\circ}$]	Edepth[km]	Edist[$^{\circ}$]	Elat[$^{\circ}$]	Elon[$^{\circ}$]	Filter[Hz]	Freq[Hz]	Quality	Incid[$^{\circ}$]
19940500737	LHUT	-68	10	0.16	0.02	234	75	4.0	104.0	0.14	-39.34	175.41	2-6	4.84	C	13.5
19940500737	LHUT	71	4	0.27	0.02	234	-35	4.0	104.0	0.14	-39.34	175.41	1-3	1.93	B	13.5
19940530525	LHUT	-33	18	0.05	0.02	0	-65	31.4	6.0	0.16	-39.09	175.56	N/A	N/A	A-AB	40.3
19940531146	LHUT	76	6	0.06	0.01	169	38	21.2	27.0	0.21	-39.46	175.61	N/A	N/A	A-AB	4.5
19940600050	LHUT	90	6	0.35	0.10	13	-21	9.9	124.0	0.46	-38.80	175.69	1-3	2.92	C	21.3
19940600305	LHUT	-23	5	0.08	0.01	284	45	20.9	13.0	0.10	-39.23	175.44	N/A	N/A	A-AB	27.8
19940620658	LHUT	-30	6	0.13	0.01	217	-68	29.5	21.0	0.68	-39.80	175.03	4-100	4.82	AB	20.9
19940620658	LHUT	-30	6	0.13	0.01	217	-68	29.5	21.0	0.68	-39.80	175.03	4-100	4.82	AB	20.9
19940681950	LHUT	0	12	0.18	0.57	42	-8	15.5	99.0	0.65	-38.77	176.12	2-6	3.96	NULLB	23.0
19940691450	LHUT	-60	9	0.10	0.01	89	-7	20.7	55.0	0.56	-39.24	176.28	1-3	1.88	A	18.2
19940691450	LHUT	-62	9	0.27	0.02	89	66	20.7	55.0	0.56	-39.24	176.28	2-6	2.34	B	18.2
19940691450	LHUT	-66	22	0.08	0.10	89	-8	20.7	55.0	0.56	-39.24	176.28	0.2-2	1.28	C	18.2
19940360458	LPUK	-42	18	0.08	0.02	307	-20	4.7	208.0	0.36	-38.92	175.18	2-6	2.87	B	3.9
19940360458	LPUK	-9	5	0.18	0.02	307	15	4.7	208.0	0.36	-38.92	175.18	1-3	1.56	AB	3.9
19940361516	LPUK	8	6	0.08	0.01	207	75	24.7	28.0	1.16	-40.18	174.87	N/A	N/A	A-AB	20.8
19940381540	LPUK	-43	6	0.10	0.02	46	-62	10.2	118.0	0.46	-38.82	175.97	2-6	2.45	B	8.4
19940381540	LPUK	-53	5	0.13	0.02	46	-75	10.2	118.0	0.46	-38.82	175.97	1-3	1.70	A	8.4
19940421323	LPUK	-73	15	0.11	0.02	27	-33	9.3	141.0	0.49	-38.70	175.84	1-3	1.32	AB	7.7
19940600050	LPUK	-61	4	0.45	0.02	18	-40	7.9	124.0	0.36	-38.80	175.69	1-3	2.17	B	6.5
19940362324	LQUA	-42	4	0.08	0.02	265	-23	28.8	28.0	0.56	-39.27	174.82	N/A	N/A	A-AB	24.7
19940381236	LQUA	-27	5	0.11	0.01	260	19	27.4	27.0	0.44	-39.30	174.98	N/A	N/A	A-AB	22.9
19940390558	LQUA	-12	4	0.11	0.01	260	42	28.5	25.0	0.45	-39.30	174.97	N/A	N/A	A-AB	23.9
19940451227	LQUA	-55	3	0.10	0.01	296	17	28.6	8.0	0.14	-39.16	175.38	N/A	N/A	A-AB	27.6
19940470456	LQUA	-40	19	0.13	0.22	33	14	14.8	138.0	0.88	-38.48	176.16	1-3	2.02	C	17.9
19940471421	LQUA	-3	8	0.06	0.02	288	-50	24.9	28.0	0.32	-39.12	175.15	N/A	N/A	A-AB	23.7
19940500737	LQUA	26	22	0.11	1.02	221	-9	4.3	104.0	0.16	-39.34	175.41	4-100	4.32	NULLB	4.3
19940600050	LQUA	-39	18	0.40	0.18	16	21	9.4	124.0	0.44	-38.80	175.69	1-3	1.44	B	13.9
19940600305	LQUA	-47	6	0.10	0.01	264	-4	18.9	13.0	0.08	-39.23	175.44	N/A	N/A	A-AB	16.3
19940620658	LQUA	-38	4	0.21	0.08	214	77	29.5	21.0	0.70	-39.80	175.03	2-6	2.63	AB	20.2
19940620658	LQUA	-38	4	0.21	0.08	214	77	29.5	21.0	0.70	-39.80	175.03	2-6	2.63	AB	20.2
19940620658	LQUA	-50	7	0.38	0.55	214	23	29.5	21.0	0.70	-39.80	175.03	1-3	1.76	C	20.2
19940620658	LQUA	-50	7	0.38	0.55	214	23	29.5	21.0	0.70	-39.80	175.03	1-3	1.76	C	20.2
19940651809	LQUA	35	3	0.46	0.01	54	-77	19.0	73.0	0.66	-38.83	176.22	1-3	1.23	B	20.2
19940691450	LQUA	-36	8	0.11	0.01	92	4	20.9	55.0	0.57	-39.24	176.28	0.5-3	1.97	A	18.4
19940691450	LQUA	7	6	0.29	0.02	92	-48	20.9	55.0	0.57	-39.24	176.28	4-100	4.06	B	18.4
19940692342	LQUA	-51	8	0.10	0.01	291	-15	11.4	13.0	0.03	-39.21	175.50	N/A	N/A	A-AB	13.1
19940321115	LTUR	6	5	0.05	0.02	130	26	24.7	21.0	1.23	-40.18	176.32	N/A	N/A	A-AB	19.5
19940362324	LTUR	-45	4	0.14	0.01	275	14	28.7	28.0	0.54	-39.27	174.82	N/A	N/A	A-AB	31.7

continued on next page...

Event ID	Station	Φ [$^{\circ}$]	$\pm\Phi$ [$^{\circ}$]	δt [s]	$\pm\delta t$ [s]	Baz[$^{\circ}$]	Pol[$^{\circ}$]	RayP[s/ $^{\circ}$]	Edepth[km]	Edist[$^{\circ}$]	Elat[$^{\circ}$]	Elon[$^{\circ}$]	Filter[Hz]	Freq[Hz]	Quality	Incid[$^{\circ}$]
19940381236	LTUR	-32	3	0.13	0.01	272	30	27.1	27.0	0.42	-39.30	174.98	N/A	N/A	A-AB	30.5
19940381540	LTUR	-15	8	0.29	0.01	36	-54	12.9	118.0	0.61	-38.82	175.97	2-6	4.62	B	4.5
19940381540	LTUR	-8	4	0.29	0.01	36	-60	12.9	118.0	0.61	-38.82	175.97	1-3	1.82	C	4.5
19940390558	LTUR	-36	3	0.13	0.01	272	24	27.9	25.0	0.42	-39.30	174.97	N/A	N/A	A-AB	31.2
19940451227	LTUR	-35	4	0.18	0.01	326	27	30.9	8.0	0.19	-39.16	175.38	N/A	N/A	A-AB	28.2
19940470456	LTUR	-33	18	0.10	0.02	31	21	15.7	138.0	0.97	-38.48	176.16	1-3	1.78	B	6.9
19940470456	LTUR	-70	13	0.11	0.01	31	-21	15.7	138.0	0.97	-38.48	176.16	2-6	4.07	C	6.9
19940471421	LTUR	-9	4	0.06	0.01	304	48	25.6	28.0	0.34	-39.12	175.15	N/A	N/A	A-AB	26.4
19940500737	LTUR	-43	6	0.26	0.02	253	62	2.4	104.0	0.09	-39.34	175.41	2-6	2.78	C	10.4
19940500737	LTUR	-62	7	0.11	0.10	253	10	2.4	104.0	0.09	-39.34	175.41	0.5-3	2.37	B	10.4
19940511320	LTUR	-40	4	0.13	0.01	275	15	27.0	27.0	0.41	-39.28	174.99	N/A	N/A	A-AB	30.2
19940531146	LTUR	-42	6	0.16	0.01	153	8	17.6	27.0	0.16	-39.46	175.61	N/A	N/A	A-AB	17.3
19940540442	LTUR	-32	6	0.13	0.01	273	24	28.5	24.0	0.42	-39.29	174.97	N/A	N/A	A-AB	31.7
19940600050	LTUR	-28	8	0.40	0.02	15	35	11.1	124.0	0.53	-38.80	175.69	1-3	1.65	AB	6.8
19940620658	LTUR	-16	9	0.35	0.07	218	45	29.5	21.0	0.61	-39.80	175.03	1-3	2.26	AB	33.1
19940620658	LTUR	-16	9	0.35	0.07	218	45	29.5	21.0	0.61	-39.80	175.03	1-3	2.26	AB	33.1
19940642346	LTUR	-13	11	0.10	0.01	132	32	29.5	14.0	0.28	-39.50	175.78	N/A	N/A	A-AB	23.8
19940651809	LTUR	-55	20	0.03	0.02	49	-9	19.9	73.0	0.73	-38.83	176.22	1-3	2.14	AB	8.4
19940681950	LTUR	-41	9	0.10	0.01	41	5	16.5	99.0	0.72	-38.77	176.12	0.5-3	2.55	B	6.3
19940691911	LTUR	-27	6	0.14	0.01	272	32	28.9	26.0	0.55	-39.29	174.81	N/A	N/A	A-AB	32.1
19940701435	LTUR	-25	4	0.16	0.01	73	23	11.6	8.0	0.02	-39.31	175.54	N/A	N/A	A-AB	2.3
19940710826	LTUR	-61	4	0.19	0.02	320	6	6.1	212.0	0.49	-38.94	175.12	2-6	3.82	B	10.6

Table C.1: List of individual measurements, 1994 deployment

Table C.2: List of individual measurements, 1998 deployment

Event ID	Station	Φ [$^{\circ}$]	$\pm\Phi$ [$^{\circ}$]	δt [s]	$\pm\delta t$ [s]	$\pm\delta t$ (s)	Baz[$^{\circ}$]	Pol[$^{\circ}$]	RayP[s/ $^{\circ}$]	Edepth[km]	Edist[$^{\circ}$]	Elat[$^{\circ}$]	Elon[$^{\circ}$]	Filter[Hz]	Freq[Hz]	Quality	Incid[$^{\circ}$]
19980361212	FWTB	31	6	0.14	0.01	0.01	266	-16	24.5	30.0	0.33	-39.28	175.13	1-3	2.44	AB	27.8
19980520510	FWTB	-49	8	0.03	0.01	0.01	310	66	18.1	13.0	0.07	-39.21	175.48	2-6	5.20	C	28.1
19980531508	FWTB	-2	11	0.06	0.02	0.02	249	58	27.2	10.0	0.15	-39.31	175.37	0.3-2	2.06	B	26.5
19980540756	FWTB	-61	18	0.06	0.02	0.02	123	2	25.8	16.0	0.17	-39.35	175.74	2-6	4.31	C	13.4
19980562202	FWTB	-29	4	0.19	0.02	0.02	328	21	24.6	13.0	0.15	-39.13	175.45	0.5-3	3.09	A	34.5
19980562202	FWTB	-33	4	0.19	0.01	0.01	328	18	24.6	13.0	0.15	-39.13	175.45	2-6	5.04	AB	34.5
19980611150	FWTB	-54	22	0.06	0.05	0.05	114	7	25.6	15.0	0.16	-39.32	175.74	1-3	3.31	C	15.4
19980611150	FWTB	-80	22	0.08	0.02	0.02	114	-26	25.6	15.0	0.16	-39.32	175.74	2-6	4.09	B	15.4
19980611505	FWTB	-38	8	0.05	0.01	0.01	283	90	26.1	18.0	0.20	-39.21	175.30	1-3	3.54	A	31.8
19980670552	FWTB	55	6	0.08	0.01	0.01	254	14	11.5	209.0	0.98	-39.52	174.33	N/A	N/A	A-AB	17.4
19980680255	FWTB	-29	6	0.10	0.02	0.02	224	-65	21.9	93.0	1.35	-40.23	174.33	N/A	N/A	A-AB	17.4
19980731032	FWTB	-81	16	0.08	0.02	0.02	110	-25	25.4	15.0	0.16	-39.31	175.74	1-3	3.12	C	16.3
19980731032	FWTB	88	14	0.08	0.01	0.01	110	-41	25.4	15.0	0.16	-39.31	175.74	2-6	6.77	B	16.3
19980731048	FWTB	-64	4	0.06	0.01	0.01	113	0	25.4	16.0	0.17	-39.32	175.75	2-6	5.38	B	15.5
19980802203	FWTB	-51	4	0.32	0.02	0.02	251	57	28.8	28.0	0.58	-39.44	174.84	1-3	2.28	B	28.2
19980820651	FWTB	-55	22	0.14	0.08	0.08	297	48	22.2	14.0	0.12	-39.20	175.41	2-6	5.17	C	30.4
19980831502	FWTB	-17	12	0.06	0.01	0.01	277	-78	26.2	18.0	0.21	-39.23	175.29	1-3	2.83	B	31.0
19980831502	FWTB	-45	22	0.05	0.06	0.06	277	84	26.2	18.0	0.21	-39.23	175.29	2-6	4.17	C	31.0
19980860245	FWTB	15	2	0.06	0.01	0.01	272	77	27.4	27.0	0.44	-39.24	174.99	1-3	3.30	AB	31.1
19980860245	FWTB	42	4	0.05	0.01	0.01	272	-79	27.4	27.0	0.44	-39.24	174.99	2-6	4.36	AB	31.1
19980860610	FWTB	-55	11	0.05	0.01	0.01	295	85	26.9	9.0	0.13	-39.20	175.40	0.5-3	4.40	AB	34.1
19980861055	FWTB	-40	4	0.11	0.01	0.01	263	25	29.8	19.0	0.39	-39.30	175.05	1-3	4.17	AB	31.4
19981430951	FWTB	70	4	0.08	0.02	0.02	298	51	3.0	131.0	0.14	-39.19	175.39	N/A	N/A	A-AB	15.9
19981471844	FWTB	-13	3	0.13	0.01	0.01	284	-70	29.5	22.0	0.73	-39.07	174.64	0.5-3	2.51	AB	34.8
19981562222	FWTB	-49	21	0.05	0.06	0.06	118	13	24.9	16.0	0.16	-39.33	175.73	1-3	3.56	C	14.0
19981562222	FWTB	-66	10	0.06	0.02	0.02	118	-1	24.9	16.0	0.16	-39.33	175.73	2-6	5.94	C	14.0
19981751045	FWTB	22	8	0.14	0.02	0.02	259	-16	29.1	22.0	0.44	-39.34	175.00	0.2-2	2.38	AB	30.1
19981751045	FWTB	24	7	0.14	0.02	0.02	259	-12	29.1	22.0	0.44	-39.34	175.00	0.1-1	2.21	A	30.1
19981860033	FWTB	60	4	0.48	0.41	0.41	267	51	26.3	30.0	0.41	-39.28	175.02	1-3	2.81	NULLAB	29.4
19982041621	FWTB	33	6	0.06	0.01	0.01	298	-73	26.7	10.0	0.14	-39.19	175.39	2-6	5.38	AB	34.2
19982061711	FWTB	23	7	0.08	0.01	0.01	82	58	17.9	81.0	0.66	-39.16	176.39	N/A	N/A	A-AB	18.1
19982072027	FWTB	31	6	0.13	0.02	0.02	328	1	6.4	192.0	0.46	-38.87	175.24	N/A	N/A	A-AB	19.2
19982090347	FWTB	-56	2	0.06	0.01	0.01	142	17	29.7	11.0	0.22	-39.43	175.73	2-6	5.89	AB	12.7
19982090347	FWTB	-57	7	0.06	0.02	0.02	142	16	29.7	11.0	0.22	-39.43	175.73	0.5-3	5.07	C	12.7

continued on next page...

Event ID	Station	Φ [°]	$\pm\Phi$ [°]	δt [s]	$\pm\delta t$ (s)	Baz [°]	Pol [°]	RayP [s/°]	Edepth [km]	Edist [°]	Elat [°]	Elon [°]	Filter [Hz]	Freq [Hz]	Quality	Incid [°]
19982122228	FWTB	-5	6	0.27	0.01	122	-49	29.0	30.0	0.76	-39.66	176.38	1-3	1.55	AB	16.0
19980562202	TUKI	-5	6	0.08	0.01	320	24	27.1	13.0	0.19	-39.13	175.45	2-6	4.49	C	18.4
19980562202	TUKI	8	8	0.08	0.02	320	37	27.1	13.0	0.19	-39.13	175.45	0.5-3	2.45	B	18.4
19980591316	TUKI	40	22	0.08	1.03	129	43	29.5	22.0	1.06	-39.94	176.68	1-3	1.95	NULLB	32.7
19980611150	TUKI	50	3	0.08	0.01	112	-16	20.8	15.0	0.11	-39.32	175.74	2-6	5.83	C	26.1
19980612142	TUKI	34	8	0.18	0.02	283	5	29.4	21.0	0.46	-39.17	175.03	0.5-2	1.71	C	16.3
19980612142	TUKI	82	14	0.06	0.02	283	37	29.4	21.0	0.46	-39.17	175.03	1-3	2.29	B	16.3
19980620131	TUKI	54	8	0.13	0.03	285	28	29.3	24.0	0.67	-39.10	174.78	0.5-2	1.49	A	16.3
19980620131	TUKI	60	4	0.11	0.02	285	35	29.3	24.0	0.67	-39.10	174.78	1-3	1.87	A	16.3
19980670552	TUKI	78	6	0.08	0.01	256	50	11.8	209.0	1.02	-39.52	174.33	N/A	N/A	A-AB	2.4
19980760734	TUKI	76	6	0.19	0.01	130	-45	29.5	21.0	1.04	-39.95	176.64	2-6	4.02	B	32.6
19980811134	TUKI	88	16	0.08	0.06	161	34	23.1	21.0	0.19	-39.46	175.69	2-6	4.81	C	23.9
19980860245	TUKI	3	8	0.16	0.02	175	-45	28.0	27.0	0.48	-39.24	174.99	1-3	2.81	AB	14.7
19980862111	TUKI	67	19	0.08	0.02	180	31	27.2	26.0	0.40	-39.68	175.61	1-3	2.67	C	24.7
19981020851	TUKI	36	22	0.06	0.04	293	56	18.0	17.0	0.10	-39.24	175.49	1-3	2.27	C	7.5
19981131534	TUKI	48	22	0.26	1.02	262	33	23.9	14.0	0.15	-39.30	175.42	0.5-3	1.98	NULLAB	11.2
19981271247	TUKI	-23	6	0.16	0.02	281	86	29.3	22.0	0.48	-39.19	175.00	0.5-3	2.06	C	16.1
19981281809	TUKI	29	4	0.13	0.02	39	4	9.0	84.0	0.27	-39.07	175.83	N/A	N/A	A-AB	14.9
19981291122	TUKI	-59	4	0.24	0.02	127	14	24.7	29.0	0.89	-39.82	176.53	1-3	2.97	B	28.6
19981291122	TUKI	-83	6	0.08	0.01	127	46	24.7	29.0	0.89	-39.82	176.53	2-6	4.05	C	28.6
19981310648	TUKI	-5	8	0.26	0.02	276	-61	29.6	20.0	0.64	-39.21	174.79	2-6	4.08	C	16.2
19981310648	TUKI	53	7	0.22	0.58	276	76	29.6	20.0	0.64	-39.21	174.79	1-3	2.21	NULLAB	16.2
19981310759	TUKI	4	12	0.24	0.02	275	-53	29.5	21.0	0.63	-39.22	174.80	2-6	2.95	C	16.1
19981431320	TUKI	62	2	0.14	0.02	92	-36	11.1	65.0	0.26	-39.29	175.94	4-100	6.17	NULLA	18.3
19981431320	TUKI	64	2	0.16	0.01	92	-33	11.1	65.0	0.26	-39.29	175.94	2-6	5.14	NULLA	18.3
19981550612	TUKI	46	22	0.06	0.07	220	-75	6.1	81.0	0.17	-39.41	175.47	N/A	N/A	A-AB	7.0
19981562222	TUKI	86	22	0.10	0.10	118	30	19.5	16.0	0.11	-39.33	175.73	2-6	5.77	B	24.7
19981650941	TUKI	70	21	0.08	0.02	212	-76	19.8	67.0	0.65	-39.83	175.17	N/A	N/A	A-AB	14.0
19981812010	TUKI	9	3	0.11	0.02	11	29	10.2	189.0	0.76	-38.53	175.80	N/A	N/A	A-AB	13.5
19982031628	TUKI	44	2	0.24	0.01	62	-72	21.0	59.0	0.64	-38.98	176.33	N/A	N/A	A-AB	26.0
19980781045	TURO	23	22	0.03	0.81	93	21	26.6	16.0	0.19	-39.32	175.77	1-3	2.79	NULLB	16.0
19980802203	TURO	-29	6	0.32	0.01	256	-84	28.7	28.0	0.55	-39.44	174.84	1-3	2.91	B	32.6
19980810239	TURO	45	22	0.45	1.21	349	58	28.8	23.0	0.43	-38.89	175.42	1-3	2.97	NULLAB	23.1
19980810239	TURO	5	10	0.16	0.02	349	-33	28.8	23.0	0.43	-38.89	175.42	2-6	4.80	B	23.1
19980820651	TURO	-5	13	0.08	0.02	322	34	23.5	14.0	0.14	-39.20	175.41	1-3	2.56	B	22.5
19980820651	TURO	-8	10	0.10	0.01	322	32	23.5	14.0	0.14	-39.20	175.41	2-6	5.29	B	22.5
19980831502	TURO	-37	6	0.08	0.01	294	82	26.0	18.0	0.20	-39.23	175.29	1-3	3.83	C	27.8
19980831502	TURO	-55	2	0.06	0.01	294	56	26.0	18.0	0.20	-39.23	175.29	2-6	5.72	C	27.8

continued on next page...

Event ID	Station	Φ [$^{\circ}$]	$\pm\Phi$ [$^{\circ}$]	δt [s]	$\pm\delta t$ (s)	Baz[$^{\circ}$]	Pol[$^{\circ}$]	RayP[s/ $^{\circ}$]	Edepth[km]	Edist[$^{\circ}$]	Elat[$^{\circ}$]	Elon[$^{\circ}$]	Filter[Hz]	Freq[Hz]	Quality	Incid[$^{\circ}$]
19980860245	TURO	-4	12	0.08	0.02	280	45	27.1	27.0	0.42	-39.24	174.99	1-3	2.96	AB	29.9
19980860610	TURO	-15	6	0.05	0.01	319	34	28.0	9.0	0.15	-39.20	175.40	1-3	3.72	AB	26.6
19980860610	TURO	-18	6	0.06	0.01	319	40	28.0	9.0	0.15	-39.20	175.40	2-6	5.23	B	26.6
19980861055	TURO	-26	4	0.22	0.01	272	-75	29.5	19.0	0.37	-39.30	175.05	0.5-3	3.40	AB	32.6
19980862111	TURO	58	9	0.08	0.02	170	33	26.8	26.0	0.37	-39.68	175.61	1-3	3.82	B	26.7
19980900705	TURO	-14	14	0.27	0.11	259	-58	27.6	29.0	0.51	-39.41	174.88	1-3	2.62	B	31.6
19980900840	TURO	-63	10	0.14	0.05	301	5	25.9	16.0	0.18	-39.22	175.33	2-6	6.39	C	27.0
19980901411	TURO	5	4	0.08	0.01	341	31	26.4	13.0	0.18	-39.14	175.45	2-6	5.24	B	22.2
19980906029	TURO	-1	4	0.16	0.01	315	43	26.4	26.0	0.36	-39.06	175.20	2-6	5.52	A	25.8
19980906029	TURO	-6	9	0.16	0.01	315	35	26.4	26.0	0.36	-39.06	175.20	1-3	4.22	A	25.8
19981011853	TURO	17	10	0.16	0.01	249	58	29.1	22.0	0.44	-39.47	174.99	1-3	4.61	B	33.2
19981011853	TURO	24	5	0.26	0.01	249	-27	29.1	22.0	0.44	-39.47	174.99	2-6	5.28	AB	33.2
19981020851	TURO	-20	12	0.05	0.01	340	13	14.5	17.0	0.08	-39.24	175.49	1-3	5.27	C	13.4
19981020851	TURO	39	6	0.06	0.01	340	-84	14.5	17.0	0.08	-39.24	175.49	4-100	7.48	B	13.4
19981040032	TURO	38	16	0.10	0.38	114	28	31.5	9.0	0.24	-39.41	175.81	1-3	3.49	NULLAB	22.9
19981071927	TURO	-52	10	0.08	0.02	119	14	29.5	23.0	0.90	-39.74	176.55	2-6	4.01	C	21.9
19981112103	TURO	34	12	0.06	0.01	292	81	27.5	29.0	0.49	-39.13	174.94	2-6	5.17	AB	29.3
19981112103	TURO	79	9	0.05	0.02	292	-37	27.5	29.0	0.49	-39.13	174.94	4-100	7.28	C	29.3
19981131534	TURO	53	3	0.11	0.01	278	-56	18.5	14.0	0.08	-39.30	175.42	0.2-2	1.92	A	22.7
19981131534	TURO	56	4	0.11	0.01	278	-48	18.5	14.0	0.08	-39.30	175.42	1-3	3.79	AB	22.7
19981131553	TURO	13	8	0.11	0.02	285	48	19.3	13.0	0.08	-39.29	175.42	2-6	5.17	B	22.9
19981131553	TURO	48	5	0.11	0.02	285	-63	19.3	13.0	0.08	-39.29	175.42	1-3	2.69	AB	22.9
19981161730	TURO	-6	8	0.06	0.01	292	32	24.3	26.0	0.27	-39.21	175.20	1-3	2.36	A	26.5
19981161730	TURO	2	5	0.06	0.01	292	46	24.3	26.0	0.27	-39.21	175.20	2-6	5.57	A	26.5
19981172018	TURO	-18	7	0.08	0.02	141	50	21.6	27.0	0.22	-39.48	175.70	0.2-2	2.65	C	18.7
19981172018	TURO	28	10	0.06	0.02	141	-89	21.6	27.0	0.22	-39.48	175.70	2-6	4.16	AB	18.7
19981172018	TURO	7	9	0.06	0.01	141	55	21.6	27.0	0.22	-39.48	175.70	0.5-3	2.98	AB	18.7
19981172030	TURO	-1	3	0.06	0.01	132	61	22.1	28.0	0.24	-39.47	175.75	1-3	3.29	A	17.8
19981172030	TURO	39	10	0.05	0.02	132	-79	22.1	28.0	0.24	-39.47	175.75	2-6	4.69	A	17.8
19981191336	TURO	37	14	0.16	0.02	207	-24	23.1	71.0	1.22	-40.40	174.81	N/A	N/A	A-AB	26.9
19981211113	TURO	-8	13	0.29	0.07	317	-62	28.4	21.0	0.33	-39.07	175.24	1-3	2.93	B	27.2
19981211113	TURO	-9	6	0.29	0.01	317	-64	28.4	21.0	0.33	-39.07	175.24	2-6	5.06	B	27.2
19981271247	TURO	-3	6	0.13	0.08	286	67	29.0	22.0	0.42	-39.19	175.00	0.5-3	3.00	C	31.1
19981271247	TURO	-6	4	0.16	0.01	286	61	29.0	22.0	0.42	-39.19	175.00	4-100	6.40	AB	31.1
19981271247	TURO	8	2	0.16	0.06	286	83	29.0	22.0	0.42	-39.19	175.00	2-6	4.88	B	31.1
19981290124	TURO	-17	8	0.21	0.01	274	-57	29.5	22.0	0.58	-39.27	174.78	2-6	5.55	C	32.5
19981290124	TURO	19	22	0.14	0.56	274	12	29.5	22.0	0.58	-39.27	174.78	4-100	7.65	NULLB	32.5
19981291122	TURO	34	2	0.54	0.10	123	28	24.7	29.0	0.93	-39.82	176.53	1-3	2.92	NULLA	18.5

continued on next page...

Event ID	Station	Φ [$^{\circ}$]	$\pm\Phi$ [$^{\circ}$]	δt [s]	$\pm\delta t$ (s)	Baz[$^{\circ}$]	Pol[$^{\circ}$]	RayP[s/ $^{\circ}$]	Edepth[km]	Edist[$^{\circ}$]	Elat[$^{\circ}$]	Elon[$^{\circ}$]	Filter[Hz]	Freq[Hz]	Quality	Incid[$^{\circ}$]
19981411433	TURO	49	4	0.14	0.01	352	4	11.0	216.0	0.96	-38.36	175.36	N/A	N/A	A-AB	9.8
19981430951	TURO	35	2	0.29	0.02	319	78	3.5	131.0	0.16	-39.19	175.39	N/A	N/A	A-AB	9.5
19981641910	TURO	59	18	0.02	0.06	201	61	29.5	22.0	0.74	-40.00	175.18	4-100	5.90	NULLC	32.1
19981641910	TURO	60	2	0.11	0.01	201	77	29.5	22.0	0.74	-40.00	175.18	2-6	5.01	NULLA	32.1
19981641910	TURO	72	22	0.11	0.70	201	88	29.5	22.0	0.74	-40.00	175.18	1-3	2.71	NULLAB	32.1
19981650941	TURO	14	14	0.05	0.02	208	-36	19.0	67.0	0.58	-39.83	175.17	N/A	N/A	A-AB	23.5
19981731421	TURO	4	10	0.03	0.02	148	70	22.9	23.0	0.21	-39.49	175.67	1-3	3.40	B	20.7
19981860033	TURO	18	6	0.10	0.01	274	74	26.0	30.0	0.39	-39.28	175.02	2-6	4.24	A	29.4
19981892134	TURO	-19	6	0.08	0.01	59	37	7.1	85.0	0.21	-39.20	175.76	N/A	N/A	A-AB	2.6
19981962106	TURO	26	5	0.08	0.01	12	63	20.4	13.0	0.09	-39.22	175.55	1-3	2.80	A	13.0
19981962106	TURO	26	8	0.08	0.01	12	62	20.4	13.0	0.09	-39.22	175.55	2-6	5.84	AB	13.0
19981971848	TURO	59	6	0.16	0.01	148	24	23.6	22.0	0.21	-39.49	175.67	2-6	4.74	AB	21.3
19982011310	TURO	44	5	0.11	0.01	286	-6	27.1	26.0	0.39	-39.20	175.04	4-100	6.94	A	29.5

Table C.2: List of individual measurements, 1998 deployment

Table C.3: List of individual measurements, 2002 deployment

Event ID	Station	Φ [°]	$\pm\Phi$ [°]	δt [s]	$\pm\delta t$ [s]	Baz[°]	Pol[°]	RayP[s/°]	Edepth[km]	Edist[°]	Elat[°]	Elon[°]	Filter[Hz]	Freq[Hz]	Quality	Incid[°]
20020730214	FWVZ	-64	14	0.08	0.03	250	-88	14.0	142.8	0.85	-39.54	174.52	2-4	3.81	C	18.1
20020771811	FWVZ	13	5	0.05	0.01	143	40	25.4	14.4	0.18	-39.40	175.69	1-3	4.70	C	9.0
20020771811	FWVZ	9	5	0.15	0.01	143	-22	25.4	14.4	0.18	-39.40	175.69	2-6	6.16	C	9.0
20020771840	FWVZ	11	4	0.05	0.01	145	36	26.5	12.5	0.17	-39.40	175.68	0.5-3	4.94	B	9.6
20020771939	FWVZ	14	6	0.15	0.01	140	-22	27.0	15.9	0.20	-39.41	175.72	2-6	6.44	C	10.8
20020791111	FWVZ	-20	16	0.05	0.01	293	-60	25.5	7.6	0.09	-39.22	175.44	0.5-3	3.68	B	32.6
20020810622	FWVZ	-65	8	0.15	0.01	263	-16	27.3	33.0	0.56	-39.32	174.83	0.5-3	2.49	AB	29.4
20021072114	FWVZ	48	3	0.73	0.03	54	-65	17.5	81.9	0.64	-38.88	176.22	0.1-1	0.84	AB	22.7
20021092051	FWVZ	-78	10	0.25	0.01	160	67	31.4	10.3	0.27	-39.51	175.67	2-6	6.54	C	12.9
20021101137	FWVZ	49	4	0.95	0.16	32	59	20.2	247.4	3.25	-36.46	177.66	0.5-3	1.68	NULLB	27.7
20021211034	FWVZ	5	3	0.08	0.01	280	63	32.4	6.7	0.26	-39.21	175.22	1-3	4.32	AB	36.7
20021291925	FWVZ	43	22	0.50	0.41	25	31	17.8	174.8	1.59	-37.81	176.40	2-6	2.83	NULLB	26.6
20021302308	FWVZ	9	2	0.08	0.01	275	70	32.3	7.7	0.27	-39.23	175.20	1-3	4.15	AB	35.7
20021320156	FWVZ	10	3	0.08	0.01	274	80	29.4	12.0	0.23	-39.24	175.25	1-3	2.41	C	33.1
20021320156	FWVZ	20	4	0.08	0.01	274	88	29.4	12.0	0.23	-39.24	175.25	2-6	5.42	B	33.1
20021320415	FWVZ	43	7	0.33	0.01	345	78	4.9	180.9	0.33	-38.94	175.44	0.2-2	2.18	AB	18.0
20021320415	FWVZ	55	12	0.30	0.02	345	88	4.9	180.9	0.33	-38.94	175.44	0.5-3	2.69	B	18.0
20021331816	FWVZ	24	4	0.08	0.01	217	-8	22.1	9.1	0.08	-39.32	175.49	0.5-3	3.61	AB	15.9
20021331816	FWVZ	52	9	0.05	0.01	217	16	22.1	9.1	0.08	-39.32	175.49	2-6	4.48	C	15.9
20021380320	FWVZ	53	6	0.30	0.01	14	-72	6.2	115.0	0.25	-39.01	175.63	0.5-3	2.79	A	18.5
20021380320	FWVZ	54	7	0.30	0.01	14	-75	6.2	115.0	0.25	-39.01	175.63	0.2-2	2.48	AB	18.5
20021431119	FWVZ	2	7	0.08	0.01	153	50	27.8	19.9	0.28	-39.51	175.72	1-3	3.21	B	9.8
20021461304	FWVZ	45	4	0.28	0.01	16	-18	3.3	98.6	0.11	-39.15	175.59	0.5-3	2.02	A	16.3
20021461304	FWVZ	62	6	0.25	0.01	16	6	3.3	98.6	0.11	-39.15	175.59	2-6	2.58	A	16.3
20021520644	FWVZ	17	3	0.35	0.11	257	-68	27.4	21.3	0.30	-39.32	175.18	1-3	2.84	NULLAB	28.3
20021521457	FWVZ	-13	5	0.12	0.01	307	14	28.3	10.4	0.18	-39.15	175.37	1-3	5.01	AB	36.5
20021521457	FWVZ	-29	15	0.05	0.05	307	-46	28.3	10.4	0.18	-39.15	175.37	2-6	6.07	C	36.5
20021521911	FWVZ	-1	2	0.10	0.01	267	58	32.5	12.0	0.56	-39.28	174.83	1-3	2.63	AB	34.5
20021560027	FWVZ	72	3	0.25	0.01	212	-43	14.0	72.5	0.39	-39.59	175.28	1-3	2.12	A	11.4
20021561837	FWVZ	-11	2	0.12	0.01	221	-38	23.7	66.3	1.33	-40.26	174.41	0.8-2	1.93	AB	17.8
20021561837	FWVZ	-14	6	0.15	0.01	221	-43	23.7	66.3	1.33	-40.26	174.41	0.5-3	2.13	B	17.8
20021600118	FWVZ	1	4	0.12	0.01	267	74	21.1	8.1	0.06	-39.26	175.47	1-3	2.32	C	25.4
20021641137	FWVZ	-35	5	0.10	0.03	282	12	29.6	16.6	0.76	-39.10	174.60	0.1-1	1.53	A	34.6
20021641137	FWVZ	-37	9	0.12	0.01	282	11	29.6	16.6	0.76	-39.10	174.60	0.2-2	2.61	AB	34.6

continued on next page...

Event ID	Station	Φ [°]	$\pm\Phi$ [°]	δt [s]	$\pm\delta t$ [s]	Baz[°]	Pol[°]	RayPs[°]	Edepth[km]	Edist[°]	Elat[°]	Elon[°]	Filter[Hz]	Freq[Hz]	Quality	Incid[°]
20021782057	FWVZ	12	18	0.05	0.01	57	63	15.4	82.9	0.53	-38.97	176.12	1-3	2.38	AB	20.9
20021950322	FWVZ	6	6	0.60	0.01	334	-49	9.0	207.8	0.73	-38.60	175.14	1-3	1.25	AB	21.4
20020540947	LHOR2	5	5	0.25	0.01	301	55	25.9	14.4	0.19	-39.24	175.23	2-3	2.80	B	23.5
20020551137	LHOR2	4	5	0.24	0.01	40	63	24.7	5.0	1.63	-38.07	176.76	2-6	5.09	C	19.0
20020580325	LHOR2	22	6	0.09	0.01	311	-25	18.3	30.1	0.19	-39.21	175.25	1-3	3.73	AB	16.7
20020710606	LHOR2	-15	5	0.25	0.01	264	31	7.0	194.1	0.51	-39.39	174.78	1-3	3.11	AB	8.1
20020730214	LHOR2	-52	10	0.15	0.05	254	-10	12.7	142.8	0.74	-39.54	174.52	2-100	4.53	AB	12.8
20020771840	LHOR2	-23	20	0.06	0.02	109	40	27.7	12.5	0.20	-39.40	175.68	0.5-3	2.34	C	21.6
20020771840	LHOR2	-46	16	0.09	0.03	109	18	27.7	12.5	0.20	-39.40	175.68	0.5-1.5	1.53	B	21.6
20020771912	LHOR2	-39	10	0.09	0.02	91	28	27.1	15.7	0.20	-39.34	175.70	1-3	2.47	C	20.7
20020791111	LHOR2	-21	5	0.15	0.01	1	22	27.5	7.6	0.12	-39.22	175.44	0.2-2	3.26	A	22.8
20020791111	LHOR2	-9	4	0.16	0.01	1	38	27.5	7.6	0.12	-39.22	175.44	1-7	6.60	A	22.8
20020830214	LHOR2	-9	6	0.31	0.02	37	54	13.0	124.6	0.66	-38.81	175.94	0.2-2	1.67	AB	9.1
20020830518	LHOR2	-18	13	0.10	0.01	322	-54	26.0	12.1	0.16	-39.21	175.31	N/A	7.58	B	22.9
20020830518	LHOR2	-25	8	0.10	0.01	322	-68	26.0	12.1	0.16	-39.21	175.31	1-10	7.29	AB	22.9
20020961020	LHOR2	-25	8	0.33	0.01	16	20	5.1	166.2	0.31	-39.04	175.55	2-7	2.87	B	3.6
20020961020	LHOR2	-27	5	0.31	0.01	16	18	5.1	166.2	0.31	-39.04	175.55	1.4-3	2.40	AB	3.6
20020980052	LHOR2	-10	4	0.11	0.01	291	-34	22.2	30.6	0.27	-39.24	175.11	0.5-3	4.85	C	20.5
20020980052	LHOR2	-12	5	0.11	0.01	291	-34	22.2	30.6	0.27	-39.24	175.11	1-3	5.22	B	20.5
20020981048	LHOR2	84	22	0.08	0.05	139	-68	29.6	12.0	1.13	-40.18	176.41	2-6	3.66	C	24.3
20021020444	LHOR2	-9	5	0.21	0.01	270	-72	32.6	12.0	0.64	-39.33	174.61	1-3	3.01	AB	30.2
20021101137	LHOR2	35	22	0.06	0.30	32	30	20.4	247.4	3.37	-36.46	177.66	0.5-3	1.86	NULLAB	15.5
20021130013	LHOR2	8	20	0.03	0.01	56	47	24.2	77.5	2.37	-37.97	177.91	1.5-7	4.69	B	18.2
20021170309	LHOR2	34	10	0.21	0.06	225	23	21.6	90.3	1.22	-40.19	174.30	0.1-1	0.96	NULLB	20.1
20021170309	LHOR2	50	22	1.16	1.58	225	68	21.6	90.3	1.22	-40.19	174.30	0.5-3	2.69	NULLC	20.1
20021211034	LHOR2	20	14	0.09	0.05	307	50	32.1	6.7	0.21	-39.21	175.22	1-7	6.97	C	29.0
20021211034	LHOR2	27	7	0.19	0.01	307	4	32.1	6.7	0.21	-39.21	175.22	0.5-3	2.12	C	29.0
20021240504	LHOR2	-64	6	0.12	0.02	154	-14	24.7	24.0	1.30	-40.50	176.19	1-3	1.31	AB	20.5
20021240504	LHOR2	-65	16	0.09	0.01	154	-23	24.7	24.0	1.30	-40.50	176.19	1-7	5.53	B	20.5
20021240504	LHOR2	-71	8	0.14	0.02	154	-23	24.7	24.0	1.30	-40.50	176.19	0.5-2	1.46	A	20.5
20021251706	LHOR2	-6	18	0.10	0.02	118	53	21.3	62.9	0.73	-39.68	176.27	0.5-3	2.27	C	16.2
20021302308	LHOR2	78	6	0.05	0.01	300	20	31.6	7.7	0.21	-39.23	175.20	1-7	5.51	C	28.7
20021311639	LHOR2	-7	7	0.36	0.02	1	49	8.6	205.6	0.69	-38.65	175.46	0.5-3	2.82	C	6.8
20021311639	LHOR2	3	7	0.35	0.11	1	67	8.6	205.6	0.69	-38.65	175.46	1-3	2.68	C	6.8
20021320415	LHOR2	-18	3	0.25	0.01	0	35	5.9	180.9	0.40	-38.94	175.44	4-100	3.36	B	4.8
20021320415	LHOR2	-9	2	0.25	0.01	0	49	5.9	180.9	0.40	-38.94	175.44	1-3	2.43	A	4.8
20021320415	LHOR2	-9	5	0.26	0.02	0	50	5.9	180.9	0.40	-38.94	175.44	0.1-1	1.17	A	4.8
20021331816	LHOR2	-6	10	0.28	0.04	67	44	16.7	9.1	0.04	-39.32	175.49	1-7	5.08	C	11.6

continued on next page...

Event ID	Station	Φ [°]	$\pm\Phi$ [°]	δt [s]	$\pm\delta t$ [s]	Baz[°]	Pol[°]	RayP[s/°]	Edepth[km]	Edist[°]	Elat[°]	Elon[°]	Filter[Hz]	Freq[Hz]	Quality	Incid[°]
20021331816	LHOR2	-7	4	0.16	0.01	67	-58	16.7	9.1	0.04	-39.32	175.49	1-3	3.51	AB	11.6
20021331816	LHOR2	0	8	0.16	0.01	67	-47	16.7	9.1	0.04	-39.32	175.49	0.2-2	3.27	B	11.6
20021380320	LHOR2	0	5	0.30	0.01	25	58	8.5	115.0	0.36	-39.01	175.63	0.1-1	1.28	A	5.8
20021380320	LHOR2	6	3	0.31	0.01	25	64	8.5	115.0	0.36	-39.01	175.63	0.2-2	1.58	A	5.8
20021380320	LHOR2	6	8	0.15	0.01	25	-56	8.5	115.0	0.36	-39.01	175.63	4-100	3.62	C	5.8
20021380320	LHOR2	7	3	0.33	0.01	25	65	8.5	115.0	0.36	-39.01	175.63	1-3	2.51	B	5.8
20021510328	LHOR2	-53	6	0.12	0.01	148	0	23.6	66.6	1.34	-40.47	176.38	1-3	2.52	B	19.3
20021512336	LHOR2	39	9	0.15	0.01	68	0	17.4	92.7	0.74	-39.06	176.32	0.5-3	2.38	B	12.2
20021520644	LHOR2	-12	5	0.16	0.01	275	48	23.6	21.3	0.20	-39.32	175.18	1-3	3.19	B	22.0
20021520644	LHOR2	-8	2	0.17	0.01	275	58	23.6	21.3	0.20	-39.32	175.18	2-6	5.98	AB	22.0
20021521457	LHOR2	11	8	0.16	0.01	344	58	29.1	10.4	0.19	-39.15	175.37	0.8-3	2.57	B	24.9
20021521911	LHOR2	11	2	0.19	0.01	277	79	32.4	12.0	0.48	-39.28	174.83	1.5-4	2.96	AB	29.9
20021551105	LHOR2	72	14	0.06	0.01	112	-73	22.8	66.5	1.03	-39.71	176.68	2-6	4.32	AB	17.4
20021560027	LHOR2	-12	6	0.09	0.01	206	-70	10.8	72.5	0.28	-39.59	175.28	1-3	2.51	AB	10.6
20021560027	LHOR2	45	10	0.08	0.01	206	8	10.8	72.5	0.28	-39.59	175.28	4-100	7.34	AB	10.6
20021560027	LHOR2	54	22	0.08	0.01	206	24	10.8	72.5	0.28	-39.59	175.28	2-6	4.83	C	10.6
20021561837	LHOR2	39	22	0.09	0.05	220	-62	23.4	66.3	1.22	-40.26	174.41	1-3	1.96	NULLB	21.6
20021600118	LHOR2	-10	6	0.17	0.01	18	42	23.4	8.1	0.08	-39.26	175.47	2-6	5.55	AB	18.5
20021600118	LHOR2	-4	4	0.17	0.01	18	43	23.4	8.1	0.08	-39.26	175.47	1-3	2.27	A	18.5
20021641137	LHOR2	-13	6	0.19	0.01	290	39	32.5	16.6	0.69	-39.10	174.60	1-3	2.37	B	29.8
20021641137	LHOR2	-14	8	0.19	0.01	290	45	32.5	16.6	0.69	-39.10	174.60	4-100	5.39	C	29.8
20021641137	LHOR2	-20	5	0.17	0.01	290	26	32.5	16.6	0.69	-39.10	174.60	0.2-2	2.54	A	29.8
20021641137	LHOR2	-7	4	0.19	0.01	290	52	32.5	16.6	0.69	-39.10	174.60	2-6	5.18	A	29.8
20021770025	LHOR2	-87	13	0.09	0.07	14	-47	24.7	12.0	1.47	-37.91	175.90	4-100	5.11	AB	19.8
20021950322	LHOR2	0	7	0.34	0.02	342	49	9.5	207.8	0.77	-38.60	175.14	1-3	2.41	A	8.3
20021950322	LHOR2	16	8	0.34	0.01	342	62	9.5	207.8	0.77	-38.60	175.14	2-6	2.73	B	8.3
20020150921	LHUT2	54	7	0.28	0.01	277	88	5.9	216.5	0.48	-39.19	174.95	1-3	2.83	AB	16.8
20020161202	LHUT2	32	11	0.10	0.01	320	-13	5.0	224.2	0.42	-38.93	175.21	4-100	4.50	B	17.9
20020161202	LHUT2	39	22	0.53	0.81	320	42	5.0	224.2	0.42	-38.93	175.21	0.2-2	1.25	NULLAB	17.9
20020161202	LHUT2	39	10	0.10	0.01	320	3	5.0	224.2	0.42	-38.93	175.21	1-10	3.19	AB	17.9
20020161202	LHUT2	43	3	0.80	0.04	320	33	5.0	224.2	0.42	-38.93	175.21	0.1-1	0.66	NULLAB	17.9
20020180109	LHUT2	1	22	0.08	0.21	243	19	13.5	196.1	1.14	-39.76	174.24	0.5-3	2.78	C	16.8
20020180109	LHUT2	20	22	0.05	0.28	243	22	13.5	196.1	1.14	-39.76	174.24	1-2	2.29	NULLB	16.8
20020200048	LHUT2	-60	7	0.08	0.01	250	-15	26.3	12.1	0.17	-39.31	175.36	0.3-3	4.83	AB	26.1
20020221745	LHUT2	-29	2	0.06	0.01	150	42	27.3	16.3	0.22	-39.44	175.70	1-7	6.24	AB	9.6
20020221745	LHUT2	-40	6	0.06	0.01	150	28	27.3	16.3	0.22	-39.44	175.70	0.5-3	5.59	AB	9.6
20020230636	LHUT2	78	5	0.84	0.03	194	-63	24.4	49.2	1.18	-40.40	175.20	0.1-1	0.81	CWEIRD	11.8
20020230636	LHUT2	81	3	0.82	0.01	194	-56	24.4	49.2	1.18	-40.40	175.20	0.5-1	0.85	CWEIRD	11.8

continued on next page...

Event ID	Station	Φ [°]	$\pm\Phi$ [°]	δt [s]	$\pm\delta t$ [s]	Baz[°]	Pol[°]	RayPs[°]	Edepth[km]	Edist[°]	Elat[°]	Elon[°]	Filter[Hz]	Freq[Hz]	Quality	Incid[°]
20020250314	LHUT2	-27	22	0.04	0.05	43	37	15.2	87.2	0.55	-38.85	176.04	0.5-3	2.44	B	22.7
20020250314	LHUT2	-39	7	0.06	0.03	43	34	15.2	87.2	0.55	-38.85	176.04	1-3	2.67	B	22.7
20020250314	LHUT2	29	22	0.26	1.12	43	21	15.2	87.2	0.55	-38.85	176.04	0.1-1	1.00	NULLAB	22.7
20020250314	LHUT2	35	10	0.08	0.08	43	57	15.2	87.2	0.55	-38.85	176.04	4-100	5.36	C	22.7
20020250314	LHUT2	36	22	0.08	0.84	43	34	15.2	87.2	0.55	-38.85	176.04	0.2-2	1.09	NULLA	22.7
20020301730	LHUT2	22	5	0.09	0.01	261	82	31.5	16.5	0.45	-39.32	174.99	0.5-3	4.35	C	32.4
2002030120	LHUT2	-35	4	0.08	0.01	277	21	28.8	26.1	0.51	-39.19	174.91	1-7	5.65	B	33.1
2002030120	LHUT2	-67	6	0.09	0.01	277	-5	28.8	26.1	0.51	-39.19	174.91	1-3	3.64	B	33.1
20020411851	LHUT2	-25	1	0.06	0.01	152	49	22.8	14.1	0.13	-39.37	175.64	4-100	7.22	A	5.6
20020411851	LHUT2	-36	2	0.06	0.01	152	34	22.8	14.1	0.13	-39.37	175.64	1-7	5.98	A	5.6
20020411851	LHUT2	-40	4	0.06	0.01	152	29	22.8	14.1	0.13	-39.37	175.64	0.2-2	5.19	AB	5.6
20020500534	LHUT2	-42	2	0.09	0.01	291	24	28.8	22.2	0.40	-39.11	175.08	1-7	4.84	A	35.2
20020500534	LHUT2	-44	2	0.08	0.01	291	20	28.8	22.2	0.40	-39.11	175.08	1-3	3.24	A	35.2
20020530147	LHUT2	-46	8	0.06	0.02	304	19	31.5	8.7	0.24	-39.12	175.31	1-3	3.06	B	39.1
20020530147	LHUT2	-78	4	0.09	0.01	304	-13	31.5	8.7	0.24	-39.12	175.31	4-100	9.60	B	39.1
20020580325	LHUT2	-56	2	0.26	0.01	280	46	21.2	30.1	0.25	-39.21	175.25	1-3	4.58	C	27.5
20020580325	LHUT2	-68	4	0.09	0.01	280	58	21.2	30.1	0.25	-39.21	175.25	4-100	8.28	A	27.5
20020710606	LHUT2	56	8	0.28	0.02	257	-82	8.4	194.1	0.62	-39.39	174.78	1-3	2.47	AB	16.3
20020730214	LHUT2	-88	4	0.05	0.01	250	-23	14.1	142.8	0.86	-39.54	174.52	2-10	5.70	AB	18.2
20020771811	LHUT2	-42	6	0.06	0.01	146	27	25.3	14.4	0.18	-39.40	175.69	0.7-3	5.28	A	8.4
20020771811	LHUT2	-50	4	0.08	0.01	146	12	25.3	14.4	0.18	-39.40	175.69	1-7	6.76	AB	8.4
20020771840	LHUT2	-25	4	0.06	0.01	148	48	26.2	12.5	0.17	-39.40	175.68	N/A	5.95	AB	8.9
20020771840	LHUT2	-39	2	0.06	0.01	148	29	26.2	12.5	0.17	-39.40	175.68	0.5-3	5.55	A	8.9
20020771912	LHUT2	-41	2	0.06	0.01	129	27	23.7	15.7	0.14	-39.34	175.70	1-3	5.58	A	10.6
20020771912	LHUT2	-47	5	0.08	0.01	129	17	23.7	15.7	0.14	-39.34	175.70	1-7	6.16	A	10.6
20020771939	LHUT2	-28	4	0.06	0.01	142	44	26.9	15.9	0.20	-39.41	175.72	4-100	7.66	B	10.4
20020771939	LHUT2	-46	4	0.06	0.01	142	22	26.9	15.9	0.20	-39.41	175.72	1-5	5.62	AB	10.4
20020791111	LHUT2	-10	6	0.21	0.01	289	13	26.0	7.6	0.10	-39.22	175.44	1-3	4.93	C	32.6
20020791111	LHUT2	-59	10	0.03	0.01	289	-1	26.0	7.6	0.10	-39.22	175.44	1-7	5.63	B	32.6
20020810622	LHUT2	-48	4	0.23	0.01	263	21	27.3	33.0	0.57	-39.32	174.83	0.5-3	5.29	B	29.4
20020830518	LHUT2	-38	4	0.17	0.01	282	75	28.0	12.1	0.20	-39.21	175.31	1-7	4.94	B	33.2
20020961020	LHUT2	33	8	0.51	0.02	358	0	3.6	166.2	0.21	-39.04	175.55	1.4-3	2.70	C	16.8
20020970004	LHUT2	-42	20	0.05	0.02	268	-15	32.4	6.5	0.26	-39.26	175.22	0.5-3	2.83	AB	34.6
20020971717	LHUT2	-56	4	0.06	0.01	270	16	32.1	12.0	0.37	-39.25	175.08	0.8-3	5.06	B	34.7
20020980052	LHUT2	26	2	0.05	0.01	272	-86	24.9	30.6	0.35	-39.24	175.11	1-7	6.19	C	29.1
20020981220	LHUT2	80	9	0.08	0.01	113	-49	23.8	62.2	1.28	-39.74	177.09	0.5-3	2.48	AB	14.5
20021001827	LHUT2	-80	22	0.05	0.01	143	-42	32.3	11.2	0.40	-39.57	175.87	2-6	4.72	B	14.8
20021001827	LHUT2	83	17	0.08	0.02	143	-63	32.3	11.2	0.40	-39.57	175.87	1-3	2.74	B	14.8

continued on next page...

Event ID	Station	Φ [°]	$\pm\Phi$ [°]	δt [s]	$\pm\delta t$ (s)	Baz[°]	Pol[°]	RayP[s/°]	Edepth[km]	Edist[°]	Elat[°]	Elon[°]	Filter[Hz]	Freq[Hz]	Quality	Incid[°]
20021072114	LHUT2	33	7	0.70	0.03	54	-86	17.4	81.9	0.63	-38.88	176.22	0.2-2	1.57	B	22.7
20021072114	LHUT2	41	6	0.68	0.03	54	-81	17.4	81.9	0.63	-38.88	176.22	0.1-1	1.31	B	22.7
20021072114	LHUT2	43	16	0.70	0.14	54	-81	17.4	81.9	0.63	-38.88	176.22	1-7	1.96	C	22.7
20021092051	LHUT2	-59	22	0.10	0.09	162	7	31.4	10.3	0.27	-39.51	175.67	1-3	2.38	B	12.9
20021101137	LHUT2	22	4	0.84	0.02	31	44	20.2	247.4	3.25	-36.46	177.66	0.2-2	1.53	C	27.9
20021101137	LHUT2	22	4	0.84	0.16	31	44	20.2	247.4	3.25	-36.46	177.66	0.5-3	1.73	C	27.9
20021211034	LHUT2	-40	6	0.09	0.01	279	11	32.4	6.7	0.27	-39.21	175.22	1-7	7.41	C	36.5
20021211034	LHUT2	-45	10	0.08	0.01	279	6	32.4	6.7	0.27	-39.21	175.22	0.2-2	3.53	AB	36.5
20021211034	LHUT2	-47	4	0.08	0.01	279	5	32.4	6.7	0.27	-39.21	175.22	1-3	4.44	A	36.5
20021211034	LHUT2	-48	5	0.10	0.01	279	3	32.4	6.7	0.27	-39.21	175.22	4-100	11.15	AB	36.5
20021240504	LHUT2	79	18	0.12	0.03	159	-58	24.7	24.0	1.34	-40.50	176.19	0.2-2	1.21	C	6.8
20021251706	LHUT2	31	7	0.10	0.01	128	76	21.0	62.9	0.70	-39.68	176.27	0.5-3	2.34	A	9.3
20021262050	LHUT2	-71	3	0.05	0.01	235	0	15.7	131.9	0.92	-39.78	174.59	4-100	6.10	B	16.4
20021262050	LHUT2	24	6	0.10	0.01	235	56	15.7	131.9	0.92	-39.78	174.59	1-2	2.14	A	16.4
20021291925	LHUT2	20	22	1.70	1.26	25	15	17.8	174.8	1.58	-37.81	176.40	0.1-1	1.39	NULLA	26.6
20021291925	LHUT2	23	22	1.62	1.81	25	19	17.8	174.8	1.58	-37.81	176.40	1-7	1.88	NULLA	26.6
20021291925	LHUT2	23	3	0.30	0.71	25	32	17.8	174.8	1.58	-37.81	176.40	N/A	1.91	NULLA	26.6
20021302308	LHUT2	-42	8	0.09	0.04	274	7	32.3	7.7	0.28	-39.23	175.20	1-7	6.50	AB	35.6
20021302308	LHUT2	-46	6	0.08	0.01	274	4	32.3	7.7	0.28	-39.23	175.20	0.5-3	4.56	A	35.6
20021302308	LHUT2	-47	6	0.08	0.01	274	3	32.3	7.7	0.28	-39.23	175.20	0.2-2	2.99	C	35.6
20021302308	LHUT2	-50	7	0.10	0.01	274	-6	32.3	7.7	0.28	-39.23	175.20	4-100	9.62	AB	35.6
20021310608	LHUT2	22	5	0.11	0.06	236	45	17.1	201.8	1.73	-40.20	173.68	1-7	4.75	NULLAB	17.3
20021311639	LHUT2	21	10	0.38	0.02	353	58	7.7	205.6	0.61	-38.65	175.46	1-3	2.66	B	20.2
20021320156	LHUT2	-43	8	0.08	0.01	273	4	29.6	12.0	0.24	-39.24	175.25	1-3	3.31	A	33.1
20021320156	LHUT2	-44	6	0.10	0.01	273	2	29.6	12.0	0.24	-39.24	175.25	4-100	8.96	A	33.1
20021320156	LHUT2	-47	7	0.09	0.01	273	1	29.6	12.0	0.24	-39.24	175.25	1-7	5.82	C	33.1
20021320156	LHUT2	-50	12	0.08	0.01	273	-3	29.6	12.0	0.24	-39.24	175.25	0.2-2	2.88	AB	33.1
20021320415	LHUT2	23	22	0.10	0.93	343	19	4.9	180.9	0.33	-38.94	175.44	0.2-2	2.19	NULLA	18.0
20021320415	LHUT2	33	8	0.49	0.10	343	6	4.9	180.9	0.33	-38.94	175.44	1-3	2.45	C	18.0
20021320415	LHUT2	39	6	0.49	0.01	343	5	4.9	180.9	0.33	-38.94	175.44	1-7	2.91	AB	18.0
20021331816	LHUT2	28	22	0.16	0.49	219	31	23.0	9.1	0.09	-39.32	175.49	1-7	6.72	NULLA	16.9
20021331816	LHUT2	32	6	0.34	0.34	219	24	23.0	9.1	0.09	-39.32	175.49	4-100	8.07	NULLAB	16.9
20021341356	LHUT2	35	3	0.34	0.04	207	51	24.7	41.8	2.40	-41.38	174.10	4-100	5.14	NULLB	15.1
20021380320	LHUT2	10	10	0.38	0.82	13	-5	6.1	115.0	0.25	-39.01	175.63	0.5-1	1.48	NULLAB	18.4
20021431119	LHUT2	-1	8	0.03	0.01	154	49	27.8	19.9	0.29	-39.51	175.72	1-7	5.78	B	9.8
20021431119	LHUT2	-40	8	0.05	0.01	154	27	27.8	19.9	0.29	-39.51	175.72	0.5-3	3.90	AB	9.8
20021431119	LHUT2	-48	6	0.06	0.01	154	21	27.8	19.9	0.29	-39.51	175.72	1-3	3.69	AB	9.8
20021461304	LHUT2	19	8	0.30	0.01	13	-33	3.1	98.6	0.10	-39.15	175.59	1-7	3.84	AB	16.2

continued on next page...

Event ID	Station	Φ [°]	$\pm\Phi$ [°]	δt [s]	$\pm\delta t$ [s]	Baz[°]	Pol[°]	RayPs[°]	Edepth[km]	Edist[°]	Elat[°]	Elon[°]	Filter[Hz]	Freq[Hz]	Quality	Incid[°]
20021461304	LHUT2	25	5	0.29	0.01	13	-32	3.1	98.6	0.10	-39.15	175.59	0.5-3	2.44	A	16.2
20020150921	LQUA2	52	18	0.11	0.03	274	-67	5.7	216.5	0.46	-39.19	174.95	1-3	1.51	C	8.1
20020161202	LQUA2	11	5	0.21	0.02	318	66	4.6	224.2	0.39	-38.93	175.21	0.4-1	0.77	A	9.5
20020180109	LQUA2	18	18	0.57	0.14	241	-37	13.5	196.1	1.14	-39.76	174.24	1-3	1.93	C	9.8
20020221745	LQUA2	-4	6	0.09	0.01	151	38	28.3	16.3	0.25	-39.44	175.70	1-3	2.53	B	18.8
20020230636	LQUA2	14	6	1.48	1.34	192	-82	24.4	49.2	1.21	-40.40	175.20	0-0.5	0.65	NULLB	14.4
20020231642	LQUA2	-37	4	0.17	0.02	152	38	28.2	20.7	0.32	-39.50	175.73	1-3	2.43	AB	18.6
20020250314	LQUA2	29	10	0.55	0.06	47	-27	15.0	87.2	0.54	-38.85	176.04	0.2-2	0.78	AB	17.4
20020250314	LQUA2	31	8	0.49	0.06	47	-27	15.0	87.2	0.54	-38.85	176.04	0.1-1	0.74	A	17.4
20020281737	LQUA2	-29	4	0.16	0.02	169	51	27.9	16.2	0.23	-39.45	175.60	1-3	2.42	AB	17.5
20020301730	LQUA2	-27	10	0.25	0.03	257	-89	31.4	16.5	0.44	-39.32	174.99	0.1-1	2.22	C	26.1
20020360844	LQUA2	11	8	0.17	0.02	233	47	18.8	179.2	1.84	-40.31	173.61	0.7-2	1.38	AB	12.9
20020390120	LQUA2	-1	10	0.14	0.01	273	41	28.7	26.1	0.49	-39.19	174.91	1-3	4.46	C	25.5
20020390120	LQUA2	9	6	0.14	0.01	273	52	28.7	26.1	0.49	-39.19	174.91	1-7	5.21	B	25.5
20020410319	LQUA2	66	22	0.15	1.02	138	50	24.9	13.7	0.16	-39.34	175.68	1-3	2.26	NULLB	16.8
20020411851	LQUA2	-3	14	0.08	0.01	153	29	25.0	14.1	0.17	-39.37	175.64	1-7	4.81	C	15.7
20020411851	LQUA2	2	6	0.09	0.01	153	36	25.0	14.1	0.17	-39.37	175.64	0.5-3	2.29	AB	15.7
20020500534	LQUA2	-24	15	0.11	0.01	287	28	28.5	22.2	0.37	-39.11	175.08	1-4	3.80	B	26.7
20020530147	LQUA2	-34	6	0.11	0.01	299	12	30.8	8.7	0.20	-39.12	175.31	1-3	3.17	A	29.8
20020671226	LQUA2	62	8	0.47	0.03	232	-62	20.9	114.0	1.47	-40.11	174.03	0.2-2	1.98	C	14.5
20020771840	LQUA2	3	12	0.09	0.01	149	39	28.1	12.5	0.21	-39.40	175.68	0.5-3	3.46	A	18.7
20020771912	LQUA2	-32	14	0.06	0.01	134	15	25.9	15.7	0.17	-39.34	175.70	1-3	2.27	AB	18.1
20020791111	LQUA2	-22	13	0.12	0.02	270	30	23.7	7.6	0.08	-39.22	175.44	0.5-2	2.31	AB	20.9
20020791111	LQUA2	-45	15	0.10	0.01	270	-4	23.7	7.6	0.08	-39.22	175.44	1-7	4.32	AB	20.9
20020830518	LQUA2	19	22	0.08	0.07	273	-63	27.1	12.1	0.18	-39.21	175.31	0.4-2	2.89	NULLB	24.0
20020980052	LQUA2	-27	6	0.05	0.01	266	32	24.5	30.6	0.33	-39.24	175.11	1-3	3.98	B	21.1
20020980052	LQUA2	-33	9	0.05	0.01	266	33	24.5	30.6	0.33	-39.24	175.11	0.5-3	4.28	C	21.1
20021010800	LQUA2	10	22	0.17	1.08	149	5	24.7	35.7	1.40	-40.41	176.49	0.4-1	0.88	NULLAB	15.7
20021072114	LQUA2	31	6	0.70	0.30	58	-42	17.3	81.9	0.63	-38.88	176.22	0.2-2	1.02	C	18.5
20021072114	LQUA2	34	11	0.74	0.31	58	-70	17.3	81.9	0.63	-38.88	176.22	0.1-1	0.87	B	18.5
20021072114	LQUA2	40	5	0.26	0.02	58	-27	17.3	81.9	0.63	-38.88	176.22	1-7	3.01	B	18.5
20021072114	LQUA2	40	8	0.25	0.03	58	-27	17.3	81.9	0.63	-38.88	176.22	1-3	1.81	C	18.5
20021211034	LQUA2	-21	7	0.10	0.01	272	22	32.3	6.7	0.25	-39.21	175.22	1-3	3.06	B	28.6
20021211034	LQUA2	-24	6	0.26	0.01	272	-68	32.3	6.7	0.25	-39.21	175.22	0.5-3	2.33	C	28.6
20021211034	LQUA2	-27	8	0.11	0.01	272	16	32.3	6.7	0.25	-39.21	175.22	1-7	3.86	AB	28.6
20021240504	LQUA2	-70	8	0.15	0.02	159	-21	24.7	24.0	1.37	-40.50	176.19	0.5-3	1.30	A	15.1
20021302308	LQUA2	-22	6	0.10	0.01	268	14	32.2	7.7	0.26	-39.23	175.20	0.5-3	3.53	AB	28.0
20021302308	LQUA2	-24	10	0.11	0.01	268	19	32.2	7.7	0.26	-39.23	175.20	1-7	4.12	C	28.0

continued on next page...

Event ID	Station	Φ [°]	$\pm\Phi$ [°]	δt [s]	$\pm\delta t$ [s]	Baz[°]	Pol[°]	RayP[s/°]	Edepth[km]	Edist[°]	Elat[°]	Elon[°]	Filter[Hz]	Freq[Hz]	Quality	Incid[°]
20021311639	LQUA2	18	8	0.38	0.02	354	68	7.3	205.6	0.57	-38.65	175.46	1-7	2.30	B	12.3
20021311639	LQUA2	27	8	0.35	0.02	354	78	7.3	205.6	0.57	-38.65	175.46	1-3	2.04	C	12.3
20021320156	LQUA2	-31	13	0.10	0.01	265	7	29.1	12.0	0.23	-39.24	175.25	1-7	4.03	C	25.0
20021320415	LQUA2	14	7	0.29	0.03	344	68	4.4	180.9	0.29	-38.94	175.44	0.5-3	1.25	A	9.8
20021320415	LQUA2	17	5	0.29	0.02	344	70	4.4	180.9	0.29	-38.94	175.44	0.2-2	0.90	A	9.8
20021380320	LQUA2	38	5	0.34	0.03	18	-81	5.4	115.0	0.22	-39.01	175.63	0.3-1	0.88	A	10.6
20021380320	LQUA2	38	6	0.34	0.03	18	-88	5.4	115.0	0.22	-39.01	175.63	0.2-2	1.20	AB	10.6
20021461304	LQUA2	4	22	0.54	1.15	29	87	2.4	98.6	0.08	-39.15	175.59	2-6	2.59	NULLB	8.1
20021461304	LQUA2	5	3	0.34	0.34	29	-79	2.4	98.6	0.08	-39.15	175.59	1-3	2.27	NULLAB	8.1
20021520644	LQUA2	-27	6	0.14	0.01	250	29	27.5	21.3	0.30	-39.32	175.18	2-6	7.07	A	21.9
20021521911	LQUA2	-26	6	0.11	0.01	264	15	32.5	12.0	0.56	-39.28	174.83	1-3	2.36	AB	27.9
20021600118	LQUA2	24	22	0.01	0.02	234	22	21.7	8.1	0.07	-39.26	175.47	1-3	3.08	NULLAB	15.3
20021641137	LQUA2	-42	9	0.09	0.01	279	2	29.6	16.6	0.74	-39.10	174.60	0.5-3	3.07	A	26.9
20021950322	LQUA2	13	6	0.34	0.02	333	66	8.6	207.8	0.69	-38.60	175.14	1-3	2.18	AB	13.0
2002150921	LTUR2	37	22	0.09	0.11	286	16	5.6	216.5	0.46	-39.19	174.95	0.5-3	2.80	C	12.2
2002150921	LTUR2	45	21	0.08	0.02	286	24	5.6	216.5	0.46	-39.19	174.95	1-7	2.99	C	12.2
20020161202	LTUR2	20	4	0.29	0.01	328	46	5.4	224.2	0.45	-38.93	175.21	0.5-3	2.43	A	9.7
20020161202	LTUR2	21	6	0.29	0.02	328	44	5.4	224.2	0.45	-38.93	175.21	1-7	2.95	AB	9.7
20020161202	LTUR2	22	2	0.29	0.01	328	52	5.4	224.2	0.45	-38.93	175.21	0.2-2	1.91	A	9.7
20020180108	LTUR2	-83	5	0.11	0.01	245	-16	13.0	196.1	1.08	-39.76	174.24	1-3	2.89	C	19.3
20020221745	LTUR2	27	4	0.05	0.01	131	50	26.4	16.3	0.19	-39.44	175.70	0.5-3	3.26	C	21.1
20020231642	LTUR2	-11	4	0.11	0.01	138	51	26.5	20.7	0.25	-39.50	175.73	1-3	3.24	C	22.2
20020250314	LTUR2	-10	7	0.25	0.03	42	-71	16.4	87.2	0.62	-38.85	176.04	0.2-2	1.17	B	6.1
20020250314	LTUR2	2	7	0.26	0.07	42	-65	16.4	87.2	0.62	-38.85	176.04	0.1-1	0.49	B	6.1
20020301730	LTUR2	-21	6	0.08	0.01	269	16	30.9	16.5	0.41	-39.32	174.99	0.5-3	3.01	AB	34.1
20020301730	LTUR2	-35	9	0.09	0.01	269	13	30.9	16.5	0.41	-39.32	174.99	1-7	2.69	B	34.1
20020301730	LTUR2	-38	9	0.06	0.01	269	12	30.9	16.5	0.41	-39.32	174.99	0.2-2	2.48	AB	34.1
20020301917	LTUR2	-15	6	0.09	0.01	270	23	26.9	26.2	0.38	-39.31	175.02	0.5-3	2.86	C	30.4
20020390120	LTUR2	-4	4	0.14	0.01	285	62	28.6	26.1	0.49	-39.19	174.91	1-3	2.78	AB	30.9
20020411851	LTUR2	26	6	0.05	0.01	120	46	21.2	14.1	0.11	-39.37	175.64	0.2-2	3.09	C	15.3
20020411851	LTUR2	27	6	0.05	0.01	120	49	21.2	14.1	0.11	-39.37	175.64	0.5-3	2.66	C	15.3
20020521025	LTUR2	-18	3	0.31	0.01	230	-88	10.2	86.0	0.32	-39.52	175.20	1-3	2.60	AB	16.9
20020522041	LTUR2	55	8	0.10	0.02	187	75	32.8	5.0	0.35	-39.66	175.46	0.3-3	2.38	NULLB	33.9
20020531312	LTUR2	-28	22	0.03	0.23	84	6	32.6	12.0	0.65	-39.24	176.35	1-3	4.00	C	20.5
20020540947	LTUR2	-31	6	0.23	0.02	288	78	27.8	14.4	0.23	-39.24	175.23	1-3	2.93	C	29.9
20020580325	LTUR2	-1	6	0.06	0.01	297	17	20.5	30.1	0.23	-39.21	175.25	1-7	6.61	C	22.9
20020710606	LTUR2	-40	4	0.11	0.01	262	23	7.8	194.1	0.58	-39.39	174.78	1-7	3.59	B	14.7
20020710606	LTUR2	-46	4	0.11	0.01	262	16	7.8	194.1	0.58	-39.39	174.78	0.5-3	2.92	A	14.7

continued on next page...

Event ID	Station	Φ [°]	$\pm\Phi$ [°]	δt [s]	$\pm\delta t$ [s]	Baz[°]	Pol[°]	RayPs[°]	Edepth[km]	Edist[°]	Elat[°]	Elon[°]	Filter[Hz]	Freq[Hz]	Quality	Incid[°]
20020771811	LTUR2	25	8	0.05	0.01	123	49	24.3	14.4	0.16	-39.40	175.69	1-3	3.26	C	18.2
20020771840	LTUR2	28	12	0.05	0.01	124	50	25.1	12.5	0.15	-39.40	175.68	0.5-3	4.12	C	19.0
20020791111	LTUR2	4	22	0.38	0.74	328	13	27.0	7.6	0.11	-39.22	175.44	1-7	5.28	NULLB	24.6
20020830214	LTUR2	8	9	0.25	0.04	33	39	12.2	124.6	0.60	-38.81	175.94	0.5-1	0.97	A	4.6
20020830518	LTUR2	4	4	0.11	0.01	303	-17	27.5	12.1	0.19	-39.21	175.31	0.5-3	2.63	B	28.2
20020871712	LTUR2	-56	20	0.16	0.05	126	14	23.8	63.0	1.30	-40.07	176.89	0.6-2	1.94	C	18.2
20020922122	LTUR2	-37	6	0.16	0.14	162	40	32.6	8.3	0.42	-39.71	175.68	0.5-3	3.29	C	30.8
20020970004	LTUR2	71	22	0.82	1.12	283	-11	32.3	6.5	0.24	-39.26	175.22	1-3	2.79	NULLAB	34.4
20020971717	LTUR2	-20	6	0.15	0.01	281	39	31.8	12.0	0.34	-39.25	175.08	1-3	2.88	AB	34.0
20020980052	LTUR2	-26	8	0.06	0.01	283	12	24.1	30.6	0.32	-39.24	175.11	0.5-3	3.49	B	27.1
20021010800	LTUR2	25	12	0.21	0.04	146	-33	24.7	35.7	1.33	-40.41	176.49	0.4-1	0.97	B	21.9
20021020444	LTUR2	-40	11	0.19	0.01	268	20	32.7	12.0	0.70	-39.33	174.61	1-3	2.24	B	35.8
20021141142	LTUR2	-67	3	0.10	0.01	144	9	27.7	12.0	0.19	-39.47	175.66	1-3	3.04	C	24.0
20021211034	LTUR2	-17	6	0.23	0.02	294	-83	32.3	6.7	0.25	-39.21	175.22	0.5-2	2.88	B	33.4
20021262050	LTUR2	-31	6	0.15	0.01	237	34	15.0	131.9	0.85	-39.78	174.59	1-2	2.03	AB	21.0
20021291925	LTUR2	-50	6	0.34	0.03	25	68	18.1	174.8	1.65	-37.81	176.40	0.5-3	1.82	C	9.5
20021291925	LTUR2	22	22	0.38	0.40	25	-16	18.1	174.8	1.65	-37.81	176.40	0.1-1	0.64	C	9.5
20021320415	LTUR2	20	16	0.28	0.12	351	45	5.7	180.9	0.38	-38.94	175.44	1-7	2.64	C	8.1
20021320415	LTUR2	22	4	0.29	0.01	351	55	5.7	180.9	0.38	-38.94	175.44	0.2-2	2.13	A	8.1
20021320415	LTUR2	22	8	0.28	0.02	351	51	5.7	180.9	0.38	-38.94	175.44	0.5-3	2.48	B	8.1
20021320415	LTUR2	25	3	0.29	0.01	351	63	5.7	180.9	0.38	-38.94	175.44	0.1-1	1.83	A	8.1
20021331816	LTUR2	-21	9	0.21	0.01	253	28	11.1	9.1	0.02	-39.32	175.49	0.5-3	2.54	B	17.6
20021380320	LTUR2	26	5	0.31	0.02	16	64	7.6	115.0	0.32	-39.01	175.63	0.1-1	1.31	A	5.9
20021380320	LTUR2	39	4	0.33	0.01	16	86	7.6	115.0	0.32	-39.01	175.63	0.2-2	2.11	B	5.9
20021380320	LTUR2	45	4	0.33	0.01	16	-83	7.6	115.0	0.32	-39.01	175.63	1-3	2.51	A	5.9
20021461304	LTUR2	12	3	0.23	0.02	20	-62	5.1	98.6	0.18	-39.15	175.59	0.5-3	1.56	AB	5.9
20021461304	LTUR2	3	4	0.19	0.32	20	80	5.1	98.6	0.18	-39.15	175.59	1-7	2.26	NULLAB	5.9
20021520644	LTUR2	-14	3	0.11	0.01	269	52	26.2	21.3	0.26	-39.32	175.18	1-3	3.02	AB	29.9
20021521457	LTUR2	-5	2	0.10	0.01	326	20	29.3	10.4	0.20	-39.15	175.37	1-3	2.70	AB	26.8
20021521911	LTUR2	-6	8	0.15	0.01	274	48	32.5	12.0	0.53	-39.28	174.83	1-3	2.85	C	35.2
20021521911	LTUR2	41	22	0.26	0.38	274	-42	32.5	12.0	0.53	-39.28	174.83	2-6	3.82	NULLAB	35.2
20021531944	LTUR2	13	10	0.05	0.01	83	62	32.1	12.0	0.37	-39.27	175.98	1-3	2.48	C	19.9
20021551105	LTUR2	-44	22	0.09	0.09	114	12	22.6	66.5	0.99	-39.71	176.68	0.5-3	2.01	C	15.5
20021560027	LTUR2	-25	3	0.06	0.01	213	37	12.2	72.5	0.33	-39.59	175.28	2-6	4.84	AB	18.1
20021561837	LTUR2	2	9	0.30	0.09	222	52	23.5	66.3	1.27	-40.26	174.41	0.5-3	2.08	A	28.0
20021561837	LTUR2	7	8	0.30	0.01	222	58	23.5	66.3	1.27	-40.26	174.41	1-3	2.98	A	28.0
20020150921	TUK2	35	20	0.14	0.04	278	8	6.7	216.5	0.55	-39.19	174.95	0.8-3	1.82	C	1.8
20020161202	TUK2	-1	6	0.26	0.03	315	-34	5.7	224.2	0.48	-38.93	175.21	0.2-2	1.83	AB	4.3

continued on next page...

Event ID	Station	Φ [°]	$\pm\Phi$ [°]	δt [s]	$\pm\delta t$ [s]	Baz[°]	Pol[°]	RayP[s/°]	Edepth[km]	Edist[°]	Elat[°]	Elon[°]	Filter[Hz]	Freq[Hz]	Quality	Incid[°]
20020180109	TUK2	-73	11	0.10	0.02	245	53	13.9	196.1	1.19	-39.76	174.24	1-3	2.65	C	7.2
20020250314	TUK2	21	4	0.99	0.08	36	-82	14.7	87.2	0.52	-38.85	176.04	0.1-1	0.88	NULLC	15.8
20020301730	TUK2	29	5	0.17	0.03	264	-32	32.2	16.5	0.51	-39.32	174.99	0.1-1	1.02	AB	23.0
20020360844	TUK2	-16	5	0.14	0.01	236	-77	19.0	179.2	1.88	-40.31	173.61	1-3	1.35	AB	11.8
20020390120	TUK2	-9	6	0.11	0.01	278	-72	29.0	26.1	0.58	-39.19	174.91	1-3	2.92	B	20.3
20020521025	TUK12	-10	12	0.19	0.01	233	-59	12.2	86.0	0.40	-39.52	175.20	1-3	2.29	C	6.1
20020531312	TUK12	62	12	0.08	0.01	86	7	32.5	12.0	0.58	-39.24	176.35	0.7-5	4.38	B	37.0
20020531312	TUK12	73	8	0.06	0.01	86	20	32.5	12.0	0.58	-39.24	176.35	1-3	3.98	AB	37.0
20020531312	TUK12	76	17	0.08	0.06	86	28	32.5	12.0	0.58	-39.24	176.35	0.5-3	4.15	C	37.0
20020771811	TUK12	-37	10	0.20	0.08	153	-87	22.9	14.4	0.14	-39.40	175.69	1-3	3.98	C	24.7
20020771840	TUK12	42	22	0.12	0.45	156	-43	23.7	12.5	0.13	-39.40	175.68	N/A	5.98	NULLA	25.0
20020771912	TUK12	43	4	0.03	0.01	132	-39	18.1	15.7	0.09	-39.34	175.70	4-100	13.09	NULLA	22.7
20020771939	TUK12	-58	12	0.01	0.01	147	-44	25.0	15.9	0.16	-39.41	175.72	4-100	12.74	B	27.1
20020791111	TUK12	3	22	0.25	0.81	294	-73	29.3	7.6	0.14	-39.22	175.44	0.6-2	2.02	NULLAB	17.0
20020791111	TUK12	8	22	0.04	0.46	294	-85	29.3	7.6	0.14	-39.22	175.44	1-3	3.63	NULLA	17.0
20020810622	TUK12	85	11	0.06	0.01	266	41	27.6	33.0	0.61	-39.32	174.83	1-7	5.55	C	14.3
20020830214	TUK12	52	22	0.03	0.79	29	51	11.1	124.6	0.53	-38.81	175.94	0.5-3	3.34	NULLA	15.7
20020830214	TUK12	67	8	0.04	0.02	29	52	11.1	124.6	0.53	-38.81	175.94	4-100	4.67	B	15.7
20020830518	TUK12	-41	10	0.20	0.01	286	22	29.5	12.1	0.24	-39.21	175.31	1-3	1.87	C	16.6
20020871712	TUK12	41	22	0.76	1.24	129	34	23.7	63.0	1.27	-40.07	176.89	0.7-2	1.15	NULLB	27.6
20020971717	TUK12	10	8	0.23	0.02	274	-13	32.3	12.0	0.41	-39.25	175.08	2-3	2.61	C	18.6
20020971717	TUK12	15	8	0.25	0.03	274	-10	32.3	12.0	0.41	-39.25	175.08	1-3	2.35	C	18.6
20020980052	TUK12	-14	8	0.10	0.02	275	-72	25.8	30.6	0.39	-39.24	175.11	1-3	2.90	AB	12.8
20020981220	TUK12	34	6	0.39	0.03	112	53	23.7	62.2	1.23	-39.74	177.09	0.6-2	1.66	B	28.6
20021001827	TUK12	84	10	0.08	0.01	145	49	32.2	11.2	0.35	-39.57	175.87	1-7	5.73	B	33.6
20021001827	TUK12	84	8	0.06	0.01	145	46	32.2	11.2	0.35	-39.57	175.87	1-3	2.78	C	33.6
20021020444	TUK12	-58	4	0.10	0.02	266	48	32.7	12.0	0.78	-39.33	174.61	1-3	3.18	AB	19.0
20021072114	TUK12	-4	16	0.05	0.02	50	48	17.1	81.9	0.62	-38.88	176.22	1-7	2.27	B	22.0
20021072114	TUK12	13	8	0.86	0.30	50	78	17.1	81.9	0.62	-38.88	176.22	0.1-1	0.86	B	22.0
20021072114	TUK12	41	22	0.04	0.03	50	40	17.1	81.9	0.62	-38.88	176.22	0.5-3	2.33	NULLAB	22.0
20021072114	TUK12	48	22	0.04	0.05	50	50	17.1	81.9	0.62	-38.88	176.22	1-3	2.34	NULLB	22.0
20021072114	TUK12	7	8	0.36	0.03	50	-55	17.1	81.9	0.62	-38.88	176.22	0.2-2	1.30	C	22.0
20021092051	TUK12	-88	8	0.06	0.02	169	34	30.6	10.3	0.24	-39.51	175.67	1-3	2.00	AB	29.2
20021151528	TUK12	34	22	1.11	1.33	66	27	17.3	72.8	0.55	-39.05	176.25	0.2-2	1.77	NULLAB	23.0
20021151528	TUK12	38	22	0.23	0.71	66	47	17.3	72.8	0.55	-39.05	176.25	0.5-3	2.13	NULLA	23.0
20021170309	TUK12	16	22	0.33	0.36	228	-81	22.1	90.3	1.36	-40.19	174.30	0.1-1	1.26	C	13.2
20021240504	TUK12	-59	22	0.05	0.11	160	-81	24.7	24.0	1.30	-40.50	176.19	1-7	4.71	C	25.3
20021240504	TUK12	-62	7	0.30	0.03	160	-4	24.7	24.0	1.30	-40.50	176.19	0.1-1	1.38	B	25.3

continued on next page...

Event ID	Station	Φ [$^{\circ}$]	$\pm\Phi$ [$^{\circ}$]	δt [s]	$\pm\delta t$ [s]	Baz[$^{\circ}$]	Pol[$^{\circ}$]	RayPs[$^{\circ}$]	Edepth[km]	Edist[$^{\circ}$]	Elat[$^{\circ}$]	Elon[$^{\circ}$]	Filter[Hz]	Freq[Hz]	Quality	Incid[$^{\circ}$]
20021251706	TUK12	88	7	0.08	0.01	128	43	20.5	62.9	0.65	-39.68	176.27	0.5-3	2.02	C	24.9
20021291925	TUK12	12	22	0.61	0.42	23	44	17.8	174.8	1.59	-37.81	176.40	0.1-1	1.21	C	20.2
20021291925	TUK12	18	6	0.59	0.19	23	53	17.8	174.8	1.59	-37.81	176.40	0.2-2	1.27	AB	20.2
20021291925	TUK12	26	12	0.56	0.19	23	60	17.8	174.8	1.59	-37.81	176.40	1-3	1.36	B	20.2
20021311639	TUK12	34	4	0.20	0.01	349	1	8.1	205.6	0.64	-38.65	175.46	1-3	3.31	AB	10.2
20021320415	TUK12	61	10	0.16	0.02	339	25	5.4	180.9	0.36	-38.94	175.44	1-3	2.38	C	8.6
20021320415	TUK12	61	6	0.15	0.02	339	20	5.4	180.9	0.36	-38.94	175.44	0.5-3	2.39	AB	8.6
20021340332	TUK12	36	22	1.83	1.92	225	40	19.8	82.3	0.84	-39.87	174.84	0.8-2	1.69	NULLAB	11.9
20021380320	TUK12	27	5	0.47	0.04	3	52	6.5	115.0	0.27	-39.01	175.63	0.2-1	0.90	B	10.8
20021431119	TUK12	37	4	0.11	0.03	160	-32	26.9	19.9	0.25	-39.51	175.72	4-100	12.32	NULLAB	27.2
20021461304	TUK12	-5	8	0.14	0.02	353	-61	3.8	98.6	0.13	-39.15	175.59	0.5-3	1.46	C	9.3
20021520644	TUK12	-16	16	0.16	0.17	263	-82	28.4	21.3	0.34	-39.32	175.18	1.2-2.4	2.09	C	15.1
20021600118	TUK12	-84	6	0.09	0.01	279	62	26.3	8.1	0.11	-39.26	175.47	1-3	2.26	A	13.3
20021600118	TUK12	89	19	0.08	0.01	279	51	26.3	8.1	0.11	-39.26	175.47	2-6	4.94	B	13.3
20021761403	TUK12	-76	6	0.19	0.01	291	-48	5.4	33.0	0.05	-39.26	175.55	1-3	2.34	B	5.2
20021782057	TUK12	45	6	0.50	0.01	52	70	14.9	82.9	0.50	-38.97	176.12	0.2-2	2.03	B	20.3
20021782057	TUK12	46	8	0.50	0.08	52	71	14.9	82.9	0.50	-38.97	176.12	1-3	2.97	B	20.3
20020150921	TUR2	-59	22	0.11	0.12	285	53	5.7	216.5	0.46	-39.19	174.95	1-7	3.58	C	12.3
20020150921	TUR2	31	22	0.08	0.07	285	7	5.7	216.5	0.46	-39.19	174.95	0.8-3	2.63	C	12.3
20020150921	TUR2	31	22	0.08	0.07	285	7	5.7	216.5	0.46	-39.19	174.95	0.8-3	2.70	B	12.3
20020161202	TUR2	27	3	0.29	0.01	327	56	5.4	224.2	0.45	-38.93	175.21	0.5-3	1.72	A	9.8
20020161202	TUR2	29	8	0.31	0.04	327	62	5.4	224.2	0.45	-38.93	175.21	0.1-1	1.09	A	9.8
20020161202	TUR2	30	4	0.30	0.02	327	62	5.4	224.2	0.45	-38.93	175.21	0.2-2	1.69	A	9.8
20020180108	TUR2	4	8	0.06	0.01	245	29	13.1	196.1	1.09	-39.76	174.24	1-7	4.21	A	19.3
20020180108	TUR2	4	9	0.06	0.01	245	29	13.1	196.1	1.09	-39.76	174.24	0.8-5	3.76	A	19.3
20020180108	TUR2	6	6	0.06	0.01	245	34	13.1	196.1	1.09	-39.76	174.24	4-100	4.89	A	19.3
20020200048	TUR2	-26	6	0.16	0.01	270	-56	23.8	12.1	0.13	-39.31	175.36	1-7	6.77	B	27.7
20020200048	TUR2	-32	6	0.16	0.01	270	-60	23.8	12.1	0.13	-39.31	175.36	1-3	4.71	B	27.7
20020250314	TUR2	33	22	0.31	0.58	41	42	16.3	87.2	0.61	-38.85	176.04	0.2-2	2.30	NULLB	6.2
20020250314	TUR2	39	22	0.12	0.52	41	26	16.3	87.2	0.61	-38.85	176.04	0.5-3	2.63	NULLB	6.2
20020250314	TUR2	42	22	0.04	0.06	41	45	16.3	87.2	0.61	-38.85	176.04	1-3	2.93	NULLB	6.2
20020301730	TUR2	-45	4	0.06	0.01	269	18	31.0	16.5	0.41	-39.32	174.99	0.5-3	2.70	AB	34.2
20020301730	TUR2	-48	8	0.08	0.01	269	13	31.0	16.5	0.41	-39.32	174.99	1-7	3.09	AB	34.2
20020301730	TUR2	-68	8	0.08	0.03	269	6	31.0	16.5	0.41	-39.32	174.99	0.1-1	2.10	C	34.2
20020301917	TUR2	-39	3	0.06	0.01	270	18	27.0	26.2	0.39	-39.31	175.02	1-3	2.68	AB	30.5
20020390120	TUR2	9	13	0.08	0.02	284	62	28.7	26.1	0.49	-39.19	174.91	1-3	2.70	C	31.0
20020411851	TUR2	44	2	0.31	0.01	123	66	20.9	14.1	0.11	-39.37	175.64	0.5-3	3.24	C	15.5
20020500534	TUR2	-11	10	0.08	0.01	300	36	28.8	22.2	0.40	-39.11	175.08	1-7	5.84	C	29.6

continued on next page...

Event ID	Station	Φ [°]	$\pm\Phi$ [°]	δt [s]	$\pm\delta t$ [s]	Baz[°]	Pol[°]	RayP[s/°]	Edepth[km]	Edist[°]	Elat[°]	Elon[°]	Filter[Hz]	Freq[Hz]	Quality	Incid[°]
20020521025	TURO2	0	10	0.09	0.02	230	54	10.4	86.0	0.33	-39.52	175.20	1-3	2.14	A	17.0
20020521025	TURO2	10	8	0.10	0.01	230	64	10.4	86.0	0.33	-39.52	175.20	2-6	4.21	A	17.0
20020521025	TURO2	17	8	0.10	0.01	230	73	10.4	86.0	0.33	-39.52	175.20	4-100	7.33	AB	17.0
20020522041	TURO2	52	22	0.24	0.48	188	67	32.8	5.0	0.35	-39.66	175.46	0.3-2	2.25	NULLAB	34.0
20020531312	TURO2	18	22	0.01	0.26	84	18	32.6	12.0	0.64	-39.24	176.35	0.5-5	4.83	NULLAB	20.5
20020540947	TURO2	40	2	0.23	0.02	287	47	28.0	14.4	0.24	-39.24	175.23	1-3	3.29	NULLAB	30.2
20020580325	TURO2	-27	6	0.04	0.01	295	13	20.7	30.1	0.24	-39.21	175.25	1-3	4.17	A	23.2
20020580325	TURO2	-55	4	0.01	0.01	295	-13	20.7	30.1	0.24	-39.21	175.25	4-100	8.44	AB	23.2
20020671226	TURO2	-68	8	0.25	0.06	235	1	20.7	114.0	1.40	-40.11	174.03	0-0.6	1.27	C	25.8
20020671226	TURO2	28	6	0.69	0.22	235	43	20.7	114.0	1.40	-40.11	174.03	0.1-1	1.29	NULLB	25.8
20020771811	TURO2	40	18	0.04	0.74	125	43	24.1	14.4	0.16	-39.40	175.69	1.5-4.5	4.18	NULLAB	18.3
20020771912	TURO2	40	2	0.35	0.11	102	34	23.7	15.7	0.14	-39.34	175.70	1-3	3.13	NULLAB	14.7
20020811252	TURO2	-49	11	0.05	0.01	247	11	14.6	172.4	1.11	-39.73	174.20	2-100	3.63	AB	20.6
20020830214	TURO2	14	6	0.28	0.03	33	39	12.1	124.6	0.60	-38.81	175.94	0.2-1	0.91	A	4.6
20020830518	TURO2	-20	18	0.04	0.04	301	11	27.5	12.1	0.19	-39.21	175.31	1-7	7.17	B	28.4
20020830518	TURO2	-24	14	0.04	0.01	301	8	27.5	12.1	0.19	-39.21	175.31	4-100	6.90	B	28.4
20020830518	TURO2	0	22	0.10	0.34	301	-7	27.5	12.1	0.19	-39.21	175.31	0.5-3	3.43	NULLAB	28.4
20020961020	TURO2	33	7	0.29	0.02	4	80	4.5	166.2	0.27	-39.04	175.55	1.4-3	2.60	AB	7.1
20020971717	TURO2	74	15	0.01	0.01	280	-15	31.9	12.0	0.35	-39.25	175.08	1-7	4.93	NULLC	34.2
20020980052	TURO2	-57	4	0.21	0.02	282	45	24.3	30.6	0.33	-39.24	175.11	1-3	3.61	B	27.4
20020980052	TURO2	29	10	0.21	0.06	282	46	24.3	30.6	0.33	-39.24	175.11	0.5-3	3.68	NULLB	27.4
20020981220	TURO2	39	12	0.20	0.02	110	77	23.8	62.2	1.28	-39.74	177.09	0.7-2.2	2.19	C	15.9
20021010800	TURO2	33	22	0.11	0.14	146	-24	24.7	35.7	1.33	-40.41	176.49	0.1-1	1.00	B	21.9
20021020444	TURO2	-8	6	0.19	0.01	268	42	32.7	12.0	0.71	-39.33	174.61	1-3	3.24	B	35.8
20021072114	TURO2	24	2	0.94	0.03	52	-82	18.2	81.9	0.69	-38.88	176.22	0.1-1	0.93	A	6.9
20021101137	TURO2	30	8	0.10	0.02	31	58	20.3	247.4	3.31	-36.46	177.66	1-7	3.19	AB	10.4
20021151528	TURO2	14	22	0.23	0.76	65	34	18.5	72.8	0.62	-39.05	176.25	0.5-3	2.25	NULLAB	7.0
20021291925	TURO2	57	14	0.53	0.06	25	4	18.1	174.8	1.65	-37.81	176.40	0.1-1	0.61	C	9.5
20021320156	TURO2	-27	11	0.16	0.06	288	-62	29.0	12.0	0.22	-39.24	175.25	1-7	4.89	C	31.0
20021320415	TURO2	17	9	0.29	0.02	350	44	5.6	180.9	0.38	-38.94	175.44	1-3	2.14	B	8.2
20021320415	TURO2	20	4	0.30	0.01	350	51	5.6	180.9	0.38	-38.94	175.44	0.2-2	1.67	A	8.2
20021320415	TURO2	23	6	0.31	0.03	350	56	5.6	180.9	0.38	-38.94	175.44	0.1-1	1.07	A	8.2
20021320415	TURO2	4	6	0.31	0.03	350	25	5.6	180.9	0.38	-38.94	175.44	1-7	2.18	C	8.2
20021331816	TURO2	-26	7	0.21	0.01	250	17	13.3	9.1	0.03	-39.32	175.49	0.5-3	2.57	C	19.5
20021331816	TURO2	-45	14	0.12	0.05	250	82	13.3	9.1	0.03	-39.32	175.49	1-7	5.16	B	19.5
20021380320	TURO2	28	9	0.29	0.04	15	67	7.5	115.0	0.31	-39.01	175.63	0.2-1	0.93	A	6.0
20021380320	TURO2	32	5	0.33	0.01	15	75	7.5	115.0	0.31	-39.01	175.63	0.2-2	1.86	A	6.0
20021380320	TURO2	45	4	0.35	0.01	15	-81	7.5	115.0	0.31	-39.01	175.63	1-3	2.07	AB	6.0

continued on next page...

Event ID	Station	Φ [$^{\circ}$]	$\pm\Phi$ [$^{\circ}$]	δt [s]	$\pm\delta t$ [s]	Baz[$^{\circ}$]	Pol[$^{\circ}$]	RayP[s/ $^{\circ}$]	Edepth[km]	Edist[$^{\circ}$]	Elat[$^{\circ}$]	Elon[$^{\circ}$]	Filter[Hz]	Freq[Hz]	Quality	Incid[$^{\circ}$]
20021380320	TURO2	47	8	0.34	0.02	15	-89	7.5	115.0	0.31	-39.01	175.63	1-7	2.32	C	6.0
20021431119	TURO2	47	4	0.08	0.02	143	53	27.0	19.9	0.25	-39.51	175.72	1-3	2.91	NULLAB	23.3
20021461304	TURO2	72	4	0.28	0.01	18	30	4.9	98.6	0.17	-39.15	175.59	1-3	2.04	C	6.1
20021512249	TURO2	15	20	0.08	0.02	241	-15	15.8	150.0	1.07	-39.82	174.30	1-3	2.92	C	21.6
20021512340	TURO2	-16	5	0.16	0.01	286	-57	32.6	12.0	0.64	-39.13	174.73	2-6	4.85	AB	34.4
20021512340	TURO2	-22	8	0.17	0.01	286	-68	32.6	12.0	0.64	-39.13	174.73	1-3	2.99	AB	34.4
20021520644	TURO2	-33	22	0.12	0.08	268	22	26.6	21.3	0.27	-39.32	175.18	2-6	5.46	B	30.3
20021520644	TURO2	-34	9	0.12	0.01	268	30	26.6	21.3	0.27	-39.32	175.18	1-3	2.82	B	30.3
20021521457	TURO2	-16	6	0.06	0.01	323	18	29.3	10.4	0.20	-39.15	175.37	1-3	2.46	B	27.2
20021521457	TURO2	-24	10	0.08	0.06	323	12	29.3	10.4	0.20	-39.15	175.37	2-6	6.45	C	27.2
20021551105	TURO2	39	10	0.19	0.03	114	73	22.6	66.5	0.98	-39.71	176.68	0.4-2	1.02	B	15.5
20021560027	TURO2	42	2	0.49	0.12	214	48	12.5	72.5	0.34	-39.59	175.28	2-6	4.90	NULLA	18.4
20021560027	TURO2	42	22	0.49	0.69	214	48	12.5	72.5	0.34	-39.59	175.28	4-100	4.98	NULLA	18.4
20021561837	TURO2	-11	6	0.26	0.01	222	41	23.5	66.3	1.28	-40.26	174.41	4-100	6.28	B	28.0
20021561837	TURO2	-5	6	0.26	0.01	222	39	23.5	66.3	1.28	-40.26	174.41	1-3	2.48	AB	28.0
20021600118	TURO2	-10	8	0.05	0.01	320	30	21.4	8.1	0.07	-39.26	175.47	2-6	5.49	AB	21.1
20021600118	TURO2	-14	4	0.05	0.01	320	25	21.4	8.1	0.07	-39.26	175.47	0.5-3	2.93	A	21.1

Table C.3: List of individual measurements, 2002 deployment

DATA PROCESSING SOFTWARE

D.1 Description of routines used

Data preparation

Once the data disk has been retrieved from the field, it is connected via SCSI port to a lab PC. Several programs of the ORION processing package are then used to further process the data, which will be described in the following (see also Figure D.1). First, the program RBTRIM is used to trim down the size of the 2GB-ringbuffer files to the actual data size. The name of the `:\USER` directory is then changed to a name consisting of the following characters: `O<ORION-number>D<DISK-number><Station-name>`. It is then

copied to the SOLARIS file system via ftp. The files of all stations are pooled in a so called *experiment directory*. Two backup copies of the raw data are made after this. Response files for the sensors are then generated with the program *Mkresponse*, or modified from the previous download. As a next step, the program *summarize* is called to extract the state of health (SOH) information and the station locations, which are placed in the experiment directory. The first step to extracting the data is the execution of the program *extractall*, which extracts the whole data set and places it (in 24 hour blocks) to files encoded in the SEED data format. These are not actually needed for the processing and are thus only written to tape for archival storage. To extract only local events that were triggered by the internal ORION triggers, a program called *extractlocal* can be run. These are also not used in this

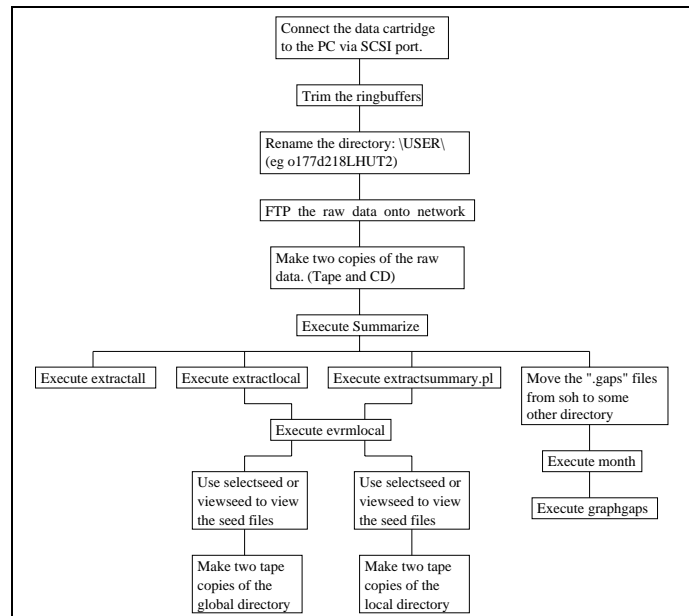


Figure D.1 Data processing flow chart

project due to sufficient local earthquake catalogue data provided by IGNS.

Earthquake catalogue data was downloaded from the GEONET web site and converted in a format that could be used by the ORION software. From this catalogue, special events were then selected with the program *weed*. The events were divided into several blocks, depending on their distance from the receivers, and their magnitude (see Table D.1). After the selection of the blocks, *summary-files* were created and then used to cut out the data with the program *extractsummary.pl*. Each of the events was placed in a single file and copied to a directory called *global/*, with subdirectories for each block. Every event file contains the data of all instruments that were recording during the time of the earthquake. The data format follows the SEED convention. Two backup copies were then made on tape. In this project, only local earthquakes were used, which means only blocks 1 to 3+ were needed for the further processing.

Block	Distance	Magnitudes
Block1	$\leq 1.5^\circ$	2.0 - 2.9
Block2	$\leq 3^\circ$	3.0 - 3.4
Block3+	$\leq 5^\circ$	≥ 3.5
Block4	$\leq 18^\circ$	4.5 - 4.7
Block5	$\leq 30^\circ$	4.8 - 4.9
Block9	$\leq 100^\circ$	5.0 - 5.9
Block10	$\leq 180^\circ$	6.0 - 6.9
Block11	$\leq 180^\circ$	≥ 7.0

Table D.1
Earthquake selection criteria
Distance is measured radially from
Mt. Ruapehu

Data selection

After extracting all events to separate files, the ones that are usable for shear wave splitting measurements had to be selected (for selection criteria see Section 3.1). A UNIX shell program called *vs* was developed by the author for this selection, based on the PASSCAL viewing software PQL (See Appendix D.2), which allows the application of different frequency filters.

After selecting the data, the SEED files are converted into the SAC file format. This means that for every recording station in a SEED event file, a triple set of files representing the three components (North, East and West) is extracted. During this process, event information (EQ source coordinates, source time, depth, magnitude,...) is written to the SAC file headers. A SAC macro program called *localhead_alex* was adapted for this task. The data was not corrected for instrument response, since the Gralp CMG-40T seismometer has a sufficiently flat response curve (see Section 3.2).

In order to view and test different frequency filters on the event file, a SAC macro called *showfilt* was developed. It applies different frequency filters to the data and also calculates a spectrum of the Signal-to-Noise ratio. This allows the experimenter to judge at which frequencies the signal is higher than the noise and to therefore choose the right filter values. After selecting a filter, the event can be saved to a new filename which has the filter frequencies appended (e.g. 2002.025.03.14.LTUR2.0.1-1.E means the trace starts at the Julian day 25 in 2002 at 3:14 am, is recorded by LTUR2 and has a bandpass filter from 0.1 to 1 Hz). Also,

the filter values are written to the headers of the files. The lower bandpass value is written to the variable “KUSER0”, the upper one is “KUSER1”. A standard Butterworth filter was used for the bandpass (see Appendix D.2 for more details on the programs).

Splitting measurements

After the frequency filters are selected, the shear wave splitting measurement is carried out by the SAC macro *split_local_alex* (or *sa*). All output of this program is written to a so called *measurement file*, which exists for every station and contains information about every measurement that was obtained at this station. Measurement files have the name extension “.amea”. The program was adapted for this project in order to also allow frequency measurements on the wavelet. After the right window for the measurement is chosen and the splitting values are obtained, the program offers the possibility to view the corrected waveforms and to give a quality mark for the measurement. Further, the user can pick the start and end time of the main wavelet, which leads to a calculation of the main frequency of this measurement. All values are then saved in the measurement file for this station. A list of all measurement files is given in Appendix C. For a detailed description of the algorithm which is used for the shear wave splitting, see Section 3.2.2.

The following parameters are included in the measurement files:

Event ID	Station name	Φ [°]	Delta (\pm) Φ [°]
Delay time (δt) [s]	Delta (\pm) δt [s]	Eigenvalue ratio	Back azimuth [°]
Initial polarisation [°]	Ray parameter [s/°]	Max. variation	# degrees of freedom
NDF fac	Inversion mode	EQ depth [km]	EQ distance [°]
EQ latitude [°]	EQ longitude [°]	Low filter value [Hz]	High filter value [Hz]
Main frequency [Hz]	Quality mark	Filename	

The quality marks that are given to every measurement range from A to C and NULLA to NULLC. A definition of the marks is given in Table 3.3. After all measurement files are created or updated, a MAKE program (usually named *Makefile*), located in the *results* directory is called. It serves as coordinator for all measurements and was written during the data processing for this project. Its purposes are to:

- collect all available measurement files (.amea) from all subdirectories (which represent different downloads of data) and save them into a general measurement file for each station.
- select data from specified criteria (e.g. mark, frequency, incidence angle, back azimuth, station) and bring them into a format that is readable by GMT scripts (for visualisation).

- project coordinates of measurements to the specified position in the plots (e.g. where a straight line between earthquake and station intersects a depth of 10 km).
- run the *meanerr* program to calculate statistical data like $\overline{\Phi}$, delay time δt , standard error, standard deviation, number of measurements, average frequency, and standard deviation of the frequencies. The output is written to the file *CHARMstatistics*.

After this Makefile is executed, the data is ready to be either plotted on maps or interpreted with mathematical software.

D.2 List of newly developed programs for future users

Several programs were developed during the completion of this thesis. Future users are welcome to change and adapt them to their purposes. This list is meant to give a brief overview over the purpose of each program. Details for the use of the program can be obtained by either just typing the name of the program, or by documentation in the source code. The programs are located on the VUW file system, but can also be requested from the author (Alex.Gerst@web.de).

D.2.1 UNIX shell, NAWK and C++ programs

Located on wellman.geo.vuw.ac.nz under /opt/software/users/bin/
(or alternatively under ~agerst/bin/)

<i>Makefile</i>	for selecting data and generating GMT input files
<i>add_station_location</i>	adds the station location (lat/long) to every line of the .amea file (further stations can be added)
<i>arrival_angle</i>	adds the conventional incidence angle of every measurement for a certain surface S-wave speed to an .amea file
<i>corr_arrival_angle</i> ..	a program to calculate the normal and corrected S-wave incidence angles from a measurement file (.amea).
<i>date2julian</i>	transforms date into Julian day
<i>distance</i>	calculates the distance (in km or °) between two points
<i>intl2wgs</i>	transforms coordinates from international lat/long into WGS84
<i>jul2date</i>	transforms Julian days into date
<i>kappa</i>	calculates the Von Mises concentration parameter from a given resultant vector length
<i>meanerr</i>	calculates several different statistical properties of an .amea file

<i>nz2int</i>	transforms NZ map grid into international lat/long
<i>project_event_locations</i>	projects event locations to points where the straight raypath intersects a certain depth
<i>project_nulls</i>	projects NULL measurements
<i>single_select</i>	allows only one measurement per event and station (e.g. no multiple frequency filters)
<i>vs</i>	bulk-views SEED files and allows to visualise different frequency filters

All programs should be well commented, or even have a little help-page (just type the program name without parameters).

D.2.2 SAC macros

Located on wellman.geo.vuw.ac.nz under /opt/software/users/SAC/
(or alternatively under ~agerst/SAC/)

<i>Makefile</i>	for preparation of SEED files and generating SAC files
<i>create_list</i>	creates a list of all event files in the current directory
<i>prepare_local_head_macro</i>	prepares the SAC input files for the splitting program
<i>local_head_alex</i>	extended and adapted from <i>local_head macro</i> . It prepares the SAC input files for the splitting program <i>sa</i>
<i>showfilt</i>	views single SEED files and allows to select the final frequency filter as output for the splitting program <i>sa</i>
<i>sa</i>	This program measures the shear wave splitting (extended from Serdhar split macro and Rick Aster's macro)
<i>shortname</i>	shortens the name of the SAC output files
<i>merge_sgfs</i>	prints three SGF graphics files on one page (written by Katrina Marson-Pidgeon)
<i>printsgf</i>	sends a number of SGF graphic files (SAC output) to the printer
<i>showsgf</i>	shows SGF files on the screen

REFERENCES

- K. Aki and P.G. Richards.
Quantitative Seismology: Theory and Methods.
W.H. Freeman and Company, San Francisco, California, 1980.
- H. Anderson and T. Webb.
New Zealand seismicity: Patterns revealed by the upgraded National Seismograph Network.
New Zealand Journal of Geology and Geophysics, 37:477–493, 1994.
- E. Angerer, S. Crampin, X. Y. Li, and T. L. Davis.
Processing, modelling and predicting time-lapse effects of overpressured fluid-injection in a fractured reservoir.
Geophysical Journal International, 149(2):267–280, 2001.
- R. C. Aster, P. M. Shearer, and J. Berger.
Quantitative measurements of shear-wave polarizations at the Anza seismic network, Southern California: Implications for shear-wave splitting and earthquake prediction.
J. Geophys. Res., 95:12,449–12,473, 1990.
- R. C. Aster, P. M. Shearer, and Berger J.
Reply.
J. Geophys. Res., 96:6415–6419, 1991.
- E.L. Audoiné.
Upper mantle and crustal seismic anisotropy across the Pacific-Australian plate boundary, New Zealand.
PhD thesis, Victoria University of Wellington, Wellington, New Zealand, 2002.
- V. Babuška and M. Cara.
Seismic Anisotropy in the Earth.
Kluwer Acad., Norwell, Mass., 1991.
- F. Bianco, G. Vilardo, F. Ferrucci, S. Gresta, M. Castellano, and G. Milano.
The seismic crises at Mt. Vesuvius during 1995 and 1996.
Physics and Chemistry of the Earth, Part A: Solid Earth and Geodesy, 24(11-12):977–983, 1999.
- H.M. Bibby, T.G. Caldwell, F.J. Davey, and T.H. Webb.
Geophysical evidence on the structure of the Taupo Volcanic Zone and its hydrothermal circulation.
Journal of Volcanology and Geothermal Research, 68:29–58, 1995.
- G.H.R. Bokelmann and H.-P. Harjes.
Evidence for temporal variation of seismic velocity within the upper continental crust .
Journal of Geophysical Research B: Solid Earth, 105(10):23,879 – 23,894, 2000.

- D. C. Booth, S. Crampin, R. Evans, and G. Roberts.
Shear-wave polarizations near the North Anatolian Fault - I. Evidence for anisotropy-induced shear-wave splitting.
Geophys J. R. Astr. Soc., 83(1):61–73, 1985.
- D. C. Booth, S. Crampin, J. H. Lovell, and Jer-Ming Chiu.
Temporal changes in shear wave splitting during an earthquake swarm in Arkansas.
Journal of Geophysical Research, 95(B7):11,151–11,164, 1990.
- D. C. Booth, M. Wyss, and D. Gillard.
Shear-wave polarization alignments recorded above the Kaoiki fault zone, Hawaii.
Geophysical Research Letters, 19(11):1141–1144, 1992.
- J.R. Bowman and M. Ando.
Shear-wave splitting in the upper-mantle wedge above the Tonga subduction zone.
Geophysical Journal of the Royal Astronomical Society, 88:25–41, 1987.
- C.J. Bryan and S. Sherburn.
Seismicity associated with the 1995-1996 eruptions of Ruapehu volcano, New Zealand: Narrative and insights into physical processes.
Journal of Volcanology and Geothermal Research, 90(1):1–18, 1999.
- I.M. Calhaem.
Heat flow measurements under some lakes in the North Island, New Zealand.
PhD thesis, Victoria University of Wellington, New Zealand, 1973.
- Tian-Chang Chen.
Shear-wave polarizations near the North Anatolian Fault - III. Observations of temporal changes.
Geophys J. R. Astr. Soc., 91(2):287–311, 1987.
- J.W. Cole.
Structural control and origin of volcanism in the Taupo Volcanic Zone, New Zealand.
Bulletin of Volcanology, 52:445–459, 1990.
- J.W. Cole, D.J. Darby, and T. Stern.
Taupo Volcanic Zone and Central Volcanic Region: Backarc structures of North Island, New Zealand.
In *Backarc basins: tectonics and magnetism*, pages 1–28. Plenum Press, New York, 1995.
- S. Crampin.
An introduction to wave propagation in anisotropic media.
Geophysical Journal of the Royal Astronomical Society, 76:17–28, 1984.
- S. Crampin.
Geological and industrial implications of extensive-dilatancy anisotropy.
Nature, 328:491–496, 1987.
- S. Crampin.
The fracture criticality of crustal rocks.
Geophysical Journal International, 118:428–438, 1994.

- S. Crampin.
Stress-forecasting: a viable alternative to earthquake prediction in a dynamic Earth.
Transactions of the Royal Society of Edinburgh Earth Sciences, 89:121–133, 1998.
- S. Crampin and D. C. Booth.
Shear-wave polarisations near the North Anatolian Fault -II. Interpretation in terms of crack-induced anisotropy.
Geophys J. R. Astr. Soc., 87:75–92, 1985.
- S. Crampin, D. C. Booth, R. Evans, S. Peacock, and J. B. Fletcher.
Comment on "Quantitative measurements of shear wave polarizations at the Anza seismic network, southern California: implications for shear wave splitting and earthquake prediction" by Richard C. Aster, Peter M. Shearer, and Jon Berger.
Journal of Geophysical Research, 96(B4):6403–6414, 1991.
- S. Crampin, E.M. Chesnokov, and R.G. Hipkin.
Seismic anisotropy - the state of art: II.
Geophysical Journal of the Royal Astronomical Society, 76:13–16, 1984a.
- S. Crampin, R. Evans, and B. K. Atkinson.
Earthquake prediction: a new physical basis.
Geophysical Journal of the Royal Astronomical Society, 76:147–156, 1984b.
- S. Crampin, J. B. Fletcher, D. C. Booth, R. Evans, and S. Peacock.
Changes in shear wave splitting at Anza near the time of the North Palm Springs earthquake.
Journal of Geophysical Research, 95(B7):11,197–11,212, 1990.
- S. Crampin and J.H. Lovell.
A decade of shear-wave splitting in the Earth's crust: what does it mean? what use can we make of it? and what should we do next?
Geophysical Journal International, 107:387–407, 1991.
- S. Crampin, T. Volti, S. Chastin, A. Gudmundsson, and R. Stefansson.
Indication of high pore-fluid pressures in a seismically-active fault zone.
Geophysical Journal International, 151(2):F1–F5, 2002.
- S. Crampin, T. Volti, and R. Stefansson.
A successfully stress-forecast earthquake .
Geophysical Journal International, 138(1):F1–F5, 1999.
- S. Crampin and S.V. Zatsepin.
Modelling the compliance of crustal rock - II. Response to temporal changes before earthquake.
Geophysical Journal International, 129(3):495–506, 1997.
- S. Crampin, S.V. Zatsepin, C. Slater, and L. Y. Brodov.
Abnormal shear-wave polarizations as indicators of high pressures and over pressures.
In *58th Conf. EAGE, Amsterdam, Extended Abstracts*, page X083, 1996.
- S. L. Crouch and A. M. Starfield.
Boundary element method in Solid Mechanics.
Allen & Unwin, London, 1983.
322 pp.

- W. B. Dade and H. E. Huppert.
Emplacement of the Taupo ignimbrite by a dilute turbulent flow.
Nature, 381:509–512, 1996.
- D.J. Darby and C.M. Meertens.
Terrestrial and GPS measurements of deformation across the Taupo back arc and Hikurangi forearc regions in New Zealand.
Journal of Geophysical Research, 100(B5):8221–8232, May 1995.
- J.C. Davis.
Analysis of directional data.
In *Statistics and Data Analysis in Geology - Second Edition*, pages 314–330. John Wiley & Sons, Inc., 1986.
- C. DeMets, R.G. Gordon, D.F. Argus, and S. Stein.
Current plate motions.
Geophysical Journal International, 101:425–478, 1990.
- J.R. Evans, B.R. Julian, G.R. Foulger, and A. Ross.
Shear-wave splitting from local earthquakes at The Geysers geothermal field, California .
Geophysical Research Letters, 22(4):501–504, 1995.
- K.M. Fischer and D.A. Wiens.
The depth distribution of mantle anisotropy beneath the Tonga subduction zone.
Earth and Planetary Science Letters, 142:253–260, 1996.
- R.V. Fisher, G. Heiken, and J.B. Hulen.
Volcanoes – crucibles of change.
Princeton University Press, New Jersey, 1997.
- J.A. Gamble, B.P. Kokelaar, I.E.M. Smith, M.T. McCulloch, and I.J. Graham.
The geochemistry and petrogenesis of basalts from the Taupo volcanic zone and Kermadec Island, S.W. Pacific.
Journal of Volcanology and Geothermal Research, 54:265–290, 1993.
- J.A. Gamble, W.C. McIntosh, N.W. Dunbar, R.C. Price, and I.E.M. Smith.
 $^{40}\text{Ar}/^{39}\text{Ar}$ geochronology of magmatic activity, magma flux and hazards at Ruapehu volcano, Taupo Volcanic Zone, New Zealand.
Journal of Volcanology and Geothermal Research, 120(3-4):271–287, 2003.
- GEONET.
The GeoNet Project - Monitoring geological hazards in New Zealand.
Website <http://www.geonet.org.nz>, 2001.
- K.R. Gledhill.
Evidence for shallow and pervasive seismic anisotropy in the wellington region, new zealand.
Journal of Geophysical Research, 96:21,503–21,516, 1991a.
- K.R. Gledhill.
Shear-wave splitting and seismic anisotropy in the Wellington region, New Zealand.
PhD thesis, Victoria University of Wellington, Wellington, New Zealand, 1991b.

- A. Gudmundsson.
Emplacement and arrest of sheets and dykes in central volcanoes.
Journal of Volcanology and Geothermal Research, 116:279–298, 2002.
- I. N. Gupta.
Premonitory variations in S-wave velocity anisotropy before earthquakes in Nevada.
Science, 182:1129–1132, 1973.
- W. R. Hackett and B. F. Houghton.
A facies model for a Quaternary andesitic composite volcano: Ruapehu, New Zealand.
Bulletin of Volcanology, 51(1):51–68, 1989.
- M. Hagerty and R. Benites.
Tornillos beneath Tongariro volcano, New Zealand.
Journal of Volcanology and Geothermal Research, (in press), 2003.
- G.P. Hayes.
Relocating the hypocentres of an earthquake swarm near Waiouru, south east of Ruapehu, North Island, New Zealand.
Master’s thesis, School of Earth Sciences, University of Leeds, 2002.
- J. Healy.
Submission to the Tangiwai railway disaster Board of Inquiry.
Government Printer, Wellington, 1954.
p. 1-31.
- S. D. Hofmann.
Seismic Anisotropy in the Crust and Mantle: A Study at the Western Edge of the Central Volcanic Region, New Zealand.
Master’s thesis, Institute of Geophysics, Victoria University of Wellington, 2002.
- B. F. Houghton, J. H. Latter, and W. R. Hackett.
Volcanic hazard assessment for Ruapehu composite volcano, Taupo volcanic zone, New Zealand.
Bull. Volcanol., 49:737–751, 1987.
- B. F. Houghton, C. J. N. Wilson, M. O. McWilliams, M. A. Lanphere, S. D. Weaver, R. M. Briggs, and M. S. Pringle.
Chronology and dynamics of a large silicic magmatic system: Central Taupo Volcanic Zone, New Zealand.
Geology, 23:13–16, 1995.
- F. Hrouda, Z. Pros, and J. Wohlgemuth.
Development of magnetic and elastic anisotropies in slates during progressive deformation.
Phys. Earth Planet. Inter., 77:251–265, 1993.
- A. W. Hurst.
Shallow seismicity beneath Ruapehu Crater Lake: Results of a 1994 seismometer deployment.
Bull. Volcanol., 60:1–9, 1998.
- A.W. Hurst and P.J. McGinty.
Earthquake swarms to the west of Mt Ruapehu preceding its 1995 eruption.
Journal of Volcanology and Geothermal Research, 90(1):19–28, 1999.

- D.M. Johnston, D. Paton, B.F. Houghton, V.E. Neall, and K.R. Ronan.
Impacts of the 1945 and 1995-1996 Ruapehu eruptions, New Zealand: An example of increasing societal vulnerability.
Bulletin of the Geological Society of America, 112(5):720–726, 2000.
- H. Jung and S.-I. Karato.
Water-induced fabric transitions in olivine.
Science, 293:1460–1463, August 2001.
- S. Kaneshima and P.G. Silver.
A search for source side mantle anisotropy.
Geophysical Research Letters, 19(10):1049–1052, 1992.
- J.M. Kendall and P.G. Silver.
Constraints from seismic anisotropy on the nature of the lowermost mantle.
Nature, 381:409–413, 1996.
- B.L.N. Kennett.
IASPEI 1991 seismological tables.
167 pp., Bibliotech, Canberra, Australia, 1991.
- H. Kern.
Laboratory seismic measurements: An aid in the interpretation of seismic field data.
Terra Nova, 2(6):617–628, 1990.
- W. C. Krumbein.
Preferred orientation of pebbles in sedimentary deposits.
Jour. Geology, 47:673 – 706, 1939.
- J. H. Latter.
Location of zones of anomalously high S-wave attenuation in the upper crust near Ruapehu and Ngauruhoe volcanoes, New Zealand.
J. Volc. Geotherm. Res., 10:125–156, 1981.
- J. H. Latter.
Volcanic risk and surveillance in New Zealand.
NZ Geol. Survey Record, 10:5–22, 1986.
- T. Lay and T.C. Wallace.
Modern Global Seismology.
Academic Press, San Diego, California, 1995.
517 pp.
- J.M. Lees and H. Wu.
P wave anisotropy, stress, and crack distribution at Coso geothermal field, California.
Journal of Geophysical Research, B104(8):17,955–17,973, 1999.
- Yun Liu, S. Crampin, and I. Main.
Shear-wave anisotropy: spatial and temporal variations in time delays at Parkfield, central California .
Geophysical Journal International, 130(3):771–785, 1997.

- A. E. H. Love.
A treatise on the mathematical theory of elasticity.
Dover publ., New York, 1944, 643 pp., 1927.
- D. Mainprice and P.G. Silver.
Interpretation of SKS-waves using samples from the subcontinental lithosphere.
Physics of the Earth and Planetary Interiors, 78:257–280, 1993.
- A. Malhoff, R.H. Feden, and H.S. Fleming.
Magnetic anomalies and tectonic fabric of marginal basins north of New Zealand.
Journal of Geophysical Research, 87:4109–4125, 1982.
- V. Manville, K.A. Hodgson, and J.D.L. White.
Rheological properties of a remobilised-tephra lahar associated with the 1995 eruptions of Ruapehu volcano, New Zealand .
New Zealand Journal of Geology and Geophysics, 41(2):157–164, 1998.
- K. V. Mardia.
Statistics of directional data.
Academic Press, New York and London, 1972.
- K. Marson.
Seismic anisotropy beneath the lower half of the North Island, New Zealand.
Master's thesis, Victoria University of Wellington, Wellington, New Zealand, 1997.
- K. Marson-Pidgeon and M. K. Savage.
Frequency-dependent anisotropy in Wellington, New Zealand.
Geophysical Research Letters, 24(24):3297–3300, December 1997.
- K. Marson-Pidgeon, M.K. Savage, K.R. Gledhill, and G. Stuart.
Seismic anisotropy beneath the lower half of the North Island, New Zealand.
Journal of Geophysical Research, 104(B9):20,277–20,286, September 1999.
- D. E. Maunder.
New Zealand seismological report 1994. Seismological Observatory bulletin E-179.
Technical report, Institute of Geological and Nuclear Sciences science report 99/1, 219pp., 1999.
- Vicki Miller.
Possible methods for monitoring Mount Ruapehu volcano: Shear wave splitting and ground deformations using GPS.
Master's thesis, Victoria University of Wellington, 2000.
- Vicki Miller and Martha Savage.
Changes in seismic anisotropy after volcanic eruptions: Evidence from Mt. Ruapehu.
Science, 293:2231–2233, 2001.
- C. G. Munson and C. H. Thurber.
Observation of shear-wave splitting on the southeast flank of Mauna Loa volcano, Hawaii.
Geophys. Res. Lett., 20:1139–1142, 1993.
- C.G. Munson, C.H. Thurber, Yingping Li, and P.G. Okubo.
Crustal shear wave anisotropy in southern Hawaii: spatial and temporal analysis.
Journal of Geophysical Research, 100(B10):20,367–20,377, 1995.

- I. A. Nairn and B. J. Scott.
Volcanic eruption at a New Zealand ski resort prompts reevaluation of hazards.
EOS, 77:189–191, 1996.
- M. Nakagawa, K. Wada, T. Thordarson, C. P. Wood, and J. A. Gamble.
Petrologic investigations of the 1995 and 1996 eruptions of Ruapehu volcano, New Zealand: formation of discrete and small magma pockets and their intermittent discharge.
Bull. Volcanol., 61:15–31, 1999.
- K. Nakamura.
Volcanoes as possible indicators of tectonic stress orientation.
J. Volcanol. Geotherm. Res., 2:1–16, 1977.
- J. Neuberg and T. Pointer.
Effects of volcano topography on seismic broad-band waveforms.
Geophysical Journal International, 143(1):239–248, 2000.
- A. Nicolas and N.I. Christensen.
Formation of anisotropy in upper mantle peridotites: A review.
In K. Fuchs and C. Froidevaux, editors, *Composition, Structure and Dynamics of the Lithosphere-Asthenosphere System*, *Geodyn. Ser.*, volume 16, pages 111–123. AGU, Washington, D.C., 1987.
- A. Nur and G. Simmons.
Stress-induced anisotropy in rock: an experimental study.
Journal of Geophysical Research, 74:6667–6674, 1969.
- O.W. Nuttli.
The effect of the Earth’s surface on the S wave particle motion.
Bulletin of the Seismological Society of America, 51:237–246, 1961.
- Y. Okada.
Internal deformation due to shear and tensile faults in a half-space.
Bulletin - Seismological Society of America, 82(2):1018–1040, 1992.
- S. Peacock, S. Crampin, D.C. Booth, and J.B. Fletcher.
Shear wave splitting in the Anza seismic gap, southern California: temporal variations as possible precursors.
Journal of Geophysical Research, 93(B4):3339–3356, 1988.
- D. W. Peterson.
Volcanoes: tectonic setting and impact on society.
In *Studies in geophysics: active tectonics*, chapter Panel on Active Tectonics, pages 2311–2346. Washington DC: National Academy Press, 1986.
- F. Press and R. Siever.
Understanding Earth.
W. H. Freeman, 3 edition, 2000.
- M. Reyners and G. Stuart.
The central North Island passive seismic experiment.
Science report 11, Institute of Geological and Nuclear Sciences, 2002.

- G. Rümpker and P.G. Silver.
Apparent shear-wave splitting parameters in the presence of vertically varying anisotropy.
Geophysical Journal International, 135:790–800, 1998.
- R.M. Russo and P.G. Silver.
Trench-parallel flow beneath the Nazca Plate from seismic anisotropy.
Science, 263:1105–1111, 1994.
- A. Ryall and W. U. Savage.
S-wave splitting: key to earthquake prediction?
Bulletin of the Seismological Society of America, 64(6):1943–1951, 1974.
- R.L. Saltzer, J.B. Gaherty, and T.H. Jordan.
How are vertical shear wave splitting measurements affected by variations in the orientation of azimuthal anisotropy with depth?
Geophysical Journal International, 141:374–390, 2000.
- M. K. Savage.
Seismic anisotropy and mantle deformation: What have we learned from shear wave splitting?
Reviews of Geophysics, 37(1):65–106, February 1999.
- M. K. Savage, X.R. Shih, R.P. Meyer, and R.C. Aster.
Shear-wave anisotropy of active tectonic regions via automated S-wave polarization analysis.
Tectonophysics, 165:279–292, 1989.
- M.K. Savage, W.A. Peppin, and U.R. Vetter.
Shear wave anisotropy and stress direction in and near Long Valley caldera, California, 1979–1988 .
Journal of Geophysical Research, 95(B7):11,165–11,177, 1990.
- S. Sherburn and C.J. Bryan.
The Eruption Detection System: Mt. Ruapehu, New Zealand.
Seismological Research Letters, 70(5):505–511, 1999.
- P.G. Silver and W.W. Chan.
Shear wave splitting and subcontinental mantle deformation.
Journal of Geophysical Research, 96(B10):16,429–16,454, September 1991.
- P.G. Silver and M.K. Savage.
The interpretation of shear-wave splitting parameters in the presence of two anisotropic layers.
Geophysical Journal International, 119(3):949–963, 1994.
- E.G.C. Smith, T. Stern, and M. Reyners.
Subduction and back-arc activity at the Hikurangi convergent margin, New Zealand.
Pure & Applied Geophysics, 129(1-2):203–231, 1989.
- I.N. Sneddon.
The distribution of stress in the neighbourhood of a crack in an elastic solid.
Proc. Roy. Soc. London, A 187:229–260, 1946.

- T.A. Stern.
A back-arc basin formed within continental lithosphere: The Central Volcanic Region of New Zealand.
Tectonophysics, 112:385–409, 1985.
- T.A. Stern.
Asymmetric back-arc spreading, heat flux and structure associated with the Central Volcanic Region of New Zealand.
Earth and Planetary Science Letters, 85:265–276, 1987.
- T.A. Stern and F.J. Davey.
Crustal structure studies within the central North Island: the Central Volcanic Region.
Dep. Sci. Ind. Res., Geophys. Div. Rep., 207:47 pp., 1985.
- T.A. Stern, E.G.C. Smith, F.J. Davey, and K.J. Muirhead.
Crustal and upper mantle structure of the northwestern North Island, New Zealand, from seismic refraction data.
Geophysical Journal of the Royal Astronomical Society, 91:913–936, 1987.
- W. Stratford and T. Stern.
Crust and upper mantle structure in a continental back-arc spreading zone: Central North Island, New Zealand.
Eos Transactions AGU, West. Pac. Geophys. Meet. Suppl., 83(22):Abstract SE32B–05, 2002.
- K. Tadokoro and M Ando.
Evidence for rapid fault healing derived from temporal changes in S wave splitting .
Geophysical Research Letters, 29(4):6–1 to 6–4, 2002.
- A. Takada.
The influence of regional stress and magmatic input on styles of monogenetic and polygenetic volcanism.
J. Geophys. Res., 99:13,563–13,573, 1994.
- W. C. Tapley, J. E. Tull, L. Miner, and P. Goldstein.
SAC2000 Command reference manual Version 10.5d.
University of California, 1990.
- B. Taylor and G.D. Karner.
On the evolution of marginal basins.
Reviews of Geophysics and Space Physics, 21(8):1727–1741, 1983.
- S. Toda, A. Yoshida, R.S. Stein, P.A. Reasenberg, and J.H. Dieterich.
Stress transferred by the 1995 $M(w) = 6.9$ Kobe, Japan, shock: Effect on aftershocks and future earthquake probabilities.
J. Geophys. Res., 103(B10):24,543–24,565, 1998.
- J. Townend and M. D. Zoback.
How faulting keeps the crust strong.
Geology, 28:399 – 402, 2000.
- P. Villamor and K. Berryman.
A late Quaternary extension rate in the Taupo Volcanic Zone, New Zealand, derived from fault slip data.

- New Zealand Journal of Geology and Geophysics*, 44(2):243–269, 2001.
- L.P. Vinnik, V. Farra, and B. Romanowicz.
Azimuthal anisotropy in the Earth from observations of SKS at GEOSCOPE and NARS broadband stations.
Bulletin - Seismological Society of America, 79(5):1542–1558, 1989.
- L.P. Vinnik, L.I. Makeyeva, A. Milev, and A.Y. Usenko.
Global patterns of azimuthal anisotropy and deformations in the continental mantle.
Geophysical Journal International, 111(3):433–447, 1992.
- R.I. Walcott.
Geodetic strains and large earthquakes in the axial tectonic belt of North Island, New Zealand.
Journal of Geophysical Research, 83(B9):4419–4429, September 1978.
- R.I. Walcott.
Reconstructions of the New Zealand region for the Neogene.
Palaeogeography, Palaeoclimatology, Palaeoecology, 46(1-3):217–231, 1984.
- P. Wessel and W. H. F. Smith.
The Generic Mapping Tools (GMT) version 3.4, Technical Reference & Cookbook.
SOEST/NOAA, 2001.
- Karen Williams.
Volcanoes Of The South Wind - A field guide to the volcanoes and landscape of Tongariro National Park.
Tongariro Natural History Society, PO Box 238, Turangi, New Zealand, 2001.
- C. J. N. Wilson, B. F. Houghton, M. O. McWilliams, M. A. Lamphere, S. D. Weaver, and R. M. Briggs.
Volcanic and structural evolution of Taupo Volcanic Zone, New Zealand: a review.
J. Volc. Geotherm. Res., 68:1–28, 1995.
- J. Wookey, J.M. Kendall, and G. Barruol.
Mid-mantle deformation inferred from seismic anisotropy.
Nature, 415:777–780, February 2002.
- I.C. Wright and R.I. Walcott.
Large tectonic rotation of part of New Zealand in the last 5 Ma.
Earth and Planetary Science Letters, 80:348–352, 1986.
- S. V. Zatsepin and S. Crampin.
Modelling the compliance of crustal rock - I. Response of shear-wave splitting to differential stress.
Geophys J Int., 129:477–494, 1997.
- Z. Zhang and S. Y. Schwartz.
Seismic anisotropy in the shallow crust of the loma prieta segment of the san andreas fault system.
Journal of Geophysical Research, 99:9651–9661, 1994.

J. C. Zinke and M. D. Zoback.

Structure-related and stress-induced shear-wave velocity anisotropy: Observations from microearthquakes near the Calaveras Fault in Central California.

Bulletin of the Seismological Society of America, 90(5):1305–1312, 2000.

M. D. Zoback and J. Townend.

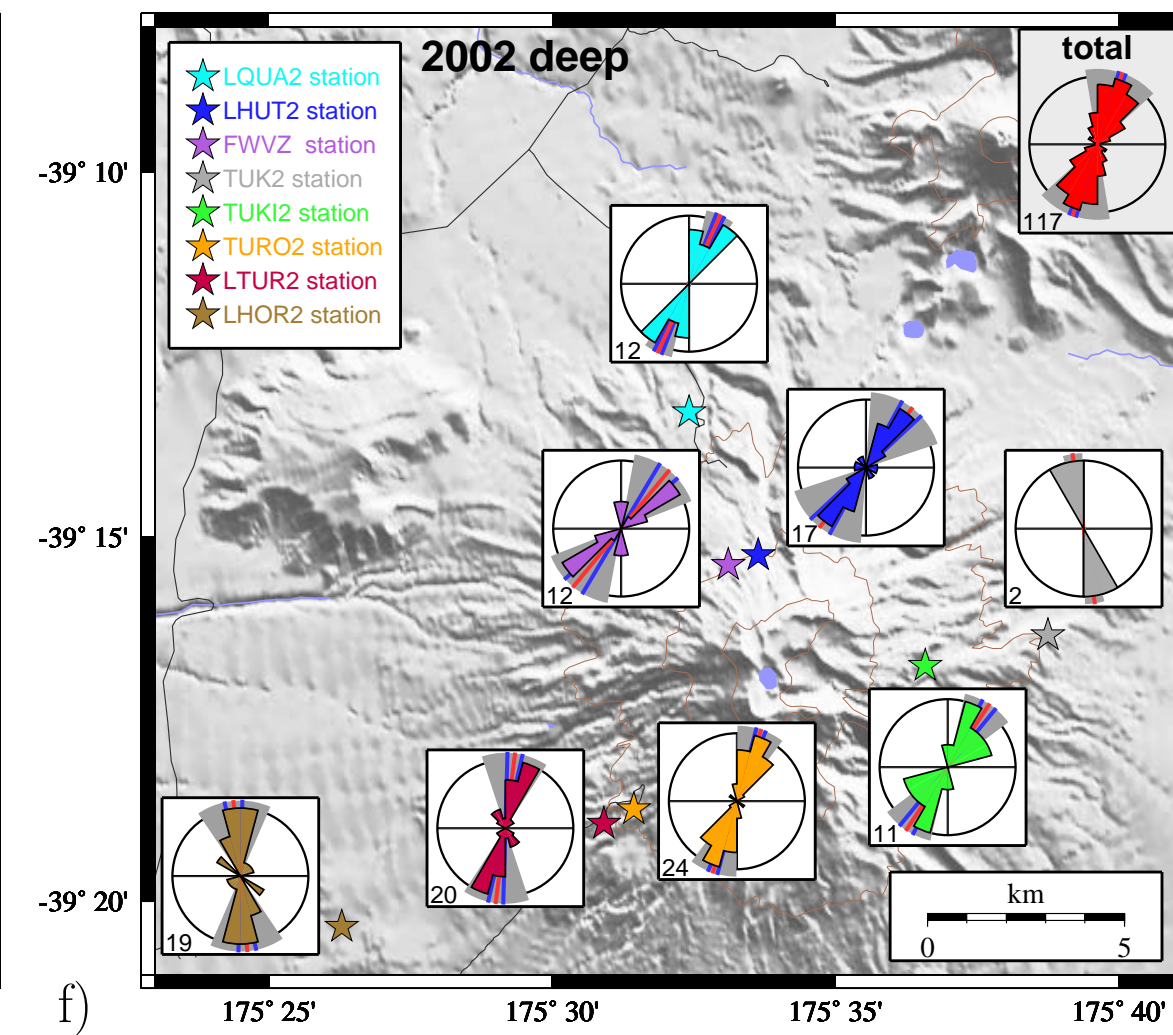
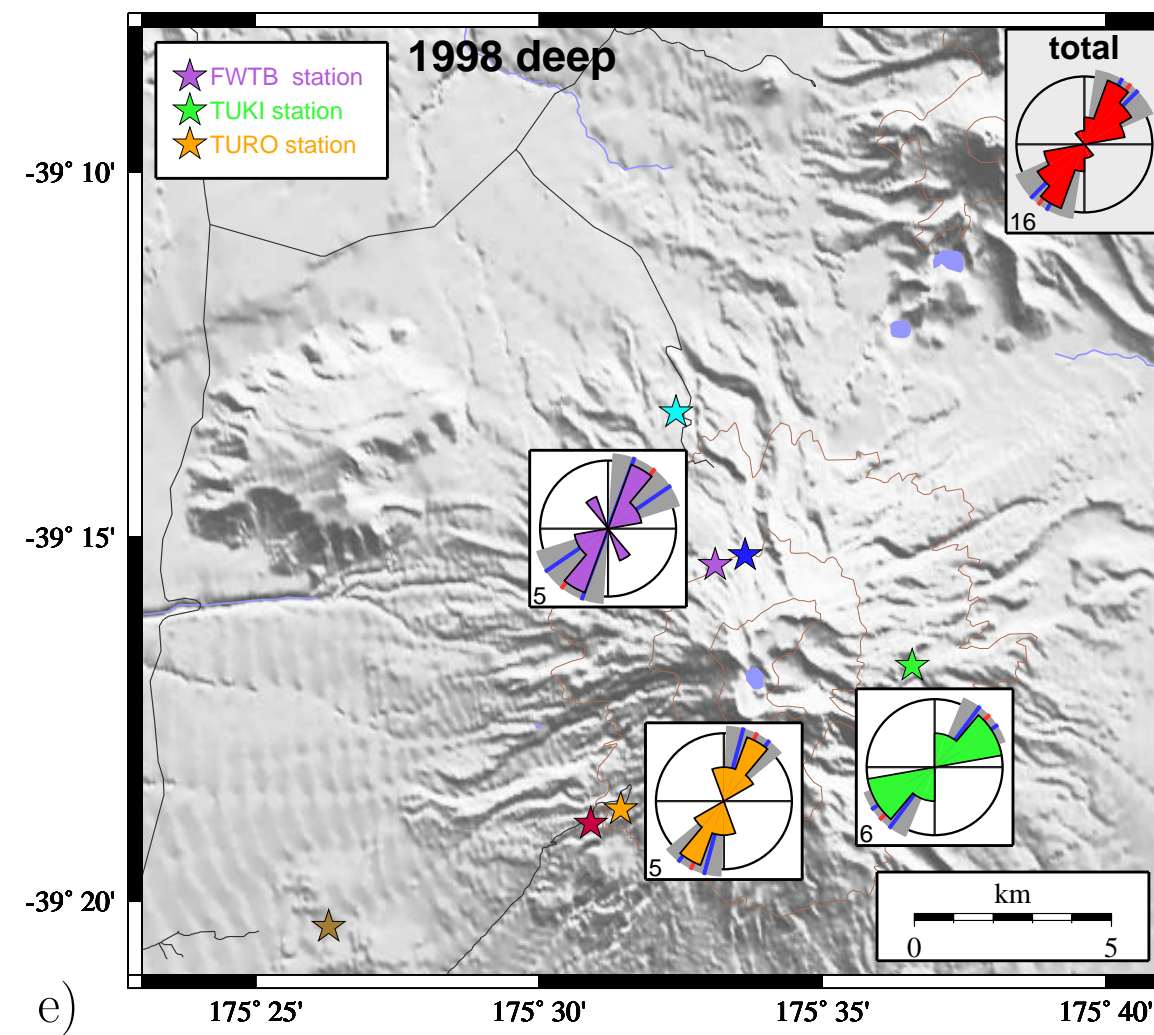
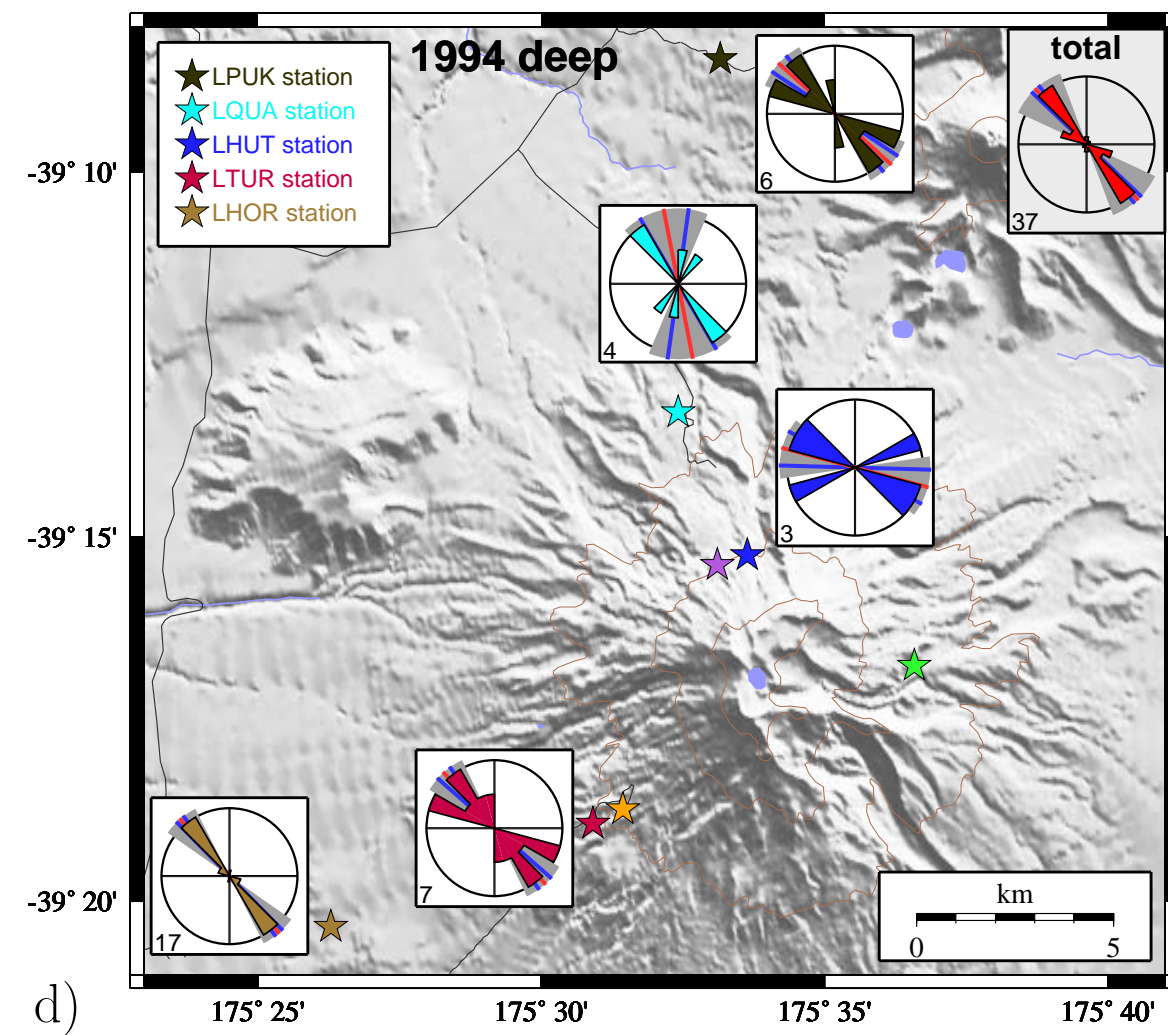
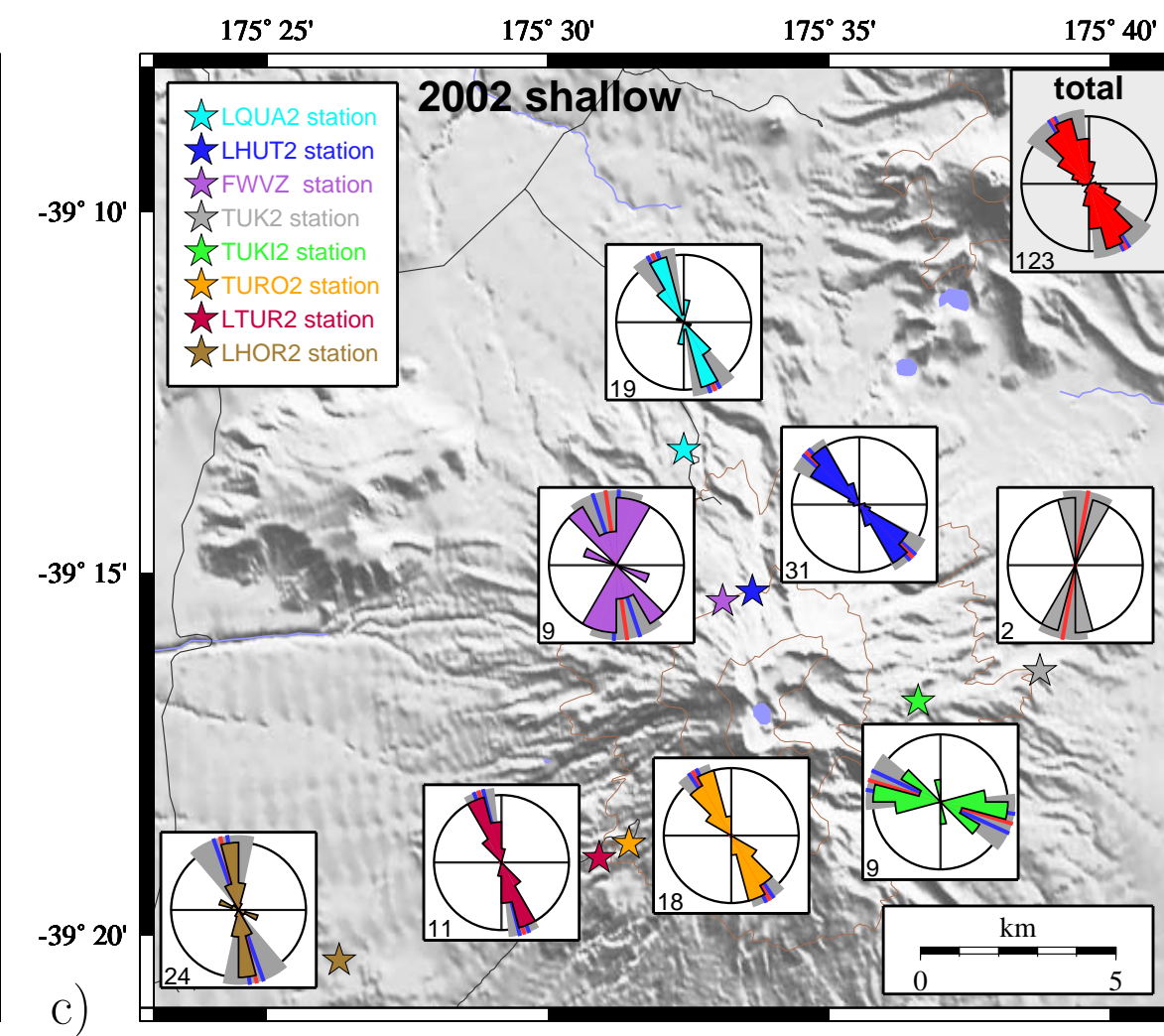
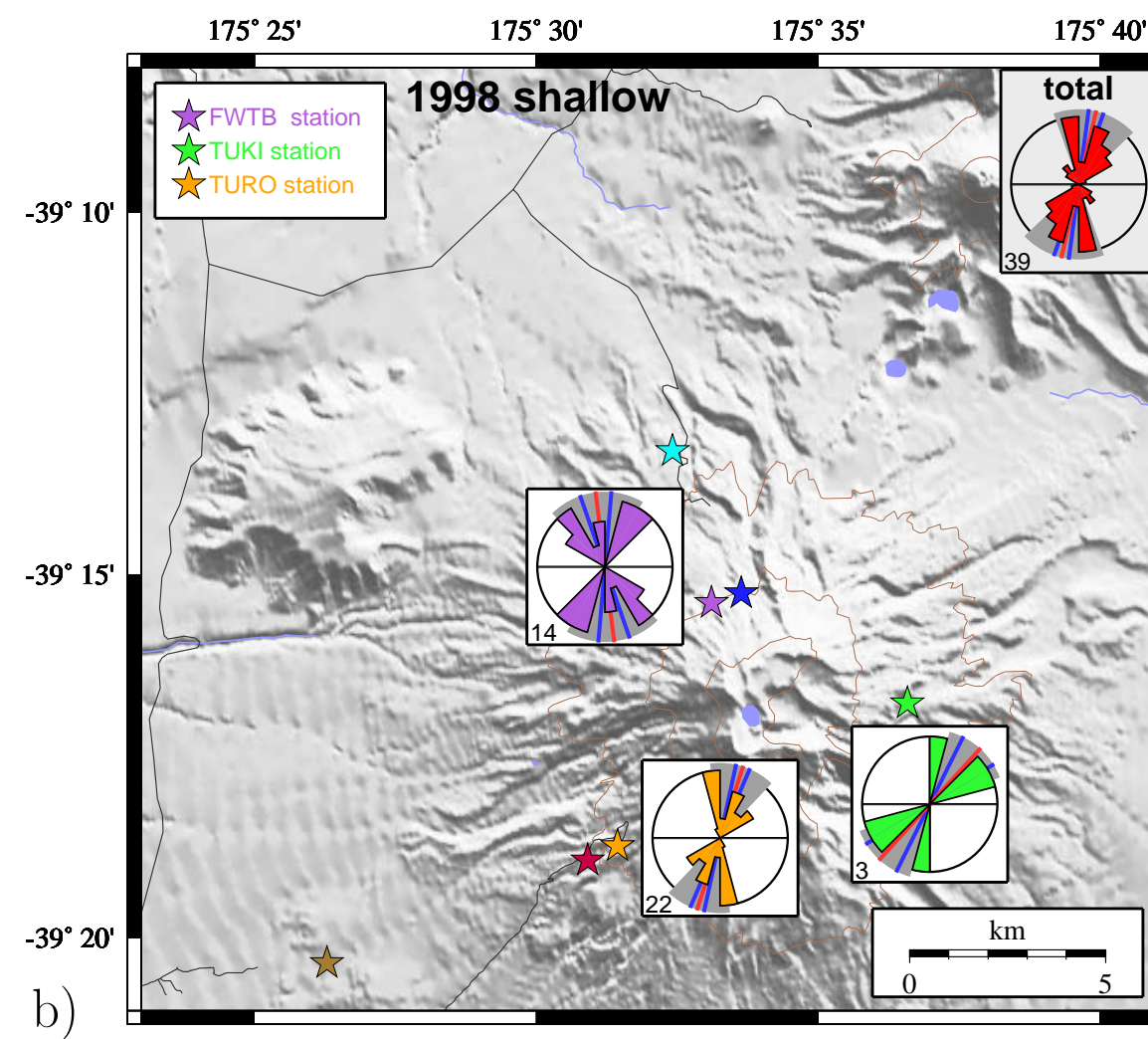
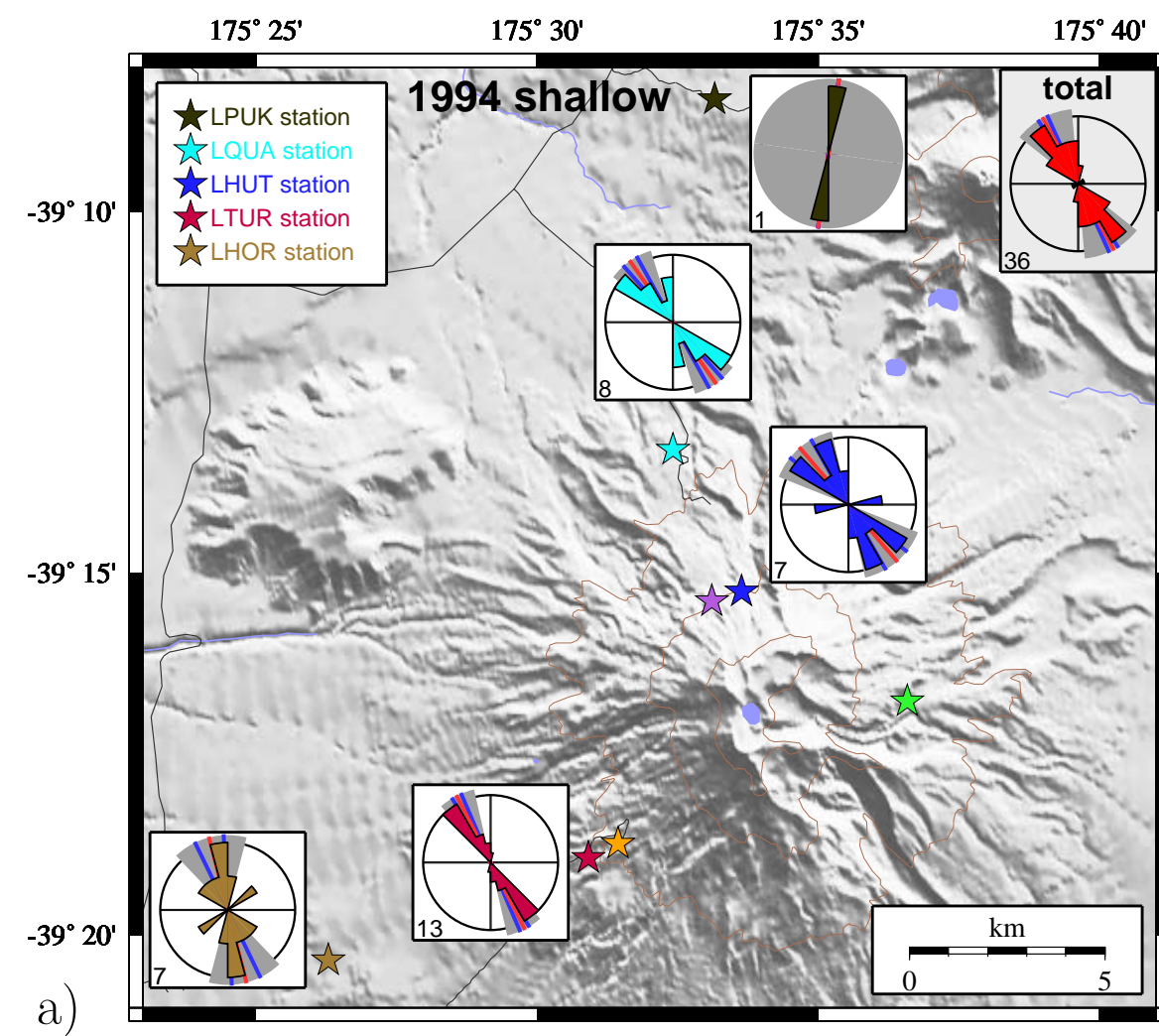
Implications of hydrostatic pore pressures and high crustal strength for the deformation of intraplate lithosphere.

Tectonophysics, 336:19–30, 2001.

Index

- Aki and Richards (1980), 18, 92, 171
 Anderson and Webb (1994), 5, 11, 171
 Angerer et al. (2001), 124, 171
 Aster et al. (1990), 32, 171
 Aster et al. (1991), 32, 171
 Audoine (2002), 3, 9, 25, 26, 28, 37, 103, 104, 110, 171
- Babuška and Cara (1991), 3, 17, 19, 20, 23, 27, 28, 137, 171
 Bianco et al. (1999), 30, 31, 171
 Bibby et al. (1995), 9, 171
 Bokelmann and Harjes (2000), 33, 171
 Booth et al. (1985), 3, 31, 32, 171
 Booth et al. (1990), 33, 172
 Booth et al. (1992), 30, 31, 172
 Bowman and Ando (1987), 25, 172
 Bryan and Sherburn (1999), 14, 109, 117, 126, 172
- Calhaem (1973), 7, 172
 Chen (1987), 3, 31, 33, 172
 Cole (1990), 5, 7, 9, 11, 172
 Cole et al. (1995), 9, 103, 172
 Crampin (1984), 17, 24, 172
 Crampin (1987), 23, 172
 Crampin (1994), 23, 29, 108, 172
 Crampin (1998), 120, 172
 Crampin and Booth (1985), 23, 29, 173
 Crampin and Lovell (1991), 23, 24, 28, 29, 122, 173
 Crampin and Zatsepin (1997), 34, 173
 Crampin et al. (1984a), 23, 24, 32, 173
 Crampin et al. (1984b), 23, 31, 173
 Crampin et al. (1990), 23, 32, 108, 173
 Crampin et al. (1991), 32, 42, 173
 Crampin et al. (1996), 124, 125, 173
 Crampin et al. (1999), 33, 173
 Crampin et al. (2002), 124, 125, 173
 Crouch and Starfield (1983), 117, 173
- Dade and Huppert (1996), 4, 173
- Darby and Meertens (1995), 9, 174
 Davis (1986), 52, 53, 55, 57, 76, 174
 DeMets et al. (1990), 5, 6, 174
- Evans et al. (1995), 31, 174
- Fischer and Wiens (1996), 25, 174
 Fisher et al. (1997), 4, 174
- Gamble et al. (1993), 9, 174
 Gamble et al. (2003), 11, 12, 14, 174
 GEONET (2001), 174
 Gledhill (1991a), 31, 174
 Gledhill (1991b), 3, 174
 Gudmundsson (2002), 106, 174
 Gupta (1973), 32, 175
- Hackett and Houghton (1989), 10, 12, 175
 Hagerty and Benites (2003), 29, 175
 Hayes (2002), 15, 175
 Healy (1954), 4, 175
 Hofmann (2002), 7, 175
 Houghton et al. (1987), 12, 13, 175
 Houghton et al. (1995), 9, 175
 Hrouda et al. (1993), 120, 175
 Hurst (1998), 15, 64, 175
 Hurst and McGinty (1999), 103, 126, 175
- Johnston et al. (2000), 13, 14, 175
 Jung and Karato (2001), 25, 176
- Kaneshima and Silver (1992), 25, 176
 Kendall and Silver (1996), 25, 176
 Kennett (1991), 49, 176
 Kern (1990), 23, 176
 Krumbein (1939), 53, 176
- Latter (1981), 14, 49, 105, 106, 117, 125, 130, 176
 Latter (1986), 4, 176
 Lay and Wallace (1995), 18, 50, 92, 137, 176
 Lees and Wu (1999), 30, 176
 Liu et al. (1997), 33, 42, 176

- Love (1927), 21, 176
- Mainprice and Silver (1993), 25, 177
- Malhoff et al. (1982), 8, 177
- Manville et al. (1998), 13, 177
- Mardia (1972), 52–56, 177
- Marson (1997), 26, 103, 177
- Marson-Pidgeon and Savage (1997), 3, 116, 177
- Marson-Pidgeon et al. (1999), 103, 177
- Maunder (1999), 65, 177
- Miller (2000), 3, 8, 11, 64, 65, 70, 145, 177
- Miller and Savage (2001), 1, 2, 31, 37, 119, 125, 177
- Munson and Thurber (1993), 3, 30, 177
- Munson et al. (1995), 3, 30, 31, 177
- Nairn and Scott (1996), 12–14, 109, 117, 177
- Nakagawa et al. (1999), 109, 117, 178
- Nakamura (1977), 10, 178
- Neuberg and Pointer (2000), 29, 178
- Nicolas and Christensen (1987), 24, 178
- Nur and Simmons (1969), 23, 178
- Nuttli (1961), 28, 178
- Okada (1992), 117, 178
- Peacock et al. (1988), 32, 108, 178
- Peterson (1986), 4, 178
- Press and Siever (2000), 106, 178
- Rümpker and Silver (1998), 116, 178
- Reyners and Stuart (2002), 11, 178
- Russo and Silver (1994), 26, 27, 179
- Ryall and Savage (1974), 32, 179
- Saltzer et al. (2000), 3, 116, 179
- Savage (1999), 19, 25–27, 29, 108, 179
- Savage et al. (1989), 3, 23, 29, 31, 179
- Savage et al. (1990), 27, 31, 179
- Sherburn and Bryan (1999), 13, 60, 179
- Silver and Chan (1991), 24, 25, 38, 40, 41, 179
- Silver and Savage (1994), 3, 28, 29, 110, 116, 179
- Smith et al. (1989), 7, 179
- Sneddon (1946), 120, 179
- Stern (1985), 7, 9, 179
- Stern (1987), 7, 9, 180
- Stern and Davey (1985), 7, 9, 180
- Stern et al. (1987), 7, 180
- Stratford and Stern (2002), 7, 180
- Tadokoro and Ando (2002), 34, 180
- Takada (1994), 121, 180
- Tapley et al. (1990), viii, 180
- Taylor and Karner (1983), 7, 180
- Toda et al. (1998), 117, 180
- Townend and Zoback (2000), 120, 180
- Villamor and Berryman (2001), 8, 180
- Vinnik et al. (1989), 26, 181
- Vinnik et al. (1992), 24, 181
- Walcott (1978), 5, 181
- Walcott (1984), 7, 181
- Wessel and Smith (2001), viii, 181
- Williams (2001), 12, 181
- Wilson et al. (1995), 7–9, 181
- Wookey et al. (2002), 25, 181
- Wright and Walcott (1986), 7, 181
- Zatsepin and Crampin (1997), 109, 124, 181
- Zhang and Schwartz (1994), 31, 124, 181
- Zinke and Zoback (2000), 31, 124, 181
- Zoback and Townend (2001), 121, 182



Enlargement of Figure 5.5: Overview over the splitting results from 1994 (left), 1998 (center), and 2002 (right).

Results for shallow events are shown in the top figures, results for deep events are shown at the bottom figures.

The histograms visualise the number of measurements in every 15° angle segment of the fast direction for each station. In each histogram, the underlying grey area shows the standard deviation of the fast directions, the red bar shows the mean fast direction, and the blue bar shows the standard deviation of the mean fast direction (= std. error). The numbers in the corner of the histograms show the number of measurements that were taken into account.

The histogram in the upper right corner of each plot shows the overall trend of the respective subset, and includes fast directions from all stations.